



This work is protected by copyright and other intellectual property rights and duplication or sale of all or part is not permitted, except that material may be duplicated by you for research, private study, criticism/review or educational purposes. Electronic or print copies are for your own personal, non-commercial use and shall not be passed to any other individual. No quotation may be published without proper acknowledgement. For any other use, or to quote extensively from the work, permission must be obtained from the copyright holder/s.



Kinematics and age spreads of the young star-forming region NGC 2264

Amy Dobson

A thesis submitted to Keele University
for the Degree of Doctor of Philosophy

Department of Astrophysics, University of Keele.

July 2016

Abstract

While stars are relatively well understood, the timescales on which they form are still debated. The young cluster NGC 2264 is an ideal region in which to test hypotheses about the timescale of star and cluster formation. Co-eval stars at any given effective temperature are expected to have similar luminosities and radii, but previous research on clusters, including NGC 2264, has found that this may not be the case. In this thesis, fibre spectroscopy from the FLAMES spectrograph is used to find radial and projected equatorial velocities for many low-mass pre-main sequence stars in NGC 2264. Projected radii are estimated by combining these data with published rotation periods. The projected radius distribution is compared with models incorporating radius and age dispersions. These methods circumvent many uncertainties that arise when using luminosities to infer ages from the Hertzsprung-Russell diagram (HRD). Comparisons of models and data favour a spread of radii that is inconsistent with a coeval population but consistent with the spread of ages seen in the HRD. Model-dependent, but distance-independent, ages of 1 - 2.6 Myrs are found, and agreement with ages determined from the HRD is found for a cluster distance of 770 ± 46 pc. The cluster velocity dispersion is well resolved, and a connection between spatial and kinematic substructure is established. The substructure is unlikely to be responsible for the observed age dispersion. A catalogue of 547 spectroscopic observations of stars in NGC 2264 is presented, with measurements of radial and projected equatorial velocities.

Acknowledgements

This Ph.D. was funded by the STFC and supported by Keele University. I remain thankful to both for making this research possible.

I would like to thank my supervisor Rob Jeffries for providing me with the opportunity to perform the research in this thesis, for the time spent teaching me about the topic, and for his guidance throughout the project. I would also like to thank Richard Jackson for his assistance throughout the first few years of the project, and my second supervisor, Barry Smalley, for his discussions on the final chapters of this thesis.

I am grateful to my family, particularly my parents, for supporting me throughout my education, and to Tom and Honor for reminding me that there is life outside of academia. To my friends, Liz, Laura, Lianne, Stefan and Laura W - 16 years and counting! Finally, I thank Jason, my partner in crime, for his support and patience, and for making me realise that nothing is ever out of reach.

Contents

Abstract	iii
Acknowledgements	iv
1 Introduction	1
1.1 Star formation	1
1.1.1 Molecular cloud collapse	1
1.1.2 Embedded protostellar phase	2
1.1.3 T Tauri stars	3
1.1.4 Angular momentum evolution	4
1.1.5 Observationally defined classifications	5
1.1.6 Star clusters	6
1.1.7 Cluster definition	8
1.2 Timescales for star formation	10
1.2.1 Fast versus slow star formation	11
1.2.2 Theories of slow star formation	11
1.2.3 Theory of fast star formation	12
1.2.4 Observational evidence	13
1.2.5 Luminosity and age spreads	14
1.3 Pre-Main sequence evolutionary models	16
1.3.1 Pre-Main sequence model comparisons	19
1.3.2 Accreting pre-main sequence models	21
1.3.3 Converting between the theoretical and observational plane	23
1.4 Kinematics in young clusters	24
1.5 The young cluster, NGC 2264	27
1.5.1 Distance	28
1.5.2 Ages and age spreads	29
1.5.3 Cluster reddening	34
1.5.4 Cluster substructure	35
1.5.5 Rotation	38
1.6 Unanswered questions on star formation	39
2 Instrumentation and data reduction	41
2.1 Introduction	41
2.2 Instrumentation: FLAMES and the Giraffe spectrograph	42
2.3 Data reduction pipeline	43
2.3.1 Processing the calibration files	44
2.3.2 Optimal extraction	45
2.3.3 Wavelength calibration	46
2.3.4 Sky Subtraction	48

2.3.5	The median spectra	50
2.3.6	Telluric correction	52
3	Spectroscopic observations and the determination of stellar parameters	54
3.1	Introduction	54
3.2	Target selection	55
3.2.1	Contamination by non-members of the cluster	56
3.3	Instrumental setup and observations	58
3.4	Radial and rotational velocity measurements	61
3.4.1	Using the cross-correlation technique to measure RVs and $v \sin i$ s	61
3.4.2	Projected equatorial rotational velocities	64
3.4.3	Radial velocity and $v \sin i$ errors	67
3.4.4	External validation of RVs and $v \sin i$ s	70
3.5	Extinction and cluster reddening	70
3.5.1	Individual extinctions	71
3.5.2	Is the V–I colour affected by accretion?	77
3.6	Luminosity and effective temperature determination	79
3.6.1	Effective temperature errors	80
3.6.2	Luminosity errors	81
3.7	Calcium triplet lines	82
3.7.1	Measurements of CaT equivalent widths	82
3.8	Summary	89
4	Probing age spreads with rotation rates	91
4.1	Introduction	91
4.2	Ages estimated from the HR diagram	92
4.2.1	Applying a binary correction factor	96
4.3	Modelling the $R \sin i$ distribution	98
4.3.1	Observational constraints, limits and biases	99
4.4	Models for the intrinsic radius distribution	101
4.5	Results	102
4.5.1	Projected stellar radii	102
4.5.2	A coeval model	107
4.5.3	Testing the dependence on assumed T_{eff} errors and threshold inclination angle	109
4.5.4	Modelling the radius dispersion	109
4.5.5	A log-normal age distribution	112
4.5.6	An exponential distribution of ages	117
4.5.7	Ages based upon the HR diagram and the cluster distance correction	120
4.6	Does the adopted value of the extinction affect the results?	124

4.7	Conclusions and summary	126
5	Substructure in NGC 2264	128
5.1	Introduction	128
5.2	Kinematic substructure in NGC 2264	129
5.2.1	How radial velocity correlates with position, $R \sin i$ and age . .	130
5.2.2	Is there evidence of a foreground or background population? .	135
5.3	Stars around S Mon and HD 47887	151
5.4	Accreting stars in NGC 2264	155
5.5	Summary	157
6	Discussion and recommendations for future work	160
6.1	Implications for NGC 2264	160
6.1.1	Ages and age spreads	160
6.1.2	Structure and sub-clusters	165
6.1.3	Radius spreads caused by structure	169
6.2	Future work	170
6.3	Thesis summary	171
A	Appendix 1	173
A	Appendix 2	194
	Bibliography	196

List of Figures

1.1	The expected spectral energy distributions (SEDs) of class 0, I, II and III sources (from Lada (1999b)). The vertical lines mark $2.2\mu\text{m}$	7
1.2	The Dartmouth, DAM97 and SDF00 theoretical evolutionary isochrones and mass tracks for low-mass pre-MS stars.	18
1.3	A comparison of three sets of pre-MS isochrones.	20
1.4	The colour-magnitude diagram of NGC 2362 cluster stars with the isochrones at 1, 3, 10, 30, and 100 Myrs and masses between 0.1 and $1 M_{\odot}$	22
1.5	A labelled image of NGC 2264	36
2.1	Examples of a raw arc image, flat field, science image and simcal. . . .	45
2.2	Example of an arc spectrum. The dashed lines were those used in the arc process of the data reduction pipeline.	47
2.3	Example of a sky spectrum.	48
2.4	Representative high signal-to-noise spectra of a target in the open cluster NGC 2264 along with the median of these.	51
2.5	An example of two telluric standards of different airmass used in the telluric correction process.	53
3.1	Spatial distribution of targets in the open cluster NGC 2264.	57
3.2	Rotation periods of main sequence stars.	58
3.3	An example of a cross-correlation function.	62
3.4	An example a CCF from which an RV or width was unable to be measured.	63
3.5	A histogram of the RVs between 15 and 30km/s (which includes 95% of the measured RVs) obtained for the primary and secondary targets in NGC 2264. The standard deviation of the RV dispersion is 3.55km/s.	64
3.6	The calibration curve produced when artificially broadening a standard template spectrum to $v \sin i$ values between 0 and 70km/s.	66
3.7	The $v \sin i$ values of the primary and secondary targets with a clear peaks in the CCF.	67
3.8	A curve fit to the data which shows a relation between the spectra SNR and the measured $v \sin i$	69
3.9	A histogram of the difference in RVs between the targets in our catalogue and the RVs from Tobin et al. (2015).	71
3.10	The photometric V–I colours and V–I colours expected from spectral classification.	72
3.11	The individual reddening values against RA and DEC.	74
3.12	The positions of the targets used to determine individual reddening values.	75

3.13	The distribution of $E(V-I)$ with the best-fitting Gaussian. The values of $E(V-I)$ were determined by comparing the colours, and the colours expected from spectral classification. The standard deviation is 0.17mag.	76
3.14	The relation between the difference in bolometric magnitude derived from the V and I bands against the bolometric magnitude derived from the V band for both the primary targets and the candidate members (secondary targets).	78
3.15	Images showing the measurements of CaT EWs of target stars.	85
3.16	The EW measurement process for stars with small CaT EWs that are unlikely to be due to accretion.	86
3.17	Images showing the measurements of CaT EWs of target stars exhibiting large and broad of CaT emission, characteristic of heavily accreting stars.	87
3.18	The relation between the measured EWs for the 8542Å line and the 8498Å line.	88
3.19	An example of the difference spectrum and the regions of the spectrum used to estimate the EW error associated with noise in the spectrum on either sides of the peak.	89
4.1	A HR diagram showing the sample of observed targets in NGC 2264 and the targets with known rotation periods which are within the limits and thresholds described in section 4.3.1 with the Dartmouth isochrones.	93
4.2	A HR diagram showing the sample of observed targets in NGC 2264 and the targets with known rotation periods which are within the limits and thresholds described in section 4.3.1 with the DAM97 isochrones.	94
4.3	A HR diagram showing the sample of observed targets in NGC 2264 and the targets with known rotation periods which are within the limits and thresholds described in section 4.3.1 with SDF00 isochrones.	95
4.4	Histograms showing the ages and \log_{10} ages of the sample targets used in this analysis derived from the HR diagrams in Figures 4.1, 4.2 and 4.3	97
4.5	The normalised projected radii against T_{eff} for the rotation sample.	103
4.6	As Figure 4.5 with the DAM97 isochrones.	104
4.7	As Figure 4.5 with the SDF00 isochrones.	105
4.8	The distributions of $(R \sin i)_{\text{obs}}/R_{3\text{Myr}}$ compared with models assuming a coeval population and the cumulative distributions used for the KS tests.	106
4.9	The distribution of $(R \sin i)_{\text{obs}}/R_{3\text{Myr}}$ compared with the models that have a Gaussian dispersion in $\log_{10}R$ (σ_r).	110
4.10	The relative probability that the observed data distribution of $(R \sin i)_{\text{obs}}/R_{3\text{Myr}}$ can be represented by a model consisting of a log-normal distribution of ages as a function of the central (log) age and the dispersion in (log) age.	114

4.11	The normalised probability density plot showing the age distribution which decays exponentially on a time-scale of λ_a from a maximum at the zero point age.	116
4.12	The normalised probability density, integrated over all possible ages, showing the age distribution which decays exponentially on a time-scale of λ_a from a maximum at the zero point age.	118
4.13	The distributions of the normalized projected radii (also shown in Figures 4.8) along with the cumulative distribution functions of these distributions.	121
4.14	The distributions of the normalized projected radii along with the cumulative distribution functions of these distributions.	123
5.1	RV versus right ascension (RA) for the primary targets.	132
5.2	RV versus declination (DEC) for the primary targets.	132
5.3	RV versus $R \sin i$ for the primary targets.	133
5.4	RV versus age determined from the HR diagram using the SDF00 model isochrones for the primary targets.	134
5.5	The targets separated into 2 km/s bins and plotted according to their position over the Digitized Sky Survey images (from STScI) image. . .	136
5.6	Histograms showing the distributions of the RVs of the primary targets along with the four separate sub-groups used to examine any possible RV substructure.	137
5.7	Density plots illustrating the density of the targets according to their position in the cluster.	139
5.8	The distributions of $(R \sin i)_{\text{obs}}/R_{3\text{Myr}}$ for the four separated groups, along with the models of a Gaussian dispersion in radius of σ_r which minimise the KS statistic when compared with the modelled distribution. 141	
5.9	Comparing the cumulative distribution functions of $(R \sin i)_{\text{obs}}/R_{3\text{Myr}}$ for each group, with each other group.	147
5.10	Comparing the cumulative distribution functions of HR diagram age distributions of each group, with each other group.	148
5.11	Comparing the cumulative distribution functions of the $(R \sin i)_{\text{obs}}/R_{3\text{Myr}}$ distributions of each group, with the distribution of those targets not in that group.	149
5.12	Comparing the cumulative distribution functions of HR diagram age distributions of each group, with the distribution of those targets not in that group (see Table 5.1 for a definition of each RV group).	150
5.13	The positions of the primary targets and those targets used as subgroups. 152	
5.14	The cumulative distribution functions of comparing the HR diagram age distributions and the $(R \sin i)_{\text{obs}}/R_{3\text{Myr}}$ distributions of each group, with the distributions of either; those targets not in the group, or those targets in the other group.	154

5.15	A histogram of the CaT equivalent widths of the primary targets and the stars showing accretion signatures.	156
5.16	The positions of the primary targets, the targets around S Mon, the targets around HD 47887, and finally the targets showing accretion signatures.	157
5.17	Histograms showing the age and \log_{10} age of the primary targets and those which are assumed to be accreting according to their CaT line strengths.	158
6.1	The distribution of ages of the sample of stars used in the modelling of the radius distribution compared with the larger sample from Sung et al. (2008).	164

List of Tables

1.1	A summary of the treatment of equation of state (EOS), convection, atmospheres and opacity in the evolutionary models used in this thesis.	17
1.2	Ages that have been presented in the literature for NGC 2264, using a variety of measurement techniques.	32
1.3	The recent age spreads that have been presented in the literature for NGC 2264.	33
3.1	A numerical description of the observations of NGC 2264.	60
4.1	The results obtained when using a Gaussian distribution of $\log(R)$ about a central single isochrone with various standard deviations in \log_{10} normalised radius (σ_r) for three different evolutionary models.	108
4.2	The effect on σ_r when testing the coeval model whilst altering the assumed values of the T_{eff} error and i_{th} . Column 2 shows the age which minimised the KS statistic, and column 5 shown the range of radii dispersions which enclose 90% of the probability.	111
4.3	The results from the KS tests of comparing the observed distribution of $(R \sin i)_{\text{obs}}/R_{3\text{Myr}}$ with models using a log-normal distribution in age.	115
4.4	The results from the KS tests of comparing the observed distribution of $(R \sin i)_{\text{obs}}/R_{3\text{Myr}}$ with models using an exponential distribution in age.	119
4.5	The results of comparing $(R \sin i)_{\text{obs}}/R_{3\text{Myr}}$ distributions with radii distributions determined from the HR diagram ages with KS tests prior to binary correction (discussed in 4.5.7) and using the distance of 760pc to construct the HR diagram.	120
4.6	The results of comparing $(R \sin i)_{\text{obs}}/R_{3\text{Myr}}$ distributions with radii distributions determined from the HR diagram ages (after correcting the luminosities for a binary fraction of 0.5) with KS tests.	122
4.7	The results obtained when using a Gaussian distribution of $\log(R)$ about a central single isochrone with various standard deviations in \log_{10} normalised radius (σ_r) for three different evolutionary models.	125
5.1	The KS test result from comparing the $(R \sin i)_{\text{obs}}/R_{3\text{Myr}}$ distribution with a Gaussian distribution of $\log_{10}R$ about a central value.	142
5.2	The KS test result from comparing the $(R \sin i)_{\text{obs}}/R_{3\text{Myr}}$ distribution with a Gaussian distribution of $\log_{10}R$ about a central value, with altered RV bin ranges.	143
5.3	The results of the KS tests when comparing $R \sin i$ or HR diagram age distributions between RV groups.	145
5.4	A summary table of the results found when comparing the $(R \sin i)_{\text{obs}}/R_{3\text{Myr}}$ distribution with a model assuming a central age and with a Gaussian dispersion in radius of σ_r .	152

5.5	The results of the KS tests between $(R \sin i)_{\text{obs}}/R_{3\text{Myr}}$ distributions of the S Mon and HD 47887 groups, and HR diagram age distributions between the two groups.	153
-----	--	-----

1 Introduction

Research into stellar evolution in the 20th and early 21st centuries has extensively progressed due to both the development of instrumentation and the recent interest in extra-solar planets. Prior to the 20th century, only basic equipment was available to obtain information on the nature and the life of a star. Since the beginning of the 21st century, modern instrumentation has begun to revolutionise our understanding of stars, including their formation and lifetime, the environments in which they are born and die, and the stellar parameters of both single and populations of stars. The majority of stars are thought to have formed as part of stellar associations or clusters (Lada & Lada 2003), with a vast range of stellar masses, luminosities and temperatures found in the same cluster. Stages of star formation can be defined by their observable properties. In this chapter I first present an overview of the stages of the low-mass star formation process, the classes of protostellar objects, and further describe and compare the various models for pre-main sequence (MS) stellar evolution. Finally, I provide an overview of the current literature concerning the young cluster NGC 2264, upon which the research in this thesis is based.

1.1 Star formation

1.1.1 Molecular cloud collapse

The interstellar medium (ISM) consists of gas and dust distributed in the otherwise unoccupied space in a galaxy. The densest regions of the ISM, giant molecular clouds (GMCs) composed predominantly of molecular hydrogen, are the locations in which star formation occurs. GMCs are concentrated towards the galactic plane, specifically within the spiral arms of the Galaxy (Lee et al. 2001) and exhibit cool gas temperatures of between approximately 10 and 20K (Bergin & Tafalla 2007). A process external to the GMC, such as a nearby supernovae or spiral density waves (Shu 1991)

, could be the cause of a disturbance in the distribution of gas and dust, producing dynamical instabilities and forcing the production of high density cores surrounded by the remaining gas and dust from the cloud. For a spherical cloud with mass M , temperature T and radius R , the cloud's kinetic energy is

$$K = \frac{3Mk_B T}{2\mu m_H} \quad (1.1)$$

where μ is the mean molecular weight and m_H is the mass of H_2 . The gravitational energy of the cloud, assuming that it is both spherical, and of uniform density, is

$$U = -\frac{3GM^2}{5R} \quad (1.2)$$

Combining these equations, provides the Jeans length (R_J) and mass (M_J) which provides a limit to the stability of the cloud

$$R_J = \sqrt{\frac{15k_B T}{4\pi m_H \mu G \rho}} \quad (1.3)$$

$$M_J = \left(\frac{3}{4\pi\rho}\right)^{1/2} \left(\frac{5k_B T}{m_H \mu G}\right)^{3/2} \quad (1.4)$$

where ρ is the density of the cloud. A typical Jeans length in the solar neighbourhood is 1 kpc (Bertin 2014). For collapse to occur, gravity must overcome thermal pressure, so star formation only happens in cold clouds (Bergin & Tafalla 2007). If there is insufficient thermal pressure the cloud becomes unstable (Jeans 1902). The distribution of high density regions of a cloud at the birth stage of the star cluster, is a factor in understanding the distribution of stellar masses later on (initial mass function, IMF). It is within these dense regions or cores that star formation occurs.

1.1.2 Embedded protostellar phase

Throughout the protostellar phase, the high density areas in the cloud grow through the accretion of material from the surrounding envelope of gas and dust remaining from the parent molecular cloud. An inflow of this material towards the high density

core produces sub-millimetre emission. The protostellar phase occurs when approximately half of the mass of the core is contained within the accreting protostar, and the remainder in the surrounding region (Andre, Ward-Thompson & Barsony 1993). The protostar remains optically invisible due to the opaque envelope of material masking the protostar's emission. The accretion material slows on the plane perpendicular to the axis of rotation, which causes a build up of material in this vicinity, evolving into a rotating circumstellar disc (Yorke, Bodenheimer & Laughlin 1993).

1.1.3 T Tauri stars

Young, pre-MS stars that are convective descend on near-vertical Hayashi tracks on a Hertzsprung-Russell (HR) diagram (with approximately constant temperature), before reaching the stage where the energy released from the star is dominated by nuclear burning, rather than accretion. The stars evolve with decreasing luminosities (L) with time (t), according to the relation: $L \propto t^{-2/3}$ (Hartmann 2001).

Low-mass and high-mass stars exhibit different evolutionary timescales. The majority of stars have low masses and these will be the focus of this thesis. A T Tauri star is a low-mass, pre-MS variable star with a stellar mass $< 2 M_{\odot}$, and with spectral types F-M (Hartmann 1998). They exhibit strong magnetic fields of a few kG (e.g. Johns-Krull 2007) and strong emission lines. They are optically visible and surrounded by circumstellar discs.

The evolution from a core situated within a molecular cloud to a young star occurs through the process of accretion, whereby the innermost material from the circumstellar disc falls onto the star allowing the star to become hotter. Magnetic fields probably play an important role in the evolution of the disc, forcing infalling material to be channeled along magnetic field lines through the stellar magnetosphere (Hartmann 1998). Disc material from the inner disc is drawn along magnetic field lines with high (free-fall) velocities and impact the surface of the star producing strong blue and UV emission lines and an optical continuum, while the emission in the near infrared J, H, K and L bands arises from the warm dust in the inner disc. Typical dust

temperatures can lead to excess emission in the K-band, especially among low-mass stars. $H\alpha$ (6562.6 Å) and the Calcium triplet emission lines (8498, 8542 and 8662 Å) are often observed in T Tauri stars (e.g. Hillenbrand, Hoffer & Herczeg 2013), which, if stronger than expected from a magnetically heated chromosphere, can be attributed to the accretion process of the star-disc system. These accretion indicators can be used to detect young stars in clusters.

Several surveys have shown two distinctive groups of T Tauri stars, each exhibiting distinguishable features: classical T Tauri stars (CTTSs) and weak-lined T Tauri stars (WTTS, e.g. Herbig & Bell 1988). The division between a CTTS and WTTS when using spectroscopy is often a line equivalent width (EW) caused by accretion, such as $H\alpha$. A $H\alpha$ EW of $>10\text{Å}$ is often used to define CTTSs and $<10\text{Å}$ for WTTSs (Hartmann 1998).

WTTSs differ from CTTSs in that they are not actively accreting material from an optically thick disc. The emission lines of a WTTS are therefore, narrower and weaker when compared to the emission lines from CTTS. The rotational velocities of CTTSs have been measured to be lower than those of WTTSs (e.g. Bouvier et al. 1993), which could show that the interaction between the star's magnetic field and circumstellar disc controls the evolution of angular momentum (see section 1.1.4).

1.1.4 Angular momentum evolution

Angular momentum is conserved throughout the star formation process, and causes the disc to form around the rotating star (Terebey, Shu & Cassen 1984). During the earliest stages of formation, angular momentum loss can be attributed to magnetic torques between the collapsing cloud core and the surrounding material (Larson 1973; Fleck & Hunter 1976). The contraction of the star adds to the increase of angular velocity. As accretion continues in the CTTS phase, angular momentum is transported away from the star and disc via strong winds, jets and outflows (Bouvier et al. 2014). The process of how the star, disc and wind combine to transfer and regulate angular momentum is currently unknown. Observationally, there is evidence that outflow activity is strongly

correlated with the presence of discs and accretion activity (Konigl & Pudritz 2000). The disc removes angular momentum from the protostar which allows the protostar to grow. A proposed theory for the removal of angular momentum by the disc is ‘disc-locking’, which is described as the interaction between the stellar magnetosphere and the disc which reduces the angular velocity of the star (Camenzind 1990; Shu et al. 1994). Correlations have been found between rotation periods and the presence of circumstellar discs in young star clusters supporting disc-locking (e.g. Cieza & Baliber 2009 and Lamm et al. 2005). However, Littlefair et al. (2005) found a difference in period distributions between the two similarly aged young clusters, NGC 2264 and IC 348, presenting a challenge to the disc-locking scenario, considering the similarity in disc fractions between the two clusters.

1.1.5 Observationally defined classifications

The stages of low-mass star formation can be defined observationally, by their spectral energy distributions (SEDs). Lada (1987) proposed three classes of young stellar objects (YSOs), class I, II and III. These classes are ordered by their stage of evolution, and are based upon their spectral index (α) relating their frequency (ν) and flux density (F_ν):

$$\alpha(\nu) = -\frac{d\log(\nu F_\nu)}{d\log \nu}. \quad (1.5)$$

The fourth class (0), proposed by Andre, Ward-Thompson & Barsony (1993), was introduced to include very young objects. The timescales of these classes are based on counting relative numbers of stars in each of the phases, and are ultimately dependent on the age scale for young CTTS/WTTS, which is quite uncertain. The classes are defined as follows,

- **Class 0** objects exhibit extended sub-millimetre continuum emission (see Figure 1.1) due to the presence of a circumstellar dust envelope, and they have a high sub-millimetre to bolometric luminosity ratio, which suggests that the dust envelope mass exceeds the central stellar mass (Andre, Ward-Thompson

& Barsony 2000). The class 0 phase is expected to last no longer than 0.1 Myr (Evans et al. 2009).

- **Class I** SEDs peak at far-IR $\lambda \sim 100\mu\text{m}$ (see Figure 1.1). Their large IR flux is produced by large amounts of circumstellar dust, and they are deeply embedded in dense molecular cloud cores. Optical emission is rarely detected in class I objects (Lada 1999). The class I phase lasts approximately 0.5 Myr (Evans et al. 2009).
- **Class II** exhibit a power-law shape of the IR portion of their SED (see Figure 1.1), which suggests that the IR excess arises in a circumstellar disc which is optically thick. Class II objects lack large infalling envelopes of gas and dust. The transition from class I to class II happens in 0.1-0.4 Myrs for 0.3-3 M_{\odot} stars (Evans et al. 2009). When class II stars have been placed on the HR diagram with isochrones, the derived ages are commonly between 0.5 and 3 Myrs (Feigelson & Montmerle 1999). The disc disperses within ~ 1 Myr for low-mass stars and < 1 Myrs for higher mass stars (Strom 1995). For stars with masses $< 0.5 M_{\odot}$, the accretion discs may persist for ages in excess of 10 Myrs.
- **Class III** SEDs typically peak at visible and IR wavelengths and beyond $\sim 2\mu\text{m}$, the SEDs decrease more rapidly than the SEDs of class II objects. By definition, the class III objects do not display IR excess. The shape of their SEDs are similar to single temperature blackbodies (see Figure 1.1), hence are thought to be dominated by the photospheres of young stars (Lada (1999)).

1.1.6 Star clusters

Clustered stars are thought to form from a single parent molecular cloud, and over their pre-MS lifetime they disperse spatially, with a non-uniform spatial distribution. Young clusters (a few Myrs) have not had sufficient time to disperse on large spatial scales from their initial birth positions and are often still embedded in their parent

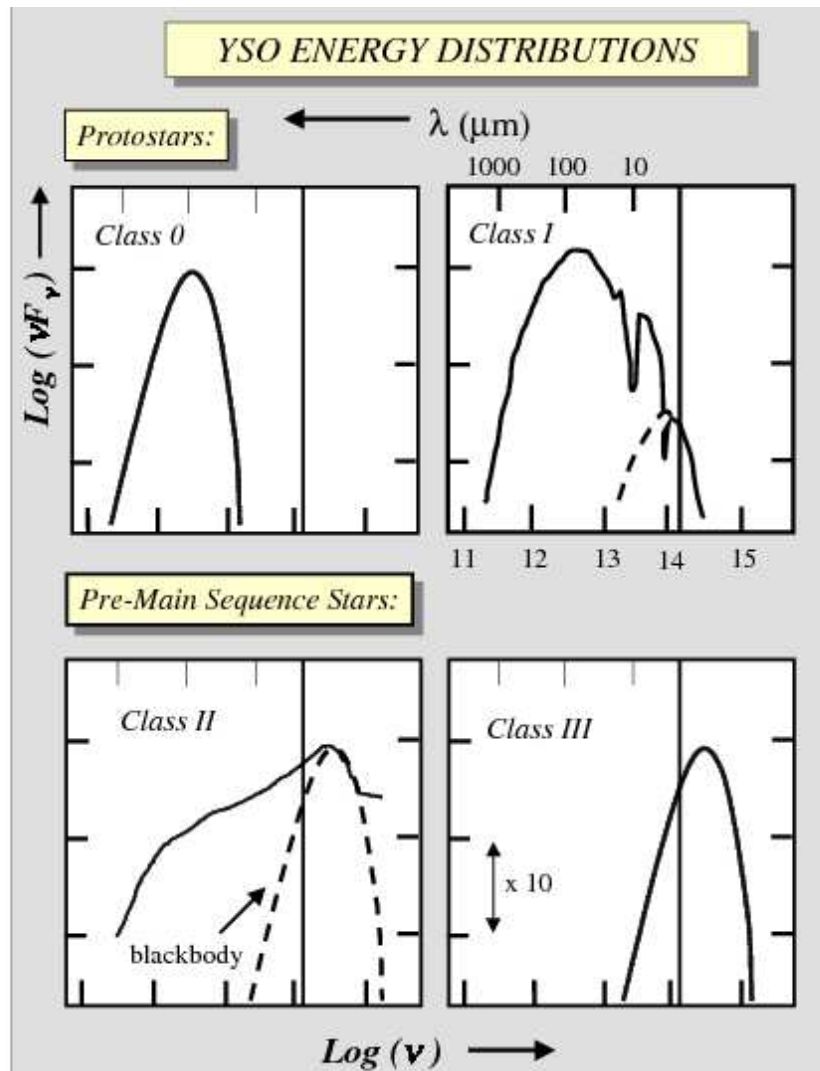


Figure 1.1: The expected spectral energy distributions (SEDs) of class 0, I, II and III sources (from Lada (1999b)). The vertical lines mark $2.2\mu\text{m}$.

molecular cloud (Lada & Lada 2003). Hence, the positions of stars in the early pre-MS phase very closely reflects their birth position (Chabrier 2003). Since massive star formation occurs more rapidly than low-mass star formation due to higher temperatures and pressures, observing high mass stars in clusters gives us a direct insight into the earliest stages of cluster formation. Low-mass stars provide the opportunity to study in detail, spatial distributions and age distributions. There are two types of star clusters, gravitationally bound and unbound. It is possible that unbound groups consist of stars which were formed in dense cores of weakly bound or unbound cloud structures, such as the Taurus star forming region (e.g. Elmegreen et al. 2000). It is also possible that clusters become unbound when they lose their primordial gas (e.g. Baumgardt & Kroupa 2007). A fundamental aspect of determining star formation histories is the position in which stars form in relation to other stars or molecular gas. Lada & Lada (2003) suggested that 70-90% of stars are formed in embedded clusters (groups of stars which are partially or fully embedded in interstellar gas and dust within molecular clouds). Some of these continue to be gravitationally bound, and evolve into open clusters, but most disperse into the Galactic field.

1.1.7 Cluster definition

An underlying problem in star formation studies is determining what constitutes a clustered or non-clustered group of stars. Bressert et al. (2010) studied surface densities of young stellar objects (YSOs) in the solar neighbourhood. They showed a smooth, continuous distribution of stellar surface densities for 12 regions of star formation, and were unable to distinguish between clustered and isolated star formation. Hence, defining clusters based solely on surface density is unreliable.

An alternative approach to defining star clusters is by using a minimum spanning tree (e.g. Gutermuth et al. 2009; Schmeja 2011), which is a network of branches that connect a set of points together, such that the total branch length is minimised and there are no closed loops. The approach allows immediate partitioning of clustered distributions (e.g., Cartwright & Whitworth 2004; Bastian et al. 2009) after adoption of

a threshold as expressed by a critical branch length. The method is useful for separating clusters from a crowded background of stars, and can also be used to detect substructure within clusters. A problem with this method, however, is that the threshold is chosen arbitrarily, with no obvious maximum path threshold with which to define a cluster.

Star clusters can also be defined by the binding energy (BE) of a group of stars, where a negative BE shows a bound system. Extending on this approach, Gieles & Portegies Zwart (2011) define bound clusters based upon the age of the stars (A) and the crossing time ($T_{CR} = \frac{R}{V}$) of the star forming region (SFR) of size R and average velocity V . They suggest that bound clusters have $A/T_{CR} > 1$ and unbound clusters have $A/T_{CR} < 1$.

The definition of a star cluster is difficult, and remaining a debated topic in star formation studies. When clusters are discussed in this thesis, we are referring simply to an over-density with respect to the galactic field population.

1.2 Timescales for star formation

Star formation timescales are a topic of ongoing debate. In this section, I outline the theoretical and observed timescales of the initial stages of the star formation process for low-mass stars.

The free-fall timescale (t_{ff}) of a spherical cloud with density ρ and in the absence of a pressure gradient, is defined as

$$t_{ff} = \left(\frac{3\pi}{32G\rho} \right)^{\frac{1}{2}}. \quad (1.6)$$

which is the time required for the collapse of the cloud to infinite density from a state of rest (Spitzer 1978). Equation 1.6 includes gravitational forces but neglects resistive forces acting such as magnetism and turbulence (a scenario in which kinetic energy cascades from large scales to small scales, Ballesteros-Paredes et al. 2007).

For the typical densities of molecular clouds, the free-fall time (or dynamical time) is ~ 0.4 Myrs (Evans et al. 2009). Very few embedded clusters are found that are older than a few Myrs (Lada & Lada 2003) suggesting that the molecular cloud disperses in the first few millions years the lifetime of a cluster.

The more dense inner regions of the cloud collapse more rapidly than the less dense outer regions. Hence, the density distribution of the collapsing cloud should become increasingly centrally peaked (Larson 1973). The lack of known molecular clouds which are free from star formation indicates that the time between cloud and star formation is short, where the timescales for star formation epochs must not be much more than a few Myr, after which the star forming gas becomes dispersed (Hartmann, Ballesteros-Paredes & Bergin 2001, Ballesteros-Paredes & Hartmann 2007).

The overall pre-MS phase from the birth of the star to the ZAMS strongly depends on the stellar mass (M) according to the Kelvin-Helmholz timescale (t_{KH}):

$$t_{KH} \simeq \frac{GM^2}{RL} \quad (1.7)$$

where R and L are the stellar radius and luminosity respectively.

1.2.1 Fast versus slow star formation

The overall timescale of star formation is widely debated with several proposed scenarios; star formation happens on free-fall timescales (e.g. Ballesteros-Paredes, Hartmann & Vázquez-Semadeni 1999; Elmegreen 2000, see section 1.2.3), is governed by ambipolar diffusion lasting up to ~ 10 Myrs (see sections 1.2.2), or is regulated by feedback from stellar winds or outflows that regenerate turbulence. Since pre-MS stars evolve along near-constant temperature and decreasing luminosity tracks (Hayashi 1961), a widely used method to constrain age spreads in SFRs involves using a HR diagram combined with evolutionary models. The stars are placed onto the diagram along with multiple isochrones of different ages (see section 1.3), and assuming that the luminosity is closely related to the stellar age, both the average age of the cluster and the age spread can be inferred. The age spread determination is important in low-mass star formation studies as a large spread of ages in a SFR might indicate a slow star formation scenario (see section 1.2.2) as opposed to a rapid star formation scenario (see section 1.2.3).

1.2.2 Theories of slow star formation

Ambipolar diffusion is the drift of charged particles with respect to neutral particles, caused by a magnetic field, and is a means by which magnetic flux escapes from interstellar clouds (Mestel & Spitzer 1956). A star formation model presented in Shu (1977), and reviewed in Shu, Adams & Lizano (1987) proposed that structures within molecular clouds last tens of Myrs, and are in dynamical equilibrium. In structures where the density reaches 10^5 cm^{-3} , ambipolar diffusion causes a slow collapse of the core. Neutral molecules collide with the ions in the magnetic field, in which the ionisation fraction is low enough to permit slow diffusion through the magnetic field, removing flux from the core.

The pre-stellar core gains mass through several millions of years of ambipolar diffusion and enough magnetic flux is removed from the core to allow gravitational

forces to dominate. When the gravitational potential energy in the high density regions within the cloud overcomes the thermal pressure, the core collapses to become a protostar. The diffusion timescales are different for cores with different densities (Tassis & Mouschovias 2004), where the formation of cores takes place on a timescale between 10^5 and a few 10^7 yr, depending on the initial mass-to-flux ratio, and degree of ionization of the parent cloud. This results in the dynamical, but slower than free-fall contraction of the cores. Tan, Krumholz & McKee (2006) argue that the time taken for clusters to form is at least several local dynamical times. They argue that star formation takes place over a few to 10 free-fall times because of this.

A problem with the theory of slow star formation is that it lacks strong observational evidence so an alternative ‘fast star formation’ theory has been proposed which we explain in the following section. In section 1.2.4 we have discussed observational evidence of star formation timescales.

1.2.3 Theory of fast star formation

More recently, an alternative star formation scenario based on a rapid timescale has been presented and is continually being developed (Hartmann 2001; Hartmann, Ballesteros-Paredes & Heitsch 2012). The model is as follows; the high density areas of the GMCs collapse on free-fall timescales, with supersonic turbulence governing the star formation rate by removing enough flux to allow free-fall collapse. Theoretically shorter magnetic flux reduction timescales have been achieved, by enhancing ambipolar diffusion by turbulent motions of the gas (e.g. Ciolek & Basu 2001, Fatuzzo & Adams 2002 and Nakamura & Li 2005). Hence, the clouds are extremely short-lived, with pre-stellar collapse happening instantaneously after a gravitational instability in the high density regions. In this model, molecular clouds are not envisaged as quasi-static entities. Instead they are magnetically supercritical transient objects (Hunter et al. 1986; Elmegreen 1993; Nakano 1998; Ballesteros-Paredes et al. 1999a,b) with large-scale turbulent flows of molecular hydrogen.

1.2.4 Observational evidence

Proposed timescales for the star formation process vary significantly. Age spreads in star forming regions (see section 1.2.5) provide evidence supporting the slow star formation scenario. Evidence of accelerating star formation lasting at least several Myrs, many times the free-fall timescale, in young star forming regions (Taurus-Auriga, Lupus, Chamaeleon, ρ Ophiuchi, Upper Scorpius, IC 348, and NGC 2264) was found by Palla & Stahler (2000), supporting a quasi-static collapse and a slow star formation scenario.

Listed here are several observationally supported arguments against the slow star formation scenario outlined in 1.2.2;

- All of the regions studied by Palla & Stahler (2000), who propose ‘accelerating star formation’ share a very recent peak in star formation activity (1-2 Myrs). However, there is lack of an explanation of the sudden and recent increase in star formation over the last few millions of years. Hartmann (2003) shows that uncertainties in the HR diagram ages can lead to the appearance of accelerating star formation.
- Assuming a slow star formation scenario, starless molecular clouds would be expected prior to star formation. However, observations show that most clouds are exhibiting ongoing star formation, with little evidence for starless cores (Briceño et al. 2007; Hartmann, Ballesteros-Paredes & Heitsch 2012). The implications of this are that the lifetime of the clouds must be short, and that star formation begins promptly and happens rapidly.
- Regular structures would be expected within a quasi-static cloud. However, this is not the case, with clouds and cores exhibiting irregular structure with areas of long-lived low-density cores and short-lived high-density cores (Elmegreen 2007).
- Hartmann, Ballesteros-Paredes & Heitsch (2012) show that the presence of a few older stars in young clusters is consistent with rapid star formation. In

this study, numerical simulations were performed to show that it is possible that dynamic models of cloud formation can account for age spreads in clusters comparable to those observed without having turbulent or magnetic field support. This is due to fluctuations in initial conditions as a function of position, which can result in regions of the cloud collapsing faster than others. They found that the models exhibit gravitational collapse on timescales similar to those predicted by the ‘accelerating star formation’ model inferred from observations (Palla & Stahler 1999, Palla & Stahler 2000).

The observed star formation efficiency, is less than expected for free-fall timescales (‘inefficient’ star formation). Elmegreen (2000) has suggested that the inefficiency of large scale star formation arises, not from the magnetically driven slow collapse of the cloud, but rather from the inability of most molecular gas to produce stars, which arises from turbulent internal structure (Falgarone, Phillips & Walker 1991), where either the gas density is too low, or the clump is too small for gravitational collapse (Padoan 1995).

1.2.5 Luminosity and age spreads

The luminosities of pre-MS stars are greatly affected by variability, unresolved binary or multiple star systems, the presence of circumstellar discs, which shield radiation from the star, and other observational uncertainties (Hartmann 2001, see section 1.3.3 for an estimation of the amount that these effects contribute to the luminosity). Another possible explanation for the luminosity spread is variable episodes of heavy accretion during the class I phase (Baraffe et al. 2012) discussed in more detail in section 1.3.2). Variability can be used as a youth indicator as young pre-MS stars undergo major physical changes during their evolution towards the main sequence. The HR diagrams of young clusters often have luminosity spreads of an order of magnitude at any given effective temperature (T_{eff}). Given the placement of model isochrones to deduce the ages from the positions in the HR diagram, the spread in luminosities has

been observed to imply 10 Myr spread of ages in a cluster (Palla & Stahler 1999; Palla & Stahler 2000). Star formation histories derived from HR diagrams are debatable and the large age spreads derived from luminosity spreads in HR diagrams are upper limits to the actual age spreads (Hartmann 2001).

Alternative age spread determination methods are required. These should include methods that are not reliant upon the stellar luminosity for age estimations, such as measuring the lithium depletion, the disc population, and stellar rotation. Jeffries (2007) combined rotation periods and projected equatorial velocities to estimate projected radii and hence, under the assumption of random axial orientations, modelled the distribution of radius at a given T_{eff} . A spread in radii larger than could be explained by the coeval models was found, failing to rule out the possibility of a true age spread greater than the median cluster age.

Lithium is relevant as an age indicator as it is depleted through a stars' pre-MS lifetime and can be observed in the photosphere of a pre-MS star (e.g. Bildsten et al. 1997). Using lithium lines as age-indicators for stars in the Orion Nebula Cluster (ONC), Hillenbrand (2009) and Sacco et al. (2007) also failed to rule out large cluster age spreads. Sacco et al. (2007) found some examples of older Li-depleted stars and Hillenbrand (2009) found a dispersion in sodium line strengths, indicative of a spread in surface gravities. This, however, does not necessarily mean there is a spread in age if the episodic accretion models of Baraffe, Chabrier & Gallardo (2009) are reliable.

Circumstellar discs are involved in the rotational evolution of pre-MS stars. According to the assumption that stars with discs eventually lose their discs, and that diskless stars once had discs, young disc-bearing stars should be rotating, on average, more slowly than those in which their discs have dispersed. Littlefair et al. (2011) found this not to be the case when considering stars in the ONC and Jeffries et al. (2011) found that age distributions from the HR-diagram were similar for stars with and without discs. Yet, Bertout, Siess & Cabrit (2007) compared the ages of WTTS and CTTS and found a low probability of them being drawn from the same parent population, with CTTS being younger, on average, than WTTS, again highlighting the problem of reliable age determination methods for young star clusters.

1.3 Pre-Main sequence evolutionary models

Stellar ages are required to infer age spreads in clusters and to determine the star formation history. In pre-MS clusters, ages and masses are commonly estimated by the comparison of stellar parameters, such as luminosity and temperature, or colour and magnitude, with theoretical evolutionary tracks or isochrones. Although there are many developed pre-MS isochrones in the literature, the current differences in the physical inputs between them result in significant differences in the inferred ages for stars with the same luminosities and effective temperatures (Hillenbrand 1997, Park et al. 2000, Dahm & Simon 2005, Lamm et al. 2005). Recent work by Bell et al. (2013) for 13 pre-MS (specifically <30 Myr) clusters has shown that pre-MS ages may have been underestimated in the literature. They created new semi-empirical pre-MS isochrones incorporating existing stellar interior models, an empirical bolometric correction- T_{eff} relation and theoretical corrections for the dependence on gravity. The new isochrones were used to calculate ages from the pre-MS populations and they find that the ages are typically a factor of 2 older than current literature estimates.

Evolutionary models require a full consideration of the governing physics of the state of a star during its evolution. This includes the opacity, equation of state (EOS), stellar atmospheres and convection. The models are generally designed around both the stellar interior, and the atmospheric properties of the star, which when combined, define properties such as radius and luminosity. The significant differences between models lie with the treatment of convection, the opacity source, the EOS and the boundary condition between the star and atmosphere (Hillenbrand 2005). Hillenbrand & White (2004), for example, discuss the discrepancies between the masses of stars derived from evolutionary models and empirically determined masses from observations, and find large systematic discrepancies between empirical and theoretically derived masses, particularly for those stars with masses between 0.3 and $1.2M_{\odot}$.

Table 1.1: A summary of the treatment of equation of state (EOS), convection, atmospheres and opacity in the evolutionary models used in this thesis.

Model	Mass range (M_{\odot})	EOS	Convection Model	Atmospheres	Opacity
Feiden, Chaboyer & Dotter (2011) (Dartmouth)	0.1-5	General ideal gas EOS with the correction given in Chaboyer & Kim (1995)	MLT ^a $\alpha=1.94$	PHOENIX model atmospheres (Hauschildt et al. 1999a, 1999b)	OPAL ^b
D'Antona & Mazzitelli (1997) (DAM97)	0.02-3	Mihalas, Dappen & Hummer (1988) MHD	FST ^c	Grey atmosphere models	Alexander & Ferguson (1994)
Siess, Dufour & Forestini (2000) (SDF00)	0.1-7	Pols et al. 1995	MLT ^a $\alpha = 1.605$	Analytic fit of $T(\tau)$, as a function of effective temperature, surface gravity and metallicity with parameters constrained by Plez (1992)	Alexander & Ferguson (1994)

NOTES: ^a Mixing length theory, ^b Iglesias & Rogers 1996, ^c Full Spectrum of Turbulence (Canuto & Mazzitelli 1991)

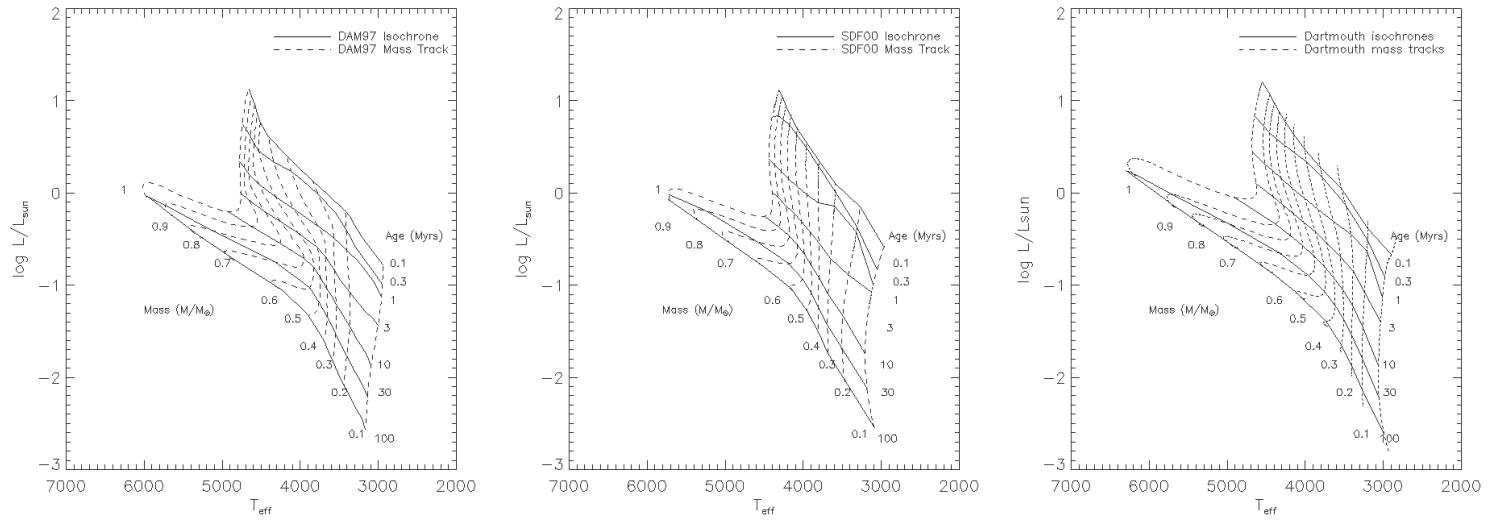


Figure 1.2: The Dartmouth, DAM97 and SDF00 theoretical evolutionary isochrones and mass tracks for low-mass pre-MS stars. The dashed lines show mass tracks in the range $0.1-1M_{\odot}$ and the solid lines show isochrones covering the pre-MS range of $0.1-100$ Myrs.

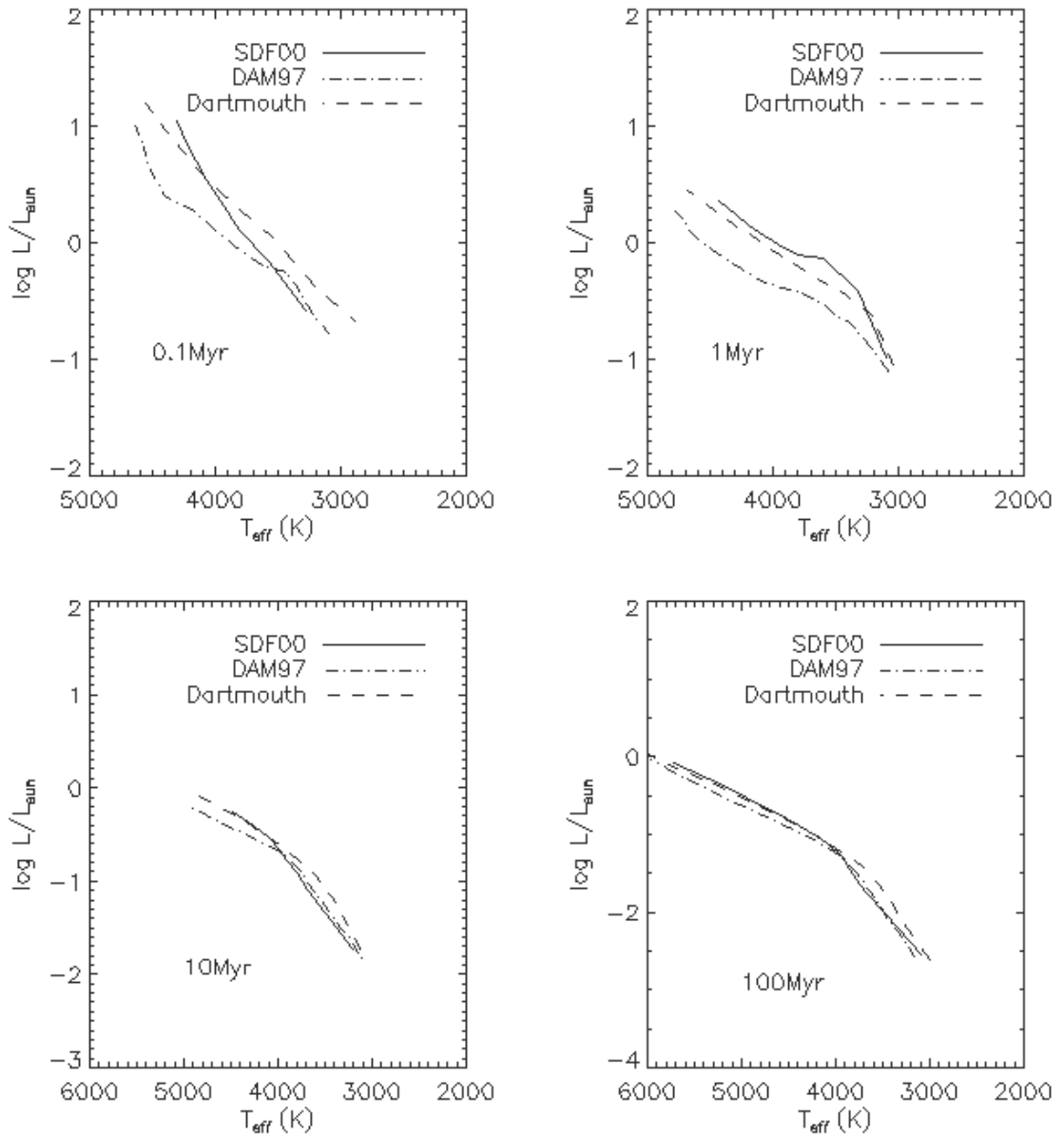
The evolutionary models that are used in this thesis are shown in Figure 1.2 and 1.3 and are summarised in Table 1.1. Other widely used evolutionary models (e.g. Baraffe et al. 1998; Tognelli, Prada Moroni & Degl’Innocenti 2011, PISA; Bertelli et al. 2008, PAdova) do not cover the age range required for use with the data used in this thesis.

1.3.1 Pre-Main sequence model comparisons

Examining which star formation scenario presented in sections 1.2.2 and 1.2.3 gives the most accurate description of the star formation process requires extensive knowledge of the timescales of the star formation process. Attaining this information requires not only accurate observations, but also accurately calculated pre-MS models. Differences have been found in ages and masses of stars depending on the evolutionary models used. For example, Rebull et al. (2002) used DAM97 and SDF00 models in a spectroscopic study of the young cluster NGC 2264, and found differences of a factor of two in mass, and an order of magnitude difference in age between the models using the same data. Figure 1.3 shows the isochrones from the models described in section 1.3, spanning the pre-MS ages of 0.1 to 100 Myrs. Although the 100 Myr isochrones are in agreement (to a reasonable extent), the younger isochrones (which are more relevant to the data used in this thesis) exhibit clear discrepancies. For example, the SDF00 and DAM97 1 Myr isochrones at solar luminosity show a difference in T_{eff} of $\sim 700\text{K}$ and in log luminosity of ~ 0.4 . The differences might be caused by the variation of convection models and opacities used in the production of the models (see Table 1.1). The isochrones from different models also intersect, i.e, one model does not give consistently younger ages than another (see Figure 1.3).

Choosing which sets of isochrones to use can be problematic. Prior to examining the age spreads in young clusters, or using the models to determine individual ages, it is useful first to compare the models to an independent dataset to determine the differences in ages that can be caused by the choice of model. This thesis will predominantly focus on the young cluster NGC 2264 (see section 1.5). We used stars from NGC 2362 to

Figure 1.3: A comparison of three sets of pre-MS isochrones. The plots show the predicted luminosities and effective temperatures for stars of masses between 0.1 and $1 M_{\odot}$ and ages of $0.1 - 100$ Myrs. Where the plots of more evolved stars (100 Myrs) show little differences between the models, the 0.1 , 1 and 10 Myrs isochrones show clear discrepancies.



compare the ages which can be derived from the three sets of models in section 1.3. The distance to NGC 2362 is 1.5 Kpc (Moitinho et al. 2001), and is approximately 5 Myrs old (Dahm & Simon 2005). Figure 1.4 shows a colour-magnitude diagram of NGC 2362 using photometry from Irwin et al. (2008) and the DAM97 isochrones. The median cluster age derived from Figure 1.4 is 5.5 Myrs using the Dartmouth isochrones, 4.2 Myrs using the DAM97 isochrones and 6.1 Myrs when using the SDF00 isochrones.

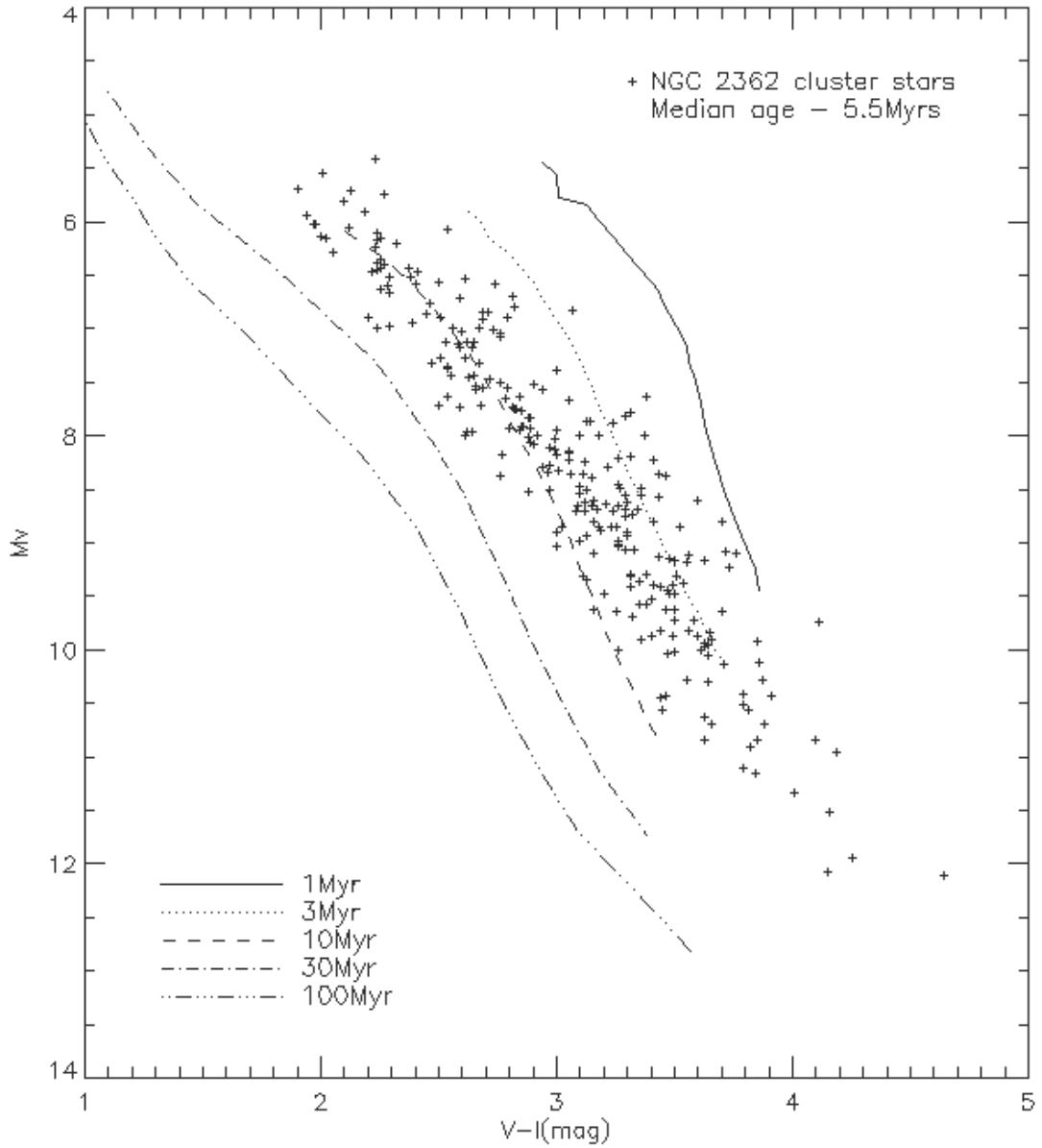
1.3.2 Accreting pre-main sequence models

Considering the wide spread of luminosities seen on the HR diagram for similarly-aged stars, Baraffe, Chabrier & Gallardo (2009) propose that the varying accretion from the parent molecular cloud during early star formation can explain this spread. They suggest that every protostar has a unique accretion history. If each protostar undergoes random and unpredictable episodes of accretion in the protostellar phase, resulting in random initial positions on the HR diagram, then one cannot define a definite ‘birthline’ (a predicted line on the HR diagram that separates protostars, radiating only in IR, from observable pre-MS stars, Stahler 1983).

They developed hydrodynamic numerical simulations of pre-stellar core collapse based upon accretion histories of collapsing protostellar cores. They simulate the luminosity spread in the pre-MS phase according to different accretion rates in the protostar phase, and different initial pre-stellar core masses. This episodic, heavy accretion occurs during the class I (protostellar) phase (see section 1.1.5).

The authors suggest that early accretion during protostar formation and evolution can explain the observed luminosity spread in young clusters without invoking any significant age spread, and that the concept of a well-defined birthline does not apply for low-mass objects. Although theoretically these results could show that luminosity spreads can be explained by periods of rapid accretion, robust physical foundations are required to probe the accuracy and reliability of these simulations. The accretion histories argument outlined above affects the ages from the HR diagram at very young ages <10 Myrs.

Figure 1.4: The colour-magnitude diagram of NGC 2362 cluster stars with the isochrones at 1, 3, 10, 30, and 100Myrs (from the DAM97 models) and masses between 0.1 and $1M_{\odot}$. The median age of cluster stars is ~ 5.5 Myrs. A reddening of $E(V-I) = 0.05$ and extinction of $A_V=0.31$ and distance of 1.5 kpc were assumed (Irwin et al. 2008).



There is an alternative argument by Hosokawa, Offner & Krumholz (2011), that this process of early accretion is not capable of explaining the luminosity spread of pre-MS stars. They find that non-accreting isochrones can overestimate stellar ages for stars with $T_{\text{eff}} > 3500$ K, which explains why there are sometimes systematic age differences between more and less massive stars in the same cluster. They suggest that the inferred ages and spreads from the HR diagram for cool stars are, in fact, reliable, assuming the observed bolometric luminosities and effective temperatures are accurate.

1.3.3 Converting between the theoretical and observational plane

This section is focussed on discussing the problems with converting observed data to the luminosities and temperatures that are plotted in a HR diagram, or converting the luminosities and temperatures predicted by evolutionary models to compare with observed colour and magnitude data. Even if it was the case that the evolutionary isochrones were in good agreement for pre-MS stars, the underlying problem remains of converting between the theoretical and observational planes. Effects of extinction and reddening, photometric variability and a binary population make the problem more challenging.

The process of converting from the observational to theoretical planes includes converting apparent magnitudes to absolute magnitudes, correcting for extinction, converting to bolometric magnitudes using a bolometric correction, and then to luminosities, for a given distance. The colours are converted to T_{eff} by correcting for reddening, and then using a colour- T_{eff} relation to infer a T_{eff} . Intermediate colour tables which allow for the conversion between the theoretical and observational plane for both main sequence and pre-MS stars are available in various bands and also include bolometric corrections. (e.g. Kenyon & Hartmann 1995, Pecaut & Mamajek 2013).

Empirically, the magnitudes in at least two photometric bands are measured (and sometimes the spectral type, which allows a reddening estimate to be made). The extinction and reddening adds to the challenge of converting precisely between

observations and theory, particularly for young stars as they are often still partly embedded in the molecular cloud. Further to this, a wavelength range which is not strongly affected by either accretion or circumstellar emission must be used.

Soderblom et al. (2014) discusses the uncertainties in the basic parameters required to place stars on the HR diagram. They suggest that a 0.01-0.1mag error on photometry measurements with a 10% uncertainty in the mean cluster distance is required. Reggiani et al. (2011) estimate that the typical (log) luminosity error is 0.1. In the case that observed luminosity spreads are much greater than these values, the authors suggest that they are genuine luminosity spreads.

The effect that binarity has on the HR diagram is to make stars with companions appear brighter than they are. This shifts the median luminosity to higher luminosities than their true luminosity and consequently broadens the luminosity distributions. There are models available in the literature, such as that from Hartmann (2001, used in the later chapters of this thesis), that provide a way of correcting for a given binary fraction in a cluster.

1.4 Kinematics in young clusters

The motions of stars in three-dimensions are often used in the study of star formation (e.g. Tobin et al. 2015). The velocity can be measured both along the plane of the sky relative to more distant objects (tangential velocity), and in the radial direction (the radial velocity, RV). Kinematics can be used to determine the current dynamical state and to infer the past and future behaviour of the cluster, and where there are measurements of entire clusters or populations, kinematics can be used to determine membership of a cluster or association (e.g. Geller, Latham & Mathieu 2015), and to assist in determining the presence of substructure within a cluster (e.g. Jeffries et al. 2014). For a cluster in virial equilibrium, a typical velocity dispersion in a cluster aged <10 Myrs is a few km/s (Gieles, Sana & Portegies Zwart 2010). Cottaar et al. (2012) developed a correction mechanism which amounted to a few km/s for solar-type

stars, but this depends on the mass and the size of the cluster and would be larger for higher-mass stars .

Most stars are formed in clusters (see section 1.1.6). Due to nearby and background stars, it is often challenging to determine which stars belong to the cluster in question. Kinematics can assist with membership determination. Since cluster members were born from the same molecular cloud, they are assumed to have similar velocities. Therefore, if stars have common velocities they can be assigned to the same cluster. RVs of low-mass stars are often used in membership determination for young clusters (e.g. Jeffries, James & Thurston 1998, Pozzo et al. 2003, Kenyon et al. 2005, Luhman 2007). Collective RVs for many stars in the cluster can help to include and rule out cluster members and non-members respectively. The use of kinematics is popular for membership determination as it relies on observations alone (model-independent). Spectrographs such as Giraffe at the VLT (FLAMES, Pasquini et al. 2002) allow simultaneous observations of up to 130 targets, which can provide spectra of populations of stars with a high enough resolution to determine reliable RVs. All-sky missions such as Hipparcos (Perryman et al. 1997) , and recent advancements in instrumentation such as the Gaia satellite will enable more reliable membership assignment to a cluster or group. However, several problems occur when using the kinematics of young stars for membership determination, the identification of substructure or the estimation of ages. Single-lined spectroscopic binaries are those in which one star in the system is much more massive than the other, so the spectra are dominated by emission from only the more massive star. The redshift of the spectral lines may vary at different points in the orbit and the spectral lines of stars in a multiple star system can merge to form a single line. This is a common problem for RV membership determination; stars with RVs that do not lie around the mean cluster RV cannot be completely ruled out as cluster members in the case of single-lined binary systems. Dolan & Mathieu (1999) found examples of stars with similar RVs which would be assigned to a young cluster, were lacking in lithium, so were likely to be field stars rather than cluster members. Other studies have shown that despite stars having common proper motions in the same region, they may not exhibit other pre-MS indicators and are, therefore unlikely

to be cluster members (e.g. Preibisch et al. 1998). Kinematic measurements should therefore, be complemented with other data such as X-ray activity, lithium abundance, or photometry in several wavelength bands.

Kinematics can also be used in cluster structure studies. During the class 0 phase of star formation, the collapsing cloud can form several high density regions of gas, which evolve to produce structured areas of star formation. If the cluster is structured then there may have been several star formation events which occurred several millions of years apart, which can be a cause of cluster age spreads. Precise RVs can be used to probe the current dynamical state of clusters and associations, and can be used to assess kinematic gradients within the line of sight to indicate whether structure exists within a given region, or reveal multiple stellar populations. Fűrész et al. (2008) and Tobin et al. (2009) analysed RVs in the ONC, and determined that the kinematic stellar structure closely resembles the velocity structure of gas traced by ^{13}CO . Any fine structure is smoothed out by gravity within the first few million years (Kroupa 2001), so the presence of substructure for the ONC suggests that the cluster cannot be much older than a crossing time. The increasing sensitivity of both ground-based and space-based instruments has made searching for kinematic substructure more feasible. Kinematically determined sub-clusters of different average ages have been found in nearby associations such as the σ Orionis association (Jeffries et al. 2006). The difference in age of sub-clusters can provide an explanation for cluster age spreads (Alves & Bouy 2012).

Deducing the ages of young stars is crucial to our understanding of the formation history of stars. Several methods in which RVs have been used to determine ages are; measuring the expansion of a population as a function of position (e.g. Brown, Dekker & de Zeeuw 1997), tracing back in time the orbits of cluster or members of groups to a minimum dispersion (e.g. Fernández, Figueras & Torra 2008) and placing “runaway stars” back in their parent clusters. As shown in section 1.3.1 there are discrepancies between the ages inferred from different evolutionary models. Kinematic age estimation methods, such as those listed above, could provide a model-independent technique for deducing stellar ages, and can be used in situations where other age estimation

methods are insensitive or strongly model-dependent (such as lithium depletion in clusters $<20\text{Myrs}$).

1.5 The young cluster, NGC 2264

Determining accurate ages and age spreads of stars in clusters is crucial to understanding their formation histories and evolution, and nearby, young clusters are often used in these studies. The young cluster NGC 2264 is an excellent region to examine star formation due to its age, position, extinction, structure and disc population. A list of the recent surveys and catalogues that are available for NGC 2264 is presented in the appendix (A2).

NGC 2264 is an open cluster in the Monoceros OB1 association with up to several thousand members (Makidon et al. 2004, Lamm et al. 2004, Fűrész et al. 2006, Cody et al. 2013). It has a small amount of nebular emission (Park et al. 2000), and is situated in front of a large dust cloud which obscures background stars (Herbig 1954). There are also regions of continuing star formation (Mayne & Naylor 2008) which allows observations of stars at a variety of ages and evolutionary phases. A large photometric study of NGC 2264 recently took place with simultaneous time-series photometry with use of Spitzer (Werner et al. 2004), Chandra, MOST (Microvariability and Oscillations of STars, Walker et al. 2003) and CoRoT (CONvection ROTation and planetary Transits, Auvergne et al. 2009). The cluster has been observed in many wavelengths, including X-ray (e.g. Dahm et al. 2007), optical (e.g. Fűrész et al. 2006), infrared (e.g. Ramírez et al. 2004) and radio (Trejo & Rodríguez 2008). These detailed studies have allowed researchers to build up a comprehensive view of star and cluster formation in NGC 2264 and the surrounding region.

This thesis will focus on NGC 2264, due to its age, distance and low extinction. The age, age spread, and substructure in the cluster are the primary foci. In the following sections, the literature relating to NGC 2264 is reviewed.

1.5.1 Distance

Literature values for the distance in NGC 2264 vary by hundreds of parsecs from ~ 400 pc to ~ 900 pc. Listed below is a summary of the more recent distances to NGC 2264 presented in the literature;

- *Sung, Bessell & Lee (1997)* Using UBVRI H α photometry of 13 B-type stars in NGC 2264, Sung, Bessell & Lee (1997) calculated the mean of the distance moduli to the individual stars as **760 pc**.
- *Baxter et al. (2009)* The observed distribution of the inclination angle of stars in the cluster was modelled and compared with distant-dependent values of $\sin i$. They adjusted the distance assumed in the observed $\sin i$ distribution until it matched the modelled distribution. Using 97 cluster members a distance of **913 \pm 110 pc** was found. Although this is $\sim 20\%$ larger than the commonly used distance of 760 pc, (Sung, Bessell & Lee 1997) both values are consistent within the sum of the statistical and systematic errors.
- *Turner (2012)* UBV photometry from Walker (1956) was re-examined and a distance of **777 pc** was determined from the colour-magnitude diagram.
- *Dzib et al. (2014)* Proper motions observed for the sources in HH 124 IRS radio cluster within NGC 2264 suggest that the region is situated at ~ 400 pc from the Sun, which is significantly nearer than most other distance measurements. When the Hipparcus parallaxes were re-analysed, however, a generalised kinematic analysis of sources in NGC 2264 also argue in favour of the nearer distance of 400 pc. They argue that both the radio cluster and NGC 2264 are located approximately twice as near than usually measured.

The distance measurements to NGC 2264 vary significantly, as do the techniques used to measure the distances. The outliers to the distance measurements are 400 pc (Dzib et al. 2014) and 913 pc (Baxter et al. 2009). This could either be due to observational variations caused by the different techniques, or indicate two clusters in

the line-of-sight. However, the radio sources used in the measurements by Dzib et al. (2014) are situated further to the north of the positions of stars used by Baxter et al. (2009, which is also the region that the research in this thesis covers, see Table 3.1 and Figure 3.1 for details). Although accurate stellar distances are required for many single-star age determination techniques (including deriving stellar ages from the HR or colour-magnitude diagrams), they are not essential for age spread determinations if quantified in terms of a dispersion, as variations in the measured distance only shifts stars vertically on the HR or colour-magnitude diagrams. We have adopted the widely used value of 760 pc from Sung, Bessell & Lee (1997) in this thesis. One of the aims of this research is to use a distance-independent method to estimate the cluster age. By assuming that this distance-independent age should share a similar value to the distance-dependent age provided by the HR diagram, a range of acceptable distances to the cluster are measured in Section 4.5.7.

1.5.2 Ages and age spreads

NGC 2264 has been inferred to be young given the large OB stellar population and high disc frequency (Dahm 2008). Age estimates and measurements for the cluster date back over half a century (e.g. Walker 1956). In chapter 4 and 5 of this thesis, we studied both the age and age spreads in NGC 2264 using a range of methods and evolutionary models. Table 1.2 lists the recent age estimates in the literature for the cluster along with a brief description of the method used to measure these. By taking a mean of the ages listed in the table, the average age from the literature is 2.5 Myrs. These ages were determined using a variety of methods, such as inferring ages from the HR diagram using evolutionary models.

Age spreads have been inferred in NGC 2264 (e.g. Park et al. 2000, who found age spreads of >5.5 Myrs inferred from the HR diagram, see Table 1.3). Sergison et al. (2013) found that the dispersion in the strength of the lithium line (6708\AA) may imply an age spread that is similar in size to the apparent age spread, inferred from luminosity spreads in the HR diagram. Venuti et al. (2014) monitored the UV excess of

stars in NGC 2264 over several weeks, and find that there is a dispersion in the average accretion rate that is not completely accounted for by the variability, and suggest that a non-negligible age spread could have effectively contributed to the observed spread in accretion rates at any given mass.

Using the ages derived from colour-magnitude diagrams, Sung & Bessell (2010) separated the stars into several SFRs (see section 1.5.4 for a discussion of substructure in NGC 2264). The maximum difference in median age between regions is less than the age spread within each region. The authors suggest that this is due mainly to their age spread. Other age spread studies found in the literature for NGC 2264 are listed in Table 1.3 and range from 2.7 Myrs to >10 Myrs.

Some of the inferred absolute age spreads from methods such as placing the stars on HR diagrams are strongly model-dependent (see, for example, Park et al. 2000 in Table 1.3). The different evolutionary models used to estimate ages and age spreads could explain some of the differences between the values shown in the tables (discussed further in Chapter 6). Using the HR diagram to measure stellar ages also depends on the distance to the cluster. If, for example, the stars in the cluster were the same age but at different distances, then these would appear to be different ages in the HR diagram. Determining which age and age spread are closer to the ‘true’ age and spread has its difficulties, but methods that rely less heavily on pre-MS evolutionary models could perhaps provide a closer estimation of the true age.

Most of the research listed in this section use CMDs or HR diagrams to estimate ages and age spreads, which has the benefit of allowing comparisons of ages and age spreads to be made between different pre-MS clusters. However, the disadvantage of using HR diagrams is that the uncertainties in luminosity measurements, extinction and binary fraction can be large for pre-MS stars. One of the methods used to measure the ages and age spreads in this thesis is not distance dependent (see Sections 4.1 and 4.3), circumventing many of the specific problems relating to many of the age estimations found in the literature that rely on the HR diagram or CMDs. Luminosity and age spreads are discussed in Section 1.2.5, and the effect that binary stars have on the luminosity measurements are discussed in Section 4.2.1. The limitations of using the

luminosities of pre-MS stars in relation to the results produced by this research are discussed in section 6.1.1.

The positions of the observations could also contribute to the spread of ages, age spreads and distances to the cluster. The research on kinematics by Tobin et al. (2015) and Fűrész et al. (2006), and by Baxter et al. (2009) who measured a distance of 913pc covers a similar region of the cluster as our research. Teixeira et al. (2012), Sung, Stauffer & Bessell (2009), and Dahm et al. (2007) focus their research more around the Cone Nebula and S Mon. An image showing the positions of targets used in the research in this thesis is shown in Chapter 3, Figure 3.1.

Citation	Age (Myrs)	Method
Park et al. (2000)	2.1, 0.9, 4.3, 2.7	Ages were derived from the HR diagram with UB-VRI and H α photometry and four sets of evolutionary models ^a .
Dahm & Simon (2005)	1.1	Using nearly 500 H α emission stars identified within the immediate cluster vicinity the age was inferred from a colour-magnitude diagram with isochrones from DAM97.
Mayne & Naylor (2008)	\sim 3	Ages were estimated from a colour-magnitude diagram (V, V-I) and the SDF00 isochrones, with data from 70 bright (V<13) stars obtained from Mendoza V. & Gomez (1980).
Baxter et al. (2009)	1.5	Sin <i>i</i> measurements were used to derive a new cluster distance and a revised age was estimated using the new distance. They applied a magnitude correction corresponding to the new distance to a 1 M _{sol} star's H-band magnitude at 3 Myrs, and calculated the difference in age from 3 Myrs.
Turner (2012)	\sim 5.5	Photometry from Walker (1956) was re-analysed to create a colour-magnitude diagram and an age was estimated from B-type stars using the models from Palla, Stahler & Parigi (1993).
Barentsen et al. (2013)	3	Graphical Bayesian networks were used to construct hierarchical probabilistic models, and applied to photometry from Sung et al. (2008) and the IPHAS catalogue, of 587 known low-mass cluster members.
Mariñas et al. (2013)	1	An age was estimated from a HR diagram using FLAMINGOS photometry, and the isochrones of Baraffe et al. (1998), Chabrier et al. (2000) and SDF00. The stars in the sample cover a large range of spectral types (A8-M8). They used a cluster distance of 780 pc, and individual extinctions to construct the HR diagram.

NOTES: ^aSwenson et al. (1994), D'Antona & Mazzitelli (1994), Baraffe et al. (1998)-I (Ratio of mixing length to pressure scale height=1.0), Baraffe et al. (1998)-II (Ratio of mixing length to pressure scale height=1.9)

Table 1.2: Ages that have been presented in the literature for NGC 2264, using a variety of measurement techniques.

Citation	Age Spread (Myrs)	Method
Adams, Strom & Strom (1983)	> 10	Using a deep photometric survey of the cluster to create a HR diagram of probable cluster members, and inferred a significant age spread of > 10 Myr.
Soderblom et al. (1999)	4	A HR diagram was constructed, and since most of the cluster members (filtered by their RVs) lay between the 1 and 5 Myr isochrones (Siess, Forestini & Dougados 1997) an age spread of 4 Myr was inferred.
Park et al. (2000)	8, 5.5, 15.3, 10	UBVRI and H α photometry was used to create a HR diagram, and age spreads were estimated using four sets of evolutionary models ^a .
Rebull et al. (2002)	6	UVI photometry was used to construct a color-magnitude diagram, and the age spread was measured from the DAM94 models.
Dahm & Simon (2005)	\sim 5	Using nearly 500 H α emission stars identified within the immediate cluster vicinity, the age spread was measured from a colour-magnitude diagram with isochrones from DAM97.
Barentsen et al. (2013)	2.7	Using graphical Bayesian networks to construct hierarchical probabilistic models and applied to photometry from Sung et al. (2008) and the IPHAS catalogue. The spread quoted in column two is the difference between the 25 and 75% quartiles of the distribution of individual ages.

NOTES: ^aSwenson et al. (1994), D'Antona & Mazzitelli (1994), Baraffe et al. (1998)-I (Ratio of mixing length to pressure scale height=1.0), Baraffe et al. (1998)-II (Ratio of mixing length to pressure scale height=1.9)

Table 1.3: The recent age spreads that have been presented in the literature for NGC 2264.

1.5.3 Cluster reddening

The radiation emitted by stars is often significantly attenuated by the dust that lies between the star and the observer. Dust grains absorb and scatter shorter wavelength ($\lesssim 1$ micron) radiation incident upon them and will themselves re-radiate at the much longer wavelengths appropriate to their typically much cooler grain temperatures. Measuring the effect of reddening is especially important when studying young clusters, as nebulosity remaining from the parent molecular cloud is often still present between the cluster stars. The reddening effect is often measured in terms of the intrinsic colour and apparent colour. The intrinsic colour ($(B-V)_o$) is estimated from the spectral type of the star using calibrated relationships between colour and spectral type (under the assumption that the reddening will not change an estimate of a spectral type, which is usually based on a narrow part of the spectrum). The reddening can be estimated using photometry alone, or by comparing the difference between photometric and intrinsic colours,

$$(B - V) - (B - V)_o = E(B - V). \quad (1.8)$$

Often NGC 2264 is quoted to have little foreground extinction (e.g. Perez, The & Westerlund 1987). From photometric studies, the cluster reddening ($E(B-V)$) estimates of between 0.061 and 0.075 were found by Perez, The & Westerlund (1987), Sung, Bessell & Lee (1997), and Turner (2012). Walker (1956) found a slightly higher value of $E(B-V)=0.082$. Through UBV fitting of main sequence stars Mayne & Naylor (2008) found $E(B-V)$ values of between 0.04 and 0.06 using several sets of models and by shifting the stars to lie on an intrinsic locus in the U-B versus B-V plot.

Fernandes, Gregorio-Hetem & Hetem (2012) evaluated the extinction law (R_V) using theoretical expressions based on the colour excess of stars with known spectral type, and by analysing two-colour diagrams, where the observed slopes were compared with the slope expected for the mean Galactic extinction law. They developed an algorithm to reproduce the ZAMS reddened colours, hence derived the average extinction (A_V) that provides the closest fit to the observational data. They found a much higher $E(B-V)$ of 0.13 for the result based on spectral type which they suggest may be due

to circumstellar effects, but an $E(B-V)$ of 0.05 for the result based on ZAMS fitting, which is consistent with the previous results when using photometry alone.

Reddening estimates based on colour excesses for NGC 2264 are, in most cases, higher than those quoted using photometry only (e.g. Dahm & Simon 2005, Fernandes, Gregorio-Hetem & Hetem 2012). A mean $E(B-V)$ of 0.146 ± 0.03 was found by Rebull et al. (2002) using the spectroscopy of 400 stars, including 78% of stars of types K0 and later.

It is possible that some of the low-mass stars in the cluster suffer from local extinction effects such as circumstellar discs, or lie within regions of the molecular cloud (Dahm 2008). Fernandes, Gregorio-Hetem & Hetem (2012) found that part of the cluster has a large dispersion of R_V values. In section 3.5 of this thesis, a reddening value has been estimated using several photometric and spectroscopic catalogues, and I explore whether one value of reddening can be applied to all of the stars in the cluster.

1.5.4 Cluster substructure

Chapter 5 of this thesis is dedicated to the study of structure in NGC 2264. Sung, Stauffer & Bessell (2009) performed mid-IR photometry using the images obtained with the Spitzer Space Telescope Infrared Array Camera and Multiband Imaging Photometer. They identified two sub-clusterings of Class I and II objects in the southern region surrounding the Cone nebula (see Figure 1.5). They also found that the disked stars in the region surrounding S Monocerotis (S Mon, see Figure 1.5) are mostly Class II objects. These regions show a distinct difference in the distribution of SED slopes. They found that the fraction of primordial discs is low near the most massive star S Mon and increases with distance from S Mon, although their method suffers from a bias towards finding accreting CTTS, and against finding stars with weak or no discs. Teixeira et al. (2012) analysed the spatial distribution of disked sources. They found that sources with optically thick discs ($-0.5 > \alpha_{IRAC} \geq -1.8$, α_{IRAC} is the SED slope from $3.6 \mu\text{m}$ to $8 \mu\text{m}$) segregate into sub-clusterings, whereas they found no evidence of clustering of the older sources that possess anaemic discs ($-1.8 > \alpha_{IRAC} \geq -2.56$). They

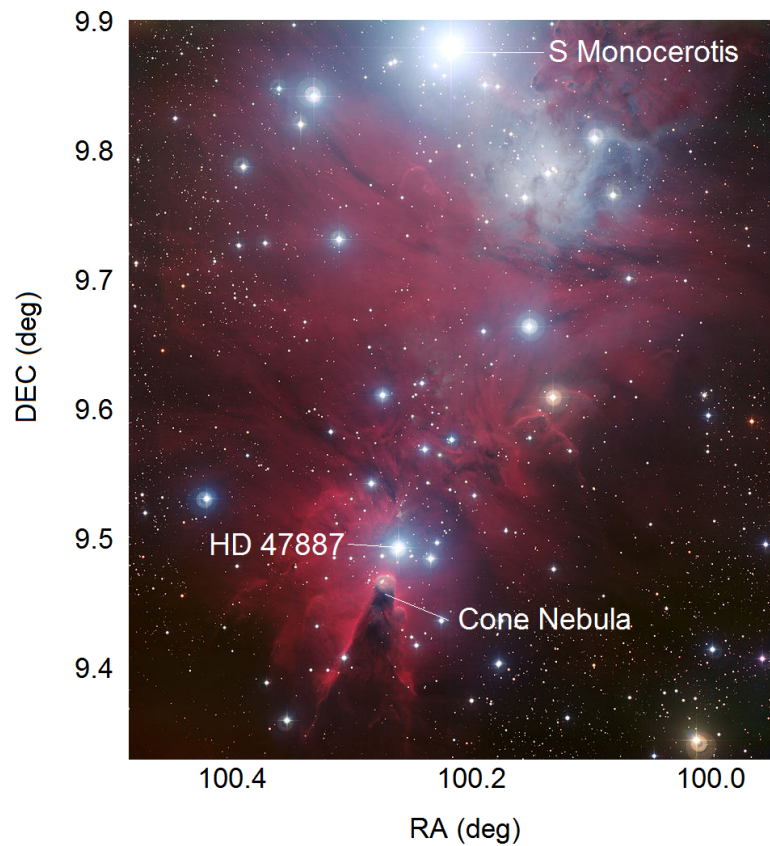


Figure 1.5: The positions of the massive stars, S Mon and HD 47887, and the cone nebula, along with an image of NGC 2264 (image credit: ESO). The image was created from data taken through four different filters (B, V, R and H-alpha) with the Wide Field Imager at ESO's La Silla Observatory .

also found that objects with anaemic discs are not embedded in molecular material, whereas the clustered sources with optically thick discs tend to be embedded within the cloud. They suggest that more than one star forming event has occurred, where stars with anaemic discs formed separately, and earlier, than stars with optically thick discs. They also suggest that stars with anaemic discs are older and have had more time to spatially disperse.

Rapson et al. (2014) compared the number of stars with discs in the NGC 2264 region and the surrounding region. Using Spitzer data, they find that the disc fraction (fraction of stars with IR excess emission indicative of circumstellar discs) is 45% in the region of the cluster (an area around S Mon of ~ 5 arcmin radius, and an area around the cone nebula of ~ 5 arcmin diameter), whereas the surrounding cloud shows a disc fraction of 19%. They suggest that this result could be explained by the presence of an older, more dispersed population of stars. A caveat to this method is that the discs around cluster members in closer proximity to the massive stars may be dissipated more rapidly by the winds from the massive stars, than those further away, resulting in these stars appearing older (due to having a lower disc frequency) than their actual age. Fűrész et al. (2006) found a gradient of radial velocity with declination ($\sim 6.6 \text{ km(s deg)}^{-1}$) in the cluster. A benefit of the research on kinematics by Fűrész et al. (2006) and Tobin et al. (2015) is that, although they select their sample from surveys that are biased towards finding CTTS and against finding WTTS, they complement their sample with large catalogues of X-ray sources that are sensitive to finding WTTS from, for example, Flaccomio et al. (1999) which has the effect of correcting this bias. Tobin et al. (2015) confirmed the gradient found by Fűrész et al. (2006) and also found a blue-shifted population of stars with respect to the background molecular gas. They defined a red-shifted population of stars in the northern end of the cluster, and suggested that stellar and gas kinematics of this region are the result of triggered star formation from a bubble driven by the wind from S Mon in northern region.

A common problem when studying structure in young star forming regions is the contamination by foreground or background non-members. Fűrész et al. (2008) suggested that the northern half of NGC 2264 is surrounded by less dust than the

southern region. If this is the case, it is likely that stars observed in the northern region will more likely include background stars than in the southern region, where the dust acts as a shield between the cluster and background stars. A similar problem arises when treating all of the stars with the same reddening correction in regions of patchy extinction. This causes similarly aged stars to appear to have different ages. An issue affecting kinematic studies in NGC 2264 is that there is a possibility of using optically-biased radial velocity samples, in that stars with higher radial velocities move deeper into the background molecular cloud, resulting in much higher extinctions.

So far, it is known that there are clumps of stars in NGC 2264 positioned around S Mon and the Cone Nebula, situated in the northern and southern regions, respectively (see Figure 1.5). There is kinematic substructure that separates a group of stars that are red-shifted with respect to the molecular cloud. It is also known that some of the stars are deeply embedded in molecular clumps in what Kuhn et al. (2014) calls ‘line chains’ in which the subclustering was at least partially inherited from the filamentary chain of molecular cloud clumps, although this work is biased by variations in gas absorption (so samples from deeply embedded regions may be deficient in X-ray probable members), possibly hiding the youngest stars.

There is still much that is unknown about the structure in NGC 2264. How many distinct clusters are there? Are the subclusters the same age? Does the kinematic structure correlate with the spatial structure? In chapter 5 of this thesis I examine structure in the cluster, focussing on kinematic structure, and whether there is evidence of a foreground or background population of stars (Sections 5.2 and 5.3).

1.5.5 Rotation

Photometric variability surveys have been effective in identifying pre-MS stars in NGC 2264, such as that by Kearns et al. (1997), who reported several G and K-type stars in NGC 2264 with periodic variability. Adding to this are the surveys by Lamm et al. (2004) and Makidon et al. (2004) which are both used extensively in this thesis. The latter two studies derived rotation periods for stars with already known periods

and they find good agreement in both cases. Most recently there has been a large photometric variability survey with CoRoT. Affer et al. (2013) present rotation periods for 209 cluster members using CoRoT. They find that CTTSs have a median rotation period of 7 days, compared with the WTTSs median rotation period of 4.2 days.

The period distribution is similar to that of the ONC, but shifted to shorter periods (Lamm et al. 2005), which corresponds to an older cluster age. Evidence for disc-locking would be that CTTSs are expected to be rotating more slowly on average than WTTSs (see section 1.1.4). Lamm et al. (2005) found evidence supporting disc-locking in NGC 2264 with an average rotation period of ~ 8 days among the higher mass stars, and a few days for lower-mass stars. Based on mid-IR observations, Cieza & Baliber (2007) also found a lower disc fraction (20%) in objects with short rotation periods (<2 days) than stars with periods of >2 days which showed a disc fraction of 46%, perhaps evidence that the disc-bearing phase of pre-MS evolution reduces the angular momentum of the star. However, a rotation study of NGC 2264 by Dahm & Simon (2005) found no significant difference between the rotation periods of CTTSs and WTTSs in the cluster (defining the limit between CTTS and WTTS as a H α emission EW of 10 Å). They found no correlation between rotation period and stellar age in the cluster as determined from the HR diagram, hence no evidence of the spin-up phase after the disc has been dissipated. However, due to the young age of the cluster, there may have been insufficient time for the stars to spin up after disc-dispersal.

1.6 Unanswered questions on star formation

Despite the recent advancements in the research relating to the formation and evolution of stars, many unanswered questions about star formation still remain. These include;

1. What is the timescale of the star formation process, from the stellar birthline to the hydrogen burning (main sequence) phase?
2. Do large luminosity spreads in the Hertzsprung-Russell diagram correspond to

large age spreads in young clusters?

3. Can the slow star formation scenario produce the kinds of age spreads that have been detected in young clusters?
4. If significant age spreads occur in young star forming regions, can they be explained by multiple star forming regions or cluster substructure?
5. Are the current age and age spread determinations reliable enough to draw accurate conclusions about star formation timescales?

NGC 2264 is a well-studied cluster that may be typical of the environments in which low-mass stars are born. Nevertheless, there still remains some outstanding questions about the cluster that are addressed in this thesis, and that contribute to what is currently known regarding the points listed above.

Reviewing the literature presented in this chapter, it is well-known that NGC 2264 is a young (pre-MS) structured cluster. However, the age estimates differ significantly. The presence and cause of a possible age spread is still poorly understood, as is the cause and extent of the structure. The analysis in this thesis provides a quantitative assessment of the age spread and cluster structure, which contributes to the understanding of the star formation history in NGC 2264.

Chapter 2 describes the instrumentation used to obtain the spectroscopy in thesis, along with the data reduction pipeline and any amendments to the pipeline. Chapter 3 describes the instrumental setup, the observations, the measurements of RVs $v \sin i_s$, and CaT (EWs) and an examination of reddening in the cluster. Chapter 4 explores ages and age spreads in the cluster, and defines a new range of acceptable cluster distances. Chapter 5 is focussed on examining substructure or parameter gradients in the cluster, and finally in chapter 6, I discuss the implications of the main results.

2 Instrumentation and data reduction

2.1 Introduction

Open clusters can be observed efficiently using multi-fibre spectrographs due to their small angular extent. This allows many targets to be observed at once. The instrumentation used to obtain stellar spectra from NGC 2264, along with the software used and implemented to reduce and analyse low signal-to-noise (SNR) spectra, is described in this chapter.

The data reduction pipeline used to reduce the data in this thesis was written originally for the AF2 wide field fibre optic spectrograph (WYFFOS) on the William Herschel telescope (WHT) and the Giraffe multi-fibre spectrograph (described in section 2.2), as no other software packages were available to reduce data to the required precision for radial and rotational velocity measurements.¹ The pipeline is described in detail in Jackson & Jeffries (2010b) and has recently been developed to reduce data over a range of optical and infrared wavelength bands, including the far-red region of the electromagnetic spectrum (8000 to 8700Å). It has been used previously to reduce data in Jeffries et al. (2009), Jackson & Jeffries (2010b) and most recently by Jackson & Jeffries (2012) who also use data in a similar wavelength range to the data used in this thesis. The pipeline has also been used to assist the quality control process in the reduction of spectra for the Gaia-ESO survey (Gilmore et al. 2012) by comparing its output against an independently developed pipeline written at Cambridge University in order to identify problems with either pipeline. The automation of the pipeline allows datasets of several hundred spectra to be reduced simultaneously. A description of the instrumentation used to obtain the spectra in this thesis has been described in

¹The reduction software offered by ESO for the Giraffe spectrograph provides raw CCD images and pipeline reduced data for the science spectra. At the time of the analysis, optimal extraction methods were not used in the standard ESO pipeline, and the pipeline did not offer a process to correct the data for scattered light.

section 2.2, followed by a description of the pipeline and the data reduction process in the remainder of this chapter.

2.2 Instrumentation: FLAMES and the Giraffe spectrograph

This thesis is devoted to a detailed investigation of the kinematics and age spreads of the young cluster NGC 2264. Stars in open clusters at distances of several hundreds of parsecs can be faint, and so very few instruments have the required sensitivity needed for observations of these objects. All of the spectra used in this thesis have been obtained with the **Fibre Large Array Multi-Element Spectrograph** (FLAMES) mounted at the Nasmyth A platform of UT2 at the European Southern Observatory's (ESO's) Very Large Telescope (VLT), situated in Paranal, Chile. FLAMES has the capacity to observe many objects simultaneously, of intermediate–high resolution, and over a 25 arcmin diameter field of view. FLAMES consists of several components: the OzPoz fibre positioner, which holds two fibre-hosting plates; the Giraffe intermediate resolution multi-object spectrograph with a resolving power of $R=7500\text{--}30000$; and the Red Arm of the high-resolution **Ultraviolet and Visual Echelle Spectrograph** (UVES) which includes 8 single 1 arcsec aperture fibres. The Giraffe spectrograph holds the MEDUSA, IFU and ARGUS fibre feeding instruments. The MEDUSA fibres, which were used for our observations, have a 1.2 arcsec aperture on the sky and allow 132 separate objects or designated sky observations to be observed simultaneously. The OzPoz fibre positioner hosts two plates which are used alternately, so that when one plate is inserted into the focal plane during observing, the other can be prepared for the following fibre set-up. This reduces dead-time between different set-ups, and although OzPoz is able to hold up to four plates, only two are currently in use. OzPoz has a fibre-positioning accuracy equivalent to 0.1 arcsec on the sky. Both of the plates feed the Giraffe and UVES spectrographs with plate 1 holding 132 MEDUSA buttons, and 30 IFU buttons, along with 8 UVES buttons, allowing simultaneous use of the Giraffe

and UVES spectrographs. Plate 2 also hosts 15 ARGUS buttons. The minimum object separation, which is limited by the button size, is 10.5 arcsec. The Giraffe spectrograph can cover the spectrum between 3700–9000Å, using a range of order-sorting filters and a choice of high or low-resolution grating to select the desired wavelength range. When an object is observed with Giraffe, the light from the star passes through one of 6 slits and through the order-sorting filter, is reflected onto a double pass collimator and through to either a high or low-resolution grating. The light is re-imaged onto a CCD with 15 micron pixels.

For the spectra in this thesis, the Giraffe spectrograph was used with the HR20A grating, which covers the wavelength range 8060–8600Å and has a resolving power of 16000. 1.2 arcsec on the sky corresponds to 6 detector pixels for the Giraffe spectrograph. Calibration bias, flat and arc images were recorded on the same day as each night’s observation. Flat frames were the median of three tungsten-lamp flat exposures.

The Red Arm of the UVES spectrograph is fed by FLAMES and has a resolving power of 47000. UVES includes three wavelength set-ups centred on 5200Å, 5800Å and 8600Å and holds 8 fibres per plate. UVES offers two CCDs and one fibre to be designated to a Thorium Argon (Th-Ar) calibration spectra which assists in precise RV measurements.²

2.3 Data reduction pipeline

The pipeline mentioned in section 2.1 and written by Jackson & Jeffries (2010b), has been described below along with any alterations which were made to reduce the data used in this thesis. The pipeline is a series of modules corresponding to various processes of the data reduction procedure, written in the Interactive Data Language (IDL). It was designed specifically for reduction of low signal-to-noise spectra of low-mass stars from multi-object fibre spectrographs. The pipeline takes the bias, flat, dark, arc and

²The UVES spectra used in this thesis are truncated at $\sim 8540\text{\AA}$ due to a gap in the UVES coverage.

science images recorded for that particular night, (or those closest in time to the observations where they are not taken every night) and combines them to provide optimally extracted spectra of low signal-to-noise spectra. An optimal extraction algorithm was implemented to extract the target spectra. Spectra from the Giraffe spectrograph were recorded as a series of slightly curved lines onto a CCD which displays the light which has entered each fibre on the spectrograph. They are dispersed in wavelength and the width of each of these lines covers several pixels. The electron count was summed in an appropriately weighted manner over the width. The pipeline was also used to perform a wavelength calibration (section 2.3.3), sky subtraction (section 2.3.4) and a process which measures the median of the repeated spectra (section 2.3.5). The pipeline has been described in more detail in the following sections.

2.3.1 Processing the calibration files

The pipeline runs through a series of modules corresponding to either a calibration or a science image. Accompanying the science data from the spectrograph are sky data, bias images, dark images, and flat fields which were recorded with a tungsten lamp illuminating all of the fibres. The pipeline modules which processed these are *bias*, *flat*, *mask* and *circ*. In the *bias* and *flat* modules, median bias images were produced from a set of bias images (typically 11 or more), taken on the same day prior to the observations, to produce a single master bias and flat image. Each flat was debiased by the master bias and then combined to form a master flat. Over time, the DC bias can vary and this was accounted for with a comparison of the master bias file to the signals in the overscan areas of the CCD. The mask file was prepared from one or more dark frames recorded prior to an observing run. ‘Hot’ pixels (pixels which showed more than a specified number of counts per hour) were recorded and masked out in the optimal extraction process. The final step in processing the calibration files (*circ*) takes the coordinates of the pixel nearest to the centre line of the spectral trace of individual fibres across the CCD. The *circ* setup was generated from a flat field/twilight image recorded with the spectrograph configured to illuminate all fibres which were functioning on the

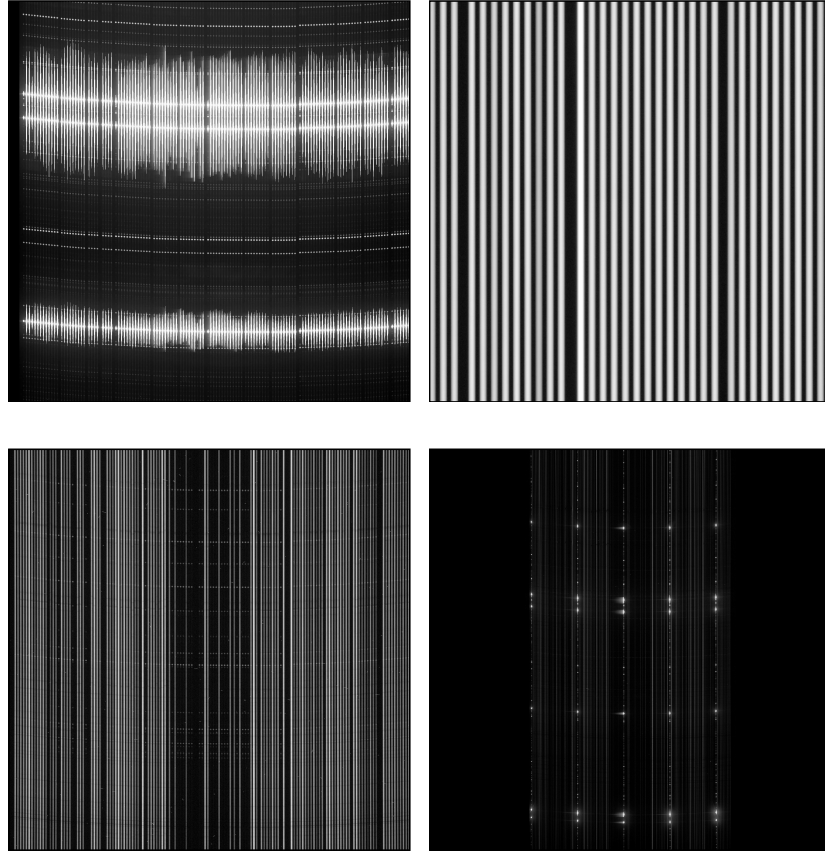


Figure 2.1: Examples of a raw arc image (top left), flat field (top right), science image (bottom left) and simcal (bottom right) .

observation night.

2.3.2 Optimal extraction

To prepare the files for optimal extraction, an image array was created. The image array contained: the original x position (per y value) of the line centre on the CCD image; the raw signal of the line spectra; the median signal between adjacent lines which gave an estimate of the scattered light in the CCD. The effects of scattered light were reduced by interpolating the median background level from either side of the line

centre, and removing this from each element of the measured spectrum.

The optimal extraction algorithm follows that of Horne (1986). A non-uniform weight to pixels was applied in order to minimise statistical noise whilst preserving photometric accuracy. The optimal weighting function used was the normalised spatial profile of the image at any given wavelength. The spatial profile of the image was determined from a boxcar average of the profile of the flat field spectrum (over 20 pixels in the x direction), which averages out variations in the response of individual pixels, whilst also allowing the averaged profile to track variations in the x position of the centre of the spectrum with wavelength. When using a smooth spatial profile, the total electron count of each pixel in the wavelength direction depended on the weighted mean pixel response across the spectral line. To allow for this dependence, the spectra of the measured image, and a flat image were extracted and the ratio of these used to determine the final science spectrum. This process corrects the variations in pixel response. If the variation in pixel response was low enough to invalidate the adopted spatial profile, the effects of local variations in pixel response were cancelled. The ratio between measured and flat images was multiplied by the mean value of the flat spectrum in order to normalise the ratio. This is to ensure that the final science spectra gave an approximate (but weighted according to the relative spectral intensity of the flat field lamp) measure of the total number of electrons at the pixel position corresponding to a given wavelength.

2.3.3 Wavelength calibration

The flat and arc wavelength calibration images were recorded in the day prior to the night-time observations. Hence, the wavelength scale may have drifted between the daytime calibration and the time the observations were carried out. (An image of a raw arc frame and flat image are shown in the upper two plots of Figure 2.1.) The pipeline accounts for this possibility and calibrated the wavelength in two stages;

1. *Standard calibration* The Th-Ar lamp exposure was used to make a standard

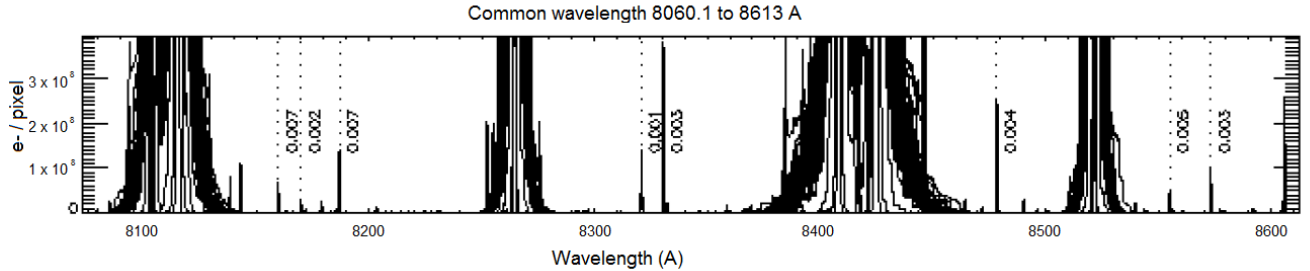


Figure 2.2: Example of an arc spectrum. The dashed lines were those used in the arc process of the data reduction pipeline.

calibration. Several unsaturated arc lines from the arc spectra, once extracted using the same process as the observations, were identified with the spectral atlas of the calibration lamp. Only arc lines with a well-defined separation between any adjacent lines were used in this process. Figure 2.2 shows an arc spectrum with the lines used identified. Once the arc lines were identified in the spectra for each fibre, the line peak positions were found by applying a Gaussian profile to the area of the spectrum surrounding the peaks, and the peak positions were used to determine the coefficients of a third order polynomial of wavelength as a function of pixel for each fibre. These coefficients were used to create a calibrated wavelength scale of the science spectra, followed by a cubic spline interpolation over the masked sections of the spectra. The spectra were then recast onto a common wavelength scale.

2. *Fine offset calibration* The region of the spectrum on which this thesis is focused contains strong sky emission; both continuum emission and strong sky lines. These sky lines in the median sky spectra were used to apply a fine offset in wavelength. The offset was determined by measuring the wavelengths of several strong sky lines in the sky spectra and comparing them to the central wavelengths of the same sky lines in the median sky spectra of all of the sky fibres in all observations. The mean of the results were calculated per fibre

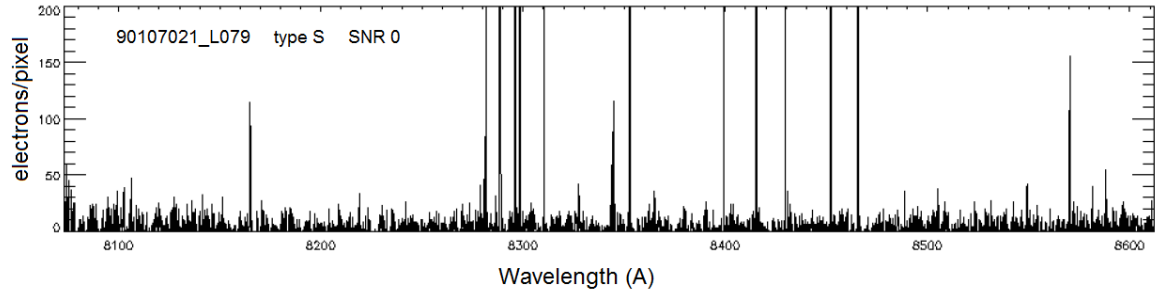


Figure 2.3: Example of a sky spectrum.

and the mean offsets varied from 0.001 and 0.0044Å, corresponding to an RV change of 0.03–0.16 km/s. Although the relative precision of the RV measurements increased through this process, the overall accuracy was not improved as the average position of the strong sky lines across all observations was used as the reference.

2.3.4 Sky Subtraction

Sky emission contaminates and often dominates the stellar spectrum in the $\sim 8500\text{\AA}$ region making determination of radial and rotational velocities, along with line equivalent widths extremely difficult. The method used to measure sky background emission for faint stars, which require long exposure times, was to place several fibres on to areas of blank sky in each observation. The targets were split into several reduction blocks according to the date they were observed. For the reduction blocks containing slightly brighter stars, approximately 10 sky fibres were allocated, and with the fainter stars ($I > 15\text{mag}$) approximately 40 sky fibres were allocated to each configuration (details of the configurations and observations are given in chapter 3). The sky fibres were placed a minimum of 15 arcsec away from any targets, and at positions containing no source in the 2MASS point source catalog. The sky spectra are dominated by strong sky lines in the far-red wavelength region. The difficulty with sky subtraction is that in areas of

star formation, the background contributed by any nebular emission can be spatially variable. This can lead to under or over subtraction. The aims of the sky subtraction process were to reduce contamination of skyline and sky continuum to determine the intrinsic stellar spectra. The sky subtraction options provided with the pipeline include subtracting a median level of sky determined from the average emission from the sky fibres and are as follows;

1. *Linear sky subtraction*: A linear sky subtraction method where a median of the signal per wavelength bin of all sky fibres in the reduction block was subtracted from the reduced stellar spectra.
2. *Scaled sky subtraction*: The scaled sky subtraction method allows for variations in the fibre to fibre transmission coefficient, by multiplying the median sky spectrum by a scaling factor according to the individual fibre. The scale factor aims to minimize the cross-correlation function of the sky subtracted stellar spectrum with the sky spectrum. This method reliably removes the sky continuum, however fails to accurately remove the strong sky lines, which are particularly prominent in some regions of the spectrum used in our observations.
3. *Scaled and masked sky subtraction*: The spectral window used in this thesis contains many strong sky lines (see Figure 2.3 for an example of a sky spectrum). A masking option is available in the pipeline in which a sky subtracted spectra was masked over the area of the strongest sky lines. A cubic spline interpolation was used to interpolate the emission across the masked sections of the spectra.

The spectra were reduced using each of these methods and compared with each other to determine the most accurate sky subtraction. This was done by applying each sky subtraction technique to the sky fibres individually, expecting that in an ideal sky subtraction, the remaining flux would be zero. However, some sky emission still remained in the spectra. Therefore, in addition to these methods, I have developed

and tested several other methods of sky subtraction in order to remove sky lines from the stellar spectra. These methods are;

4. *Linear around emission lines* This sky subtraction method included subtracting the sky continuum at $\pm 5\text{\AA}$ around the two Calcium triplet emission lines present in the our spectra (at 8498 and 8542 \AA), and subtracting the median sky from the remaining wavelength ranges separately. This effectively reduces the amount of variable sky emission from around the emission lines which would have otherwise been removed from the entire range of the spectra.
5. *Surface sky subtraction* All of the sky fibres in a reduction block were used to produce a ‘sky surface’ over the region in space of which the stellar spectra lie. The surface was produced according to fibre position and sky flux. The surface was determined by interpolating the sky level between the fibres. For each stellar spectra, the sky level was subtracted according to the interpolated surface at that position per wavelength bin.
6. *Nearest fibre sky subtraction* This was done in two ways; taking the nearest five fibres to the target per reduction block and subtracting the median sky flux, and taking the closest fibres within a given diameter around the star.

Again, comparisons were done and it was determined that method 6 gave the best results for removing the sky lines and the sky continuum. All of the data used in this thesis were analysed using method 6, subtracting the sky emission from the closest five fibres to the star.

2.3.5 The median spectra

The final standard module of the data reduction pipeline averaged the spectra recorded in each observation block (according to the night in which the observations were taken). For the data used in this thesis, either two or three exposures were taken successively within a single observation block and per object observed. In order to reduce noise

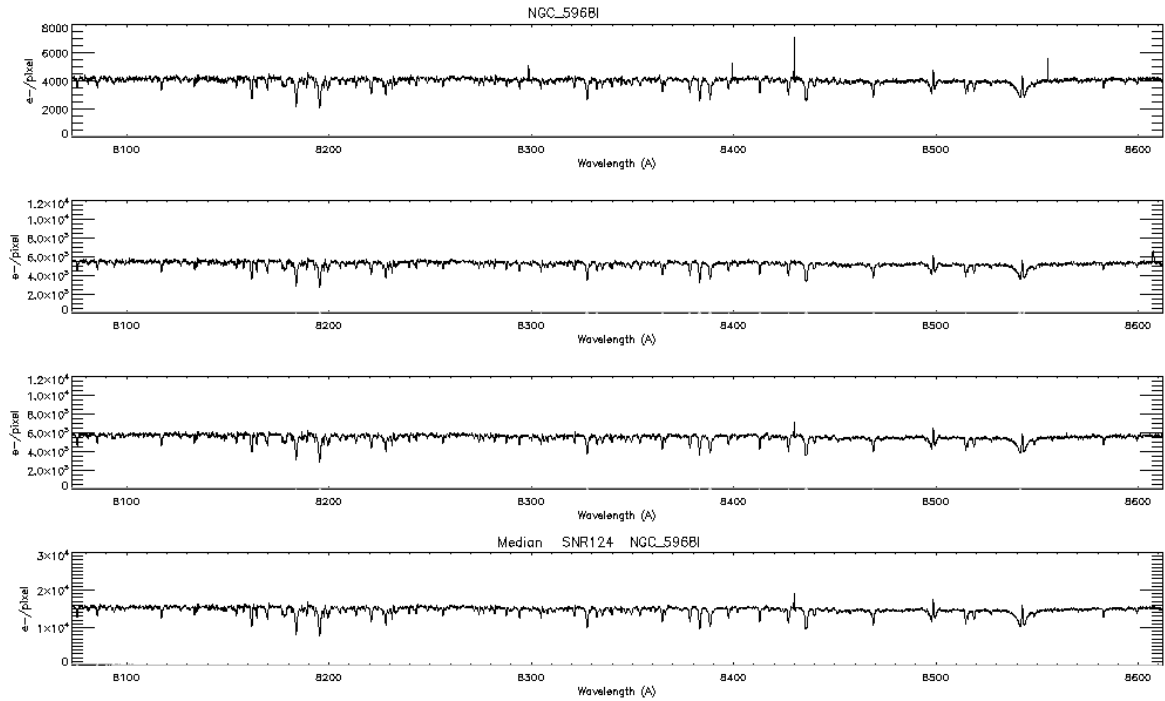


Figure 2.4: Representative high signal-to-noise spectra of a target in the open cluster NGC 2264 (upper three panels) along with the median of these (lower panel).

and the effect of cosmic rays in the spectra, the images were averaged. If two images were available, the mean of the spectra were taken, and the median if three images were available. If the difference between any two spectra (for the same star) was larger than double the uncertainty in the mean, then, to minimise cosmic ray contamination, the final spectra was taken as that with the lowest overall flux. Figure 2.4 shows three high signal-to-noise spectra of the same object in the upper three plots, followed by the median in the lower panel. As seen in Figure 2.4 at approximately 8430\AA , most prominent cosmic rays were removed in this process.

2.3.6 Telluric correction

Telluric lines arise from the Earth's atmosphere and contaminate spectra, particularly in the region 8000–8400Å. As described in section 2.2 the Giraffe and UVES spectrographs can observe simultaneously. The Giraffe spectrograph was used to observe objects in NGC 2264 whilst the UVES spectrograph, was used to observe bright, hot stars in the same field as the observed objects which were used as telluric standards. An example of two telluric standards at different airmass are shown in Figure 2.5. Although the telluric standards were truncated at $\sim 8540\text{\AA}$ due to a gap in the UVES coverage, the standards were used to correct the stellar spectra for telluric contamination. The telluric lines were strongest in the $8073\text{\AA} - 8450\text{\AA}$ region. For this reason and because of the truncation of the UVES wavelength coverage, the stellar spectrum was only corrected up to $\sim 8450\text{\AA}$ and set to unity elsewhere in the spectrum. The telluric standards were filtered to match the resolution of the Giraffe spectrograph using a Gaussian kernel, and then rebinned onto the Giraffe wavelength range. The median of the standards were scaled by the airmass of the target spectrum. The target spectra were then divided by the telluric spectra to produce telluric corrected stellar spectra.

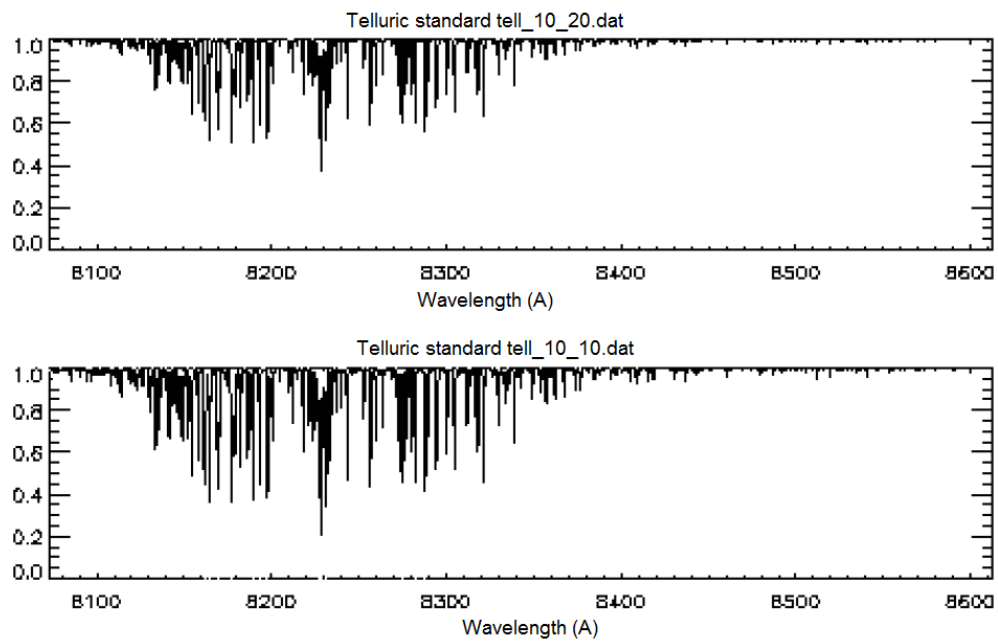


Figure 2.5: An example of two telluric standards of different airmass used in the telluric correction process.

3 Spectroscopic observations and the determination of stellar parameters

3.1 Introduction

In this chapter, the observational database of NGC 2264 is described, along with the determination of parameters used in this thesis. As mentioned in chapter 2, the data which have been used in this thesis were obtained using the Giraffe/FLAMES spectrograph. The spectra were observed over the wavelength range 8073 - 8612Å. In this wavelength range, both the radial and rotational velocities were measurable, which can provide stellar projected radii when combined with rotation periods. This wavelength range also covers the two strongest calcium triplet (CaT) infrared lines at 8498 and 8542Å. The target selection is described in section 3.2 and the observational database is explained in section 3.3. The following parameters are determined in the subsequent sections;

- Radial velocities (RVs),
- Projected equatorial rotation velocities ($v \sin i_s$),
- Cluster reddening and extinction,
- Effective temperatures (T_{eff}),
- Luminosities,
- CaT residual equivalent widths (EWs).

The parameters determined in this chapter are tabulated in appendix A1.

3.2 Target selection

The work in this thesis required spectroscopy, photometry and rotation periods. At the time at which the original proposal was made, there were several available photometric catalogues containing observations of stars in NGC 2264 that have been used in selecting the most appropriate targets for this study. The targets selected for this survey were from the Lamm et al. (2004) and Makidon et al. (2004) catalogues. The Lamm et al. (2004) catalogue consists of 405 stars with measured rotation periods and the Makidon et al. (2004) catalogue contains 201 stars with measured rotation periods. The targets were chosen so that many objects could be covered by four Giraffe fields (see section 3.3) from the spatial range $99.8772 < \text{RA}(\text{deg}) < 100.5380$ and $9.2880 < \text{DEC}(\text{deg}) < 10.0113$, and are shown in Figure 3.1.

The targets were divided into two categories;

- **Primary targets** The targets drawn from the Lamm et al. (2004) and Makidon et al. (2004) catalogues are active spotted stars, and have secure rotation periods of 0.3-18 days. They have a magnitude range of $12.5 < I(\text{mag}) < 17.5$, and colours of $(V-I) > 1.0(\text{mag})$, consistent with cluster members. The parent sample in the Lamm et al. (2004) catalogue included 10600 stars with I_C magnitudes between 9.8 and 21 mag, and approximately 5% of these are periodic variable stars with periods between 0.2 and 15 days. By comparing the distribution of the standard deviation in light curves, and the distribution of $H\alpha$ emission index for periodic variable stars with the corresponding distributions for the irregular variables, Lamm et al. (2004) found that their method used to measure rotation periods was biased towards WTTS, so the sample may be missing a representation from the younger CTTS. (They used a $H\alpha$ equivalent width of 10\AA to distinguish between CTTS and WTTS). They estimated that 23% were CTTS but detected only 15% CTTS. The distribution of primary targets, and four circled fields over plotted onto the cluster image are shown in Fig. 3.1.

- **Secondary targets** The remaining targets were selected as candidate cluster members and were included to fill the empty fibres in the configurations (see section 3.3). The list of candidates is an inhomogeneous selection based on IR and X-ray properties that was supplied by F. Favata (private communication). The Sung et al. (2008) catalogue was used to provide optical photometry for these targets. They cover a region surrounding the cluster with magnitudes and colours similar to those of the primary targets.

3.2.1 Contamination by non-members of the cluster

Lamm et al. (2004) used photometric criteria to screen their sample, which included target selection in the I_c vs $R_c - I_c$ CMD and the $R - H\alpha$ vs $R - I$ diagram to disentangle MS from pre-MS stars. This selection method excludes giants, but does not necessarily exclude foreground MS dwarfs. To estimate the extent of MS contamination, a random sample of MS stars with T_{eff} 's in the same range as the T_{eff} range of the primary targets has been selected from McQuillan, Mazeh & Aigrain (2014). The period distribution of this sample is shown in Figure 3.2, along with the period distribution of primary targets. There is a clear overlap of the MS and pre-MS period distributions. However, <10% of the stars in the primary sample have rotation periods above 10 days, compared with >90% of the MS sample. The rotation periods of the stars in our sample are mostly <10 days so they are unlikely to be MS field stars. Lamm et al. (2004) suggest that the periodic and irregular variables found in their sample are not necessarily all pre-MS stars, although variability is probably one of the best indicators of youth. We are confident that the primary sample used predominantly in chapters 4 and 5 of this thesis has little contamination from MS stars.

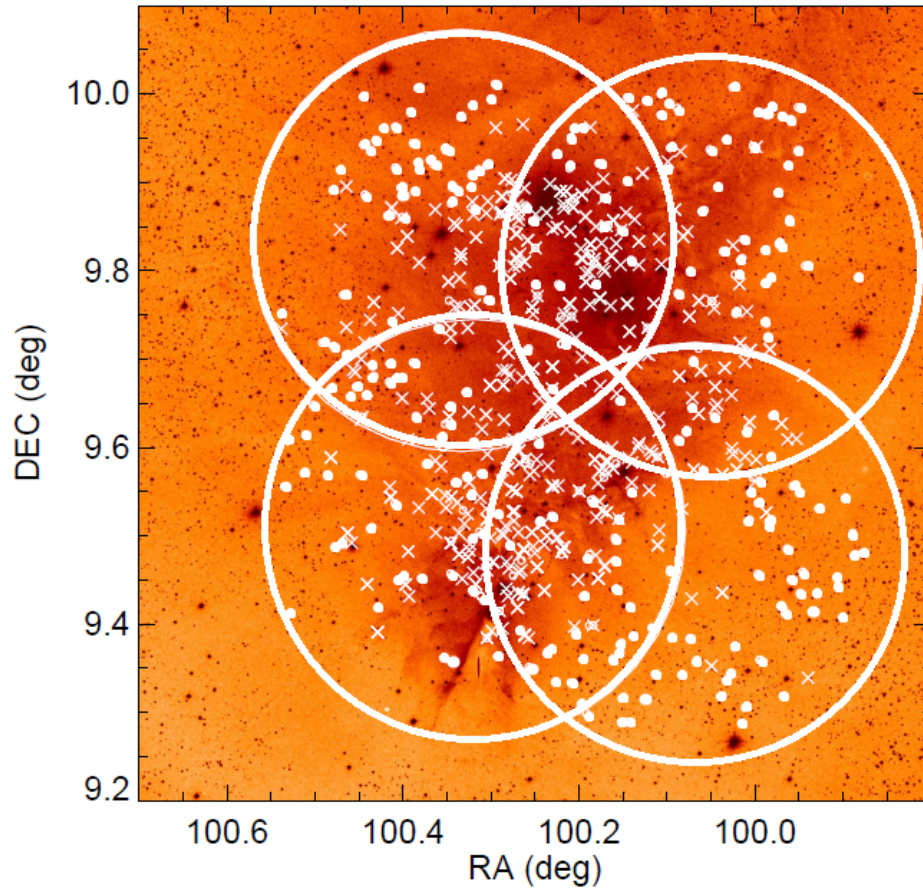


Figure 3.1: Spatial distribution of targets in the open cluster NGC 2264. The four large open circles show the boundaries defining the four Giraffe fields used in these observations. Small circles show candidate cluster members (secondary targets) and the crosses are the primary target stars and are plotted over an image of the cluster (from the Digitized Sky Survey). Details of the observations are listed in Table 3.1.

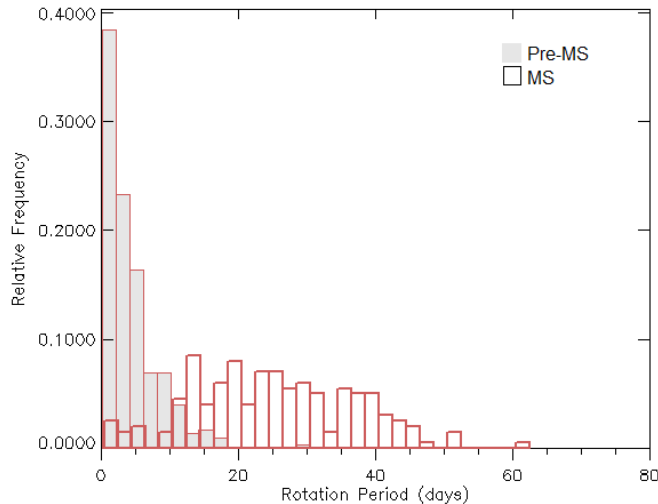


Figure 3.2: The histogram shows the normalised period distribution of 152 primary targets (filled) and the normalised period distribution of a random selection of 1000 main sequence stars with the same T_{eff} range.

3.3 Instrumental setup and observations

The targets were observed with the intermediate-high resolution Giraffe spectrograph, mounted on the FLAMES multi-fibre instrument at European Southern Observatory’s (ESO’s) 8.2-m aperture Very Large Telescope (UT-2). The Giraffe spectrograph is fed by 132 MEDUSA fibres, each with apertures of 1.2 arcsec. The Giraffe spectrograph is equipped with a range of order sorting filters. The HR20A filter was used for these observations, and in this mode, the spectra obtained cover a wavelength range of 8073\AA to 8600\AA and are centred on 8366\AA , with a resolving power of ~ 16000 . The targets were observed in service mode between January and March, 2009.

Details of the observations are shown in Table 3.1 and include four fields each with a 25 arcmin diameter, shown in Figure 3.1. The targets were separated into reduction blocks (RBs, also shown in Table 3.1) four of which contained bright stars ($12.5 < I(\text{mag}) < 15.5$) and one for each field, and nine containing ($15.5 < I(\text{mag}) < 17.5$)

faint stars. Between 64 and 106 stars were allocated in each of the RBs. The faint RBs included approximately double the number of allocated sky fibers (~ 40) than the bright configurations which assisted in performing a precise sky subtraction. A repeat of one of the faint RBs (90326007, see Table 3.1) was performed due to a low signal-to-noise ratio (SNR) of the first set of observations.

Each of the bright stars were observed with three consecutive 840 second exposures. Each of the faint stars were observed with two consecutive 1280 second exposures. In total, 1573 spectra were obtained (including sky spectra). 1063 of these are stellar spectra, 510 are sky spectra. The database includes 634 unique targets including 367 unique targets with known rotation periods. 1062 of the spectra have $\text{SNR} > 5$ and 1053 have $\text{SNR} > 10$. The RBs are listed in Table 3.1 along with the number of targets included in each RB and the catalogue from which primary targets were drawn.

Table 3.1: A numerical description of the observations of NGC 2264. The columns refer to the field centres, number of sky fibres, primary and secondary target fibres used in each RB. The final RB (90324007) was repeated due to a low SNR.

RB ^a	DD/MM/YY	UTC	RA	DEC	Sky	Primary _M ^b	Primary _L ^c	Secondary	No. ^d
Bright									
90107007	07/01/09	01:13:59.313	100.0675	9.4800	22	9	37	58	126
90107011	07/01/09	02:10:06.146	100.0508	9.8036	22	11	50	45	128
90107015	07/01/09	05:04:04.148	100.2998	9.5231	23	8	45	52	128
90107019	07/01/09	06:00:46.124	100.3333	9.8342	23	4	41	60	128
Total bright					90	32	173	215	510
Faint									
90203007	03/02/09	03:44:31.797	100.3333	9.8342	48	0	53	21	122
90204002	04/02/09	04:23:52.472	100.3333	9.8342	48	0	53	21	122
90211007	11/02/09	02:01:07.501	100.0675	9.4800	46	0	51	13	110
90211010	11/02/09	03:01:41.207	100.0508	9.8036	45	1	60	13	119
90318007	18/03/09	00:18:44.170	100.0675	9.4800	47	0	51	13	112
90318010	18/03/09	01:16:00.608	100.0508	9.8036	44	1	60	13	118
90318013	18/03/09	02:13:01.055	100.2998	9.5231	48	0	62	11	120
90324007	24/03/09	00:28:01.072	100.2998	9.5231	47	0	62	11	120
90326007	26/03/09	00:08:50.730	100.2998	9.5231	47	0	62	11	120
Total faint					420	2	514	127	1063
Total					510	34	687	342	1573

NOTES: ^aRB = Reduction Block; ^b from Makidon et al. (2004); ^c from Lamm et al. (2004); ^dtotal number of targets in RB

3.4 Radial and rotational velocity measurements

In this section the processing of spectra to determine RVs and $v \sin i$ s is described. The spectra were initially prepared using the Giraffe data reduction pipeline as explained in chapter 2. However, due to the precision required to measure RVs, further processing was required. All of the target spectra obtained for this study underwent the same procedure to measure their velocities. The procedure was written as a batch process in IDL. The process utilised the CONVOL built-in IDL program which allows spectra to be cross-correlated or convolved with other spectra or with broadening kernels that represent the instrumental resolution or rotational broadening (Gray 1992).

The RVs were determined by measuring the offset of spectral lines away from their rest wavelength. This was done by comparing the stellar spectra and the spectrum of a standard star, where the peak position offered by the cross-correlation function (CCF) represents the difference between the observed RV of the target and standard stars. The resulting velocities have to be corrected for the difference between the heliocentric corrections of the target and standard, which are specific to the time of observation. The width of the CCF then was used to measure the $v \sin i$ (Tonry & Davis 1979, see section 3.4.2).

A database of stellar spectra of standard stars from Bagnulo et al. (2003) were used in order to measure the radial and rotational velocities. The database was chosen on the basis of covering the temperature range (~ 2800 – 5100 K) of stars included in our target sample. The standard-star spectra were of slow rotators (period > 10 days) and were matched by spectral type to the target star (see section 3.4.1).

3.4.1 Using the cross-correlation technique to measure RVs and $v \sin i$ s

The standard spectral templates were processed as follows;

- The standard spectra were passed through a Gaussian filter in order to match the resolution of the Giraffe spectrograph. The Gaussian width was determined

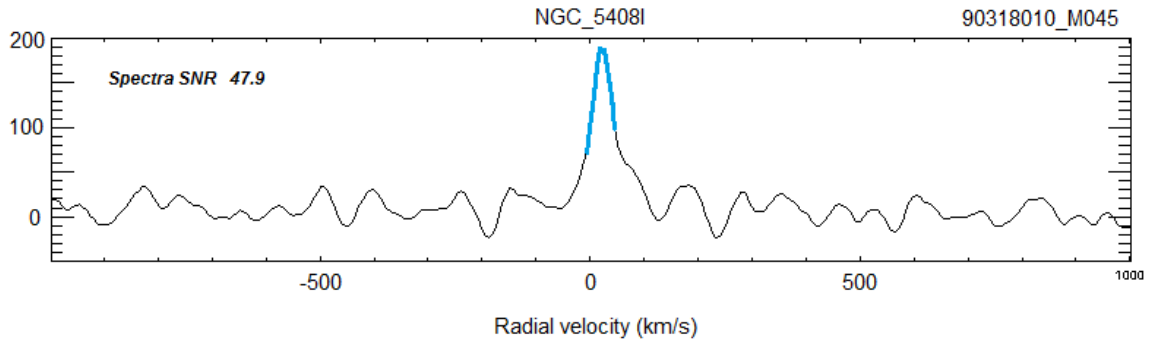


Figure 3.3: An example of a cross-correlation function. The solid black line is the cross-correlation function over the entire range of convolution. The blue curve is the region in which the width and central peak (RV and $v \sin i$) were determined from.

from the resolution and wavelength binning of the target spectra.

- The standard spectra were then recast onto the common logarithmic wavelength scale adopted for the target spectra.
- The standards were clipped to the cross-correlating region of 8245-8355Å which excludes areas of the spectrum with strong telluric lines and the CaT lines.

The stellar spectra were processed through a high-pass filtering system, effectively removing the low-frequency components of the spectra by dividing the original spectra by a polynomial using ‘SVDFIT’ in the IDL programming library. The CCF was then produced from the template spectra and the target spectra. A range of spectral templates of different spectral types (G0 to M5) were cross-correlated with the target spectra, following the process used in Tonry & Davis (1979) and using the CONVOL procedure in IDL.

The spectral template showing the highest peak in the CCF relative to the r.m.s level of the CCF remote from the peak was selected as the best fit. The selected template was then used to provide a cross-correlation waveform with a peak from which both the RV and widths were measured. An example of a cross-correlation waveform is shown in Figure 3.3.

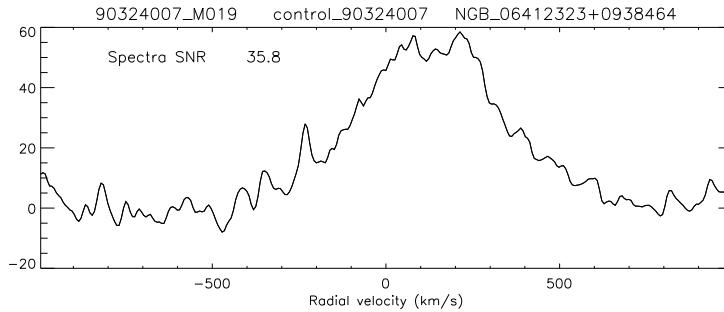


Figure 3.4: An example a CCF from which an RV or width was unable to be measured.

The central wavelength and width of the peak in the CCF were measured in three stages;

- **An initial Gaussian fit.** The central position of the CCF was estimated by fitting a Gaussian profile to a ± 1000 km/s section of the CCF. The cross-correlation peak was modelled with a Gaussian using IDLs Gaussfit procedure, and the CCF was checked for a single-peak (the remaining multiple peaked spectra were rejected).
- **Second Gaussian fit** If the width was less than ~ 38 km/s the Gaussian fit was applied again over ± 150 km/s. This was done to reduce the influence of the noisier “off-peak” component of the CCF.
- **A third Gaussian fit** The third Gaussian fit was made over a consistent region of the CCF, which corresponded to 0.8 times the standard deviation measured from the secondary Gaussian fit. Figure 3.3 shows the CCF over the wavelength range that was used in this process, the blue curve indicates the region in which the position and width was determined from.

Finally, the target RVs were derived from the measured CCF lags by applying the necessary heliocentric corrections appropriate for the times of observation and the positions of the targets. For some of the targets in the sample, we were unable to

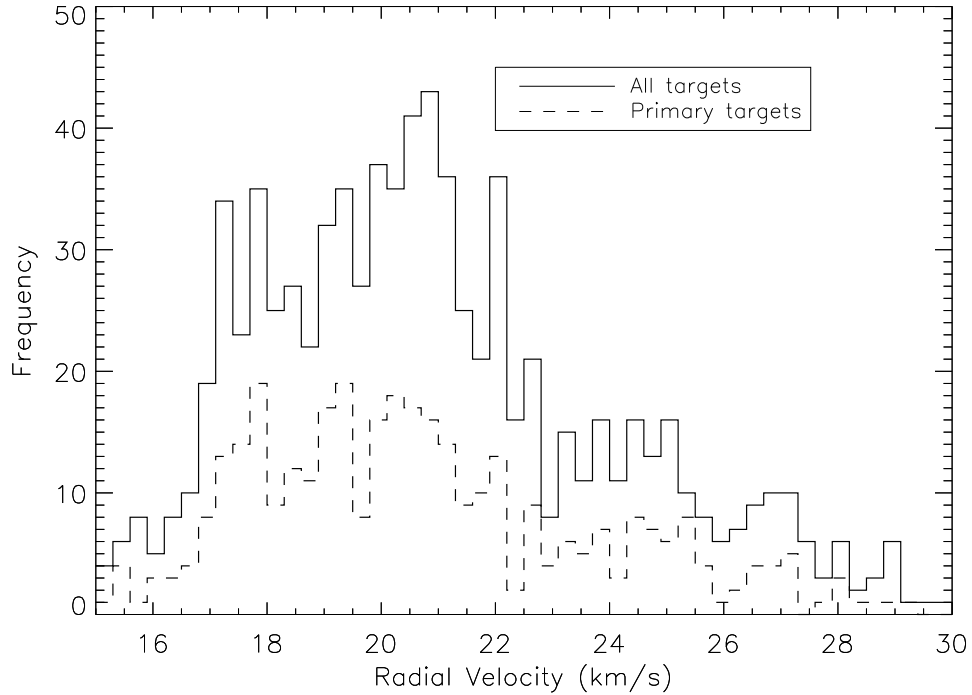


Figure 3.5: A histogram of the RVs between 15 and 30km/s (which includes 95% of the measured RVs) obtained for the primary and secondary targets in NGC 2264. The standard deviation of the RV dispersion is 3.55km/s.

determine an RV or $v \sin i$. Figure 3.4 shows an example of a CCF for which a reliable RV could not be measured as there was no clear single-peak in the CCF, possibly caused by low-SNR, a binary status or a heavily veiled spectrum. For 55 of the targets, we were unable to measure the RV. Figure 3.5 shows a histogram of the measured RVs.

3.4.2 Projected equatorial rotational velocities

The rotation of the star causes the spectral lines to broaden, and the scale of the broadening depends on the magnitude of the rotational velocity of the star. In reality the rotational velocity at the star's equator (v) and the sine of the inclination of the star's rotation axis to the line of sight (i) was measured. There are algorithms which have been produced and are available in the literature which predict the magnitude

of broadening in the stellar spectrum as a function of $v \sin i$ and limb darkening (Gray 1992). The standard spectral templates with which the stellar spectra are cross-correlated are slow rotators, so the increased width of the CCF peak over that expected from a non-rotating star was assumed to be due to the rotation of the star only.

Further to the processing of spectra in section 3.4.1, the following steps were taken to measure $v \sin i$ s ;

1. **Broaden to zero width** Although slow rotators were used as standard stars, they still contain a small level of rotational broadening. In order to allow the level of broadening in the stellar spectra to be measured correctly, the spectral templates were broadened to the width that matches the rotational velocity of the slowly rotating stars ('zero width', Z). Using 10 slowly rotating stars, we averaged their measured CCF width and found that $Z=46.6 \pm 0.9$ km/s (the error was determined from the standard deviation of the measured widths). Each of the spectral templates were broadened so that they produced CCFs that had the same width (Z) as the CCFs produced by the slowly rotating stars in our sample.
2. **Broaden by 'spinning up' rotation in the standard** After broadening to the zero width, the spectrum of standard stars were broadened by various levels of $v \sin i$, using the IDL procedure 'LSF_ROTATE' for a range of velocities. 'LSF_ROTATE' is available from NASA's IDL Astronomy Users Library (Astron) and utilises Equation 17.12 of Gray (1992). A linear limb darkening factor of 0.6 was used (Claret, Diaz-Cordoves & Gimenez 1995). The broadened standards were cross-correlated with a standard spectrum which had been broadened to the zero width. A calibration curve was produced by 'spinning-up' the template and this is shown in Figure 3.6 for an M0 type star. This curve was used to obtain a $v \sin i$ for each of the stars with measured CCF widths. The error bars correspond to the standard deviation of the width values produced with templates ranging from G0 to M5.

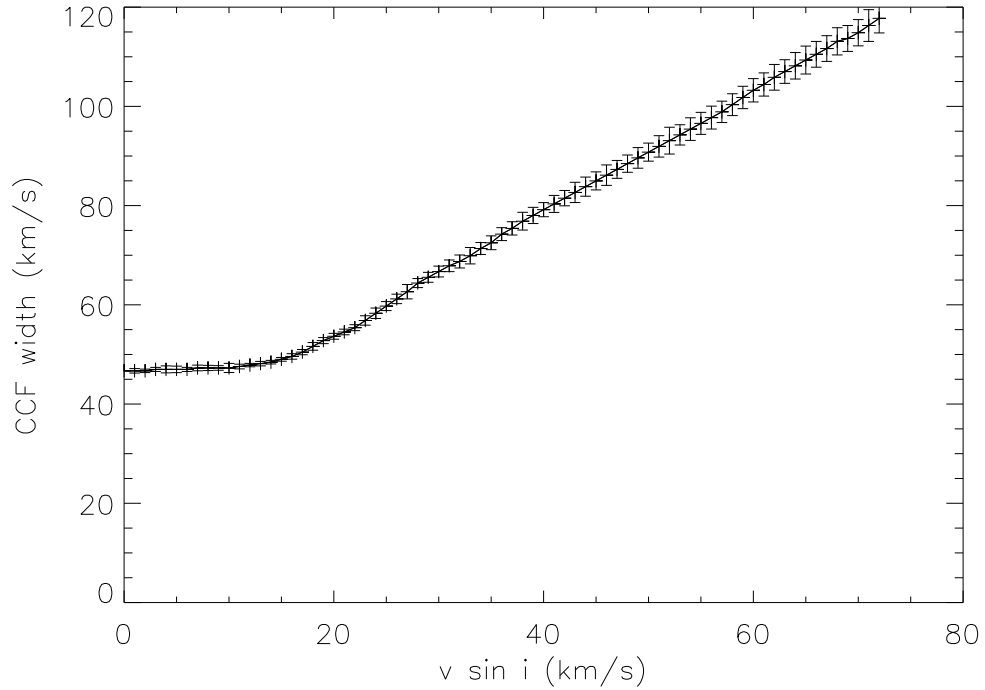


Figure 3.6: The calibration curve produced when artificially broadening a synthetic template spectrum to $v \sin i$ values between 0 and 70km/s. The error bars correspond to the standard deviation of the width values produced from various templates ranging from Types G0 to M5. This curve was used to obtain the $v \sin i$ from the measured CCF width.

3. **Simulating noise in the spectrum** This step relates to the uncertainties measured in section 3.4.3. The measurement errors corresponding to variations in SNR were simulated by injecting random noise using a Gaussian distribution into the template spectra. The results were used to determine the expected uncertainty in CCF width and hence, $v \sin i$ as a function of SNR.

Due to the instrumental resolution, we could not measure $v \sin i$ s below 8km/s. Figure 3.7 shows a histogram of the $v \sin i$ s of the targets in the sample.

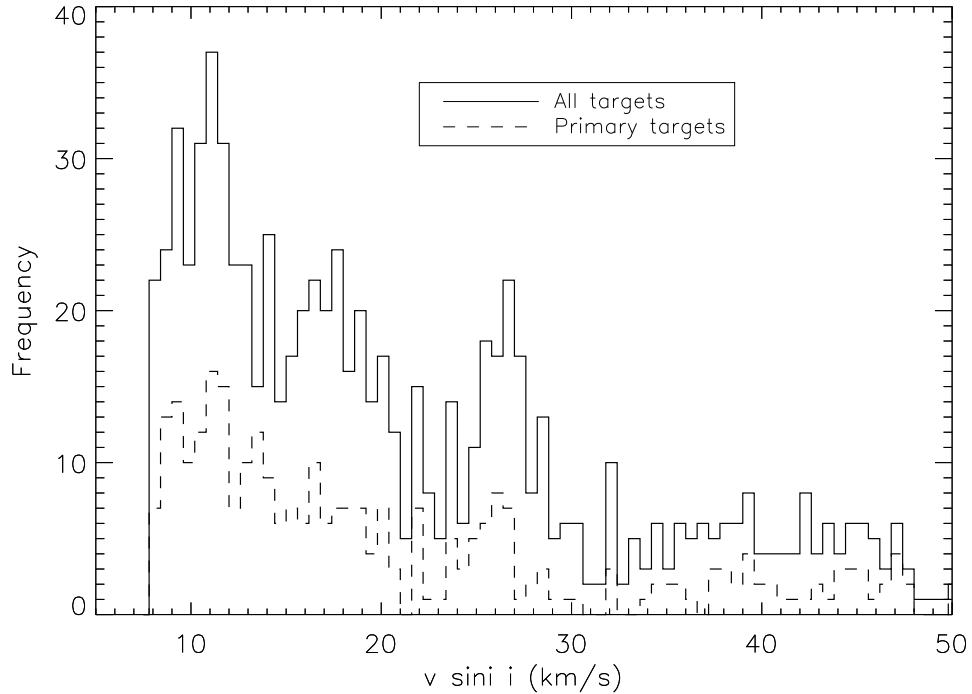


Figure 3.7: The $v \sin i$ values of the primary and secondary targets with a clear peaks in the CCF.

3.4.3 Radial velocity and $v \sin i$ errors

There are two principal sources of uncertainty in the measurements of RV and $v \sin i$, random noise and uncertainty in wavelength calibration. The first can be measured from two exposures of the same star taken at approximately the same time with the same instrumental setup. The second is found by comparing repeat observations of the same star taken on different nights and different instrumental setups. The method used in this section to measure RV and $v \sin i$ errors follows closely from that presented in (?).

Figure 3.8 was used to estimate the level of random noise in the stellar spectra. The curve shows the uncertainty in RV associated with varying levels of noise in the spectra, measured by comparing the widths from repeated observations in the same reduction block of the same target. This is plotted as a product with the SNR on the y-axis, and the measured $v \sin i$ on the x-axis. The error bars represent the standard

deviation of the curves produced when injecting random noise of values of 5, 10, 20, 50 and 100 into the spectrum of a M0 type star. The curve in Figure 3.8 shows an empirical fit to the data of the functional form $A + B(v \sin i)^2$ where A and B are fitted constants. A similar functional form is used to describe both the uncertainty in the RV and the uncertainty in the width of the CCF. This is taken to be a reasonable description of the random noise as a function of $v \sin i$ and SNR for the RV and width measurements in NGC 2264.

For very high $v \sin i$ s ($>70\text{km/s}$) the results were moderately affected by the level of SNR (see Figure 3.8). Considering the $v \sin i$'s $> 70 \text{ km/s}$ the cross-correlation function peak became distorted and unmeasurable in some cases. For high $v \sin i$ s, particularly ones with low (<10) SNR, the $v \sin i$ s were unreliable and rejected from the sample, as there was no clear peak in the CCF. This produces a bias in our sample, as the most rapidly rotating stars are likely to be missing from the final sample.

Constants A and B describing the random noise in RV were determined by comparing results of repeat observations in the same RB giving values of $A_{RV}=8.52 \text{ km/s}$ and $B_{RV}=0.02 \text{ km/s}$. The uncertainty in width for short term repeats was determined by comparing results from the same RB as $A_W=8.9\text{km/s}$ and $B_W = 0.08 \text{ km/s}$. The additional component of noise due to uncertainty in wavelength calibration and change of instrumental setup is taken to be constant (independent of $v \sin i$ and SNR). This adds in quadrature to the random noise giving a total uncertainty of;

$$\sigma = \left(\left(\frac{A + B(v \sin i)^2}{SNR} \right)^2 + C^2 \right)^{\frac{1}{2}} . \quad (3.1)$$

We found $C_{RV} = \sim 0.54\text{km/s}$ and $C_W = 1.14\text{km/s}$. (C_W is the width that is used to measure $v \sin i$.) Using the empirically determined values the total uncertainty in RV and width of the CCF is given by;

$$\sigma_{RV} = ((8.52 + 0.02(v \sin i)^2)^2 / SNR^2 + 0.54^2)^{\frac{1}{2}} \text{km/s} \quad (3.2)$$

$$\sigma_W = ((8.9 + 0.08(v \sin i)^2)^2 / SNR^2 + 1.14^2)^{\frac{1}{2}} \text{km/s} \quad (3.3)$$

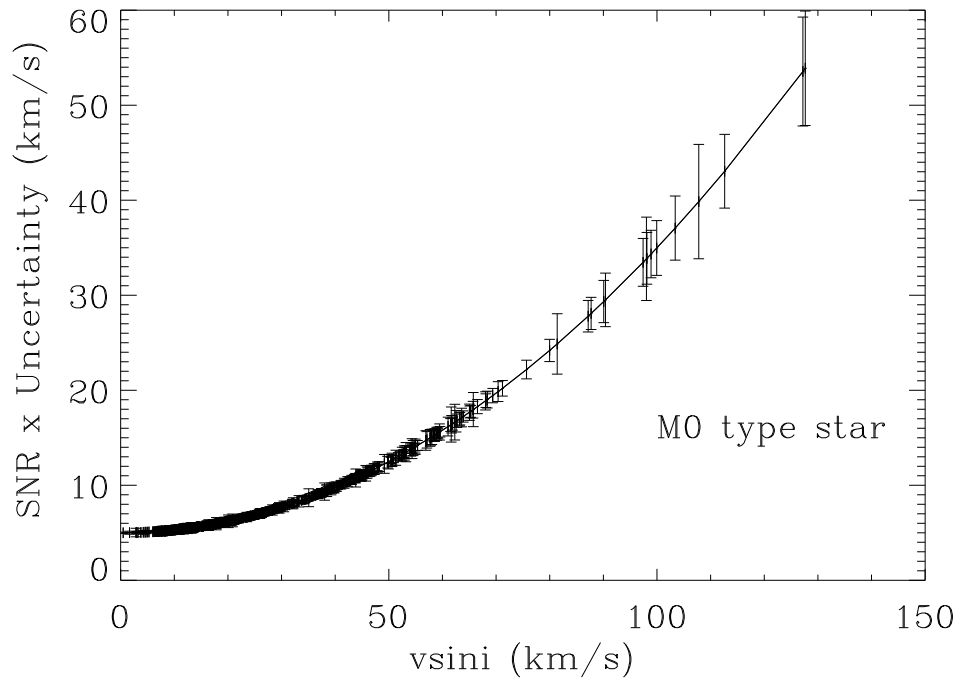


Figure 3.8: A curve fit to the data which shows a relation between the spectra SNR and the measured $v \sin i$. The measurement uncertainty in RV associated with varying levels of Gaussian noise in the spectra determined from repeats of the same target in the same reduction block on the same night is plotted as a product with the SNR and uncertainty on the y-axis, and the measured $v \sin i$ on the x-axis. The curve was produced from an M0 type star. The error bars represent the standard deviation of the curves produced when injecting random noise values of 5, 10, 20, 50 and 100 into the spectrum.

The median RV uncertainty found for stars in the primary and secondary sample is 0.68km/s. The uncertainty in $v \sin i$ is estimated from the measured uncertainty in the measured width of the CCF due to rotational broadening assuming;

$$v \sin i \propto (W - Z)^{\frac{1}{2}}. \quad (3.4)$$

This leads to an uncertainty in $v \sin i$ of

$$\sigma_{v \sin i} = v \sin i \frac{(\sigma_W^2 + \sigma_Z^2)^{\frac{1}{2}}}{2(W - Z)} \quad (3.5)$$

This approximation is valid for values of $v \sin i$ up to ~ 50 km/s but may underestimate the errors for the fastest rotation stars.

3.4.4 External validation of RVs and $v \sin i$ s

We compared the RVs and $v \sin i$ s measured in sections 3.4.1 and 3.4.2 with other catalogues in order to externally validate the measurements. The RVs were compared with the catalogue of Tobin et al. (2015) which contained averages of their RVs and those of Fűrész et al. (2006) and they quoted RV uncertainties of 1.2km/s. We compared the $v \sin i$ s with those from Baxter et al. (2009). A distribution of their $v \sin i$ errors gave $\sigma=0.2$. There were 114 targets used to compare RVs and 16 targets used to compare $v \sin i$ s. Out of 114 repeated targets, the difference in RV between the RV in our catalogue and the RV in Tobin et al. (2015) is plotted in Figure 3.9. The standard error of the RV differences is 0.79km/s, with no systematic offset. The standard error of the $v \sin i$ differences is 1.83km/s, also with no systematic offset.

3.5 Extinction and cluster reddening

A review of the literature relating to extinction and reddening in NGC 2264 is presented in chapter 1.5.3. Extinction acts to both scatter photons out of the line of sight and absorb photons. The absorption of the light is at wavelengths comparable

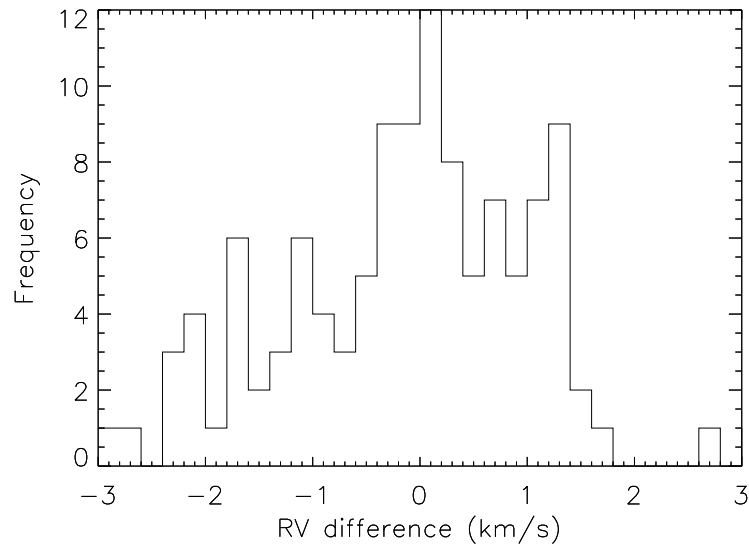


Figure 3.9: A histogram of the difference in RVs between the targets in our catalogue and the RVs from Tobin et al. (2015).

in size to the dust grains, so extinction is most prominent at shorter wavelengths. An accurate reddening value is required to determine the effective temperatures from photometric colours. We estimate the effect of reddening for individual stars by comparing photometric colours with those expected from their spectral types (section 3.5.1).

3.5.1 Individual extinctions

Since the spectral classification of stars can be accurate even in the presence of significant reddening, we used spectral classifications to assist in deducing the reddening and extinction values in NGC 2264. Deriving the reddening for stars with both spectroscopy and photometry, was done on an individual basis. We were interested in whether a single reddening value could be applied to all stars in our sample, or whether any differential reddening would significantly affect our estimation of effective temperatures. We compared observed photometric colours from the Lamm et al. (2004) photometric catalogues with colours expected from the spectral classifications from Dahm & Simon

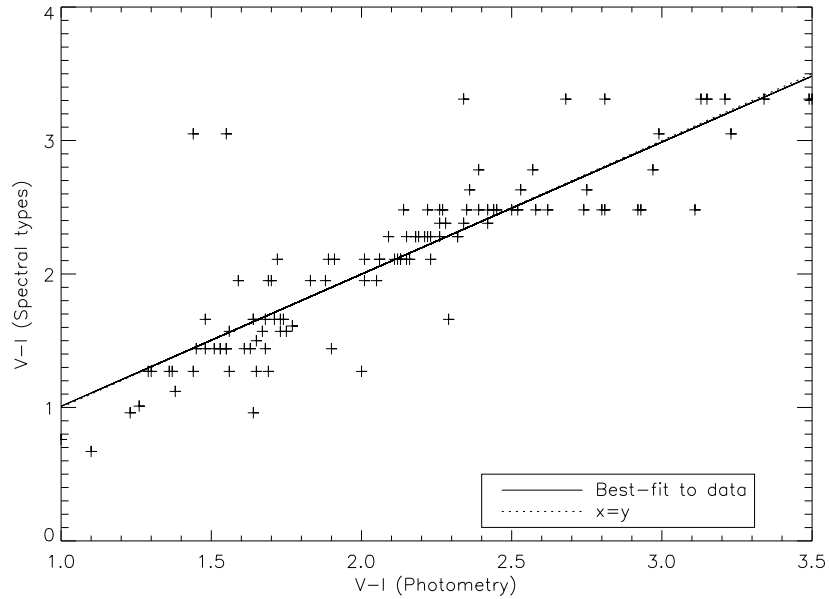


Figure 3.10: The photometric $V-I$ colours and $V-I$ colours expected from spectral classification.

(2005) to obtain estimates of colour excesses.

It was important to perform these tests in wavelength bands which are not greatly affected by the contribution of non-photospheric sources, such as circumstellar material. The $V-I$ colour was used, which limits the amount of contamination from $H\alpha$ emission and circumstellar material (the V magnitudes may be contaminated by accretion and this is discussed in section 3.5.2).

We used the Pecaut & Mamajek (2013) pre-MS empirical relationship to estimate the intrinsic colours. The photometric colours versus the colours expected from spectral classification are plotted in Figure 3.10. The errors in photometry and spectral types, and how they affect the luminosity and effective temperatures errors are discussed in sections 3.6.1 and 3.6.2).

We derived the interstellar reddening, quantified as $E(V - I)$, towards each star by taking the difference between the photometric colour and the colour predicted from

the spectral classification. The value of the ratio of extinction to reddening (or total to selective absorption) that we adopted for this work is

$$R_V = \frac{A_V}{A_V - A_I} = \frac{A_V}{E(V-I)} = 1.94 \quad (3.6)$$

from $\frac{A_V}{E(B-V)} = 3.1$ and $\frac{E(V-I)}{E(B-V)} = 1.6$ (Schultz & Wiemer (1975), Fitzpatrick (1999)).

Figure 3.11 shows the individual reddening values in V-I plotted against both RA in the left hand plot, and DEC in the right hand plot. From Figure 3.11 there appears to be no obvious areas of differential reddening across the cluster, and the spread (standard deviation) in E(V-I) is similar to the uncertainties due to spectral type uncertainties, so a single reddening value might be appropriate to the entire cluster. However, many of the stars appear to show negative reddening which could be caused by uncertainties in spectral classification (see section 3.6.1: the negative values are unlikely to be due to uncertainties in photometry as the quoted uncertainties for the photometry are 0.009 mag, Lamm et al. 2004).

Finally in Figure 3.12 we separated the reddening values into five equal bins of E(V-I) and plotted them onto a RA versus DEC plot to further examine any possible differential extinction. The open diamonds show the targets selected from the Dahm & Simon (2005) and Lamm et al. (2004) catalogues. The symbol size corresponds to the reddening value. Again, there were no regions where the stars are significantly more or less affected than other stars in the cluster. Since the spread in E(V-I) of 0.17mag is similar to that expected from the uncertainties in spectral type (1-2 spectral subclasses) we concluded that a single value can be applied to all of the stars in the cluster in our sample.

From Figure 3.13, the mean reddening in E(V-I) is 0.022(mag) with a standard deviation of 0.17(mag). This was converted into a mean extinction (A_V) using Equation 3.6 and gave a value of 0.042 ± 0.324 (mag), (the error has been derived from the Gaussian distribution of reddening values shown in Figure 3.13).

Several limitations with colour and spectral type measurements are as follows;

- The spectral classification uncertainties are a strong function of spectral type. The spectral type uncertainties are $\pm 1-2$ sub-classes. For G-type stars the

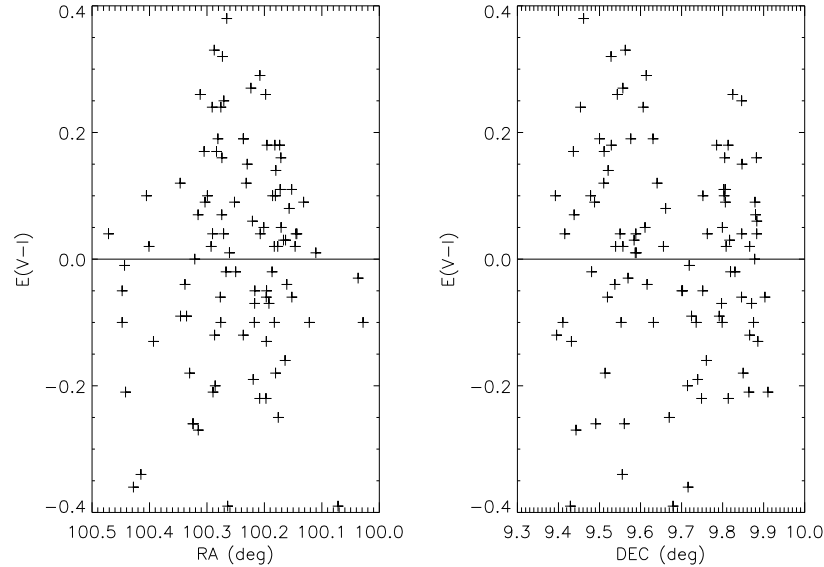


Figure 3.11: The individual reddening values against RA in the left-hand plot, and DEC in the right-hand plot. The line separates the possible values of reddening from the unphysical values (negative $E(V-I)$). There are no obvious spatial areas where reddening affects the targets more than the other stars in the sample.

difference in $V-I$ between spectral subclasses is as small as 0.01, but increases significantly to approximately 0.5 for late-M type stars. If any of the late-type stars in the sample were incorrectly classified by one subclass, the assumed photometric colour will be altered significantly, giving rise to an over or under dereddened sample (see section 3.6.1 for a discussion of T_{eff} errors).

- Veiling can increase the difference in $V-I$, making the colours appear redder than they actually are. Strong accretion activity, substantial enough to alter the $V-I$ value may have been detected (see section 3.5.2). Since later type stars have the coolest photospheres, it is possible that slight accretion activity can alter the $V-I$ colour more easily in these stars (Rebull et al. 2000).

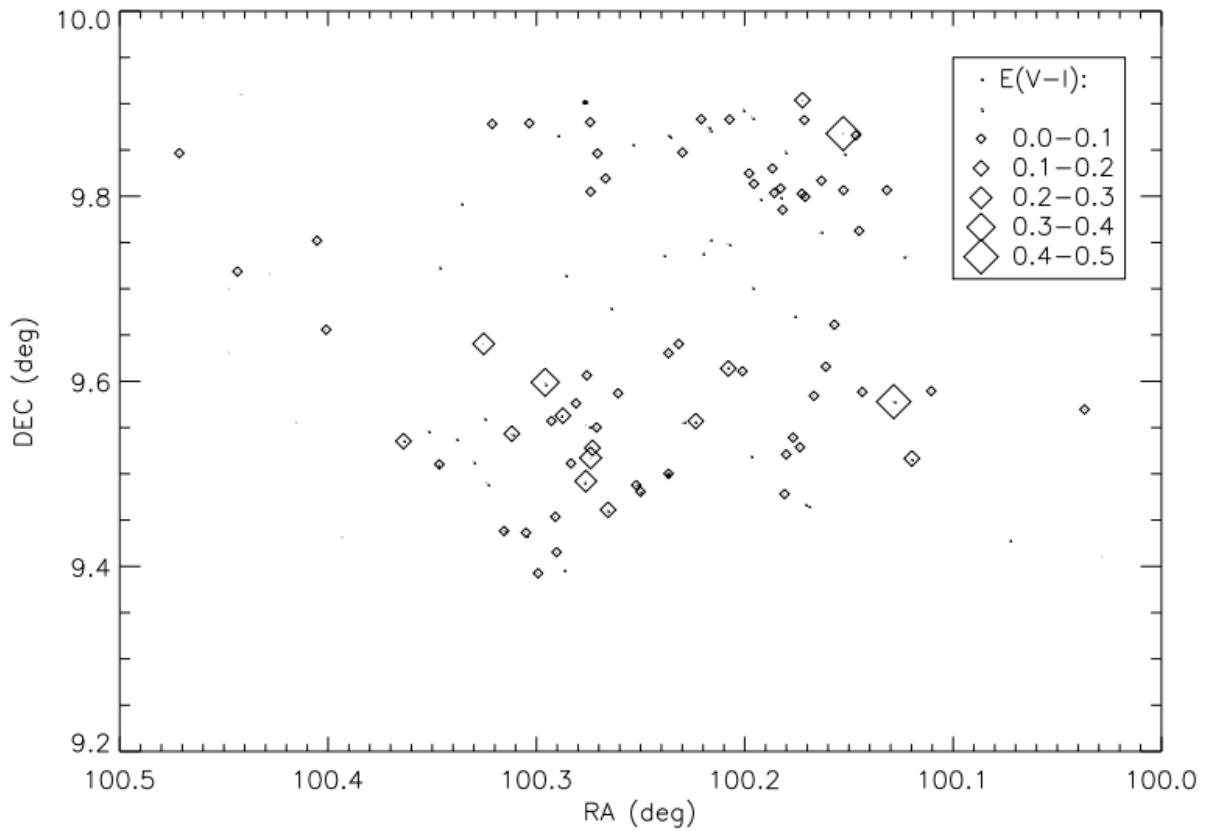


Figure 3.12: The positions of the targets used to determine individual reddening values. The symbol size corresponds to $E(V-I)$, and the small points correspond to negative $E(V-I)$. There appears to be no significant areas more or less affected by reddening from these targets.

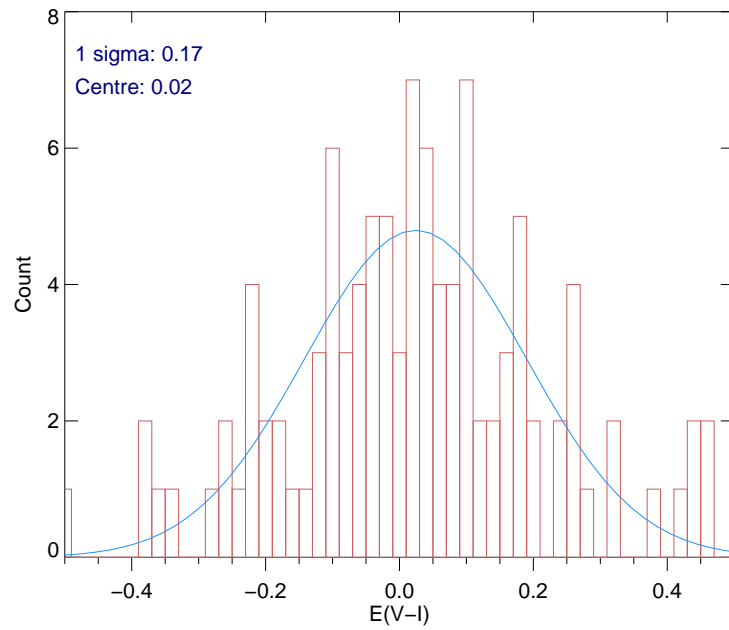


Figure 3.13: The distribution of $E(V-I)$ with the best-fitting Gaussian. The values of $E(V-I)$ were determined by comparing the colours, and the colours expected from spectral classification. The standard deviation is 0.17mag.

3.5.2 Is the V–I colour affected by accretion?

Since NGC 2264 has a proportion of disk bearing stars (Rebull et al. 2002) we were interested to examine whether accretion in the star-disk system affects the V-band magnitude, hence whether the V–I colour can be used to estimate effective temperatures. To explore this problem, we compared the bolometric magnitudes derived from the V and I band magnitudes. The process to estimate the bolometric magnitudes derived from these bands is outlined below and separated into three steps:

- **Intrinsic colours and bolometric corrections**

Since the bolometric correction in the I band (BC_I) is not provided in the Pecaut & Mamajek (2013) conversion table, it was derived using the colours provided in other bands and the bolometric correction in the J band. Firstly the intrinsic $(I-J)_o$ colours were calculated using the V–I, V–K, and H–K colours provided in the table.

$$(I - J)_o = -((V - I)_o - (V - K)_o + (H - K)_o + (J - H)_o) \quad (3.7)$$

BC_I was then converted from $(I-J)_o$ derived in equation 3.7 and the bolometric correction in the J band (BC_J) provided in the table.

$$BC_I = BC_J - (I - J)_o \quad (3.8)$$

- **Deriving the bolometric magnitude from the V band magnitude**

The V–I colours and I band magnitudes were from Lamm et al. (2004) for the primary targets $((V-I)_P, I_P)$ and Sung et al. (2008) for the secondary targets $((V-I)_S, I_S)$. The intrinsic V band magnitude (V_{P_o} or V_{S_o}) was calculated as in Equation 3.9

$$\begin{aligned} V_{P_o} &= (V - I)_{P_o} + I_{P_o} \\ V_{S_o} &= (V - I)_{S_o} + I_{S_o} \end{aligned} \quad (3.9)$$

where $(V-I)_{P_o}$ is the dereddened colour using the value derived in section 3.5.1 and the conversions provided by Rieke & Lebofsky (1985), and I_{P_o} is the intrinsic I magnitude corrected for extinction. The bolometric corrections in the V

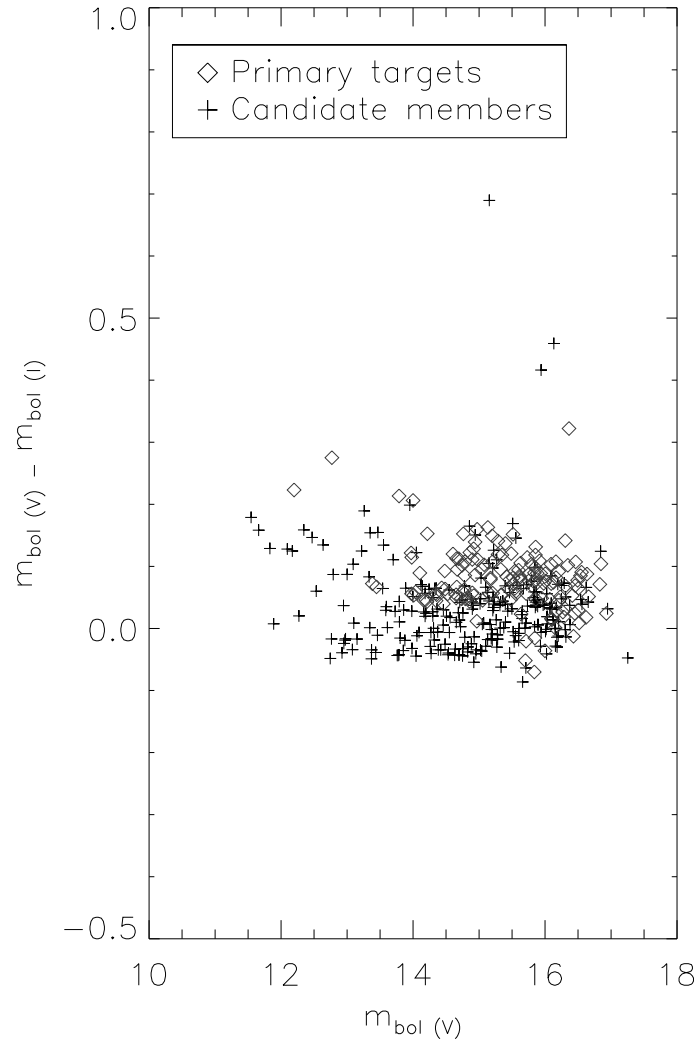


Figure 3.14: The relation between the difference in bolometric magnitude derived from the V and I bands against the bolometric magnitude derived from the V band for both the primary targets and the candidate members (secondary targets).

band (BC_V) were from Pecaut & Mamajek (2013) to estimate the bolometric magnitude:

$$\begin{aligned} m_{bol(V)_P} &= BC_V + V_{P_o} \\ m_{bol(V)_S} &= BC_V + V_{S_o} \end{aligned} \quad (3.10)$$

- **Deriving the bolometric magnitude from the I band magnitude**

To estimate the I–J colours the Lamm et al. (2004) and Sung et al. (2008) catalogues were used to obtain values of I and the 2MASS database to obtain values of J. The target magnitudes in the I and J band were the corrected for extinction using

$$\begin{aligned} I_{P_o} &= I_P - A_I \\ I_{S_o} &= I_S - A_I \\ J_o &= J - A_J \end{aligned} \quad (3.11)$$

BC_I per star were then derived using the relation between I_{P_o} – J_o or I_{S_o} – J_o , and BC_I derived in Equation 3.8. Finally, the bolometric magnitude in the I band was calculated from

$$m_{bol(I)} = BC_I + I_o \quad (3.12)$$

The bolometric magnitudes of the primary and secondary targets were compared and are shown in Figure 3.14. There is an offset between primary and secondary targets regarding the difference of bolometric magnitudes in the V and I bands. It is unlikely that this offset will significantly affect our results in chapters 4 and 5, as the primary and secondary samples are treated separately. (The primary targets are used in the majority of the research).

3.6 Luminosity and effective temperature determination

The luminosities and effective temperatures for the primary targets were calculated from the I band magnitudes and V–I colours from the Lamm et al. (2004) and Makidon

et al. (2004) photometric catalogues, and making use of Pecaut & Mamajek (2013) colour conversion table. The I magnitude and V-I colours from Sung et al. (2008) were used to obtain luminosities and effective temperatures for the secondary targets. The luminosities were calculated using BC_I , and a distance of 760pc from Sung, Bessell & Lee 1997 (see chapter 1.5.2 for a review of cluster distances). T_{eff} were estimated by dereddening the observed V-I using a single value for $E(V-I)$ estimated in section 3.5.1 and then using the relationship between intrinsic V-I and T_{eff} defined by Pecaut & Mamajek (2013) for PMS stars. We present the HR diagrams in chapter 4, along with the age distributions drawn from the diagrams.

3.6.1 Effective temperature errors

In later chapters, the results and conclusions rely upon the assumed effective temperatures and their uncertainties. Here, several available catalogues were used to estimate the approximate effective temperature and luminosity uncertainties. It was assumed that T_{eff} errors are a combination of the difference in T_{eff} between two of the same stars with photometry taken independently ($\sigma_{T_{\text{obs}}}$) and the difference in reddening between the two observations (σ_R).

We had no method of measuring the actual difference in reddening between the two observations. The temperature corresponding to the observed reddening difference ($\sigma_{R_{\text{obs}}}$) is a combination of the actual reddening difference, uncertainties in photometry (or caused by variability, σ_p) and uncertainties in T_{eff} from the spectral types (σ_{SpT});

$$\sigma_{R_{\text{obs}}}^2 = \sigma_R^2 + \sigma_p^2 + \sigma_{\text{SpT}}^2 \quad (3.13)$$

The T_{eff} error is therefore;

$$\sigma_{T_{\text{eff}}}^2 = \sigma_{R_{\text{obs}}}^2 - \sigma_p^2 - \sigma_{\text{SpT}}^2 + \sigma_{T_{\text{obs}}}^2 \quad (3.14)$$

Since $\sigma_p \sim \sigma_{T_{\text{obs}}}$, the uncertainty in T_{eff} becomes;

$$\sigma_{T_{\text{eff}}}^2 = \sigma_{R_{\text{obs}}}^2 - \sigma_{\text{SpT}}^2 \quad (3.15)$$

In section 3.5.1 we calculated $\sigma_{R_{\text{obs}}}^2$ (from the error quoted with E(V-I)) as 0.17mag, and the uncertainty in spectral types as 1-2 subclasses, which depends on T_{eff} particularly at higher temperatures.

For late K - early M type stars, and using the Pecaut & Mamajek (2013) colour conversions tables to convert between V-I and T_{eff} , a T_{eff} uncertainty was calculated as 150K, and upper limit of 200K for early K-type stars. These errors are approximate and depend strongly upon T_{eff} for stars earlier than \sim K2, but the errors reduce significantly $<$ 150K for M type stars where the difference between spectral classes produces a small T_{eff} difference, and where M-type stars can often be measured to a fraction of a spectral subclass (Dahm & Simon 2005).

3.6.2 Luminosity errors

The luminosity uncertainties contain a combination of uncertainties due to photometry, variability, extinction, accretion and binarity. The uncertainties in photometry are small (0.009 mag, Lamm et al. 2004) and therefore, these are treated as negligible. We estimated the uncertainties due to variability and variable accretion from taking the magnitudes of repeated targets from the same two photometric catalogues used earlier in this section. We found that the standard deviation divided by $\sqrt{2}$ of the magnitudes is 0.085, relating to an error in $\log_{10}L$ of 0.044. The error due to the extinction was estimated from the uncertainty in A_I of 0.12, corresponding to $\log_{10}L = 0.048$. We had no means of measuring the error due to accretion, and assumed that the uncertainties due to variable accretion are contained within the error calculated for variability. The errors in $\log_{10}L$ due to variability and extinction are therefore, $\sqrt{0.044^2 + 0.048^2}$. The error due to binarity is discussed more in chapter 4 (section 4.2.1) where an added spread in the $\log_{10}L$ distribution due to binarity was \sim 0.08.

3.7 Calcium triplet lines

The spectra used in this thesis cover the wavelengths 8073 to 8612Å. This range contains two of the three near-infrared calcium triplet (CaT) lines, with rest wavelengths of 8498Å and 8542Å. The CaT lines are significantly weaker than the blue Ca II H and K lines, however they are equally effective indicators of accretion, and are well correlated with the H and K line flux (Busà et al. 2007). CaT lines in stars of similar luminosities can exhibit much variation in the line depth. This variation is caused by different amounts of chromospheric activity, and the contribution to the line flux from accretion is usually significantly stronger than any contribution from chromospheric activity. Any accretion or chromospheric activity contribution to the CaT line consists of a relatively narrow emission component in the core of a broad, saturated photospheric absorption line. In this section a method described in Marsden, Carter & Donati (2009) was used to measure the line residual equivalent widths (the emission excess caused by accretion or chromospheric activity. See Figure 3.15 and Equation 3.18) .

3.7.1 Measurements of CaT equivalent widths

The MARCS synthetic database of spectra (Gustafsson et al. 2008) were used as templates to remove the flux of a non-rotating, non-active stars at a range of spectral types and gravities. The spectra cover the effective temperature range of 2500K to 8000K (more than the entire range of our spectra). The catalogue is split into two according to effective temperature: T_{eff} from 2500K to 4000K with steps of 100K, and from 4000 to 8000K in steps of 250K.

The CaT residual EWs were measured for the 8498Å and 8542Å lines by comparing the target spectrum with a synthetic spectrum of a similar spectral type (what is actually measured is the emission excess caused by chromospheric activity or accretion). The process to measure the EWs is as follows;

- Prepare synthetic template spectra by filtering to the resolution of the Giraffe spectrograph. The spectra were also shifted and broadened to match the target the RV and $v \sin i$, and put on a common wavelength scale.
- A proportion of the target spectrum either side of the emission line was then used to normalise to a continuum level of unity. This was repeated for the synthetic spectrum.

$$\begin{aligned} S(\lambda) &= S_s(\lambda)/S(\lambda)_o \\ T(\lambda) &= T_s(\lambda)/T(\lambda)_o \end{aligned} \quad (3.16)$$

where $S(\lambda)_o$ and $T(\lambda)_o$ ¹ are the mean values of flux either side of the stellar and template spectrum which were used to normalise the stellar spectrum ($S_s(\lambda)$) and the template spectrum ($T_s(\lambda)$) (according to the flux level enclosed in dashed boxes of Figures 3.15, 3.16 and 3.17) .

- Subtract the prepared synthetic template spectrum $T(\lambda)$ from the normalised stellar spectrum $S(\lambda)$ according to equation 3.17

$$\Delta(\lambda) = S(\lambda) - T(\lambda) \quad (3.17)$$

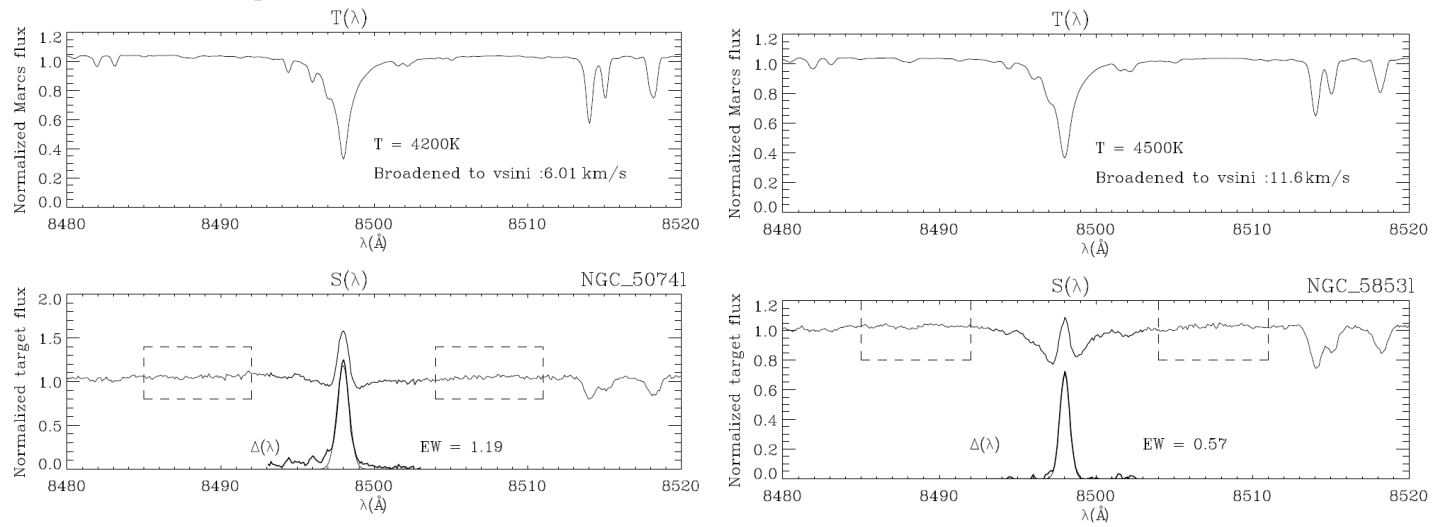
- For those stars that have low EWs the difference spectrum with which the EW is measured is often distorted by noise. Consequently, an optimal extraction technique was adopted where we used a Gaussian ($P(\lambda)$) with unit area, to represent the area under the difference spectrum produced by the CaT lines. The EW was then estimated according to Equation 3.18

$$EW = \frac{\int \Delta(\lambda)P(\lambda) d\lambda}{\int P(\lambda)^2 d\lambda} \quad (3.18)$$

¹ $S(\lambda)$ Normalised stellar spectrum, $S_s(\lambda)$ Stellar spectrum (prior to normalisation), S_o Flux level of stellar spectrum used for normalisation, $T(\lambda)$ Normalised template spectrum, $T_s(\lambda)$ Template spectrum (prior to normalisation), T_o Flux level of Template spectrum used for normalisation, $\Delta(\lambda)$ Difference spectrum, $P(\lambda)$ Gaussian profile used to determine the residual chromospheric EW from the difference spectra.

Figure 3.15 shows the EW measurement process. The upper panels show the template spectra ($T(\lambda)$) of similar spectral type to the stellar spectra, broadened to the corresponding $v \sin i$. The lower panels show the normalised stellar spectra ($S(\lambda)$), and the difference spectra ($\Delta(\lambda)$, on the y-axis) over plotted. The areas enclosed by the dashed boxes are the regions of spectra which were used to normalise the flux. Figures 3.16 and 3.17 show examples of those spectra which we conclude are either non-accretors (CaT EW $< 3\text{\AA}$), or heavy accretors ($\geq 3\text{\AA}$) respectively.

Figure 3.15: Images showing the measurements of CaT EWs of target stars. The upper panels show the normalised template spectra of similar spectral type to the stellar spectra. The lower panels show the normalised stellar spectra ($S(\lambda)$), and the difference spectra ($\Delta(\lambda)$ on the y-axis) over plotted. The dashed boxes show the regions which were used to normalise the spectra.



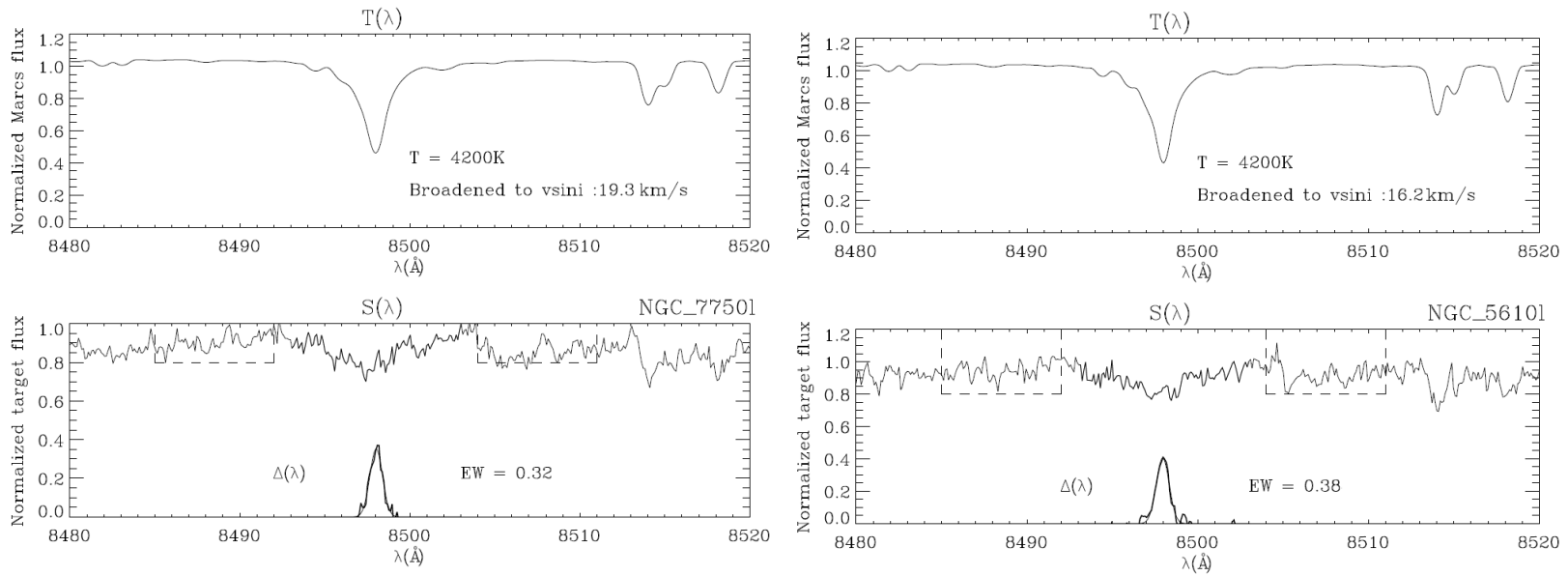


Figure 3.16: The EW measurement process for stars with small CaT EWs that are unlikely to be due to accretion. The top two panels show the template spectra of similar spectral type to the stellar spectra. The lower panels show the normalised stellar spectra ($S(\lambda)$), and the difference spectra ($\Delta(\lambda)$ on the y-axis) over plotted. The areas enclosed by the dashed boxes are the normalisation regions.

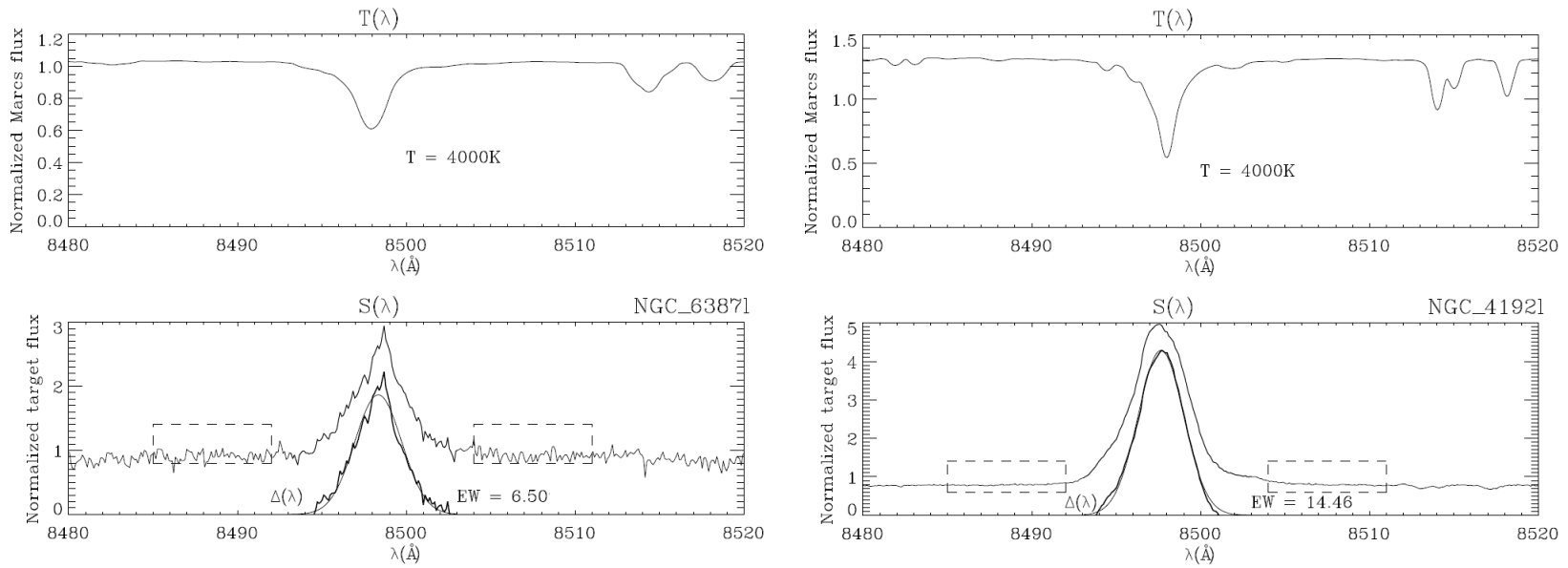


Figure 3.17: Images showing the measurements of CaT EWs of target stars exhibiting large amounts of CaT emission, characteristic of heavily accreting stars. The upper panels show the normalised template spectra of similar spectral type to the stellar spectra. The lower panels show the normalised stellar spectra ($S(\lambda)$), and the difference spectra ($\Delta(\lambda)$ on the y-axis) over plotted. The dashed boxes show the regions which were used to normalise the spectra.

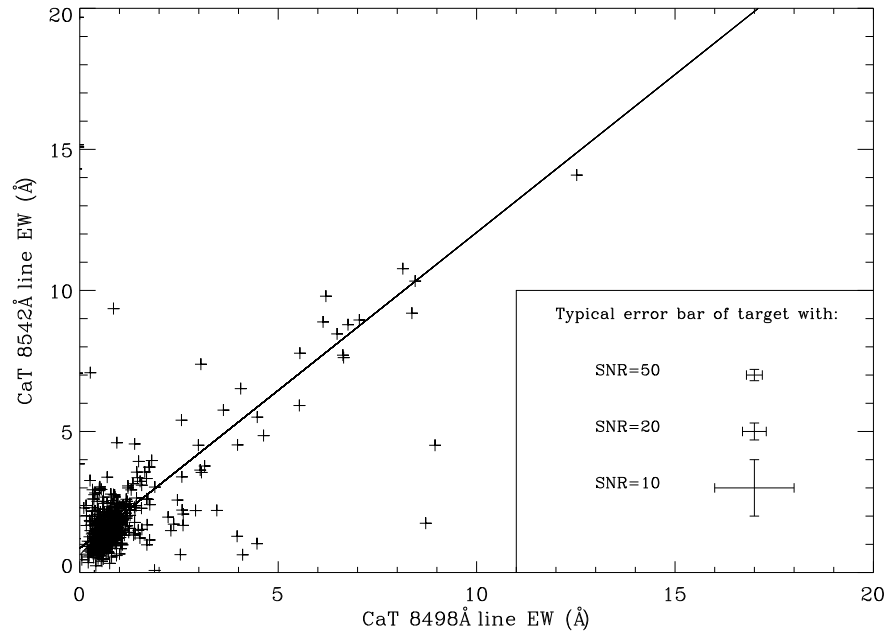


Figure 3.18: The relation between the measured EWs for the 8542Å line (y-axis) and the 8498Å line (x-axis). The gradient of the line is 1.11 ± 0.09 indicating that the EWs of 8542Å line are on average $\sim 11\%$ higher than EWs from 8498Å line. Also shown are typical error bars corresponding to several values of SNR.

Figure 3.18 is a comparison between the EWs of the two CaT lines that have been measured in this section. It shows the relation between the measured EWs for the 8542Å line (y-axis) and the 8498Å line (x-axis). The gradient of the line is 1.11 indicating that the EWs of 8542Å line are on average $\sim 11\%$ higher than EWs from the 8498Å line. Also shown are typical error bars corresponding to several values of SNR. Figure 3.19 shows an example of the difference spectrum and the regions of the spectrum used to estimate the EW error associated with noise in the spectrum on either sides of the peak. The uncertainty was estimated as the standard deviation of

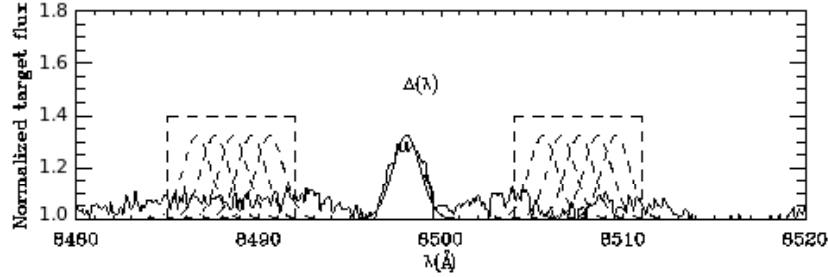


Figure 3.19: An example of the difference spectrum and the regions of the spectrum used to estimate the EW error associated with noise in the spectrum on either sides of the peak. The 10 dashed curves are used Gaussian profiles used to estimate the EW uncertainties. The solid curve is $P(\lambda)$, used to determine the EW from the difference spectra.

the EW estimates using the different extraction regions according to $\sigma_{EW} = EW_{rms}$. The r.m.s. includes the EWs measured of the ten curves shown in figure 3.19.

3.8 Summary

We measured stellar parameters and their uncertainties in this chapter and the results are presented in the appendix A1 . These include;

- **The radial velocity measurements and the associated uncertainties** $\sim 95\%$ of the primary targets that gave a clear peak in the CCF, had RVs between 15 and 30km/s. We externally validated the RVs with catalogues in the literature, and found good agreement given the quoted uncertainties, and no systematic offset.
- **The $v \sin i$ measurements and the associated uncertainties** The lowest measurable $v \sin i$ was 8km/s, and $\sim 95\%$ of the primary targets that gave a clear peak in the CCF had $v \sin i$ s between 8km/s and 30km/s. We externally validated the $v \sin i$ s with catalogues in the literature, and found that there

was reasonable agreement given the quoted uncertainties and no systematic offset.

- **The extent of reddening in the cluster using published photometric catalogues combined with catalogues containing spectral classifications** The spread of reddening values was found to be comparable to the spread expected from the given uncertainties, so we assumed that one value of reddening can be applied to all of the stars in the cluster. The $E(V-I)$ found by comparing colours with colours expected from spectral classifications is $0.022 \pm 0.17(\text{mag})$.
- **Luminosities and T_{eff} and the associated uncertainties** The luminosities and T_{eff} were calculated from I-band magnitudes and V-I colours. T_{eff} and $\log_{10}L$ uncertainties of 150K and 0.06, respectively, were also estimated.
- **CaT EWs and the associated uncertainties** Finally, CaT EWs were measured for the stars in the cluster, very few ($\sim 5\%$, see Figure 3.18) had strong EWs which could be associated with accretion.

4 Probing age spreads with rotation rates

4.1 Introduction

Age spreads constrain star formation timescales in young star clusters. A popular method of estimating the extent of age spreads in young clusters is through the use of a Hertzsprung-Russell (HR) diagram combined with evolutionary isochrones. However, the HR diagram method of assessing age spreads is open to criticism. The luminosities of young stars may not be a direct indicator of their age. Observational uncertainties, astrophysical scatter and complex accretion histories could affect the reliability of using the luminosities of young pre-MS stars to identify their age, and could add a luminosity dispersion into the HR diagram which is independent of any age spread (see section 1.2). Factors such as an unknown binary population, large amounts of reddening or spatially variable reddening, circumstellar disc presence and stellar variability affect the luminosity measurements. A second problem with using the HR diagram to estimate ages is the use of theoretical isochrones. There is currently significant disagreement (particularly at ages $<10\text{Myrs}$) between the widely used evolutionary models such as Siess, Dufour & Forestini (2000), D'Antona & Mazzitelli (1997), and Feiden, Chaboyer & Dotter (2011) (hereafter SDF00, DAM97 and Dartmouth, respectively. See section 1.3 for a comparison of pre-MS isochrones). For this reason, several sets of theoretical isochrones have been utilized in this chapter.

A method that circumvents many of these problems (though is not model-independent) is to estimate ages from the measured projected radii of pre-MS stars. The motivation is to use an independent means of estimating the radii of PMS stars and then compare the distribution of sizes with a modelled age spread or the age spread inferred from the HR diagram for the same objects. We applied this method to NGC 2264 using the dataset described in sections 3.2-3.3. The primary targets (targets with known rotation periods) have been used in this analysis, and are shown in the HR diagrams in Figures 4.1, 4.2 and 4.3 along with the isochrones produced from the

Dartmouth, DAM97 and SDF00 models. NGC 2264 is an interesting cluster to perform this analysis on as there are several studies of possible age spreads and possible sub-groups that have been highlighted in the literature (e.g. Teixeira et al. (2006) and see section 1.5.1 for a review of age spreads in NGC 2264). Jeffries (2007) undertook an investigation of this type in the Orion Nebula Cluster (ONC). He found that the projected radius distribution, derived from the product of rotation periods and $v \sin i$, was incompatible with a coeval population and that the distribution was consistent with the age spreads inferred from the HR diagram. Here we extend these methods to NGC 2264. The method used by Jeffries (2007) and also in several sections of this chapter is distance-independent (and also insensitive to extinction, accretion and binarity), and assumes that the radii, rather than the luminosity are direct indicators of the stellar age. This avoids the problem of using the luminosity as an age indicator for pre-MS stars. It combines the rotation period (P) with the projected equatorial velocity ($v \sin i$) to obtain projected radii for each of the stars in NGC 2264. The $v \sin i$ s, luminosities and T_{eff} described in sections 3.4 and 3.6 for the primary targets from our catalog of NGC 2264 are used in this chapter, along with rotation periods from Lamm et al. (2004) and Makidon et al. (2004).

4.2 Ages estimated from the HR diagram

From the HR diagrams shown in Figures 4.1, 4.2 and 4.3 and constructed in section 3.6 for three sets of evolutionary models, we estimated the model-dependent individual ages of the sample stars. We used a distance of 760pc (discussed in section 1.5.2), and a reddening of $E(V-I)=0.022$ (estimated in section 3.5) when converting from the photometric measurements to luminosities and T_{eff} in order to calculate the ages. Since there are disagreements between pre-MS evolutionary models (see section 1.3), we performed this analysis using three sets of isochrones suitable for pre-MS stars. The distributions of individual ages derived from the HR diagram using the Dartmouth, DAM97 and SDF00 isochrones are shown in Figure 4.4. The median \log_{10} (ages/Myrs)

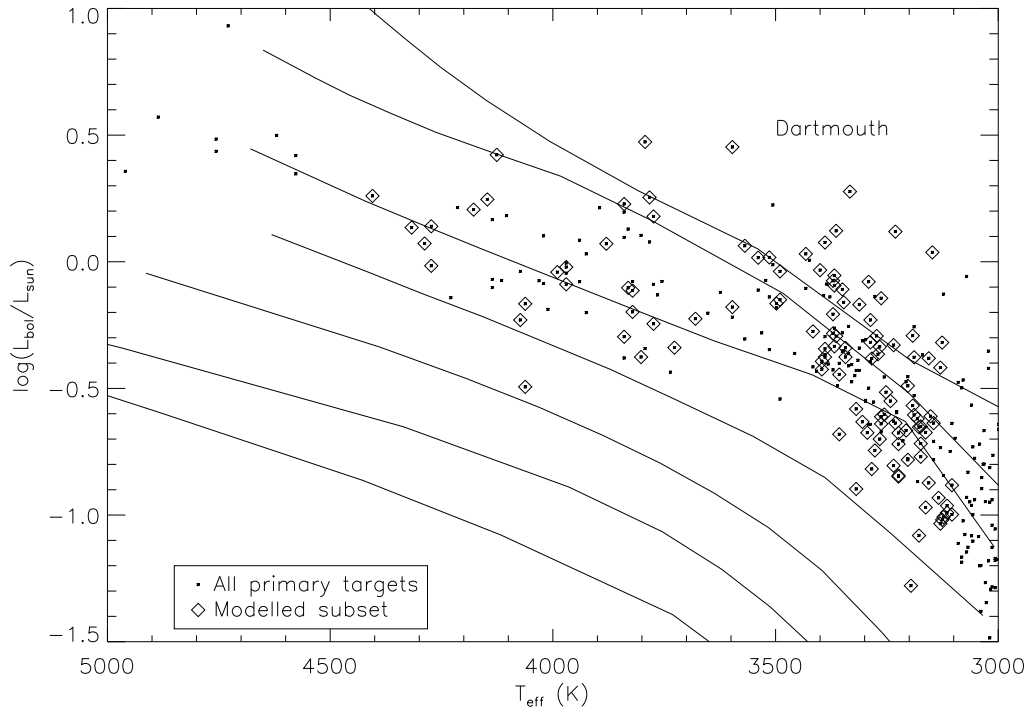


Figure 4.1: A HR diagram showing the sample of observed targets in NGC 2264 (small squares) and the targets with known rotation periods which are within the limits and thresholds described in section 4.3.1 (open diamonds), which were used in the analysis in this chapter. The 0.1 (uppermost), 0.3, 1, 3, 10, 30 and 100Myr isochrones from the Dartmouth models are shown.

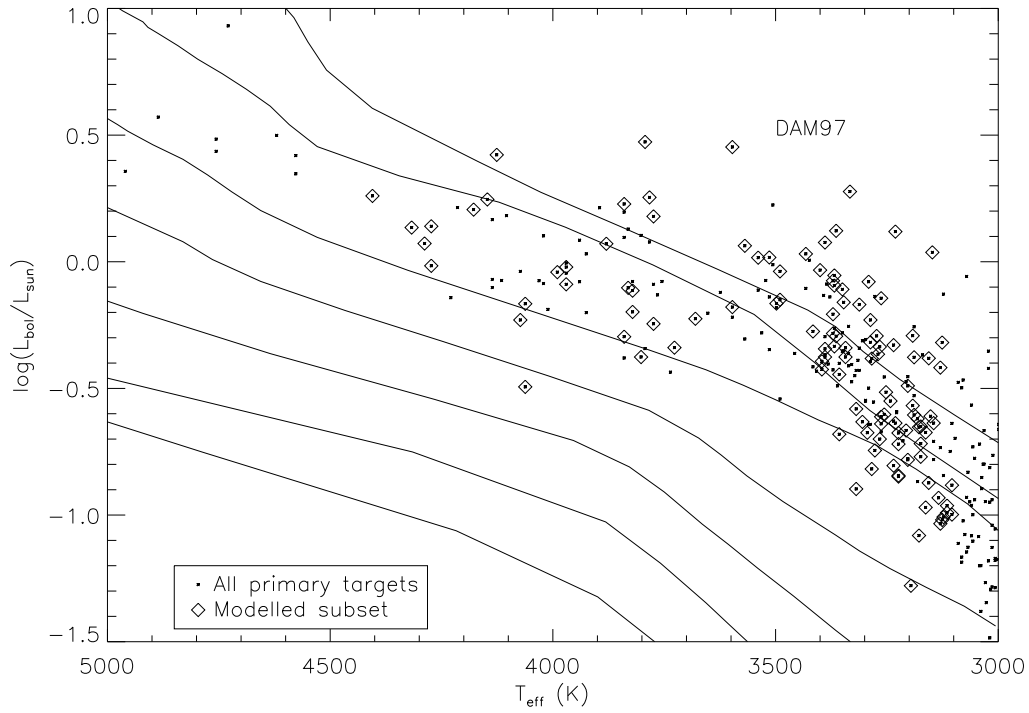


Figure 4.2: A HR diagram showing the sample of observed targets in NGC 2264 (small squares) and the targets with known rotation periods which are within the limits and thresholds described in section 4.3.1 (open diamonds), which were used in the analysis in this chapter. The 0.1 (uppermost), 0.3, 1, 3, 10, 30 and 100Myr isochrones from the DAM97 models are shown.

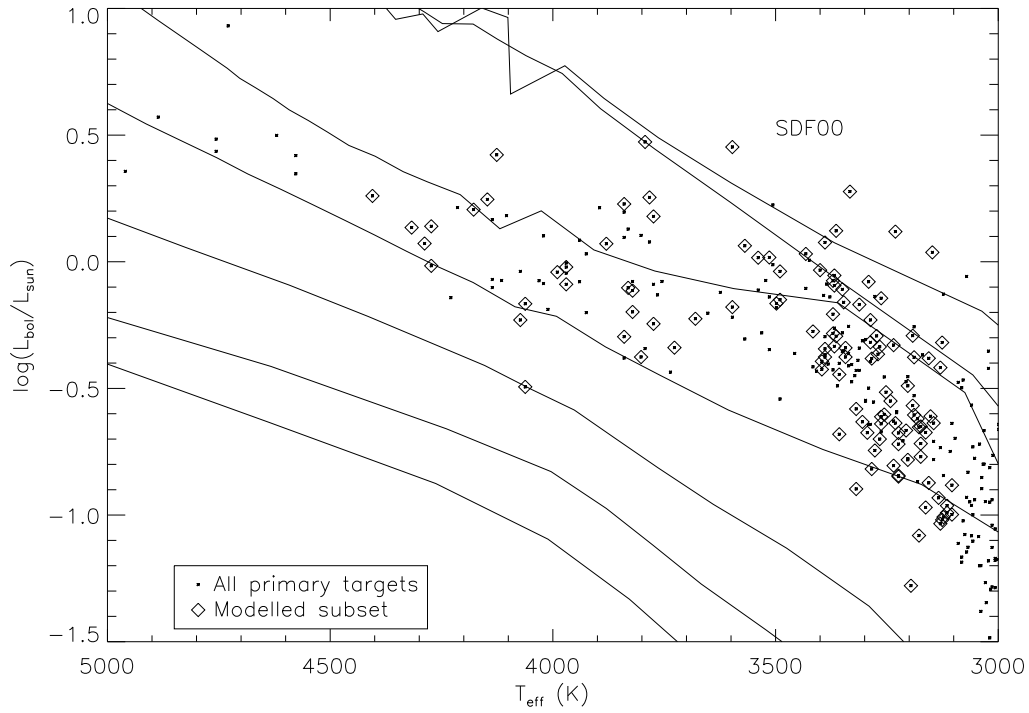


Figure 4.3: A HR diagram showing the sample of observed targets in NGC 2264 (small squares) and the targets with known rotation periods which are within the limits and thresholds described in section 4.3.1 (open diamonds), which were used in the analysis in this chapter. The 0.1 (uppermost), 0.3, 1, 3, 10, 30 and 100Myr isochrones from the SDF00 models are shown.

are 5.97, 5.76 and 6.29 for the Dartmouth, DAM97 and SDF00 isochrones respectively.

4.2.1 Applying a binary correction factor

The ages inferred from the HR diagram in section 4.2 assume only that the observed stars are single. However, a fraction of these could be unresolved binaries with combined luminosities that are larger than those of a single star at the same T_{eff} . The HR diagram luminosities are, therefore, overestimated on average, and thus the ages are underestimated on average. The contribution to the total luminosity of a companion star cannot be treated as a random error, since the luminosity estimates are systematically biased to higher values. Therefore, we use the simple binary correction model from Hartmann (2001), which assumes that the binary companion mass function is the same as in the field (a mass function which is roughly flat in $\delta \log N / \delta \log M$, where M is the stellar mass). Assuming that the luminosity is approximately proportional to mass for pre-MS stars, the luminosities of the binary companions are also drawn from a flat $\log_{10} L$ distribution. This model adds an average shift in median luminosity of $\Delta \log_{10} L \sim 0.14 \text{dex}$, if all of the stars are binaries.

The binary fraction may be different for different mass ranges: published multiplicity frequencies for low-mass stars are lower than solar-type. No significant variation of the total multiplicity frequency between early-M and late-M dwarfs has been found, since most of their companions are found at short separations (Duchêne & Kraus 2013).

The fraction of binaries in NGC 2264 is poorly constrained (Baxter et al. 2009). In regions of isolated star formation, such as Taurus, a high binary fraction (B) has been found, perhaps larger than 80% (Simon, Ghez & Leinert 1993). Regions of clustered star formation, however, show a much lower binary fraction (Köhler et al. 2006). We adopt the same binary fraction adopted in Baxter et al. (2009) for NGC 2264 of $B=0.5$, and so apply a correction to the median luminosity of $\Delta \log_{10} L = -0.07 \text{dex}$, which corresponds to a correction to median \log_{10} age of approximately 0.11dex, and a dispersion in $\log_{10} L$ of 0.08dex.

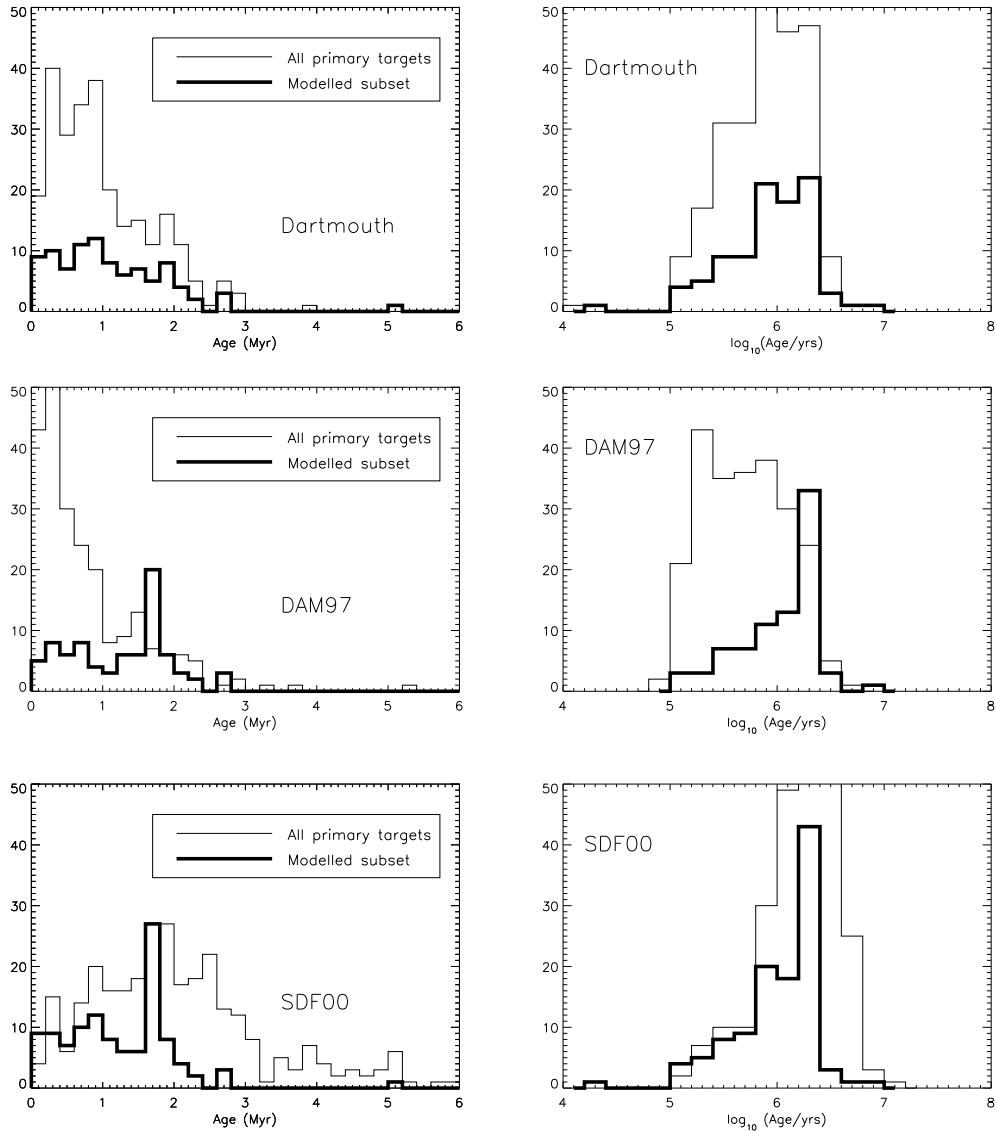


Figure 4.4: Histograms showing the ages (left-hand panels) and \log_{10} ages (right-hand panels) of the sample targets used in this analysis derived from the HR diagrams in Figures 4.1, 4.2 and 4.3. The upper two panels show ages determined from the Dartmouth models, the middle panels show those ages from the DAM97 models, and the lower two panels show ages determined from the SDF00 models. These ages have not been corrected for the presence of unresolved binaries.

4.3 Modelling the $R \sin i$ distribution

The aim of this study was to take a measured distribution of projected radii, then assuming a random orientation of the spin-axes, generate Monte-Carlo simulations of this distribution to attempt either to constrain the real distribution of stellar radii, or alternatively, constrain the model-dependent distribution of corresponding stellar ages. The advantages of using this method rather than using the ages from the HR diagram is that it is distant independent, and does not rely upon using luminosities as age indicators. In this section, the modelling of the distribution of $R \sin i$ using Monte Carlo simulations is described. The observed projected radius ($(R \sin i)_{\text{obs}}$) was estimated from the observed rotation period (P_{obs}) and the observed projected equatorial velocity ($(v \sin i)_{\text{obs}}$) according to equation 4.1, where k is a constant according to the units used.

$$(R \sin i)_{\text{obs}} = \frac{k}{2\pi} P_{\text{obs}} (v \sin i)_{\text{obs}} \quad (4.1)$$

$$k = 2\pi \frac{R_{\text{true}}}{(P_{\text{true}} v_{\text{true}})} \quad (4.2)$$

The rotation periods were taken from the literature (see section 3.2) and the $v \sin i$ s were measured from the spectra (described in section 3.4). In equation 4.2, the subscript ‘true’ denotes the real, rather than the observed value of the radius, rotation period or rotational velocity, absent from measurement uncertainties and systematic effects. We make the assumption that the true values of the rotation period and projected equatorial velocity are related to the observed values according to equations 4.3 and 4.4, when a random number (U) is drawn from a Gaussian distribution of rotation periods or velocities respectively.

$$P_{\text{obs}} = P_{\text{true}}(1 + \delta_p U) \quad (4.3)$$

$$(v \sin i)_{\text{obs}} = v_{\text{true}} \sin i(1 + \delta_v U) \quad (4.4)$$

and where δ_p and δ_v are the fractional uncertainties in the period and $v \sin i$ measurements. In equation 4.4 the value of $\sin i$ is drawn from a distribution assuming

a random axial orientation, equivalent to a uniform distribution of $\cos i$ above an inclination threshold, i_{th} (see section 4.3.1).

v_{true} and $\sin i$ are treated separately in order to model the observational lower limit to $v \sin i$ correctly when v_{true} is initially specified. The inclination angles were generated assuming a random axial orientation, and the projected equatorial radius was given by;

$$(R \sin i)_{\text{obs}} = R_{\text{true}}(1 + \delta_P U_1)(1 + \delta_v U_2) \sin i \quad (4.5)$$

where U_1 and U_2 are numbers drawn randomly from a Gaussian distribution.

The sample of stars in NGC 2264 with known rotation periods were used in this analysis. For each individual star in the sample, 10^4 random values of $(R \sin i)_{\text{obs}}$ were generated.

R_{true} was generated in several different ways: either it was drawn from a model isochrone corresponding to the T_{eff} of each star in the sample; taken randomly from either a Gaussian distribution in $\log_{10} R$ about an isochronal value (section 4.5.2 and 4.5.4), or it was generated assuming one of two possible age distribution models, namely, from a lognormal age distribution (section 4.5.5) or exponential distribution (section 4.5.6) of ages.

4.3.1 Observational constraints, limits and biases

Several factors limit our analysis. These factors are listed below and are described in more detail in this section.

- Inclination angle
- $v \sin i$ resolution
- T_{eff} errors
- Sample biases

The rotation periods were estimated from rotational modulation of inhomogeneous features (star spots) on the stellar surfaces. Star spot modulation would be

difficult to observe in stars with a low inclination, so they are less likely to be included in our sample. Hence, we assume that there is a threshold inclination angle (i_{th}), below which star-spot modulation is never seen. Work by O’Dell, Hendry & Collier Cameron (1994) and Jackson & Jeffries (2010a) have shown that rotational modulation and periodicity would not be detected below 30° , so we adopt a limit of 30° in this work. This threshold is tested in section 4.5.3. Modelled stars that have randomised inclinations which fall below this threshold are not included in the final modelled radius distribution. It was assumed that the threshold inclination angle is independent of P or the radius and temperature of the star. The $R \sin i$ can only be derived for stars with both rotation periods and $v \sin i$ measurements, so the sample used in this analysis is only a subset of the stellar population. Further sample biases are discussed in section 6.1 and shown in Figure 6.1.

The spectral resolution of the data constrains the range of $(v \sin i)_{\text{obs}}$ values which can be recorded. We accounted for this by introducing a limit to the $v \sin i$ s which were modelled. Any randomized trial producing a $v \sin i$ below the limit to which the observations were capable of resolving it was discarded. The resolution limit of the measurable $(v \sin i)_{\text{obs}}$ used in this analysis was 8km/s (see section 3.4).

When calculating R_{true} from the evolutionary models, a perturbation in T_{eff} was included to account for the slope in the isochrones (e.g. see Figure 4.6). This is necessary because the slope of the isochrone in the R versus T_{eff} plane means that an uncertainty in estimated T_{eff} will lead to an additional (artificial) dispersion in the observed values of $R \sin i$. The perturbation value used in this analysis was $\pm 150\text{K}$, which was estimated to be the approximate T_{eff} error for this sample of stars (in section 3.5.1). We test the sensitivity to the assumed T_{eff} uncertainties in section 4.5.3.

All of the isochrones were normalised to the 3Myr isochrone prior to performing the analysis. Essentially, this is a way of reducing a two-dimensional fitting space (in radius and T_{eff}) into a 1-dimensional space (the normalised radius, $R_{\text{true}}/R_{3\text{Myr}}$). However, this procedure is only valid if there is no large divergence of the isochrones at high and low T_{eff} . For this reason, we restrict the analysis to stars of a given range in T_{eff} .

4.4 Models for the intrinsic radius distribution

Several different methods have been tested in order to determine if there is a spread of radii and ages in the cluster, and the extent of these possible spreads. We were interested in determining how well the normalised projected radius ($(R \sin i)_{\text{obs}}/R_{3\text{Myr}}$) distribution of the NGC 2264 sample matches a modelled sample which has no dispersion in ages (a coeval population), or a dispersion in radius around an isochronal value. The normalisation is required to convert the comparison of 2D distributions into the comparisons of 1D distribution functions. This allows for the combination of measurements of stars with different T_{eff} s into one distribution, see section 4.5.1. Furthermore, if the modelled isochronal distributions and the $(R \sin i)_{\text{obs}}/R_{3\text{Myr}}$ distributions were not well matched, then if the radius dispersion is modelled as a dispersion in ages, what age spread is implied by the $(R \sin i)_{\text{obs}}$ distribution? Also, we attempted to determine whether either a Gaussian distribution or an exponential distribution of ages is the preferred model when comparing them to the $(R \sin i)_{\text{obs}}/R_{3\text{Myr}}$ distribution. Finally, we compared the distribution of $(R \sin i)_{\text{obs}}/R_{3\text{Myr}}$ to the distribution of radii predicted from the ages derived from the HR diagrams in Figures 4.1, 4.2, 4.3. All methods were tested using the three sets of evolutionary models mentioned in section 4.1 and are described in the following sections;

- A coeval model (section 4.5.2)
- Testing the dependence of the results on the assumed T_{eff} and i_{th} (section 4.5.3)
- A Gaussian distribution of \log_{10} radii around a coeval value (section 4.5.4)
- A Gaussian distribution of ages (section 4.5.5)
- An exponential distribution of ages (section 4.5.6)
- A comparison between the HR diagram radius distribution and the $(R \sin i)_{\text{obs}}/R_{3\text{Myr}}$ distribution (section 4.5.7)

4.5 Results

4.5.1 Projected stellar radii

The projected radii of the primary target sample described in section 3.2, was normalised using either the Dartmouth, DAM97 or SDF00 3 Myr isochrones. The individual $(R \sin i)_{\text{obs}}/R_{3\text{Myr}}$ values are shown as a function of T_{eff} in Figures 4.5, 4.6 and 4.7, along with the $R_{\text{true}}/R_{3\text{Myr}}$ isochrones derived from the respective models. Due to the slope of the isochrones at certain T_{eff} values, we applied an upper and lower T_{eff} limit to the stars used to create the $(R \sin i)_{\text{obs}}/R_{3\text{Myr}}$ distribution. The T_{eff} range used was 3100–4500K which was the maximum range covered by the isochrones when applying a T_{eff} uncertainty of 150 K. The normalisation to 3 Myrs shows an inconsistency regarding the best-fitting ages between the three sets of evolutionary isochrones: using different models provides different ages for the same stars, so we continued the analysis using all sets of isochrones. The 0.1 and 0.3 Myr isochrones are shown in Figures 4.5, 4.6 and 4.7 to illustrate the differences in measured ages for similarly aged stars when using these isochrones. The reasons for these differences are discussed further in Chapter 6. The normalised data were modelled with a straight-line for each of the three sets of isochrones. This was to determine whether the data contains a trend with respect to the isochrones which could result in an extra contribution to a $R \sin i$ dispersion discussed in the following sections of this chapter. The gradients of the straight line fits to the data normalised by the Dartmouth, DAM97 and SDF00 isochrones are as follows, $-4.5 \times 10^{-4} \pm 1.7 \times 10^{-4} \text{K}^{-1}$, $-3.2 \times 10^{-4} \pm 1.8 \times 10^{-4} \text{K}^{-1}$, $-1.9 \times 10^{-4} \pm 1.5 \times 10^{-4} \text{K}^{-1}$, respectively (see Figures 4.5, 4.6 and 4.7). There is a trend in the normalised data in all three cases. The trend adds a small additional Gaussian dispersion in \log_{10} normalised radius (σ_r) of 0.0175 when using the Dartmouth and DAM97 isochrones, and 0.0087 when using SDF00, and is considered negligible.

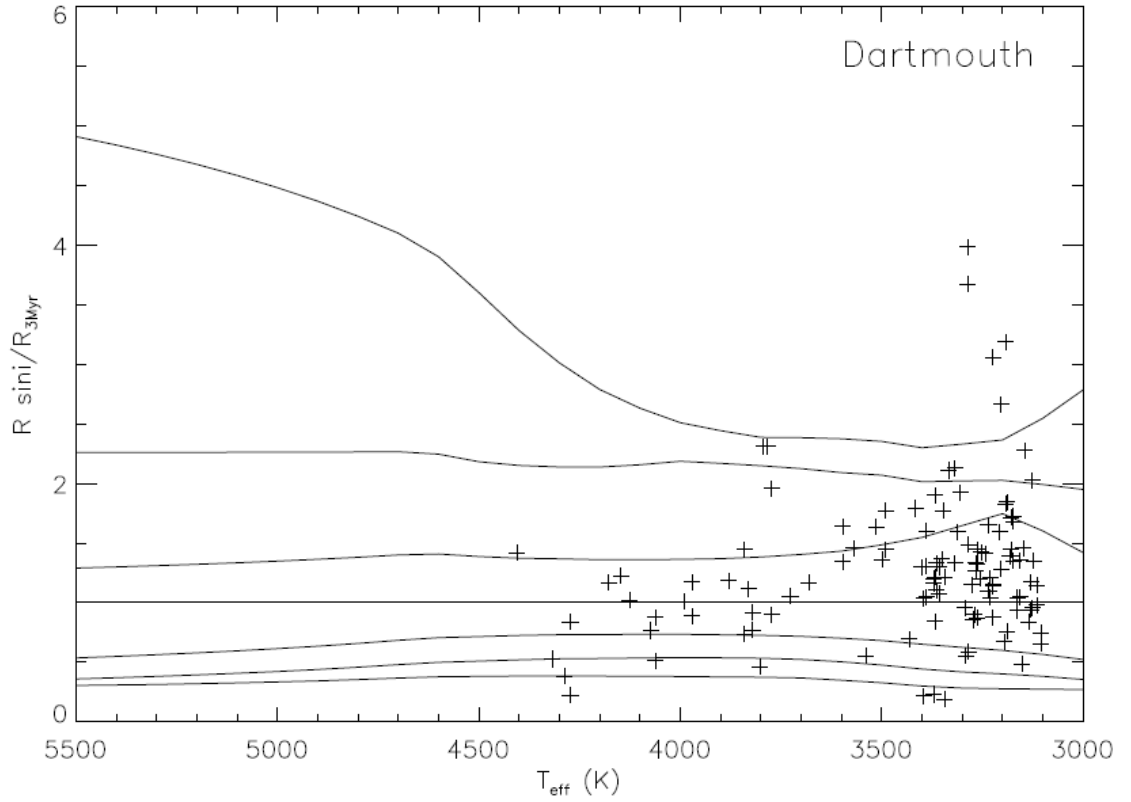


Figure 4.5: $(R \sin i)_{\text{obs}}/R_{3\text{Myr}}$ against T_{eff} for the primary targets used in the analysis in this chapter. $(R \sin i)_{\text{obs}}$ and the 0.1 (uppermost), 0.3, 1, 3, 10, 30, 100Myr isochrones were normalised against the 3Myr Dartmouth isochrones. The gradient of the unweighted best-fitting line to the points is $-4.5 \times 10^{-4} \pm 1.7 \times 10^{-4} \text{K}^{-1}$.

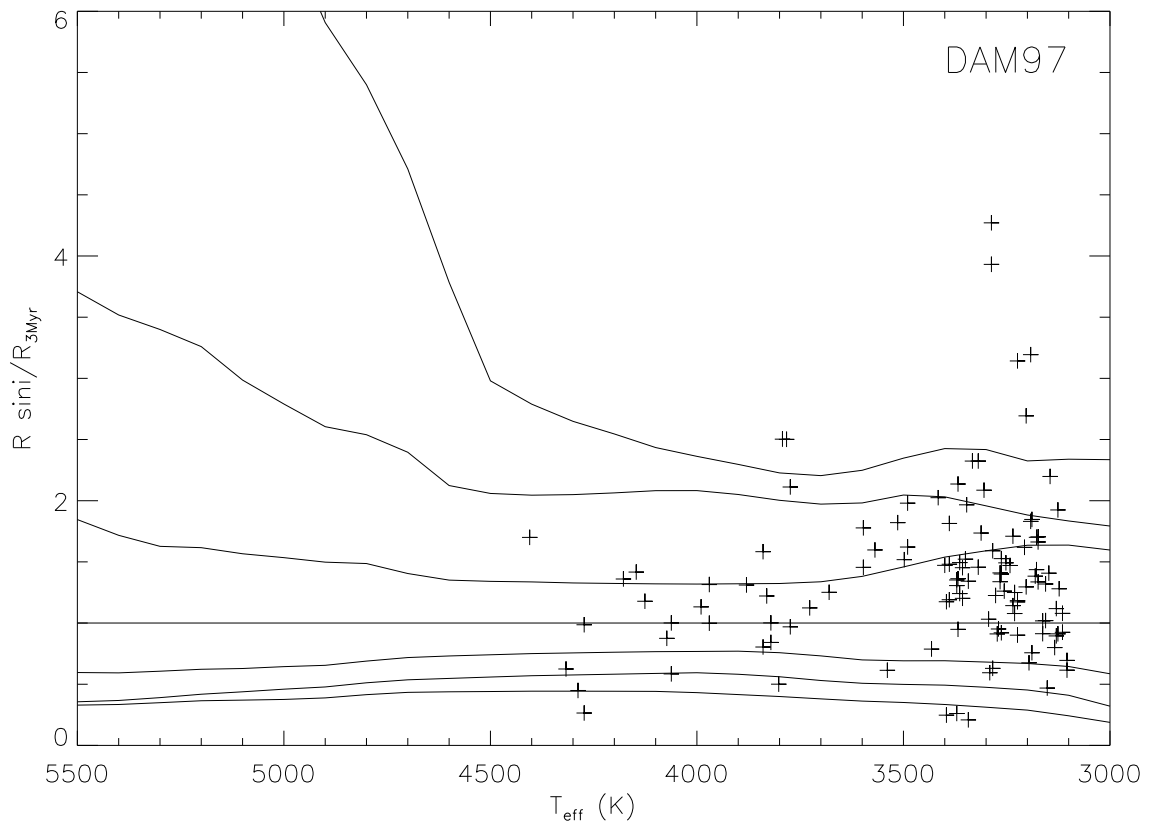


Figure 4.6: As Figure 4.5 with the DAM97 isochrones. The gradient of the best-fitting line to the normalised projected radii is $-3.2 \times 10^{-4} \pm 1.8 \times 10^{-4} \text{K}^{-1}$.

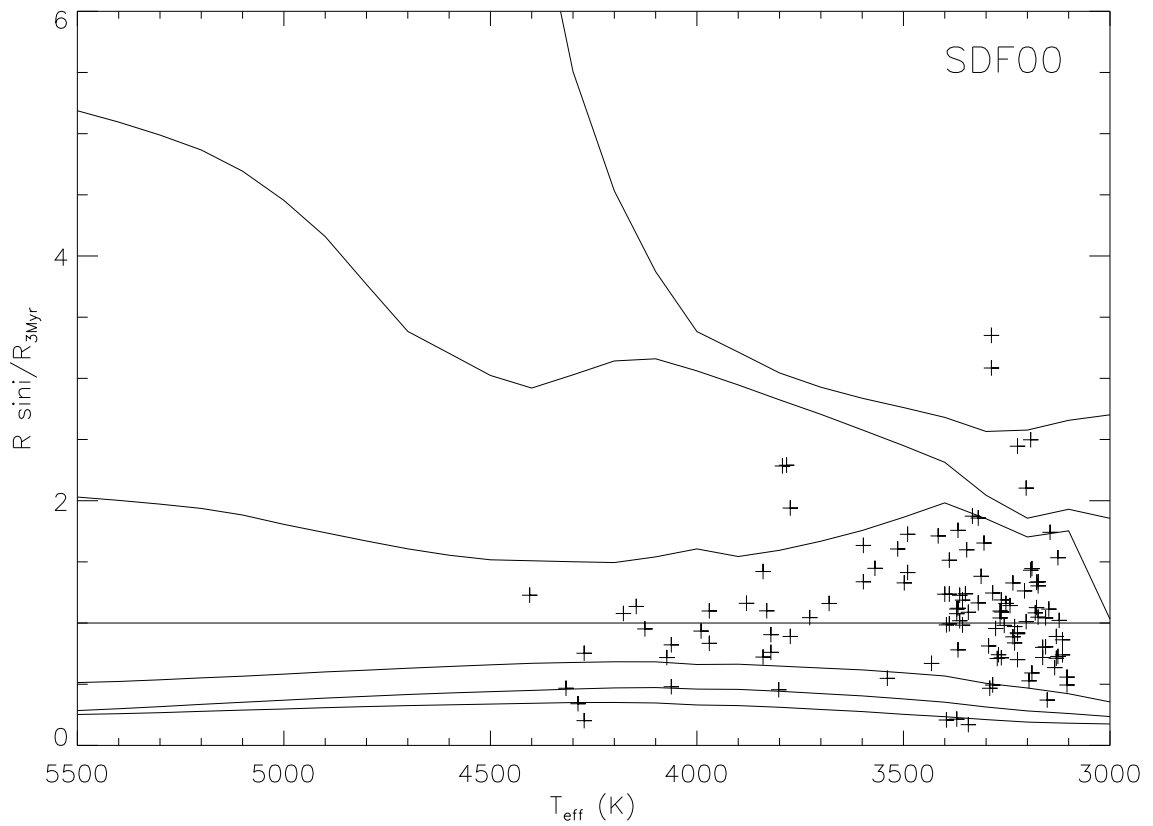


Figure 4.7: As Figure 4.5 with the SDF00 isochrones. The gradient of the best-fitting line to the normalised projected radii is $-1.9 \times 10^{-4} \pm 1.5 \times 10^{-4} \text{K}^{-1}$.

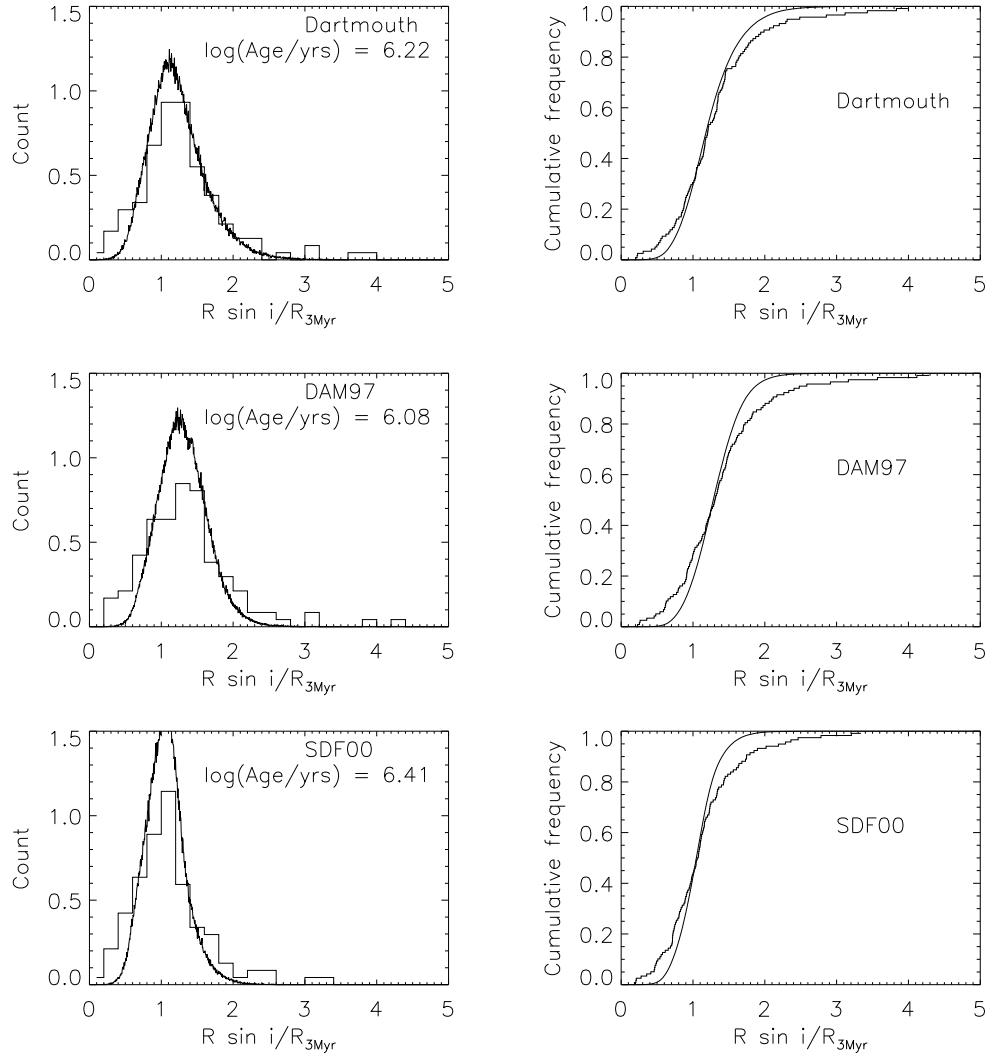


Figure 4.8: The left hand panels show the distributions of $(R \sin i)_{\text{obs}}/R_{3\text{Myr}}$ compared with models assuming a coeval population. The right hand panel shows the cumulative distributions used for the KS tests. The DAM97 and SDF00 models are marginally too narrow to fit the data (middle and lower panels), compared with the Dartmouth models which are a reasonable match to the data (upper panels).

4.5.2 A coeval model

Firstly, an R_{true} distribution of a coeval population was modelled, represented by a Gaussian distribution of $\log_{10} R/R_{3\text{Myr}}$ about a central value defined by a single isochronal age with a standard deviation of $\sigma_r=0$. A T_{eff} error of 150K and an inclination angle threshold of 30° were used (see section 4.5.3 for how varying these values affects the results).

The cumulative distribution of $(R \sin i)_{\text{obs}}/R_{3\text{Myr}}$ was tested against the Monte Carlo predictions with a specified age. In each case, the central isochrone age was tuned to give the best possible match which minimised the KS statistic. The central isochronal ages using the three sets of isochrones for the coeval case ($\sigma_r=0$) are shown in Table 4.1. The age which minimises the KS statistic is shown in column 1. Column 2 shows the Gaussian dispersion in $\log_{10} R$ (σ_r) where the values of 0.00 in this column represent the coeval model (the remaining values in this column are described in section 4.5.4). Columns 3 and 4 list the KS statistic (D_{max}) and the probability of $D > D_{\text{max}}$. The final column comments on whether the model can be excluded by the data. Figure 4.8 shows histograms of the normalised data $(R \sin i)_{\text{obs}}/R_{3\text{Myr}}$ along with the models assuming a coeval population in the left-hand panels, and the cumulative distributions in the right-hand panels. There is some disagreement in the result depending on the choice of models used. The middle and lower panels of Figure 4.8 show that the coeval models using the DAM97 and SDF00 isochrones, are slightly too narrow when compared to the data, possibly indicating a small spread in the true radii around an isochronal value. However, using the Dartmouth isochrones the coeval model is a good fit to the data. A KS test comparing the $(R \sin i)_{\text{obs}}/R_{3\text{Myr}}$ and the model can only reject the coeval model with 46% confidence.

The (\log_{10}) ages in years of the models which best fit the data (minimise the KS statistic) are 6.22, 6.08 and 6.41 for the Dartmouth, DAM97 and SDF00 models, respectively. The coeval model cannot be rejected at greater than 95% confidence for any of the three sets of evolutionary models. However, the DAM97 and SDF00 models only marginally miss this criteria and can be rejected with $> 90\%$ confidence.

Mean \log_{10} (Age/years))	σ_r (dex)	D_{max}	P($D > D_{max}$)	Comments
Dartmouth				
6.22	0.00	0.0773	0.4642	Good fit
6.22	0.11	0.0560	0.8420	Good fit
6.22	0.21	0.1060	0.1321	Too broad
DAM97				
6.08	0.00	0.1124	0.0942	Too narrow
6.08	0.05	0.1033	0.1514	Too narrow
6.08	0.15	0.0552	0.8541	Good fit
6.08	0.23	0.1068	0.1272	Too broad
SDF00				
6.41	0.00	0.1198	0.0622	Too narrow
6.41	0.06	0.1058	0.1334	Too narrow
6.41	0.16	0.0527	0.8900	Good fit
6.41	0.23	0.1039	0.1473	Too broad

Table 4.1: The results obtained when using a Gaussian distribution of $\log(R)$ about a central single isochrone with various standard deviations in \log_{10} normalised radius (σ_r) for three different evolutionary models. The models were tested with a T_{eff} error of 150K and an inclination angle threshold of 30° . The age in column 1 is the isochronal age which was adjusted to minimize the KS statistic. Column 2 shows σ_r where the values of 0.0 in this column represent a coeval model. The first row for each model gives the result for a coeval model. The subsequent three rows show results for models where the coevality assumption was relaxed and which correspond to the best fit spread in (log) normalised radius (σ_r), and then the results, which bracket the range of dispersion in log normalised radius, that cannot be rejected at more than ~ 90 confidence. Columns 3 and 4 list the KS statistic (D_{max}) and the probability of $D > D_{\text{max}}$. The final column comments on whether the model can be excluded by the data. Also, listed are models which approximately bracket the range in σ_r that yield model distributions that cannot be excluded by the data (at more than $\sim 90\%$ significance).

4.5.3 Testing the dependence on assumed T_{eff} errors and threshold inclination angle

The results presented in Table 4.1 and discussed in section 4.5.2 assume a T_{eff} error of 150K (determined in section 3.5.1) and inclination angle threshold of 30° . In this section, the dependence of the results on both the T_{eff} errors and i_{th} was examined. The dependence on T_{eff} is determined by how close to the horizontal plane the normalised radius isochrones are in Figures 4.5, 4.6 and 4.7. Changing i_{th} affects the inclusion of stars in the models with low inclination axes. A decrease in i_{th} will slightly broaden the model distribution by allowing stars with low $\sin i$, and by implication, a low modelled $v \sin i$ but relatively few stars will be affected because a small fraction of the population have inclinations below the threshold adopted.

The dependence on T_{eff} was tested for the values of 100K, 150K and 200K. Table 4.2 list the results from this section. We found that varying either the T_{eff} errors or the i_{th} had no significant effect on the results, so even if the default values of 150K and 30° were under or over estimated, the change in the results would be marginal.

4.5.4 Modelling the radius dispersion

In section 4.5.2, when using both the DAM97 modes and the SDF00 models, the coeval model could be ruled out with $>90\%$ confidence. In this section, we used a Gaussian distribution of \log_{10} normalised radius centered around a value which is defined by a single isochronal age. In this case, the models were broadened to a range of Gaussian dispersions ($\sigma_r > 0$) in order to determine the extent of a radius spread that can be rejected.

Similarly to section 4.5.2 the central isochronal age was adjusted several times over a range of ages and dispersions to find the age and dispersion which minimised the KS statistic. Secondly, a grid of central ages and σ_r were modelled in order to find a locus of model parameters that can be excluded.

The results are shown in Figure 4.9 using the Dartmouth, DAM97 and SDF00

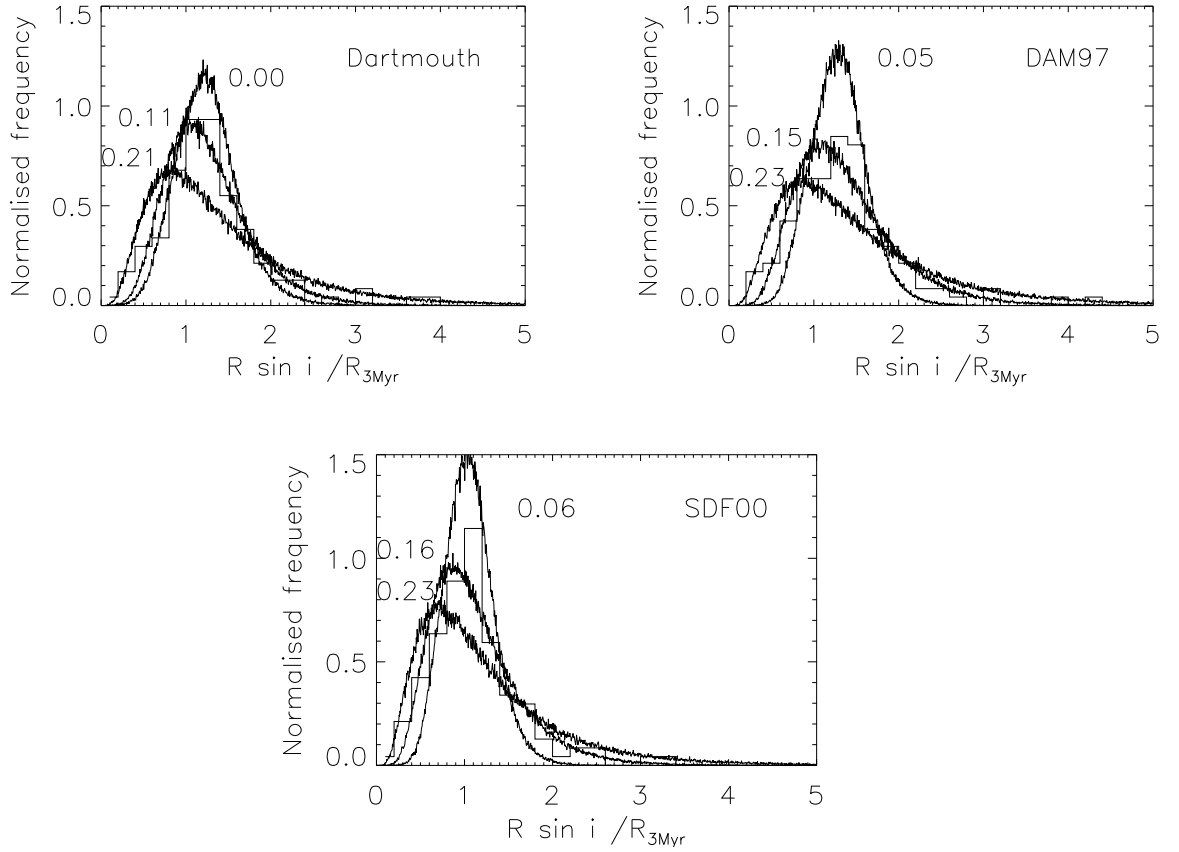


Figure 4.9: The distribution of $(R \sin i)_{\text{obs}}/R_{3\text{Myr}}$ compared with the models that have a Gaussian dispersion in $\log_{10} R/R_{3\text{Myrs}}$ (σ_r). The models shown are those that maximise $P(D > D_{\text{max}})$ and those which describe the largest and smallest values of σ_r for which $P(D > D_{\text{max}}) > 0.1$. Models with σ_r outside of this range were rejected. The values printed on the plot are σ_r (in dex) and are listed in table 4.1. $(R \sin i)_{\text{obs}}/R_{3\text{Myr}}$ was calculated using the Dartmouth, DAM97, and SDF00 models in the upper-left, upper-right and lower plots, respectively.

Model	Mean \log_{10} (age/Myr)	T_{eff} error	i_{th}	90% σ_r range
Dartmouth	6.22	100	30	0.00 - 0.22
	6.22	150	30	0.00 - 0.21
	6.22	200	30	0.00 - 0.20
	6.22	150	10	0.00 - 0.19
DAM97	6.08	100	30	0.06 - 0.23
	6.08	150	30	0.05 - 0.23
	6.08	200	30	0.03 - 0.23
	6.08	150	10	0.05 - 0.20
SDF00	6.41	100	30	0.07 - 0.23
	6.41	150	30	0.06 - 0.23
	6.41	200	30	0.04 - 0.23
	6.41	150	30	0.06 - 0.23

Table 4.2: The effect on σ_r when testing the coeval model whilst altering the assumed values of the T_{eff} error and i_{th} . Column 2 shows the age which minimised the KS statistic, and column 5 shown the range of radii dispersions which enclose 90% of the probability.

models, and are listed in Table 4.1 along with the results from section 4.5.2. The lower 90% confidence limit in σ_r was estimated by measuring the smallest value of σ_r in a grid where the corresponding $P(D > D_{\text{max}})$ was > 0.1 . Similarly, the upper σ_r 90% confidence limit was found by measuring the largest value of σ_r in a grid where the corresponding $P(D > D_{\text{max}})$ was > 0.1 . Also reported in the first row is the age and σ_r combination that gives the largest value of $P(D > D_{\text{max}})$.

The upper 90% limit to σ_r is similar for all three sets of isochrones. If σ_r lies either in the range $0.05 < \sigma_r$ (dex) < 0.23 (for the DAM97 models), or $0.06 < \sigma_r$ (dex) < 0.23 (for the SDF00 models) then the model can no longer be rejected with $>90\%$ confidence. The lower 90% confidence range using the DAM97 and SDF00 models are also in very good agreement, with both models giving a lower 90% confidence range of 0.05 and 0.06, respectively. The best-fitting values of σ_r (determined by maximising $P(D > D_{\text{max}})$) are similar between the DAM97 and SDF00 models, giving σ_r values of 0.15 and 0.16dex, respectively. The $(R \sin i)_{\text{obs}}$ spread observed when using the DAM97 and SDF00 models could be interpreted as requiring a spread of cluster ages. However,

the reasonable fit using the coeval model and the Dartmouth isochrones suggest that this result is model-dependent (discussed in section 4.7).

4.5.5 A log-normal age distribution

The results when using the Dartmouth models in section 4.5.4 showed that a spread in radius at a given T_{eff} may not be required, however the results with the DAM97 and SDF00 isochrones require a radius spread. A plausible interpretation of the latter is that a spread of ages within the stellar population causes stars of similar T_{eff} to have a range of different radii. In this section we assume that any radius spread is due to a spread of ages and measure the limits to any possible age spread.

Firstly, a model of a Gaussian distribution in \log_{10} age around a central isochrone was used. Randomly drawn ages from this distribution were converted into radii using either the Dartmouth, DAM97, or SDF00 models. The same measurement uncertainties, limits and assumptions as in section 4.3.1 were used. The $(R \sin i)_{\text{obs}}/R_{3\text{Myr}}$ distribution and the model were then compared using KS tests. A large grid of (\log_{10}) age dispersion and central (\log_{10}) ages were tested assuming that the true solution was within the range of the grid and so the total probability of the ‘true’ age and age spread lying in this grid is unity (with no possibility of the true solution lying outside the grid). The tested ranges of central isochronal \log_{10} ages (in years) were between 0 and 7, and age spreads (σ_a) of 0 dex to 3 dex for the three sets of isochrones. The $P(D > D_{\text{max}})$ values given by the KS tests comparing the models and $(R \sin i)_{\text{obs}}/R_{3\text{Myr}}$ were normalised over the grid, and the results when using the Dartmouth, DAM97 and SDF00 isochrones are shown in Figure 4.10, and listed in Table 4.3. The contours define the areas that enclose 68, 90 and 99% of the probability. Figure 4.12 shows the normalised probability distribution integrated over all possible central ages, and the vertical lines represent the limits within which 90% of the probability is enclosed.

The spread of ages depends on the choice of evolutionary models used, and when using the Dartmouth isochrones to normalise the radii, a zero age spread could not be ruled out with a high level of confidence. This result, however, still provides an upper

limit to the age spreads. The upper 90% confidence limits of the age spread are 0.46, 0.66 and 0.32dex, corresponding to the Dartmouth, DAM97 and SDF00 isochrones, and which are taken from the cumulative distribution function at a value of 0.9. (Note: these values show the upper limit to the lower 90% of the probability. The values in Table 4.3 show the limits of the parameters corresponding to >90% confidence of the observed distribution of $(R \sin i)_{\text{obs}}/R_{3\text{Myr}}$ matching models using a log-normal distribution in age.

The models produced when using the DAM97 evolutionary calculations evince the strongest evidence for a genuine age spread.

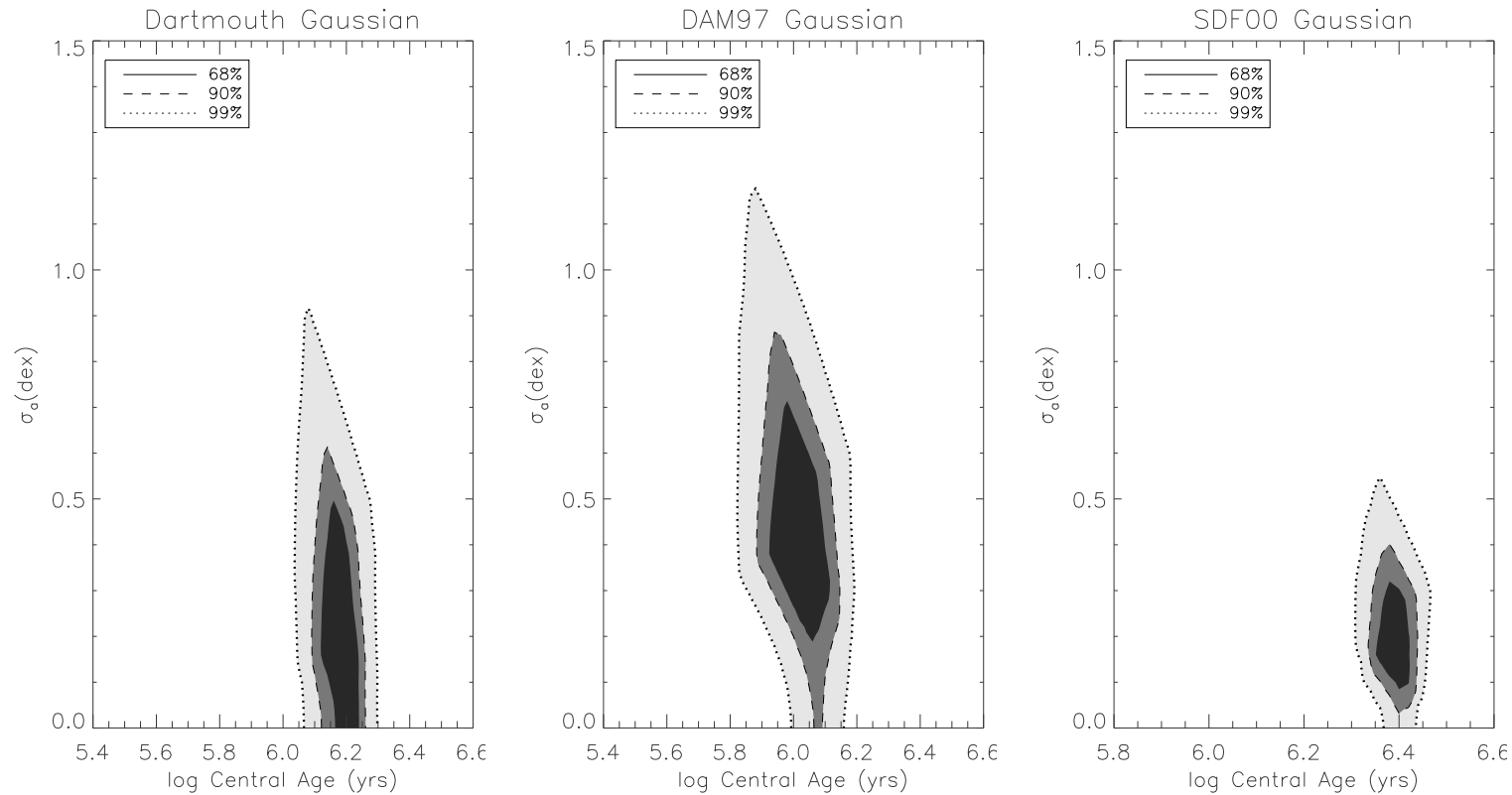


Figure 4.10: The relative probability that the observed data distribution of $(R \sin i)_{\text{obs}}/R_{3\text{Myr}}$ can be represented by a model consisting of a log-normal distribution of ages as a function of the central (log) age and the dispersion in (log) age. σ_a is the Gaussian dispersion (dex). The values of $P(D > D_{\text{max}})$ were normalised over a grid of ages and age spreads so that the total probability in the grid = 1. The contours bound the areas that enclose 68, 90 and 99% of the probability. The results were based upon the assumption of the T_{eff} uncertainties and measurement uncertainties outlined in section 4.3.1. The corresponding results are summarised in Table 4.3.

Model	\log_{10} (central age/Myrs)	σ_a (dex)	D_{\max}	$P(D > D_{\max})$	Lower σ_a 90% limit	Upper σ_a 90% limit
Log normal age spread model						
Dartmouth	6.18	0.28	0.056	0.829	0.0	0.54
DAM97	6.02	0.46	0.048	0.942	0.18	0.76
SDF00	6.40	0.20	0.062	0.738	0.06	0.36

Table 4.3: The results from the KS tests of comparing the observed distribution of $(R \sin i)_{\text{obs}}/R_{3\text{Myr}}$ with models using a log-normal distribution in age. These results correspond to Figure 4.10. The results from the Dartmouth, DAM97 and SDF00 isochrones are shown. Both the best-fitting values of the central age and σ_a are given, along with the limits of parameters corresponding to $> 90\%$ confidence. Columns 6 and 7 were determined by projecting the 2D probability distribution onto the σ_a dimension.

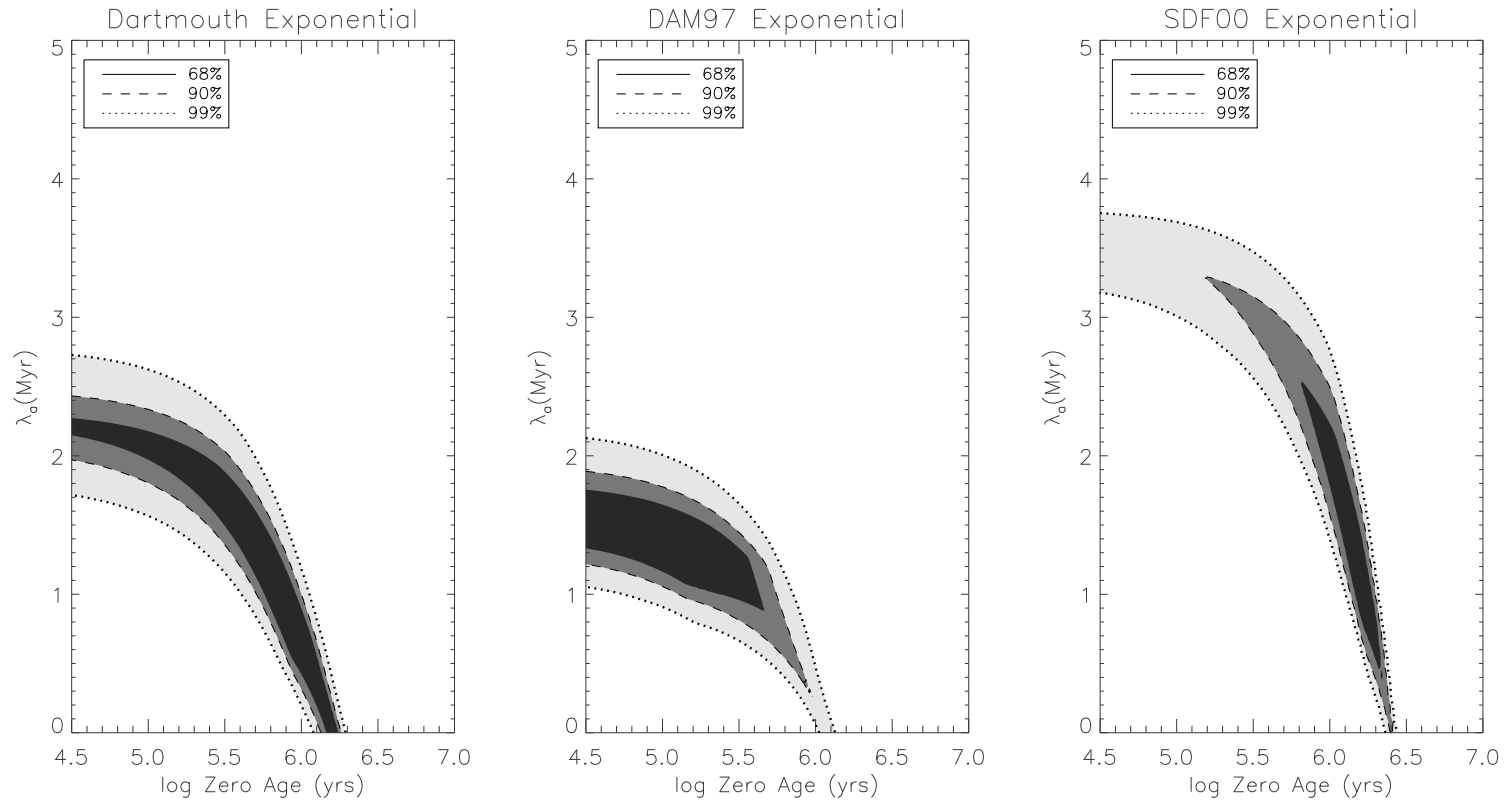


Figure 4.11: The normalised probability density plot showing the age distribution which decays exponentially on a time-scale of λ_a from a maximum at the zero point age. The contours show a 68, 90 and 99% confidence limits of the probability distribution assuming the T_{eff} uncertainties and measurement uncertainties outlined in section 4.3.1. The corresponding results are listed in Table 4.4.

4.5.6 An exponential distribution of ages

An exponentially decaying age distribution was used as a way of representing the idea of ‘accelerating star formation’ (Palla & Stahler 1999). The model simulates exponentially accelerating star formation up to a defined cut-off time in the past. If that cut-off time is small (for example, $< 10^5$ years), then star formation effectively accelerates right up to the present day. The age distribution decays exponentially from a maximum with a decay constant, λ_a (Myrs). Again, a grid of values were tested, assuming that the ‘true’ zero age and exponential decay timescale lie within the grid. The range of zero (log) ages (in years) tested for all three sets of isochrones were 4 to 7 and the range of exponential decay timescales were 0 to 7 Myrs. The grids of $P(D > D_{\max})$ from the KS tests for each set of isochrones were normalised producing relative probability grids, shown as contour plots in Figure 4.11, and the results are listed in Table 4.4. Similarly in section 4.5.5, the grid was integrated over all possible values and the results are shown in Figure 4.12.

The exponential models also were capable of producing a good fit to the data in all three cases, so we were unable to distinguish whether the Gaussian or exponential distribution best described the projected radius distribution. From Figure 4.12 the 90% confidence limits of λ_a do not encompass zero (which represents a coeval population) in all three cases.

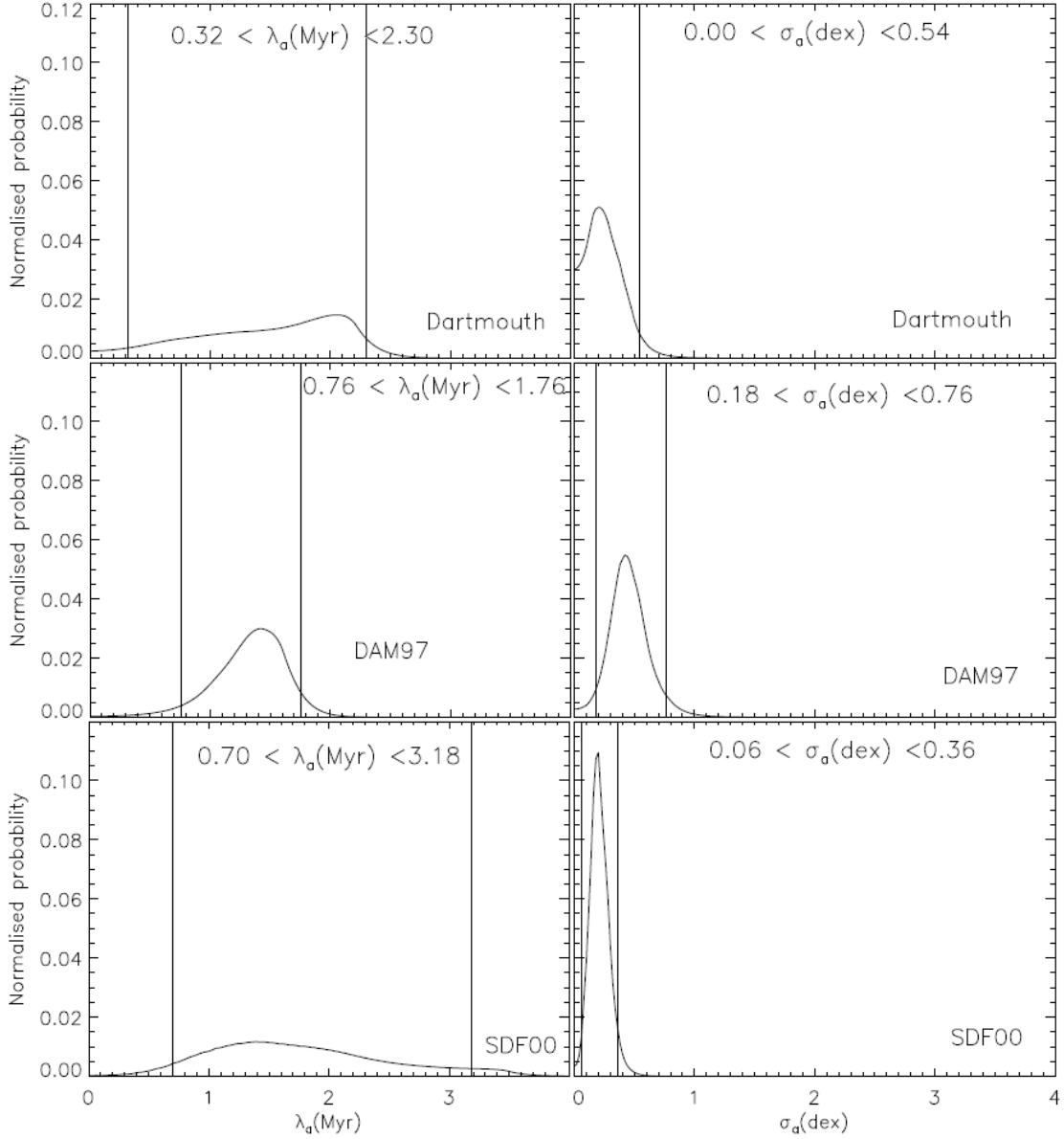


Figure 4.12: The relative probability of the zero age (left-hand panels) or log-normal age (right-hand panels) representing the $(R \sin i)_{\text{obs}}/R_{3\text{Myr}}$ distribution integrated over all possible zero or central ages is shown. λ_a is the decay constant. σ_a is the Gaussian dispersion (dex). The values of $P(D > D_{\text{max}})$ were normalised over a grid of ages and age spreads so that the total probability in the grid = 1, and integrated over all possible values of the zero or central age. The corresponding results are summarised in Tables 4.3 and 4.4.

Model	\log_{10} (zero age/yrs)	λ_a (Myrs)	D_{\max}	$P(D > D_{\max})$	Lower λ_a 90% limit (Myrs)	Upper λ_a 90% limit (Myrs)
Exponential age spread model						
Dartmouth	5.74	1.30	0.054	0.863	0.32	2.30
DAM97	4.34	1.62	0.058	0.803	0.76	1.76
SDF00	6.14	1.46	0.052	0.894	0.7	3.18

Table 4.4: The results from the KS tests of comparing the observed distribution of $(R \sin i)_{\text{obs}}/R_{3\text{Myr}}$ with models using an exponential distribution in age. The 90% limits were determined by projecting the normalised probability in Figure 4.11 onto the y-axis. These results correspond to Figure 4.11. The results from the Dartmouth, DAM97 and SDF00 isochrones are shown. Both the best-fitting values of zero age and λ_a are given, along with the limits of parameters that can be excluded at $> 90\%$ confidence.

Model	D_{\max}	$P(D > D_{\max})$
Dartmouth	0.192579	0.000256
DAM97	0.194685	0.000210
SDF00	0.208280	0.000056

Table 4.5: The results of comparing $(R \sin i)_{\text{obs}}/R_{3\text{Myr}}$ distributions with radii distributions determined from the HR diagram ages with KS tests prior to binary correction (discussed in 4.5.7) and using the distance of 760pc to construct the HR diagram.

4.5.7 Ages based upon the HR diagram and the cluster distance correction

The age distributions based upon the ages determined from the HR diagram (shown in Figure 4.4, section 4.2) prior to a binary correction were used to construct model $R \sin i$ distributions and were compared with $(R \sin i)_{\text{obs}}/R_{3\text{Myr}}$ using KS tests. The results from this test are shown in Figure 4.13 and Table 4.5. The KS tests reveal low p-values when comparing the two distributions when using all three sets of isochrones. This means that these age distributions, prior to binary correction, and at an assumed distance of 760pc do not predict a $R \sin i$ distribution that matches the data.

The radii distributions determined from the HR diagram ages are distance dependent, whereas the $(R \sin i)_{\text{obs}}/R_{3\text{Myr}}$ distributions are independent of distance. The KS tests show that when using the three sets of isochrones, the $R \sin i$ distributions predicted from the HR diagrams do not match the $(R \sin i)_{\text{obs}}/R_{3\text{Myr}}$ distribution well. Hence, we explored whether a shift in the assumed distance could bring the two distributions into agreement. The distance to the cluster used to construct the HR diagram (760pc) was then varied, until the KS tests provide values greater than 0.1, when comparing the $(R \sin i)_{\text{obs}}/R_{3\text{Myr}}$ distribution and the HR diagram ages distribution. This effectively gives a range of possible cluster distances that cannot be rejected at >90% confidence. The range of possible distances using this method are; $712 < D(\text{pc}) < 735$, $691 < D(\text{pc}) < 735$ and $733 < D(\text{pc}) < 748$, and the distances which minimised the KS statistic are 722, 704 and 740pc, corresponding to the Dartmouth, DAM97 and SDF00

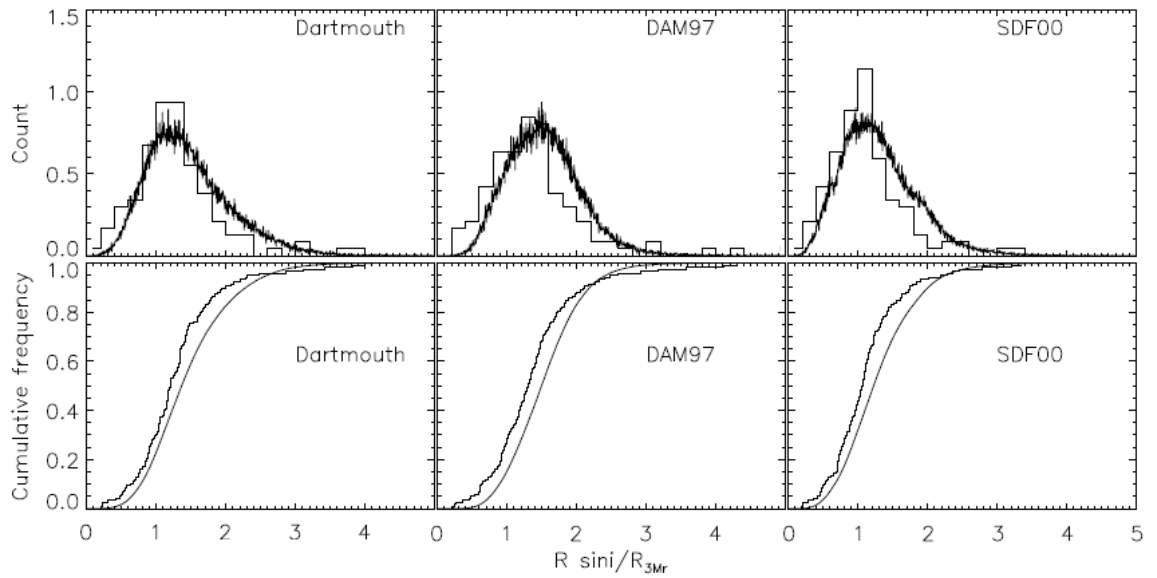


Figure 4.13: The distributions of $(R \sin i)_{\text{obs}} / R_{3\text{Myr}}$ along with the cumulative distribution functions of these distributions at a fixed distance of 760pc. The left-hand panels have been produced by normalising the data with the Dartmouth isochrones, the central panels with the DAM97 isochrones and the right-hand panels with the SDF00 isochrones. The models shown overlying the histograms were produced assuming that the stars had the ages implied by their positions in the HR diagram as derived from each set of model isochrones, prior to a binary correction.

Model	D_{\max}	$P(D > D_{\max})$
Dartmouth	0.0878	0.3086
DAM97	0.0870	0.3194
SDF00	0.1687	0.0021

Table 4.6: The results of comparing $(R \sin i)_{\text{obs}}/R_{3\text{Myr}}$ distributions with radii distributions determined from the HR diagram ages (after correcting the luminosities for a binary fraction of 0.5) with KS tests.

isochrones, respectively.

A binary correction was then applied to the luminosities using the model described in Hartmann (2001). The ages drawn from the HR diagram after the binary correction were again compared with the $(R \sin i)_{\text{obs}}/R_{3\text{Myr}}$ distribution. The results are shown in Table 4.6 and Figure 4.14. After the binary correction, two of the three models created from the ages from the HR diagram provided a good fit to the $(R \sin i)_{\text{obs}}/R_{3\text{Myr}}$ distributions with p-values of >0.1 . Again, the distances were varied to provide a range of distances corresponding to a 90% confidence range. The range of acceptable distances which give p-values of >0.1 when comparing the two distributions are; $740 < D(\text{pc}) < 772$, $740 < D(\text{pc}) < 781$ and $770 < D(\text{pc}) < 805$ corresponding to the Dartmouth, DAM97 and SDF00 isochrones, respectively. In section 1.5.1, it was noted that there was a wide range of distance measurements to NGC 2264. Dzib et al. (2014) measured the distance to a group of radio sources slightly north of the targets used in this analysis as 400pc. In this section, we are able to rule out a distance of 400pc to the primary targets with $>99.6\%$ confidence.

The results from this section show that after the luminosities have been corrected for a binary fraction of 0.5, the original distance of 760pc is acceptable when using two of the three sets of model isochrones, and is narrowly missed when using the SDF00 isochrones.

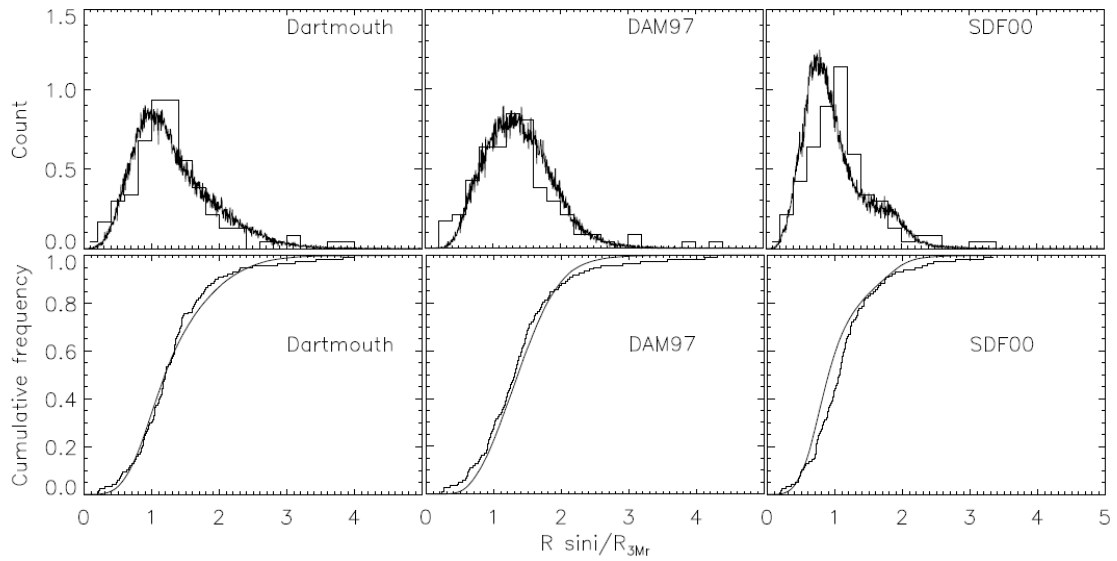


Figure 4.14: The distributions of $(R \sin i)_{\text{obs}}/R_{3\text{Myr}}$ (also shown in Figures 4.8) along with the cumulative distribution functions of these distributions. The left-hand panels have been produced by normalising the data with the Dartmouth isochrones, the central panels with the DAM97 isochrones and the right-hand panels with the SDF00 isochrones. The model normalised $R \sin i$ shown overlying the histograms were produced assuming that the stars had the ages implied by their positions in the HR diagram as derived from each set of model isochrones and corrected for a binary fraction of 0.5. (This is similar to 4.14, but after a binary correction.)

4.6 Does the adopted value of the extinction affect the results?

Table 4.7 shows the results obtained when using a Gaussian distribution of $\log(R)$ about a central single isochrone with various standard deviations in \log_{10} normalised radius (σ_r) for three different evolutionary models. The results shown in black have been produced using the higher reddening correction from Rebull (2002) of $E(V-I)=0.234$, those in blue were produced using the correction calculated in section 3.5 of $E(V-I)=0.022$, (also presented in Table 4.1) and are shown for comparison. The models were tested with a T_{eff} error of 150K and an inclination angle threshold of 30° . The age in column 1 is the isochronal age which was adjusted to minimize the KS statistic. Column 2 shows σ_r , where the values of 0.0 in this column represent a coeval model. The first row for each model gives the result for a coeval model. The subsequent three rows show results for models where the coevality assumption was relaxed and which correspond to the best fit spread in (log) normalised radius (σ_r), and then results which bracket the range of dispersion in log normalised radius that cannot be rejected at more than ~ 90 confidence. Columns 3 and 4 list the KS statistic (D_{max}) and the probability of $D > D_{\text{max}}$. The final column comments on whether the model can be excluded by the data. The results when using either the correction measured in section 3.5 or the value from Rebull (2002) were similar. The main difference was that when using the value from Rebull (2002), the SDF00 coeval isochrones could not be rejected with a high level of confidence. Despite this, the best-fitting σ_r was unchanged for the SDF00 isochrones, so the results using the higher extinction value from Rebull (2002) will not affect our conclusions. Quantitatively, this has little effect on the results.

Mean \log_{10} (Age/years))	σ_r (dex)	D_{max}	P($D > D_{max}$)	Comments
Dartmouth				
6.22 6.17	0.00 0.00	0.0773 0.0717	0.4642 0.5625	Good fit Good fit
6.22 6.17	0.00 0.00	0.0773 0.0918	0.4642 0.3996	Good fit Good fit
6.22 6.17	0.11 0.11	0.0560 0.0772	0.8420 0.8002	Good fit Good fit
6.22 6.17	0.21 0.20	0.1060 0.2322	0.1321 0.0907	Too broad Too broad
DAM97				
6.08 6.07	0.00 0.00	0.1124 0.1127	0.0942 0.0926	Too narrow Too narrow
6.08 6.07	0.05 0.05	0.1033 0.1100	0.1514 0.1442	Too narrow Too narrow
6.08 6.07	0.15 0.19	0.0552 0.0984	0.8541 0.8226	Good fit Good fit
6.08 6.07	0.23 0.23	0.1068 0.0762	0.1272 0.1319	Too broad Too broad
SDF00				
6.41 6.39	0.00 0.00	0.1198 0.0597	0.0622 0.2177	Too narrow Good fit
6.41 6.39	0.06 0.01	0.1058 0.1003	0.1334 0.1664	Too narrow Good fit
6.41 6.39	0.16 0.16	0.0527 0.0482	0.8900 0.9421	Good fit Good fit
6.41 6.39	0.23 0.23	0.1039 0.1232	0.1473 0.0922	Too broad Too broad

Table 4.7: The results obtained when using a Gaussian distribution of $\log(R)$ about a central single isochrone with various standard deviations in \log_{10} normalised radius (σ_r) for three different evolutionary models. The results shown black have been produced using the higher reddening correction from Rebull (2002), those in blue were produced using the correction calculated in section 3.5, (also presented in Table 4.1). The columns are described in the text. The results highlighted in red are those that produce different values when using the higher reddening correction.

4.7 Conclusions and summary

We have examined the $R \sin i$ distributions in NGC 2264 and compared them to the predictions of several sets of models in order to determine whether there is a spread of radii (at a given T_{eff}) or spread of ages in the cluster. Firstly the distributions of $(R \sin i)_{\text{obs}}$ were compared with models assuming a coeval population of stars in order to test whether a coeval population could be ruled out at a high level of confidence. Using two of the three sets of isochrones, a coeval age could be ruled out with greater than 90% confidence. However, when using the Dartmouth isochrones, the coeval model provided an acceptable fit to the $(R \sin i)_{\text{obs}}/R_{3\text{Myr}}$ distribution. Hence, were unable to conclude whether the radii of stars in NGC 2264 are consistent with coevality using this model.

The $(R \sin i)_{\text{obs}}$ spread observed in section 4.5.4 when using the DAM97 and SDF00 models could be interpreted as a spread of cluster ages greater than would be expected from a coeval population. Using a model with ages drawn from a log-normal distribution to test a possible spread of ages, we found that the age spreads which minimised the KS statistic were between 0.2 and 0.46 dex for the three sets of isochrones. This gives some evidence of an age spread in the cluster, however the 90% confidence range included a spread of zero when using the Dartmouth models so again we were unable to confidently rule out a single cluster age. A relatively model independent result from these tests, however, is the upper limit to the radius spread which agreed well when using all three sets of isochrones. The results from using the model which described the accelerating star formation scenario (an exponential distribution of ages), showed evidence for age spreads in all three cases. The KS test results showed >90% confidence of an age spread, hence ruling out instantaneous star formation with >90% confidence. We found that the exponential decay constants which minimised the KS statistic were between 1.3 and 1.62 Myrs using the three sets of isochrones. It was not possible to determine whether the log-normal or exponential age model best described the data although a preliminary analysis shows that it may not be possible to distinguish between the Gaussian or exponential models regarding

the best-fitting age model.

All of the age distributions drawn from the HR diagram provided acceptable fits to the $(R \sin i)_{\text{obs}}/R_{3\text{Myr}}$ distribution, providing the distance used to construct the HR diagram was shifted appropriately. The results and conclusions from this chapter and the following chapter are discussed in chapter 6.

The analysis in this chapter has provided a quantitative addition to what was previously known about ages and age spreads in NGC 2264. The analysis uses a distance-independent method to measure the age and age spread, and an independent dataset which has not previously been analysed. This analysis provides new measurements of the age and age spread in NGC 2264, whilst avoiding using luminosity as an age indicator - a method which has previously been criticised (see section 4.1).

NGC 2264 is hierarchically structured, with sub clusters of suspected members spread across several parsecs. If these substructures were present and of different ages, it would lead to an age spread in both the HR diagram and $R \sin i$ ages. In the following chapter, we examine possible areas of substructure in the cluster, and relate this to whether any of the real or apparent dispersion seen in the $R \sin i$ distributions might be due to substructures with differing ages.

5 Substructure in NGC 2264

5.1 Introduction

The sun, and most other stars, originate in clusters and many clusters contain OB-type stars (Adams 2010; Dukes & Krumholz 2012). NGC 2264 is no exception and there are several massive stars in the region, including S Mon in the northern half of the cluster and HD 47887 in the southern half (see chapter 1, Figure 1.5). One hypothesis is that clustered stars in regions containing massive stars such as these may become gravitationally unbound on the timescale in which gas is expelled from the cluster (Baumgardt & Kroupa 2007). Studying structure in these clustered regions can provide us with an understanding of star formation histories and early cluster dynamics, which can ultimately lead to a more complete understanding of the underlying dynamics that give rise to bound clusters and field star populations (for example, Kruijssen et al. 2012; Banerjee & Kroupa 2014).

It is important to understand the causes which lead to the formation of both individual stars and star clusters. As explained in more detail in section 1.2, current theories suggest that cluster formation can be explained by either (a) a highly dynamic process that occurs within a crossing time, or (b) a slow process where the contraction of the molecular cloud is slowed by long-lived turbulence or pressure due to magnetic fields. Studying the structure and kinematics of young star clusters which still contain mass in the surrounding molecular gas region can assist in determining the initial conditions of the star forming region (e.g. Jeffries et al. 2006, Fűrész et al. 2006, Cottaar et al. 2012).

In the previous chapters of this thesis, our study of NGC 2264 has been primarily focused on ages and age spreads. However, the cluster is also known to have spatial substructure (see section 1.5.4 for a review of the literature on substructure), which could provide an explanation for observed age spreads (see section 1.5.1 and chapter 4 for age spreads in NGC 2264). Finding differences in ages between sub-groups, or

finding gradients of spatial or kinematic parameters, can provide some evidence of structure and provide an account of how the cluster was initially formed.

In this chapter, we examine possible substructure in the cluster using several methods:

- Investigating the dependence of RV on position in order to determine whether there is evidence of kinematic structure or velocity gradients in the line of sight.
- Investigating the dependence of RV on projected radii (which is converted from the rotation period and $v \sin i$ as in chapter 4), to search for evidence of an RV dependence on radius (and age).
- Examining the dependence of RV on the ages determined from the HR diagram in order to probe the possibility of sub-groups at various ages or distances.
- Investigating the possibility of a foreground or background population.
- Studying the RV and position of accreting stars to determine whether they have common positions, motions or ages.

The spatial locations of the targets is biased due to the limitations of positioning the Giraffe fibres, and the way in which the targets were selected to fit in each of the FLAMES fields. Therefore, spatial substructure was not the main focus of this study. Primordial substructure has been examined previously by Teixeira et al. (2006). Our analysis in the following sections investigates features of NGC 2264 using the same targets described in section 3.2.

5.2 Kinematic substructure in NGC 2264

Section 1.4 reviewed the uses of kinematic diagnostics in star formation studies of young clusters. Evidence of spatial substructure has been found in NGC 2264 (e.g. Teixeira et al. 2006), and including RVs as a third dimension to these analyses can assist in

distinguishing between potential subgroups, or identify cluster structure, hence helping to form a more complete understanding of star formation in the cluster. Fűrész et al. (2006) and Tobin et al. (2015) have performed kinematic studies on NGC 2264. An RV gradient of $\sim 6.6 \text{ km(s deg)}^{-1}$ has previously been found in Fűrész et al. (2006), and Tobin et al. (2015) also reported that the RVs increased with declination within the cluster. Tobin et al. (2015) found evidence of a group of stars which are blue-shifted with respect to the associated molecular (^{13}CO) gas, and defined a red-shifted population at the northern end of the cluster. They suggest that both stellar and gas kinematics of the red-shifted region are the results of a bubble driven by a wind from S Monocerotis (S Mon), an O7 type star with an RV of 33.2 km/s (Wilson 1953).

In section 3.4.1 we measured the radial velocities to the primary sample of stars in NGC 2264 (a histogram of these are shown in Figure 3.5). The dispersion of RVs is much larger than the associated uncertainties, so we were interested in whether the dispersion is connected with properties such as position, radius or age in the following section. Further to this, we examined the possibility of either a foreground or background sub-group in section 5.2.2.

5.2.1 How radial velocity correlates with position, $R \sin i$ and age

The RVs were compared with their positions on the plane of the sky. Figures 5.1 and 5.2 show the target RVs as a function of their right ascension (RA) and declination (DEC). The blue points are the RV and RA (or DEC) of the primary targets. The error bars on the blue points correspond to the individual RV errors (calculated in section 3.4.3), and the line represents a best-fitting gradient for all of the primary targets (using a least-squares fit) The red triangles show the mean RV and mean RA (or DEC) separated into equally populated RA (or DEC) bins. The error bars shown on the red binned points are the standard deviations of RV within each bin. The thicker line in Figure 5.2 is a fit to the data from Fűrész et al. (2006), who found an increase in RV with DEC when taking the average of their two sets of RVs. We found no significant trend

of RV with RA across the cluster (gradient of $1.59 \pm 1.73 \text{ km(s deg)}^{-1}$). The trend of RV and DEC (gradient of $3.8 \pm 1.3 \text{ km(s deg)}^{-1}$) is smaller than that found by Fűrész et al. 2006, $\sim 6.6 \text{ km(s deg)}^{-1}$).

Figure 5.1: RV versus right ascension (RA) for the primary targets. The blue points show RV and RA for all of the targets and the error bars correspond to the RV errors calculated in section 3.4.3. The red triangles show the mean RV and RA when separated into equally populated RA bins, and the error bars on the red points show the standard deviation of RV within these bins. Our data shows no significant correlation between RV and RA (gradient of $1.59 \pm 1.73 \text{ km(s deg)}^{-1}$).

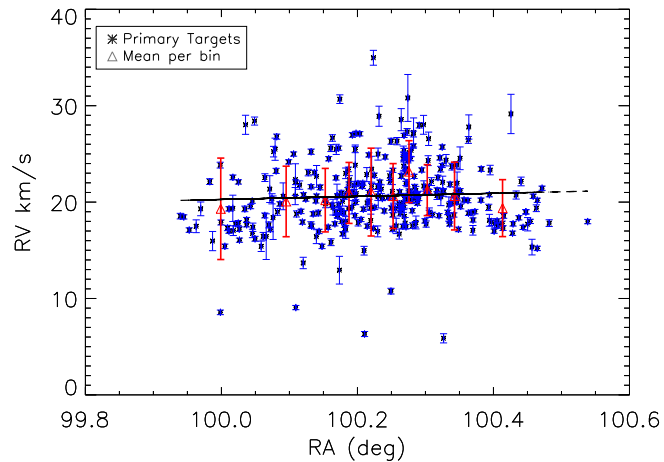
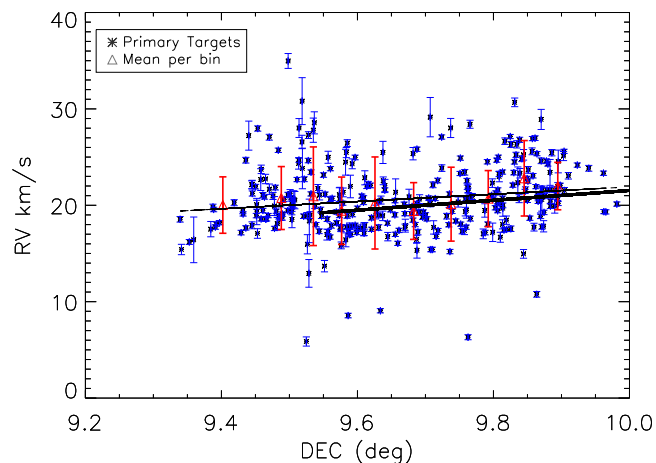


Figure 5.2: RV versus declination (DEC) for the primary targets. The blue points show RV and DEC for all of the targets and the error bars correspond to the RV errors calculated in section 3.4.3. The red triangles show the mean RV and DEC when separated into DEC bins, and the error bars on the red points show the standard deviation of RV within these bins. Our data shows a trend between RV and DEC (gradient of $3.8 \pm 1.3 \text{ km(s deg)}^{-1}$). For comparison with previous work, the thicker black line shows the trend obtained by fitting the data presented by Fűrész et al. (2006) in a similar way.



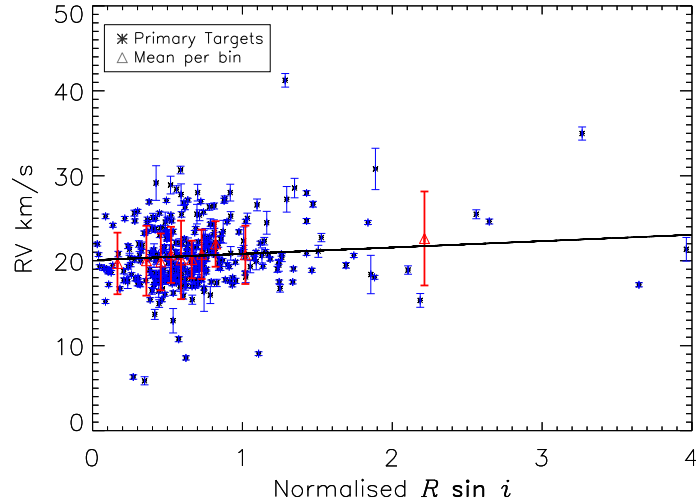


Figure 5.3: RV versus $R \sin i$ for the primary targets. The blue points show RV and $R \sin i$ for all of the targets and the error bars correspond to the RV errors calculated in section 3.4.3. The red triangles show the mean RV and $R \sin i$ when separated into $R \sin i$ bins, and the error bars on the red points show the standard deviation of RV within these bins. Our data shows a trend between RV and $R \sin i$ (gradient = $0.74 \pm 0.28 \text{ km s}^{-1} [\text{normalised } R_{\sin i}]^{-1}$).

We then plotted RV as a function of both the projected radius ($R \sin i$) derived from the rotation period and $v \sin i$ (Figure 5.3), and the ages determined from the HR diagram using the SDF00 isochrones (Figure 5.4). We found a trend of RV with projected radius (gradient = $0.74 \pm 0.28 \text{ km s}^{-1} [\text{normalised } R_{\sin i}]^{-1}$) and a marginally significant gradient of $-1.41 \pm 0.58 \text{ km}(\text{s yrs})^{-1}$ when plotting RV against ages from the HR diagram.

The gradients of RV with DEC, $R \sin i$ and HR diagram ages found in this section could reveal subclusters at the upper and lower end of the RV distribution which may have different ages or positions to the remaining stars in the cluster. We examined this possibility further in the following section.

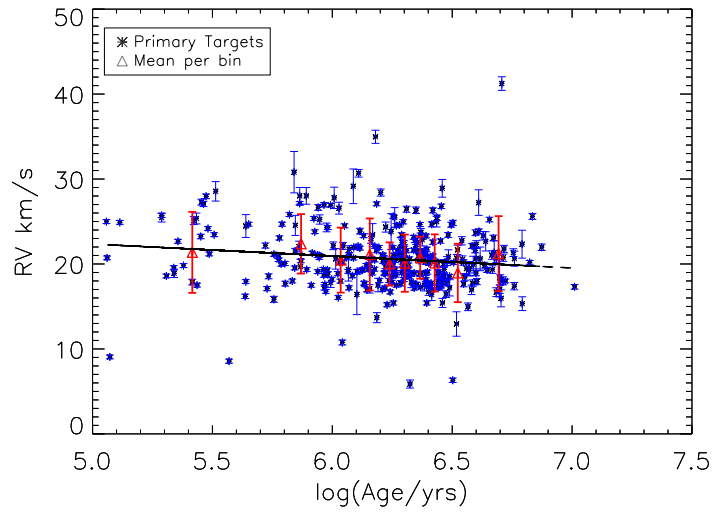


Figure 5.4: RV versus age determined from the HR diagram using the SDF00 model isochrones for the primary targets. The blue points show RV and age for all of the targets and the error bars correspond to the RV errors calculated in section 3.4.3. The red triangles show the mean RV and age when separated into age bins, and the error bars on the red points show the standard deviation of RV within these bins. Our data shows a marginally significant trend between RV and age (gradient = -1.41 ± 0.58 km s^{-1}).

5.2.2 Is there evidence of a foreground or background population?

In section 5.2.1 gradients were found when comparing RVs with DEC, $R \sin i$ and ages from the HR diagram. In this section, we have explored whether these gradients could be disguising a more structured distribution of objects in the cluster. There are significant variations between the distances to the cluster (or targets within the cluster) quoted in the literature (see section 1.5.2). These vary from 400pc (Dzib et al. 2014) to ~ 900 pc (e.g. Baxter et al. 2009). One scenario that could cause such variation is several populations or subgroups in the line of sight. We therefore examined whether our data can distinguish between a foreground or background population or sub-group of stars in the line-of-sight.

Firstly, the targets were separated into 2 km/s bins. Figure 5.5 effectively shows the cluster ‘sliced’ up into eight equally sized RV bins, and overplotted onto the Digitized Sky Survey image to compare the positions of the stars with areas of molecular gas. From Figure 5.5, the targets in the higher RV bins (>22 km/s) appear to be situated closer to the darker region on the image, and so more closely related to the molecular gas. The targets with lower RVs, on the other hand (in the upper four panels), appear to be more dispersed. This could show an older (hence, more dispersed) population, and a younger (less dispersed) cluster lying deeper within the areas of molecular gas.

This possibility was further examined by separating the targets into four equally populated RV groups between 10 and 34 km/s, characteristic of cluster members, each bin containing 85 points. RV histograms of these separate groups are shown in Figure 5.6. For each of the bins, we plotted a density plot of target position, shown in Figure 5.7. The positions of the targets in each group are also shown. The plots again show that the targets with higher RVs (lower right hand panel) are more compact and the targets with lower RVs are more dispersed (upper left hand panel). We calculated the mean separation (\tilde{s} , the mean distance between all of the targets in a sample on the plane of the sky) between all of the targets in each group. \tilde{s} was calculated by

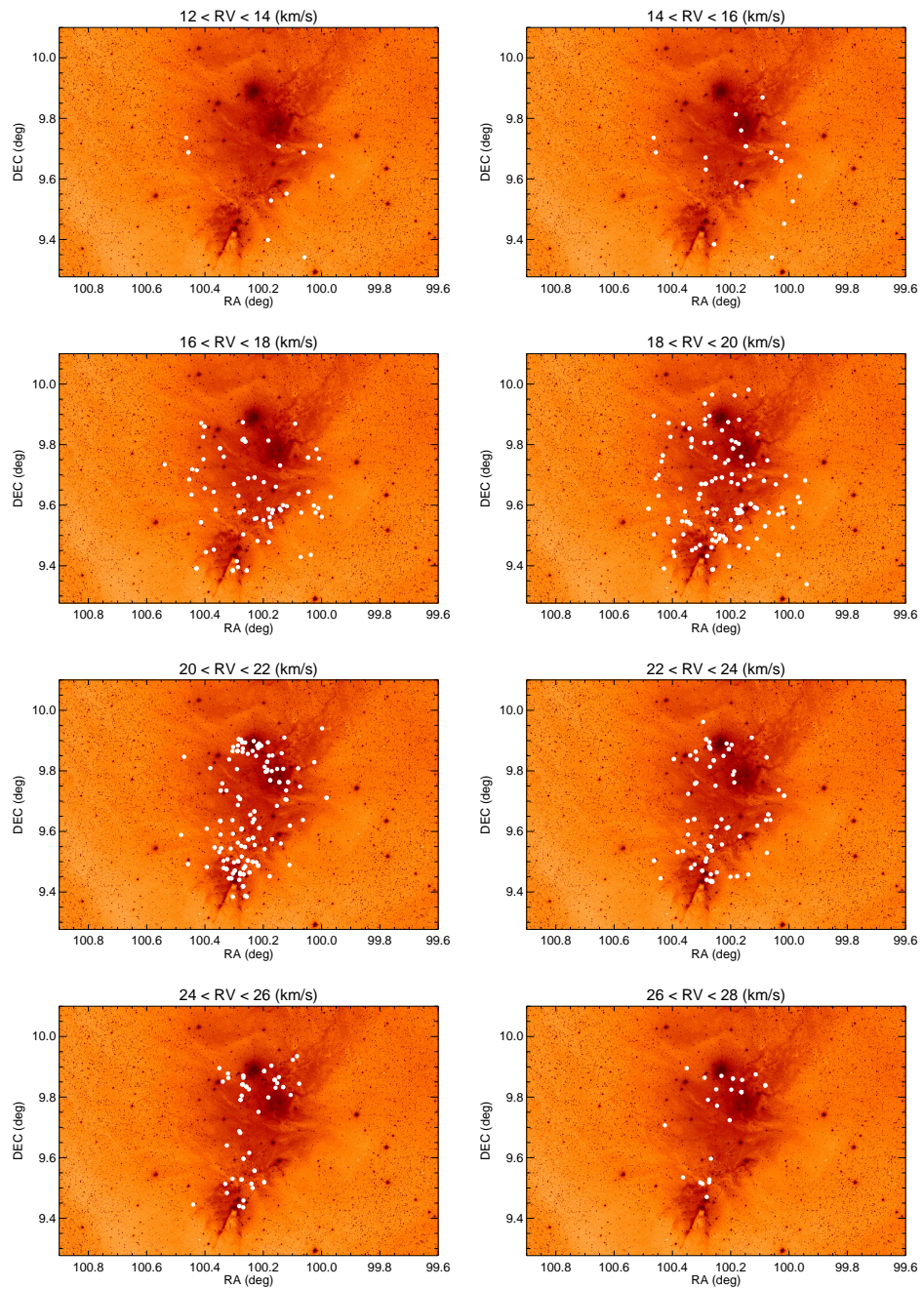


Figure 5.5: The targets separated into 2 km/s bins and plotted according to their position over the Digitized Sky Survey images (from STScI) image.

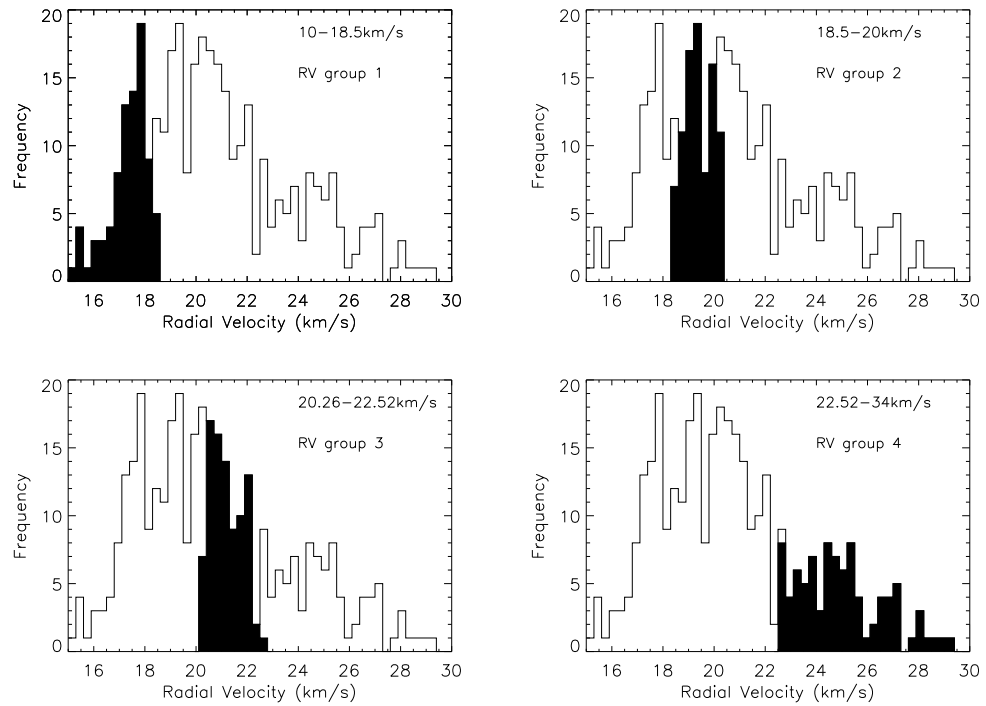


Figure 5.6: Histograms showing the distributions of the RVs of the primary targets along with the four separate sub-groups used to examine any possible RV substructure.

measuring the distance between each target and each other target in the group using their RA and DEC. There is a decrease in the mean separation with RV within the groups. For each of the four groups shown in Figure 5.7, $\tilde{s} = 0.259, 0.238, 0.219$ and 0.211 degrees, confirming our observation from Figure 5.5, and possibly indicating an older, more dispersed population, and a younger cluster, where stars have had less time to become more dispersed.

The conclusions in this section are based on the assumption that the primary targets are a spatially-unbiased sample representing the cluster. There is a chance that the primary sample may exclude stars closely spaced to each other due limitations in button size on the plates of the spectrograph, which have a minimum object separation of 10.5 arcsec. However, care was taken in the preparation of targets to avoid this bias. It is also unlikely that the results were effected by a selection bias, because the RVs were not known prior to target selection.

We further explored the hypothesis of an older and younger sub-cluster by examining the age distributions and their dispersions between the four RV groups. The method used in this section is described fully in section 4.3. We used the projected radii of the targets, determined from their rotation periods and $v \sin i$ s (see section 3.4 for $v \sin i$ determination), as distance-independent age indicators for the stars in the cluster. We normalised $(R \sin i)_{\text{obs}}$ by the 3 Myr SDF00 isochrone ($(R \sin i)_{\text{obs}}/R_{3\text{Myr}}$). We compared the distribution of $(R \sin i)_{\text{obs}}/R_{3\text{Myr}}$ for each of the four groups shown in Figures 5.6 and 5.7, with a Gaussian distribution of $\log_{10}R$ about a central value defined by a single isochronal age and with a standard deviation of σ_r from the SDF00 isochrones, as in chapter 4.

The results are shown in Figure 5.8 and listed in Table 5.1, where columns 1 and 2 show the group and RV range of the four groups. Column 3 shows the age that minimised the KS statistic when comparing the $(R \sin i)_{\text{obs}}/R_{3\text{Myr}}$ distribution and the model (in the rest of this discussion we refer to this as the ‘ $R \sin i$ age’). The upper and lower margins show the limits whereby the p-values were collapsed onto the age axis, and which contain 90% of the distribution. Column 4 shows the mean ages ($\log_{10}(\text{age}/\text{yrs})$) inferred from the same stars’ positions in the HR diagram

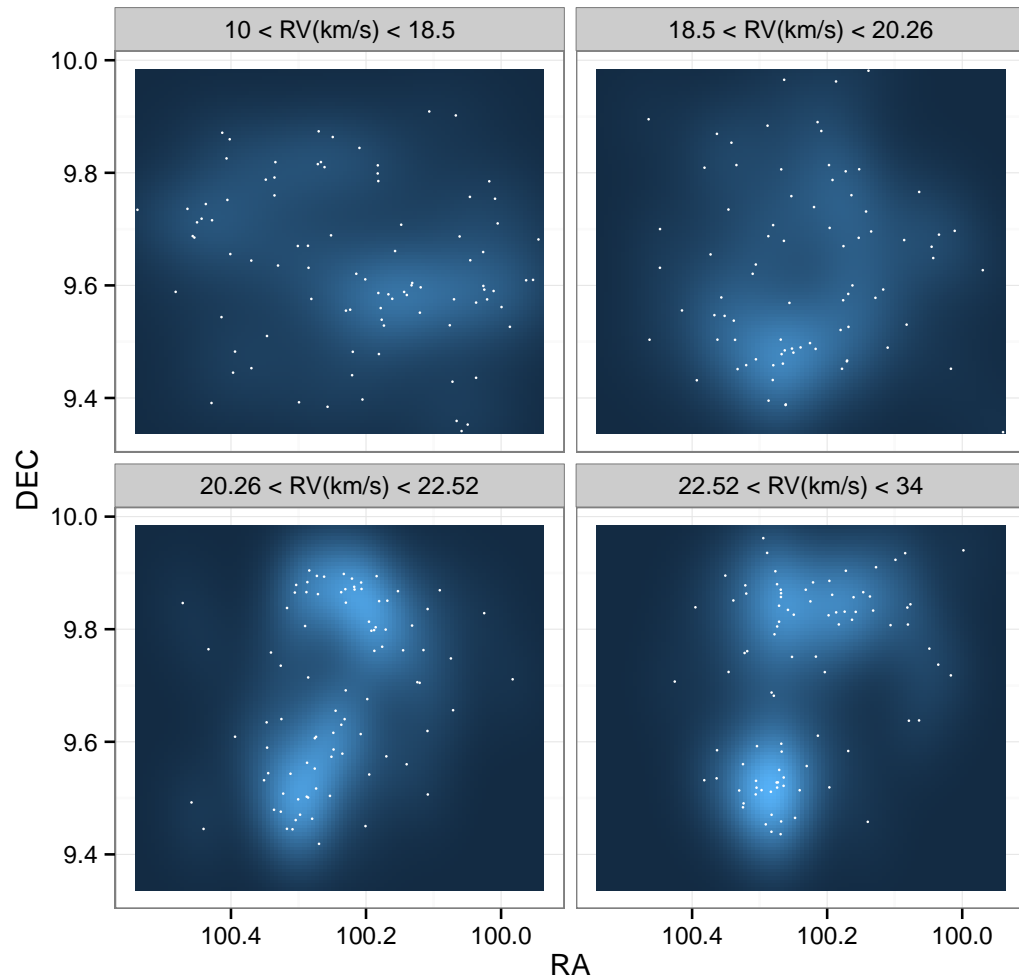


Figure 5.7: Density plots illustrating the density of the targets according to their position in the cluster. The four groups are equally populated. The mean target separations in each group are $\tilde{s} = 0.259, 0.238, 0.219$ and 0.211 corresponding to the upper left, upper right, lower left and lower right plots, respectively. There is a decline of \tilde{s} with the four RV groups.

(referred to hereafter as the ‘HR diagram age’) assuming a common distance of 760 pc and determined from the SDF00 isochrones. The standard error in the mean (and standard deviations of the distributions) are also shown in column 4. σ_r in column 5 is the Gaussian sigma of the model which, when combined with the age in column 3, gives the best-fit to the $(R \sin i)_{\text{obs}}/R_{3\text{Myr}}$ distribution. Columns 6 and 7 show the results of the KS tests. In all cases, the models with the parameters shown in the columns 4 and 6 are a reasonable match to the data. The $R \sin i$ ages suggest a decrease with increasing RV, but could be consistent within their 90% confidence intervals. The HR diagram ages show the same trend with increasing RV groups as the ages determined from the $(R \sin i)_{\text{obs}}/R_{3\text{Myr}}$ distributions. Figure 5.8 shows the $(R \sin i)_{\text{obs}}/R_{3\text{Myr}}$ distributions for the four individual groups, along with the model, with ages and dispersions listed in Table 5.1 which minimise the KS statistic when compared with the $(R \sin i)_{\text{obs}}/R_{3\text{Myr}}$ distribution. These results are consistent with the scenario of a younger, high-RV population and an older, low-RV population, as found in section 5.2.1.

The effects of varying the RV bin sizes and boundaries are shown in Table 5.2. The sample was split into groups of two, three and five and the $R \sin i$ ages were measured for each group. In all cases, our results show an older low-RV group and a younger high RV group, although the ages do not consistently decrease with increasing RV (see groups 10, 11, 12, 13 and 14 in Table 5.2). This examination further supports our results from this section, suggesting a younger, high-RV population and an older, low-RV population. The fact that the cluster appears to become more structured at higher RVs is not consistent with an interpretation that the sample is contaminated by foreground stars.

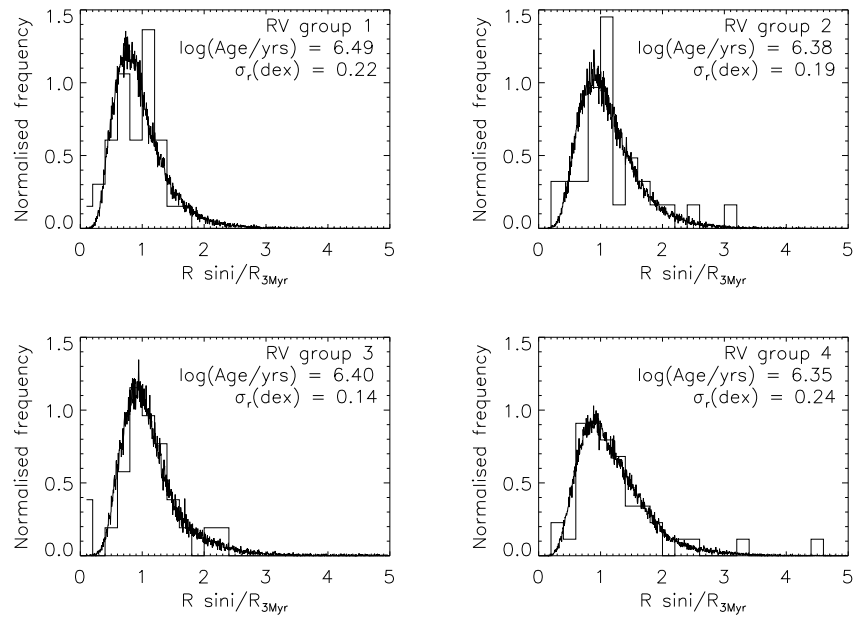


Figure 5.8: The distributions of $(R \sin i)_{\text{obs}} / R_{3\text{Myr}}$ for the four separated groups, along with the models of a Gaussian dispersion in radius of σ_r which minimise the KS statistic when compared with the modelled distribution.

Group	RV range (km/s)	Mean $\log_{10}(\text{age}/\text{yrs})$	Mean $\log_{10}(\text{age}/\text{yrs})$ (HR diagram)	σ_r (dex)	D_{max}	$P(D > D_{\text{max}})$
1	$10 < \text{RV} < 18.5$	$6.49^{+0.10}_{-0.09}$	6.38 ± 0.004 (0.3)	0.22	0.1081	0.8135
2	$18.5 < \text{RV} < 20.26$	$6.38^{+0.08}_{-0.15}$	6.25 ± 0.004 (0.29)	0.19	0.0918	0.9463
3	$20.26 < \text{RV} < 22.52$	$6.40^{+0.10}_{-0.11}$	6.29 ± 0.003 (0.27)	0.14	0.0838	0.9904
4	$22.52 < \text{RV} < 34$	$6.35^{+0.09}_{-0.12}$	6.20 ± 0.005 (0.41)	0.24	0.0640	0.9919

Table 5.1: The KS test result from comparing the $(R \sin i)_{\text{obs}}/R_{3\text{Myr}}$ distribution with a Gaussian distribution of $\log_{10}R$ about a central value defined by a single isochronal age (column 3) with a standard deviation of σ_r (column 5). The HR diagram ages are also shown in column 4 with the standard error in the mean (and standard deviation) of their distributions.

Group	RV range (km/s)	Mean $\log_{10}(\text{age}/\text{yrs})$
5	10 < RV < 22	$6.49^{+0.09}_{-0.09}$
6	22 < RV < 30	$6.37^{+0.08}_{-0.10}$
7	10 < RV < 19	$6.48^{+0.10}_{-0.09}$
8	19 < RV < 25	$6.38^{+0.07}_{-0.12}$
9	25 < RV < 34	$6.35^{+0.10}_{-0.11}$
10	10 < RV < 17.5	$6.52^{+0.10}_{-0.10}$
11	17.5 < RV < 21	$6.42^{+0.08}_{-0.17}$
12	21 < RV < 23	$6.40^{+0.10}_{-0.12}$
13	23 < RV < 25	$6.41^{+0.09}_{-0.13}$
14	25 < RV < 34	$6.35^{+0.10}_{-0.11}$

Table 5.2: The KS test result from comparing the $(R \sin i)_{\text{obs}}/R_{3\text{Myr}}$ distribution with a Gaussian distribution of $\log_{10}R$ about a central value defined by a single isochronal age (column 3) with altered RV bin ranges.

The trend in mean HR diagram ages between the four RV groups, could suggest either that there are sub-populations of stars with different mean ages, or that there are stars at different distances. There is a trend of $R \sin i$ age with RV group, however, due to the wide 90% confidence range, these groups could have consistent ages. To test these hypotheses statistically, two-sided KS tests we performed on;

- The $(R \sin i)_{\text{obs}}/R_{3\text{Myr}}$ distributions of each group with each other group (cumulative distribution function (CDF) shown in Figure 5.9).
- The HR diagram age distributions of each group with each other group (CDF shown in Figure 5.10).

-
- The $(R \sin i)_{\text{obs}}/R_{3\text{Myr}}$ distribution of each group with those targets not in that group (for example, group 1 with every target not in group 1, CDF shown in Figure 5.11).
 - The HR diagram age distributions of each group with those targets not in that group (CDF shown in Figure 5.12).

The results of these tests are listed in Table 5.3.

Distribution 1	Distribution 2	D_{\max}	$P(D > D_{\max})$
($R \sin i$) _{obs} / $R_{3\text{Myr}}$ distributions			
Group 1	Group 2	0.218	0.035
Group 1	Group 3	0.298	0.001
Group 1	Group 4	0.214	0.037
Group 2	Group 3	0.125	0.507
Group 2	Group 4	0.122	0.539
Group 3	Group 4	0.131	0.419
Group 1	! Group 1	0.230	0.003
Group 2	! Group 2	0.085	0.784
Group 3	! Group 3	0.166	0.061
Group 4	! Group 4	0.116	0.370
HR Diagram age distribution			
Group 1	Group 2	0.252	0.009
Group 1	Group 3	0.190	0.095
Group 1	Group 4	0.249	0.009
Group 2	Group 3	0.136	0.402
Group 2	Group 4	0.210	0.048
Group 3	Group 4	0.236	0.015
Group 1	! Group 1	0.209	0.008
Group 2	! Group 2	0.146	0.154
Group 3	! Group 3	0.112	0.406
Group 4	! Group 4	0.223	0.004

Table 5.3: The results of the KS tests when comparing $R \sin i$ or HR diagram age distributions between RV groups ('!' denotes 'not included in'). The values highlighted in red are those with $P(D > D_{\max}) < 0.1$.

When comparing the $R \sin i$ distributions between the four RV groups, we have no evidence that groups 2, 3 and 4 are from different populations ($P(D > D_{\max}) > 0.05$ in each case). We noticed, however, that in all comparisons that include group 1, the KS-tests revealed that there is a low probability of the distributions being drawn from the same parent population ($P(D > D_{\max}) < 0.05$ in each case). A similar result was found when using the age distributions from the HR diagram, in that when comparing the distribution of ages of group 1, with all other groups resulted in low p-values from the KS tests. Considering these results, and the mean $R \sin i$ and HR diagram ages shown in Table 5.1, we conclude that the stars in group 1 are older, on average, than the remaining cluster stars. The fact that the mean separation of stars in group 1 is larger than the other groups, supports this scenario.

We assumed that group 4 has a similar age to groups 2 and 3, which is suggested by their similar $R \sin i$ distributions. The comparison between $(R \sin i)_{\text{obs}}/R_{3\text{Myr}}$ distributions in group 4 and the remaining stars in the cluster shows a (reasonably) high p-value (0.37). However the KS test results from comparing the HR diagram age distributions in group 4 with the distribution of the remaining stars in the cluster reveals a low p-value of 0.004. We incremented the (log) luminosity values of group 4 and repeated the KS-tests which compared the HR diagram ages of group 4 and the remaining targets, until the KS statistic was minimised. A luminosity shift corresponding to a distance shift of group 4, to groups 2 and 3, from 760 to 632^{+30}_{-29} pc is required to bring the HR diagram age distributions into agreement.

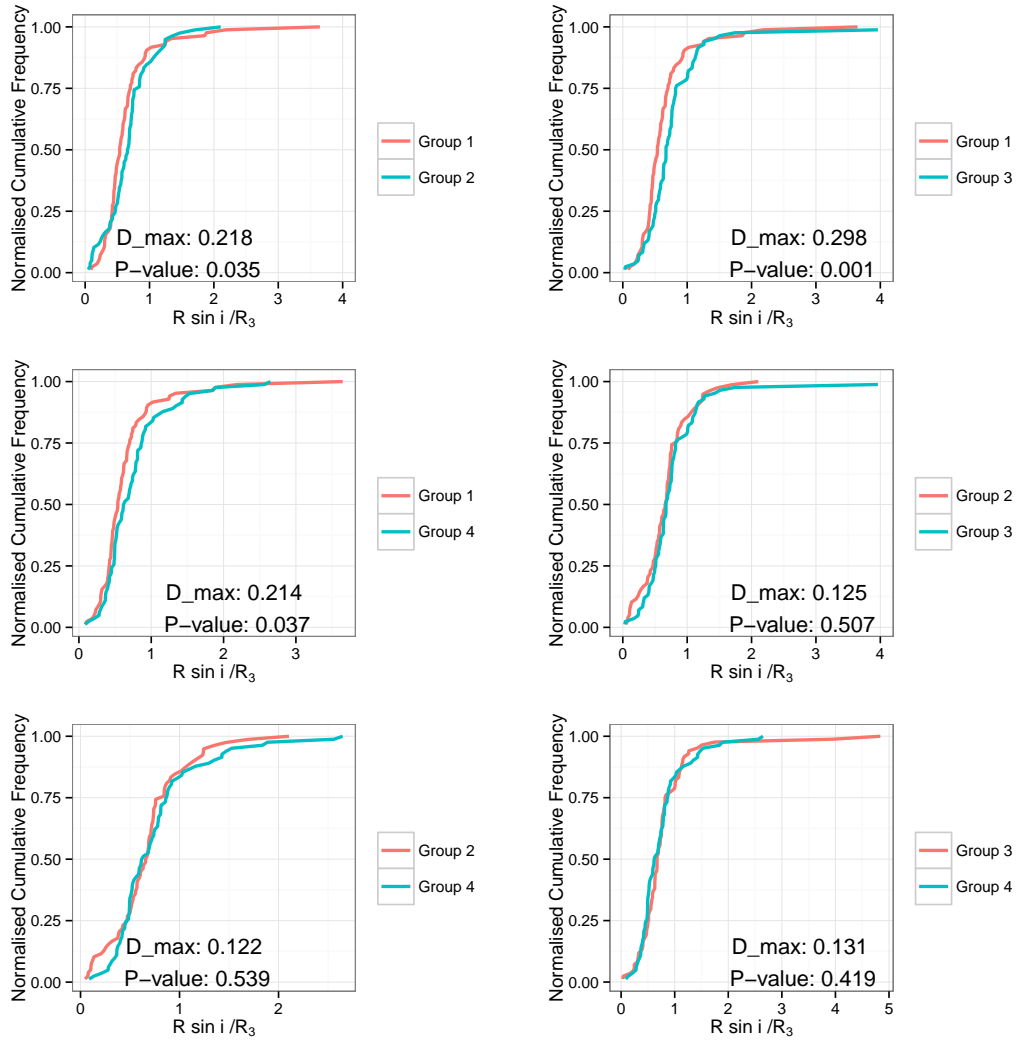


Figure 5.9: Comparing the cumulative distribution functions of $(R \sin i)_{\text{obs}}/R_{3\text{Myr}}$ for each group, with each other group (see Table 5.1 for a definition of each RV group) .

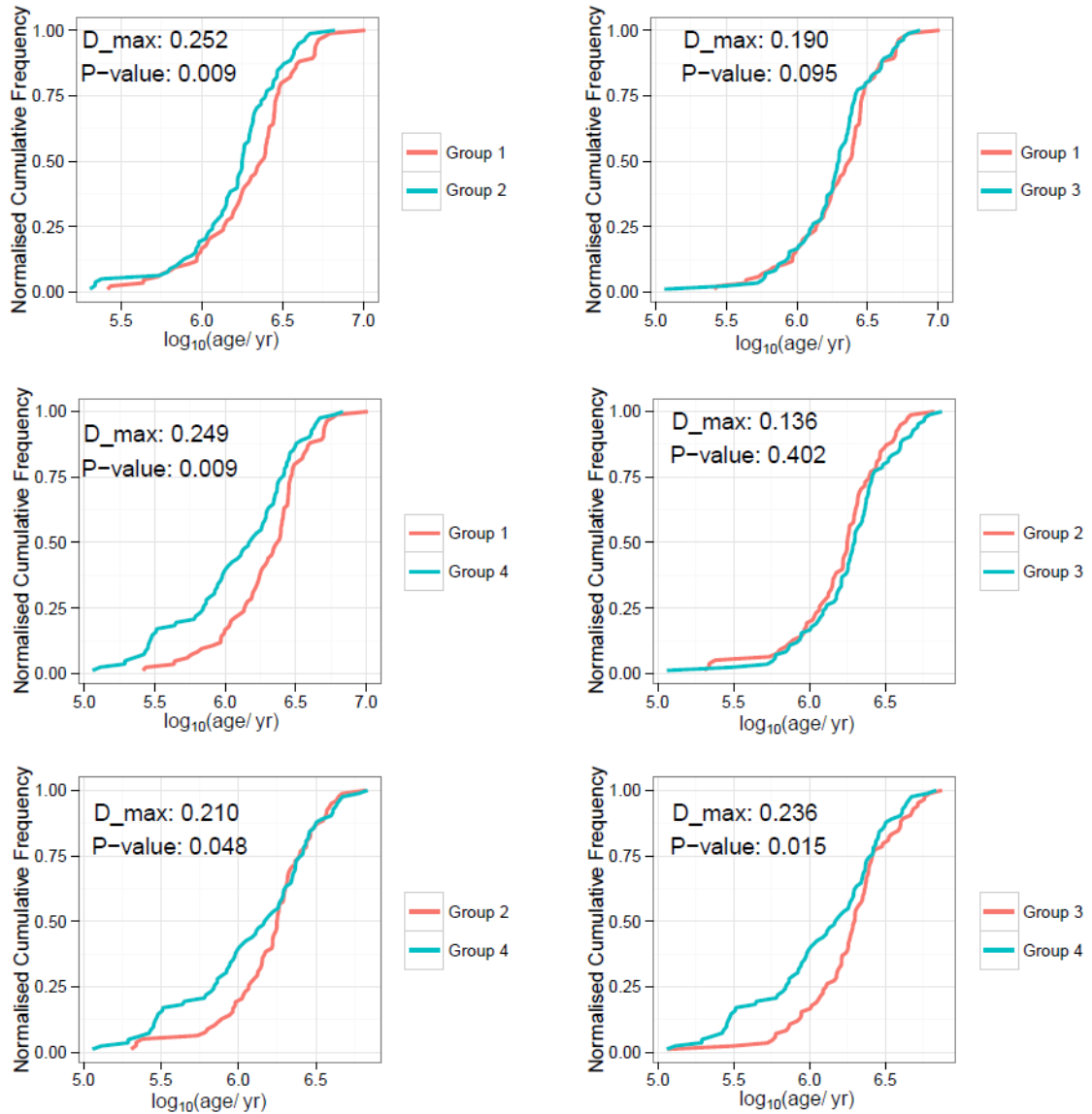


Figure 5.10: Comparing the cumulative distribution functions of HR diagram age for each group, with each other group (see Table 5.1 for a definition of each RV group).

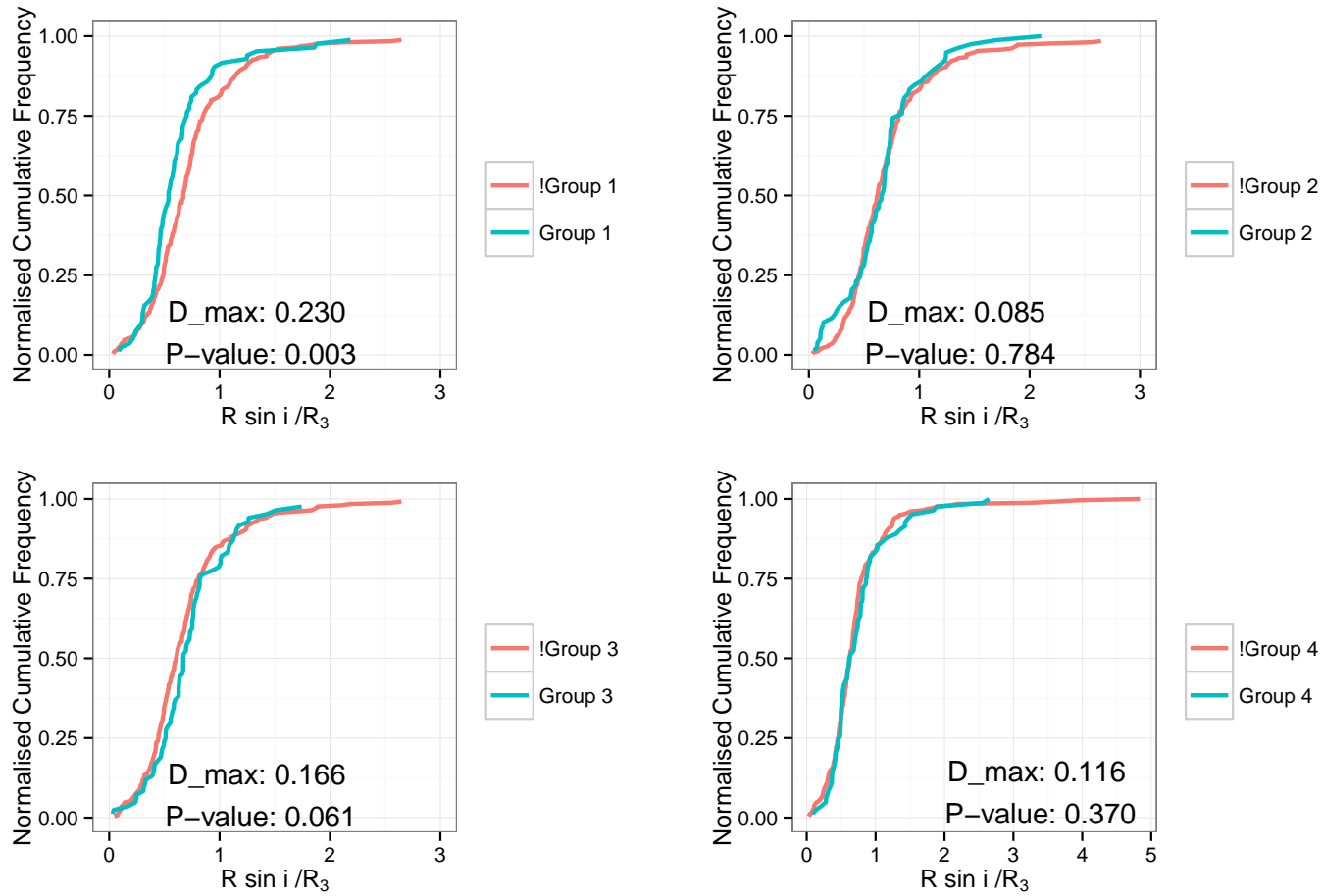


Figure 5.11: Comparing the cumulative distribution functions of $(R \sin i)_{\text{obs}}/R_{3\text{Myr}}$ distributions of each group, with the distribution of those targets not in that group (see Table 5.1 for a definition of each RV group).

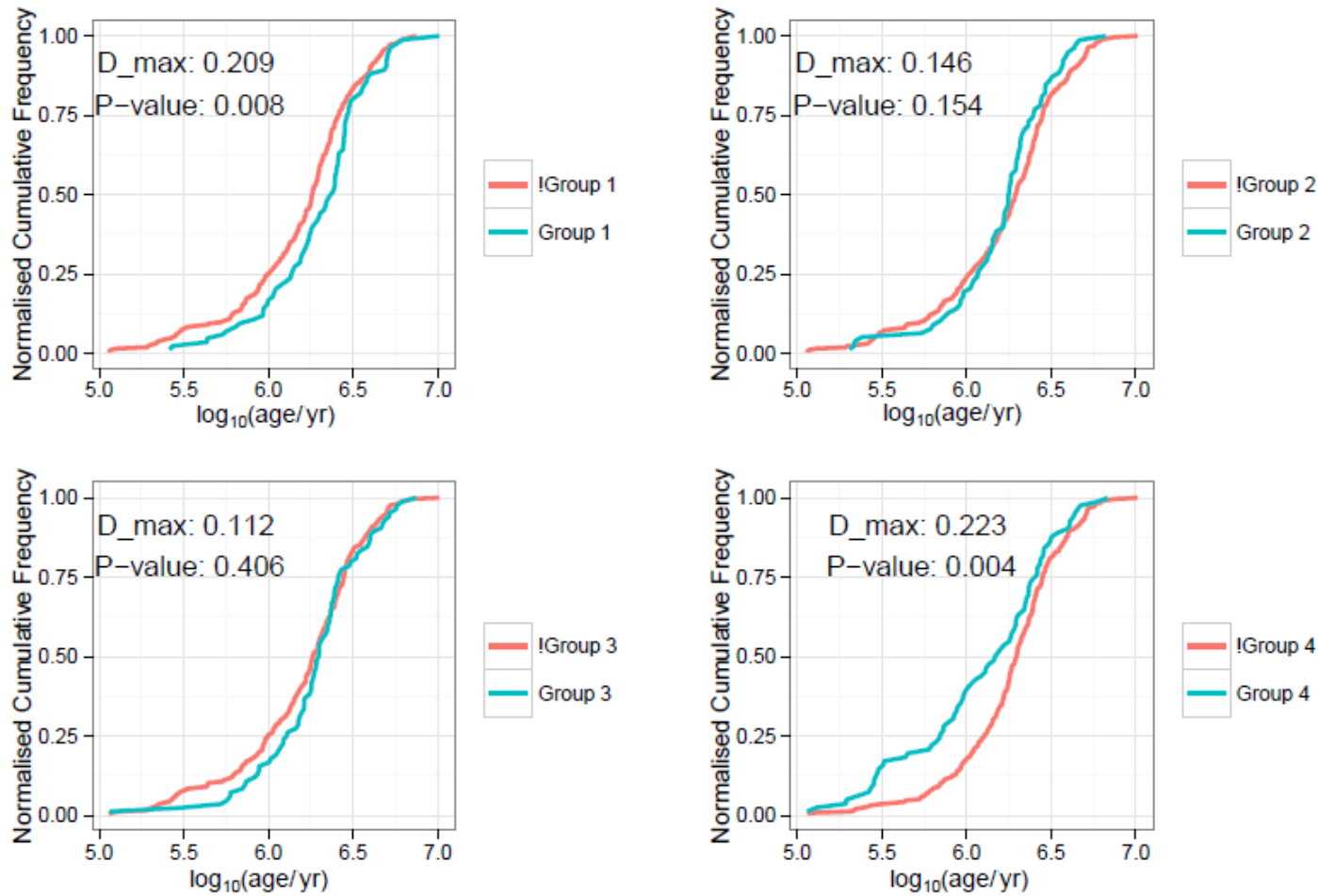


Figure 5.12: Comparing the cumulative distribution functions of HR diagram age distributions of each group, with the distribution of those targets not in that group (see Table 5.1 for a definition of each RV group).

There is a consistent difference between the $R \sin i$ ages and HR diagram ages (see Table 5.1) of ~ 0.12 dex for each group. In section 4.2.1 a binary fraction 0.5 was assumed, and could explain this discrepancy.

To summarise this section, group 1 (low-RVs) was found to be older, on average, than the other groups according to both the $R \sin i$ ages and the HR diagram ages. This hypothesis is supported by the larger mean separation between targets in group 1. Evidence was also found for a foreground population at $\sim 632_{-29}^{+30}$ pc, for group 4 (high-RVs). In the following section, the scenario of sub-clusters situated around two of the brightest stars in the cluster has been explored.

5.3 Stars around S Mon and HD 47887

Spatial substructure has been found in NGC 2264 (for example, Teixeira et al. 2006, see section 1.5.4). By observing Figure 5.5, dense areas of gas are seen, rather than a smooth distribution across the cluster. S Monocerotis (S Mon) and HD 47887 are bright stars situated in NGC 2264 (their positions are shown in Figure 5.13). S Mon is situated in the northern section of the cluster and HD 47887 in the southern area. We selected members of the cluster in our sample from the projected regions surrounding S Mon and HD 47887 in order to examine whether these regions have different radii, ages or RV distributions. Figure 5.13 shows these selected targets along with the rest of the primary targets in the cluster, and S Mon and HD 47887 are situated centrally to these selected groups. The spatial divisions of the S Mon and HD 47887 groups were chosen as ± 0.2 degrees in either RA and DEC, and each group contains ~ 70 targets.

The same analysis as in section 5.2.2 (and chapter 4) was performed on these targets (a comparison of their $(R \sin i)_{\text{obs}}/R_{3\text{Myr}}$ distributions with a modelled lognormal radius distribution). The results are shown in Table 5.4. There is good agreement between the ages from the $(R \sin i)_{\text{obs}}/R_{3\text{Myr}}$ distribution of the S Mon group and the HD 47887 group within their uncertainties. The upper and lower 90% limits quoted in column 3 are those that contain 90% of the probability when totalled over

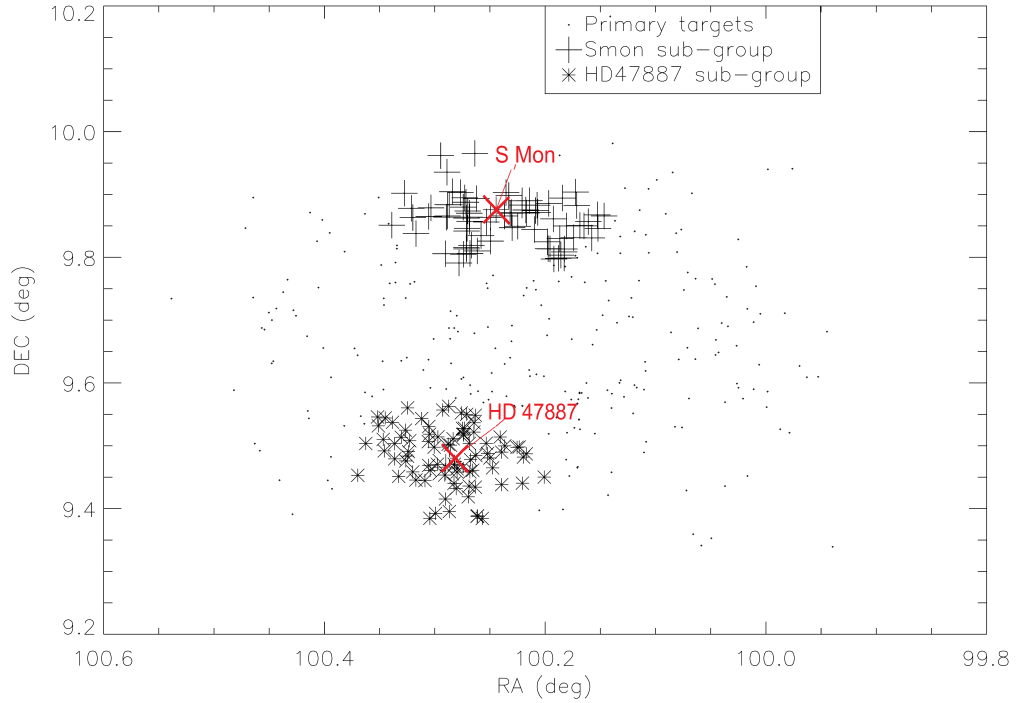


Figure 5.13: The positions of the primary targets (small points), and those targets in the selected sub-groups. The crosses show the targets situated near to the bright star ‘S Monocerotis’, and the asterix show the targets situated near to the bright star HD 47887.

Group	No. of targets	mean $\log_{10}(\text{age}/\text{yrs})$	σ_r (dex)	D_{\max}	$P(D > D_{\max})$	mean $\log_{10}(\text{age}/\text{yrs})$ (HR diagram)
S Mon	70	$6.39^{+0.09}_{-0.17}$	0.10	0.0699	0.9972	6.25 ± 0.004 (0.3)
HD 47887	67	$6.34^{+0.06}_{-0.19}$	0.09	0.1004	0.8715	6.19 ± 0.005 (0.37)

Table 5.4: A summary table of the results found when comparing the $(R \sin i)_{\text{obs}}/R_{3\text{Myr}}$ distribution with a model assuming a central age and with a Gaussian dispersion in radius of σ_r . The ages from the HR diagram are also listed, along with the standard errors in the mean (and standard deviations) of the age distributions for both of the subgroups tested.

Distribution 1	Distribution 2	D_{\max}	$P(D > D_{\max})$
<i>R sin i</i> distributions			
S Mon group	HD 47887 group	0.210	0.051
HD 47887 group	! HD 47887 group	0.238	0.0003
S Mon group	! S Mon group	0.073	0.882
HR diagram age distributions			
S Mon group	HD 47887 group	0.1445	0.333
HD 47887 group	! HD 47887 group	0.211	0.012
S Mon group	! S Mon group	0.075	0.857

Table 5.5: The KS test results of comparing $(R \sin i)_{\text{obs}}/R_{3\text{Myr}}$ distributions of the S Mon and HD 47887 groups, and HR diagram age distributions between the two groups. ‘!’ denotes ‘not included in’.

the age axis. The targets surrounding S Mon are slightly older from their $(R \sin i)_{\text{obs}}/R_{3\text{Myr}}$ distributions on average, than the targets around HD 47887 (but could have consistent ages given the 90% confidence range).

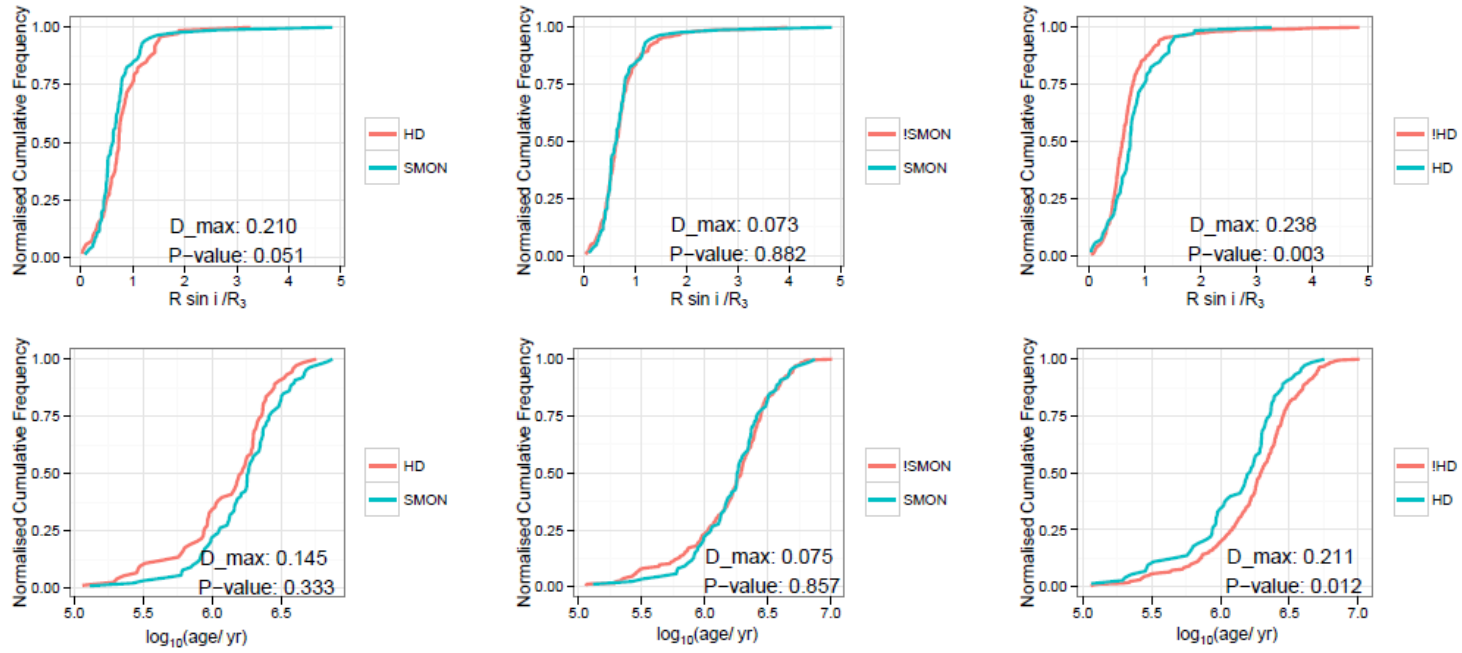


Figure 5.14: The cumulative distribution functions of comparing the HR diagram age distributions and the $(R \sin i)_{\text{obs}}/R_{3\text{Myr}}$ distributions of each group, with the distributions of either; those targets not in the group, or those targets in the other group.

The HR diagram ages and $R \sin i$ ages are inconsistent by ~ 0.15 dex. Most of this difference is covered by the shift introduced ($\sigma \log_{10}(\text{age}/\text{yrs}) = 0.12$) when considering a binary fraction of 0.5. Therefore, we assume that no distance shift is required to bring the ages into agreement.

KS tests were performed on the distributions of $(R \sin i)_{\text{obs}}/R_{3\text{Myr}}$ and HR diagram ages for the S Mon and HD 47887 sub-groups. The results are listed in Table 5.5 and shown in Figure 5.14. The KS-test results suggest that there is no strong evidence that the S Mon and HD 47887 distributions are from different parent populations, when comparing either their HR diagram age distributions or their $(R \sin i)_{\text{obs}}/R_{3\text{Myr}}$ distributions. To further compare the stars around S Mon and HD 47887, and to determine whether any differences between the S Mon and HD 47887 groups could explain the trend in RV with DEC seen in figure 5.2, KS tests were performed on the RV distributions of the two groups. This test was inconclusive and revealed $P(D > D_{\text{max}}) = 0.15$ ($D_{\text{max}} = 0.17$).

Interestingly, from the KS test results, there is strong evidence that the HD 47887 group is drawn from a different parent population than the remaining cluster stars when comparing both their $(R \sin i)_{\text{obs}}/R_{3\text{Myr}}$ distributions ($P(D > D_{\text{max}}) = 0.0003$) and their HR diagram age distributions ($P(D > D_{\text{max}}) = 0.012$).

The stars around HD 47887 appear younger and might be more likely to show evidence of accretion. In the following section, the ages and positions of a small sample of accreting stars were examined.

5.4 Accreting stars in NGC 2264

The spectra used in this thesis, and described in section 3.3, cover the wavelength range containing two of the calcium triplet (CaT) lines. The strengths of these lines were measured in section 3.7. The calcium triplet lines can be used as accretion indicators to detect the presence of a circumstellar disc around a young star. A small set of 16 stars in our sample were identified, which show signs of accretion (see Figure 5.15). The

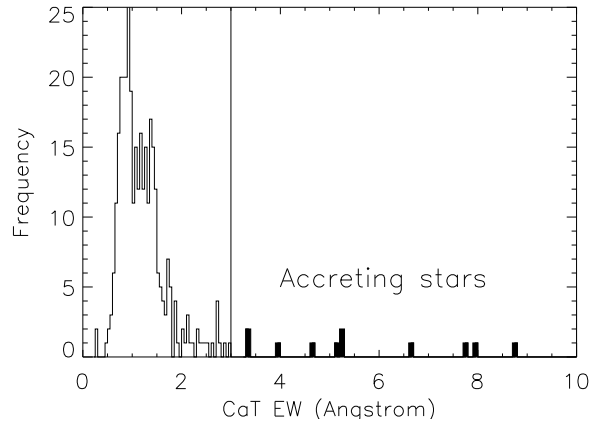


Figure 5.15: A histogram of the CaT line residual equivalent widths of the primary targets, highlighting those showing accretion signatures (filled lines).

positions of these accreting stars are plotted on Figure 5.16 along with the positions of the primary targets, and the S Mon and HD 47887 groups as a comparison. The triangles on Figure 5.16 show the stars with strong CaT lines and their size is proportional to the RV of the star. If there are sub-groups within the cluster of different ages, then we might expect the stars showing accretion signatures to be confined within the younger groups. From Figures 5.16, the stars with accretion signatures do not appear to be grouped kinematically, and (almost) equally populate the regions surrounding S Mon and HD 47887.

The ages and \log_{10} ages determined from the HR diagram of the primary targets and those which are assumed to be actively accreting according to their CaT line strengths are shown in Figure 5.17. The ages of the accreting targets are scattered across the range of the larger sample of targets, and so we were unable to use these stars as further evidence of a younger population or sub-group. The scatter also indicates that the HR diagram ages may not be a good indicator of their true age (discussed further in chapter 6), however, a much larger sample stars showing accretion signatures is required to draw strong conclusions.

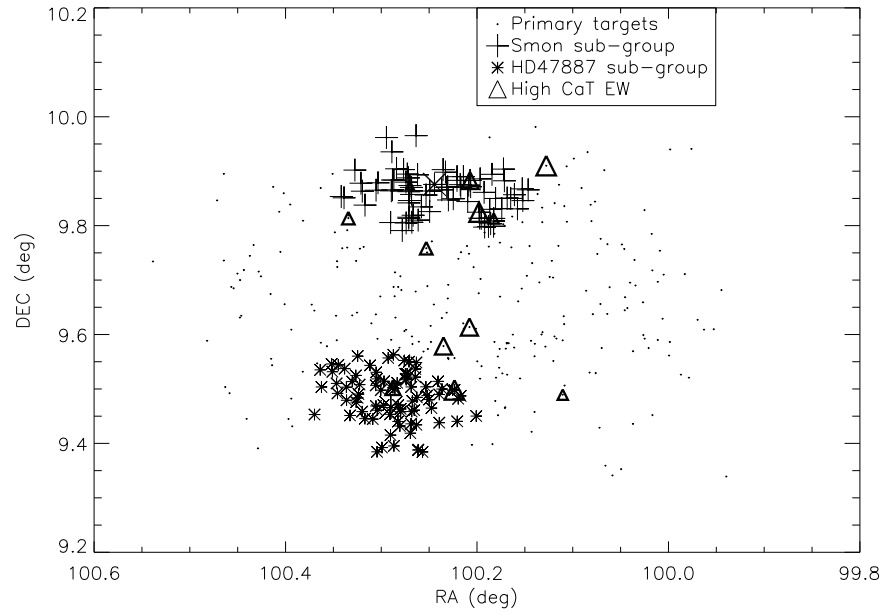


Figure 5.16: The positions of the primary targets, the targets around S Mon, the targets around HD 47887, and finally the targets showing accretion signatures. The size of the triangles (targets showing accretion signatures) is proportional to their RV.

5.5 Summary

NGC 2264 is complex cluster with several known sub-clusters and varying distance and age estimations. The aim of the work in this chapter was to use the data obtained for NGC 2264 to investigate gradients or structure in the cluster. The results presented in this chapter continue the complexity of the cluster dynamics.

The analysis in this chapter has provided both quantitative and qualitative additions to the knowledge of structure in NGC 2264. The analysis is based on an independent dataset that has not previously been analysed, and considers fainter stars than many other studies of structure in NGC 2264 (e.g. Teixeira et al. 2012).

The main results are as follows;

- Gradients were found when comparing the RVs with DEC, $R \sin i$ and HR diagram age, of $3.8 \pm 1.3 \text{ km(s deg)}^{-1}$, $0.74 \pm 0.28 \text{ km/s}$ and $-1.4 \pm 0.58 \text{ km/s}$, re-

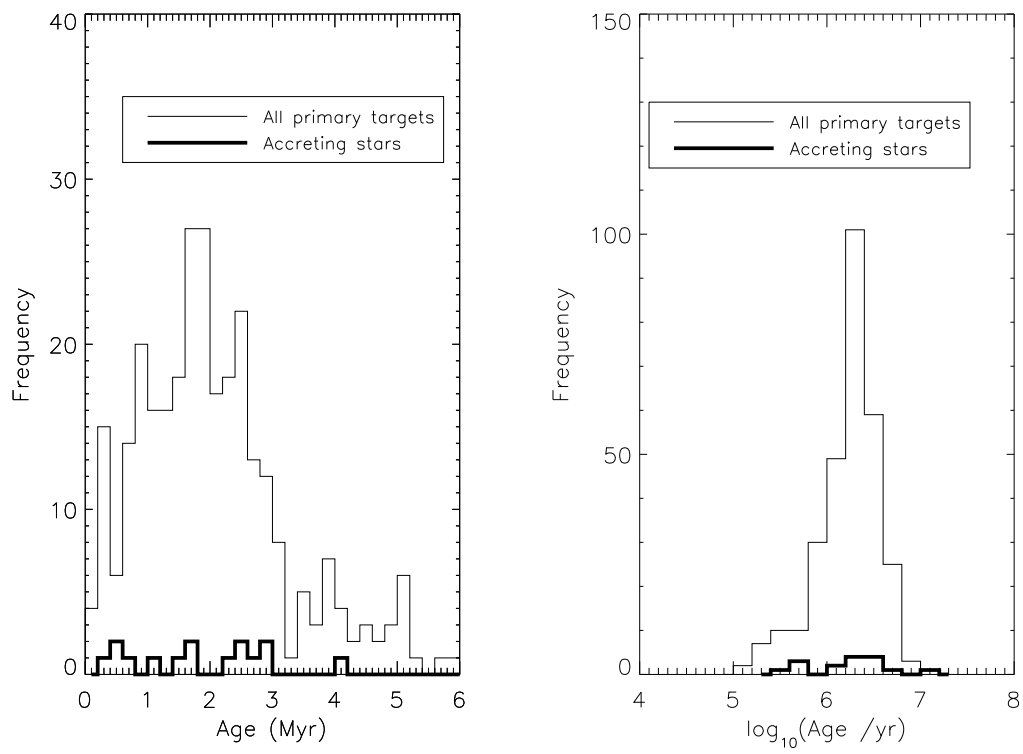


Figure 5.17: Histograms showing the age and \log_{10} age of the primary targets and those which are assumed to be accreting according to their CaT line strengths.

spectively (section 5.2.1).

- Differences in ages, and age distributions were found between a group of stars with low RVs (group 1), which had mean $R \sin i$ and HR diagram ages that were older than the mean ages for the remaining cluster stars, and had a higher mean target separation (\tilde{s}) than found in other RV groups (section 5.2.2)
- A group of stars with high RVs were found that had similar $R \sin i$ distributions, but different HR diagram age distributions when comparing with the distributions of the remaining cluster stars. A shift in the distance to 632^{+30}_{-29} pc used to place these stars on the HR diagram was required to bring the HR diagram distributions into agreement with the stars in groups 2 and 3 (section 5.2.2).
- The group of ~ 70 stars around the bright star, HD 47887, had $R \sin i$ and HR diagram age distributions that showed a low-probability of being drawn from the same parent population as the remaining cluster stars, when comparing the distributions with KS tests (section 5.3).

The implications of the results found in this chapter and the previous chapters are discussed in chapter 6. Future work on this topic could include kinematic subsamples selected by other disc or youth indicators such as X-ray emitters or H α EWs.

6 Discussion and recommendations for future work

This thesis is focussed on exploring the ages and kinematics of stars in NGC 2264. The main aim was to more fully understand the nature of the cluster, and to investigate any scenarios that may help to understand early star formation or stellar evolution within the cluster. More specifically, our questions were concerned with whether there are radius spreads determined from $v \sin i$ s and rotation periods, or whether a spread of radii is consistent with a coeval population. We were also interested in whether the observed radius distributions resembled the radius distributions inferred from the HR diagram. The data were compared with several models to answer these questions and in most cases, the results suggested a spread of normalised radius that is not consistent with a coeval population. Structure within the cluster was then explored to determine whether any sub-groups or gradients could explain the radii (or age) spreads. Evidence of a spatio-kinematic relationship was found, which suggests that the cluster has not fully relaxed, and began life in a structured way. In this chapter, the results of this thesis are summarised and discussed, and recommendations for future work are provided.

6.1 Implications for NGC 2264

6.1.1 Ages and age spreads

The age of NGC 2264 From chapter 4, projected radii of stars were measured using their rotation periods and $v \sin i$ s. This method is distance-independent and is also insensitive to the assumed extinction. The mean $\log_{10}(\text{ages/yr})$ established from the $(R \sin i)_{\text{obs}}/R_{3\text{Myr}}$ distributions (section 4.5) were between 6.02 and 6.41 (or 1.0Myrs and 2.6Myrs), depending on the choice of evolutionary models. A motivation for this work was to explore an alternative method to measure the ages and age spreads of

young stars, considering the known issues with the more commonly used method of drawing ages from the HR diagram (see sections 1.2.5 and 1.5.2). However, the ages agree well with many presented in the literature, which used the HR diagram method of measuring ages. These include work by Sung, Bessell & Lee (1997) and Park et al. (2000) (using isochrones from Baraffe et al. 1998-II, see Table 1.2) who both used a distance of 760pc to construct HR diagrams. Particularly, Mariñas et al. (2013) used the SDF00 isochrones (also used in this thesis), and a distance of 780pc to construct the HR diagram and estimated a mean cluster age of 1 Myr. This is lower than that found in section 4.5 when using the same set of isochrones (2.6Myrs), however, the data used by Mariñas et al. (2013) covered a much larger range of spectral types (A8–M8) and used individual extinctions to construct the HR diagram.

The ages found in this thesis, however, are younger than that found by Mayne & Naylor 2008 (3Myrs) who use main-sequence stars, and considerably younger than 5.5Myrs found by Turner (2012), who re-analysed photometry of B-type stars and measured ages from a colour-magnitude diagram using the Palla, Stahler & Parigi (1993) models. These stars have higher masses than the stars in used in this thesis, so the differences in ages between the high and low-mass samples could be due to a problem with evolutionary models at lower masses, or alternatively it could indicate that the high mass stars form first. Ultimately, whether using distance-independent, or distance-dependent methods of measuring ages in young clusters, a significant limitation lies with the use of pre-MS evolutionary models, which when used along with the positions of stars on the HR or colour-magnitude diagram, allow a range of mean ages for the same group of stars to be inferred, or can give a range of ages for an individual star at the same T_{eff} . A second limitation of HR diagram ages is the measurements of the distances to stars in the cluster, but the Gaia mission will reduce this problem significantly (see section 6.2).

Distance to NGC 2264 The distances presented in the literature vary significantly for NGC 2264, depending on the sets of stars used in the measurements. For example, a distance of ~ 400 pc was found by Dzib et al. (2014) using early-type stars, and a dis-

tance of 913pc (with uncertainties of 40pc and 110pc corresponding to sampling and systematic effects) was found by Baxter et al. (2009) using mostly K and M type stars. The latter study used a luminosity-independent technique of measuring the distance, (the observed distribution of the inclination angle of stars in the cluster was modelled and compared with distance-dependent values of $\sin i$. They adjusted the distance assumed to the observed $\sin i$ distribution until it matched the modelled distribution). In section 4.5.7, we used a similar method and compared the distribution of $(R \sin i)_{\text{obs}}/R_{3\text{Myr}}$ with the distributions of radii estimated from their HR diagram ages. The radius distribution determined from the HR diagram ages was adjusted to match the distribution of $(R \sin i)_{\text{obs}}/R_{3\text{Myr}}$. This allowed an estimate of the distance to the cluster to be made. These distances are precise, and do not vary greatly between the evolutionary models. The distances measured in section 4.5.7 are $740 < D(\text{pc}) < 772$, $740 < D(\text{pc}) < 781$ and $770 < D(\text{pc}) < 805$ corresponding to the Dartmouth, DAM97 and SDF00 isochrones, respectively. A binary fraction of 0.5 was assumed and a distance of 770pc was found to be acceptable within a 90% confidence range for all sets of evolutionary models used, agreeing well with that presented in Sung, Bessell & Lee (1997) and Turner (2012) (see section 1.5.1) and is marginally closer (25pc) than that from Baxter et al. (2009) given the closest distance allowed within their uncertainty range.

Age spreads in NGC 2264 In chapter 4, some evidence for radius spreads at a given T_{eff} was found, and if this is interpreted as an age spread, then a coeval age was ruled out at >90% confidence using two sets of evolutionary models. Although the work in this section is strongly model-dependent, the results set an upper 90% limit to the radius spread of 0.19dex, which agrees well between all three sets of evolutionary models. Using a model representing the accelerating star formation scenario (Palla & Stahler 1999) we were able to rule out instantaneous star formation with >90% confidence. ‘Best-fitting’ age spreads of 0.2 and 0.46 dex were also found, when modelling the $(R \sin i)_{\text{obs}}/R_{3\text{Myr}}$ in terms of a log-normal age distribution, but are strongly model dependent and an upper limit to the age spread was found as 0.66 dex (using

the DAM97 isochrones, 0.32 and 0.46 using the SDF00 and Dartmouth isochrones, respectively). The $R \sin i$ distributions can be reproduced well by assuming that the stars have the age distribution implied by their positions in the HR diagram, (when assuming a binary fraction of 0.5 and a cluster distance of 770pc).

The research in this thesis supports the view that stars in NGC 2264 have a spread of radii at a given T_{eff} that may not be consistent with a coeval population. The exact form of the dispersion, however, cannot be determined, due to the lack of age resolution inherent to the projected radius technique. An alternative interpretation of our results is that the radius of a pre-MS star is not a direct indicator of its age, and that the differing radii for stars at a given T_{eff} could be the result of varying accretion histories in the protostellar stage of star formation (e.g. Tout, Livio & Bonnell 1999, Baraffe, Chabrier & Gallardo 2009, Baraffe, Vorobyov & Chabrier 2012, Vorobyov & Basu 2015). However, we note that Hosokawa, Offner & Krumholz (2011), argue that theoretically, this process of early accretion is incapable of explaining the luminosity spread of pre-MS stars. They find that non-accreting isochrones can overestimate stellar ages for stars with $T_{\text{eff}} > 3500\text{K}$, explaining why there are sometimes systematic age differences between more and less massive stars in the same cluster, concluding that the inferred ages and spreads from the HR diagram for cool stars are, in fact, reliable, assuming the observed bolometric luminosities and effective temperatures are accurate. Work by Padoan, Haugbølle & Nordlund (2014) show that infall rates in turbulent clouds are comparable to accretion rates inferred from protostellar luminosities or measured in pre-main-sequence stars, and the authors claim that the luminosity problem is solved once evolutionary models account for realistic protostellar infall histories, with no need for extreme accretion episodes.

A problem with the technique that has been deployed in this thesis is that the results are model dependent. When using the Dartmouth sets of isochrones to model the spread of radii, a coeval cluster age could not be ruled out with a high level confidence. The reasons behind this are discussed by Baraffe et al. (2002), who show that there are significant differences in the pre-MS models of stars $< 1\text{ Myr}$ due to the sensitivity of the models to the input parameters. The effect is that different sets of

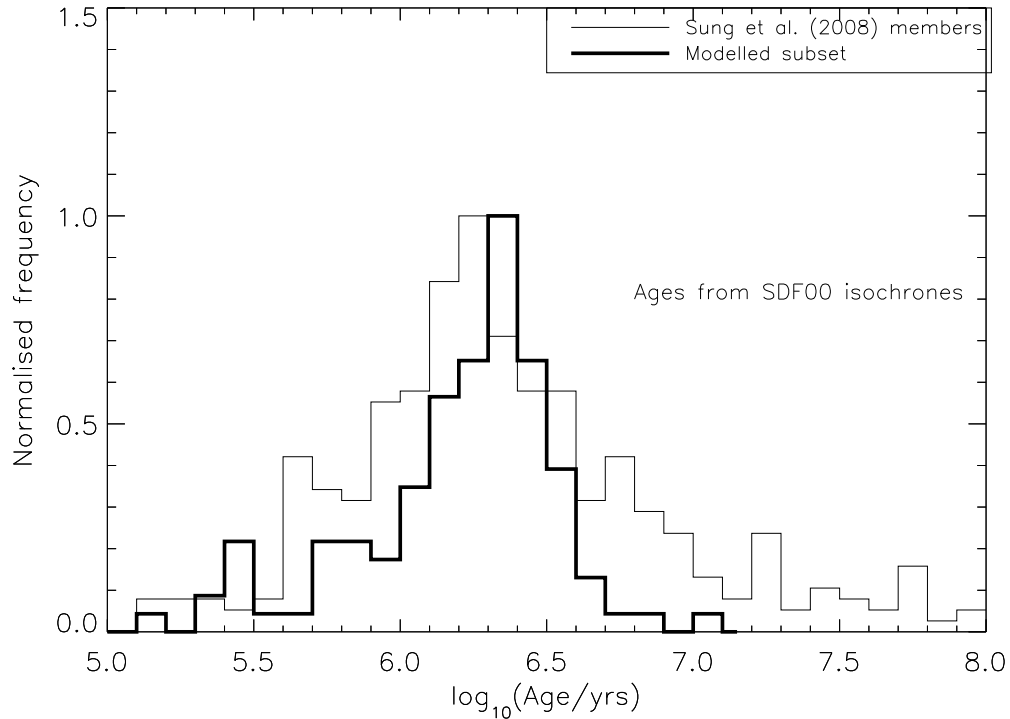


Figure 6.1: The distribution of ages of the sample of stars used in the modelling of the radius distribution compared with the larger sample from Sung et al. (2008).

evolutionary isochrones have different time dependencies for their radius evolution.

Limitations of this work include biases in the sample (in that the stars must be bright enough to obtain spectroscopy), and only stars with measurable rotation periods could be included. The sample of stars used in this thesis lacks a tail of older stars (see Figure 6.1), so the spreads in radii inferred from the $(R \sin i)_{\text{obs}}/R_{3\text{Myr}}$ distributions are likely to be lower limits to the actual radius spread and the mean ages are likely to be underestimated from the $(R \sin i)_{\text{obs}}/R_{3\text{Myr}}$ distribution. The models account for the possible absence of stars with low $v \sin i$ s by applying a lower limit to the $v \sin i$ s which are included in the models, but the sample possibly lacks stars with very high $v \sin i$ s as their cross-correlation peaks were, in some cases, unmeasurable (section

3.4.2).

Hartmann, Ballesteros-Paredes & Bergin (2001) suggested that spreads in the HR diagram ages could be a combination of uncertainties from variability, differential reddening, binarity and the presence of interstellar disks. In section 4.5.7, we found that the radius distribution determined from the HR diagram ages is an acceptable fit to the $(R \sin i)_{\text{obs}}/R_{3\text{Myr}}$ distribution. One interpretation of this is that the ages from the HR diagram directly reflect their radii, and the measurement uncertainties in determining ages from the HR diagram (estimated as 0.16 in section 3.6.2) do not have a great effect on the HR diagram age dispersion, which we found to be $\sigma \log_{10} t = 0.4, 0.35,$ and 0.38dex , corresponding to the Dartmouth, DAM97 and SDF00 isochrones.

Despite the known problems with using the HR diagram to infer ages and age spreads for young stars, the inferred ages are far from meaningless, and allow star clusters to be ranked in terms of median ages and age spread. Comparing the results with those on the ONC by Jeffries (2007), the two clusters have similar ages when using the same method to measure the ages as used in chapter 4, with NGC 2264 being older than the ONC (which had $R \sin i \log(\text{age}/\text{Myr})$ of 5.88 and 6.25 corresponding to the DAM97 and SDF00 isochrones, respectively).

6.1.2 Structure and sub-clusters

It is well-known in the literature that NGC 2264 is both spatially and kinematically structured (e.g. Teixeira et al. 2012, Sung et al. 2008, Tobin et al. 2015, see chapter 1.5.4.). Chapter 5 of this thesis focused on exploring the extent of structure in the cluster. In this section, we discuss several scenarios; i) the cluster is structured kinematically, ii) there are several populations in the line-of-sight, iii) there have been separate star forming events in the northern and southern regions of the cluster.

i) Kinematic structure

The cluster has been kinematically resolved and its overall RV dispersion (3.55km/s) is much larger than the uncertainties in the RV measurements ($\sim 0.68\text{km/s}$). Signifi-

cant gradients were found when comparing RV with DEC, $(R \sin i)_{\text{obs}}/R_{3\text{Myr}}$ and HR diagram age, of $3.8 \pm 1.3 \text{ km/s (deg)}^{-1}$, $0.74 \pm 0.28 \text{ km/s}$ and $-1.4 \pm 0.58 \text{ km/s}$, respectively (section 5.2.1). A decline in the mean separation of stars was also found, when grouping the targets according to their RV. These results suggest that the cluster may have been born with significant substructure, and has not had sufficient time to dynamically relax. Simulations by Baumgardt & Kroupa (2007) have shown that the removal of gas in the cluster in less than the free-fall time can lead to the dispersion of most of the cluster stars, resulting in a bound remnant of stars surrounded by an expanding halo of stars, which are stable against expansion through stellar evolution (Gieles 2010). Gas expulsion leading to a bound remnant would not lead to the kind of structure seen in NGC 2264, in which star formation is expected to happen over a significant duration.

Some evidence for kinematic sub-structure was found (section 5.2.2). A group of stars with lower RVs on average than the rest of the cluster stars, were older by $\sim 0.1 \text{ dex}$, according to both their $(R \sin i)_{\text{obs}}/R_{3\text{Myr}}$ ages and HR diagram ages. This is supported by the higher mean separation of stars in this group, which could suggest that they have had more time to disperse. Sung & Bessell (2010) also found a halo population of stars distributed throughout the cluster, supporting this scenario.

The kinematic structure of NGC 2264 shows a similarity to the structure found in other clusters, such as the ONC, where a velocity gradient with position and a blue-shifted population was found, with a high degree of agreement between the gaseous and stellar components (Fűrész et al. 2008; Tobin et al. 2009; Tobin et al. 2015).

ii) *Line-of-sight populations*

The large range of distances measured to the cluster for different groups of stars suggests that there may be several populations in the line-of sight. For example a distance of $\sim 400 \text{ pc}$ was found by Dzib et al. (2014) using early-type stars, and 913 pc by Baxter et al. (2009) using mainly late-type stars. We have found some evidence which may support this scenario. A possible foreground population of stars with higher average RVs than the remaining cluster stars was found (group 4, section 5.2.2).

By adjusting the distance used to create the HR diagram until the HR diagram

age distribution of group 4 agreed with age distributions of groups 2 and 3, an approximate distance to group 4 was estimated. If we assume that this population is the same age as groups 2 and 3, (as suggested by the similarity in $(R \sin i)_{\text{obs}}/R_{3\text{Myr}}$ distributions) then a shift in assumed distance to 632_{-29}^{+30}pc allows the HR diagram age distributions to agree. This result agrees with work by Fűrész et al. (2006) who also found a red-shifted population of stars in NGC 2264.

However, the stars in group 4 are less dispersed than in the other groups, possibly indicating that they are younger than the other stars. If so, they could be more embedded in the molecular gas, so could be more highly extinguished by the molecular cloud, so the assumption that the extinction is constant across the cluster would be invalid. This is unlikely as we did not find evidence for gradients in extinction in section 3.5.1.

It is possible that the primary sample of stars in this thesis includes a spatial bias caused by the limitations of fibre spectroscopy in positioning fibres on closely spaced targets. The effect that this bias could have on the results is to exclude stars that are situated closely together, affecting dense regions more than the less dense regions, and resulting in group 4 being even less dispersed than observed. This would further support our suggestion of a younger high-RV population. Individual distances to stars in the cluster are required to draw stronger conclusions from this work (see section 6.2).

iii) *Separate star formation events in the northern and southern regions*

There are clear areas of more dense gas in the region of the massive star, S Mon, and in the southern region around the Cone Nebula (see Figure 5.5). The results in this thesis showed that a group of stars around S Mon were not significantly different in age as the southern (HD 47887) group, from their mean $(R \sin i)_{\text{obs}}/R_{3\text{Myr}}$ ages, and their HR diagram age distributions. The group around HD 47887, however, has a low probability of being drawn from the same parent population as the stars in the rest of the cluster, according to both the $(R \sin i)_{\text{obs}}/R_{3\text{Myr}}$ distribution and the HR diagram age distribution.

We found no trend in the presence or absence of youth indicators based on CaT

EWs with position on the sky, but the sample was too small to draw strong conclusions, and would benefit from a much larger dataset of accreting stars.. However, WTTSs are preferentially selected in the primary sample. The effect that this could have on the results is to make the cluster appear older than its true age, and could potentially be hiding groups of younger CTTS which have not been included in the primary sample.

Sung & Bessell (2010) and Teixeira et al. (2012) found spatial substructure relating to these distinct areas of the cluster. Sung, Stauffer & Bessell (2009) found three sub-groups of stars, and found that the stars near to S Mon were older than the stars in the southern half of the cluster (near to the Cone Nebula or HD 47887). Although we found that the group of stars around S Mon were marginally older than the southern group, the error bars on these ages were too large to confidently comment on whether the groups have different ages. A result found by Barentsen (2012) shows that the median age of stars around S Mon and the Cone Nebula did not have statistically significant age differences (2.9Myrs and 2.6Myrs, respectively) and could be consistent within the uncertainties. However, they found a lower frequency of accretors in the S Mon region, suggesting that the stars in this region are more evolved, on average, than the stars around the Cone Nebula.

Research by Kroupa (2007) and Weidner & Kroupa (2006) suggests that there may be an organisation in the formation of stars within a cluster, starting from the least massive to the most massive stars. In this scenario, the pre-cluster core undergoes gravitational contraction, and the gas densities and local fluctuations in the turbulent medium ultimately lead to low-mass star formation. During contraction, and prior to feedback from the young stars disrupting the cloud, star formation activity increases in density fluctuations. This process stops when the massive stars supply sufficient feedback to disrupt the cloud. It could be the case in NGC 2264 that most of the low-mass cluster stars were formed first, followed by the massive stars, such as S Mon, which further triggered star formation in the background cloud (also suggested by Tobin et al. 2015). Adams et al. (1983) suggest that sequential star formation has occurred beginning with the low-mass stars and continuing with the massive star formation of cluster members.

We can conclude with a high level of confidence that although the mean ages of stars in the northern and southern groups are similar, the $(R \sin i)_{\text{obs}}/R_{3\text{Myr}}$ and HR diagram ages distributions of those stars in the group around the massive star, HD 47887 are not well-representative of the rest of the cluster stars.

6.1.3 Radius spreads caused by structure

One of the purposes of this work was to determine the cause of any possible dispersion in radius at a given T_{eff} in the cluster. There is currently considerable debate about the timescale for stars to form in clusters. The rapid star formation model, where turbulence in molecular clouds is dissipated quickly, and which allows free-fall collapse on short timescales, argues for a short star formation timescale (Hartmann 2001). Age spreads in NGC 2264 could support an alternative view, that turbulence is regenerated or cloud collapse is moderated by magnetic fields.

Chapter 4 shows that there may be a radius spread amongst stars of the same T_{eff} and that this spread is consistent with the ages inferred from the HR diagram. This is a valuable result since the $R \sin i$ data are insensitive to errors in the individual extinction to the stars, variability and binarity, which inflate age dispersion seen in the HR diagrams. Unfortunately, our sample of stars is too small to definitely measure the age spread in this way, however, an upper limit of 0.19dex on the radius spread at 90% confidence, was measured.

In chapter 5, evidence was uncovered for non-coevality between different subgroups, either separated by spatial position or RV. Although the differences in the mean ages of these groups (as judged by their $R \sin i$ distributions) was small, there are significant differences between the $(R \sin i)_{\text{obs}}/R_{3\text{Myr}}$ distributions which suggest the differences are real. The effect of this will be to cause some of the radius or age spread seen in the entire sample of stars. As these separate subsamples may represent different star formation events, these may in part be responsible for the age spreads inferred from the HR diagrams, although the mean age differences seem too small to entirely account for this.

6.2 Future work

The Gaia mission will chart a 3-dimensional map of the Galaxy, to reveal the composition, and formation of the Milky Way. The mission will provide precise positions for $\sim 1\%$ of the galactic stellar population, with accuracies required to build a stereoscopic and kinematic census of the population (Perryman 2005, Lindegren et al. 2008). Positions and proper motions for stars with $V < 17$ (mag) with precisions better than $40\mu\text{as}$ and $30\mu\text{as yr}^{-1}$, and parallax data with $55\mu\text{as}$ (Lindegren et al. 2008) should be achieved. The data which will be obtained by the Gaia satellite has the necessary precision to quantify early formation, and chemical and dynamical star formation and evolution of the Milky Way. The tangential velocities will provide a relationship to be studied between the velocity and position of stars, hence could reveal the expansion or contraction of clusters. The precisions obtained with Gaia will make measuring distances to individual stars in NGC 2264 possible, which obviates uncertainties from extinction and reddening.

The Gaia mission is supported by the Gaia-ESO public spectroscopic survey (Gilmore et al. 2012), targeting $>10^5$ stars, which obtained precise RVs and chemical abundances for many of the stars observed with Gaia. The Gaia-ESO survey covers the bulge, thick and thin discs, halo, and open clusters of all ages and masses using the Giraffe and UVES spectrograph. The spectra quantify individual elemental stellar abundances, and yield precise RVs, which can be used to probe kinematic gradients and structure throughout the Milky Way, in order to follow the formation, and evolution of clusters. NGC 2264 is one of the ~ 30 young ($<100\text{Myrs}$) clusters in the solar neighborhood ($<1500\text{pc}$, in the range of Gaia where will obtain transverse velocities) which have been observed as part of the Gaia-ESO survey. Many stars used in this thesis have been observed as part of the survey. An interesting follow-up study would be to obtain gravity signatures such as sodium lines, and to determine whether these correlated with radius and age in the expected way. The Gaia-ESO survey data should yield gravity sensitive indicators.

Ultimately, the work in this thesis has been highly focussed on one star forming

region, and it is unknown whether this region is representative of all star clusters in the Galaxy. To put this work into context, the research in this thesis could be repeated on other young clusters. The $R \sin i$ study used in this thesis was firstly performed on the ONC by Jeffries (2007). There are many other young clusters for which this study could be performed, which already have, or will soon have many measured rotation speeds and periods. An example of a cluster that has been observed as part of the Gaia-ESO survey is ρ Oph, which has an age of 2.1 Myr (Wilking et al. 2005), and has many known rotation periods from Parks et al. (2014) and Alves de Oliveira & Casali (2008). The Gaia-ESO survey will provide spectra for 223 stars in the cluster, 35 of which have been classified as T-Tauri stars (Lanzafame et al. 2015).

The Gaia-ESO survey has also obtained data with the required precision to determine the possibility and extent of kinematic structure in young clusters, and work on γ Velorum by Jeffries et al. (2014) has recently revealed kinematic structure in the cluster. Two examples of young clusters observed in the survey that have RVs of the required precision to determine kinematic structure are NGC 3293 and Chamaeleon I, both of which are aged ≤ 10 Myrs.

6.3 Thesis summary

In summary, the ages, radius and age spreads, and structure have been explored for stars in NGC 2264. A method used to measure ages and age spreads which is independent of distance, and therefore, circumvents some of the uncertainties associated with measuring ages from the HR diagram was used. This involved measuring the $R \sin i$ s of stars from their $v \sin i$ s and rotation periods, and modelling the radii and age distributions in a variety of ways. An upper limit to the radius spread was found (0.19 dex) using three sets of evolutionary models, and the $\log_{10}(\text{age}/\text{yrs})$ of the cluster was measured as 6.02-6.41. We were able to rule out instantaneous star formation with a high-level of confidence when modelling the radii as an exponential distribution of ages, reflecting the accelerating star formation scenario (Palla & Stahler 2000). When

assuming a binary fraction of 0.5, we have found the distance to the cluster of 770pc, which agrees between three sets of isochrones with a high-level of confidence.

Some evidence has been found of a non-coeval cluster age when using two sets of evolutionary models. Gradients have been found when comparing RV with Declination, $(R \sin i)_{\text{obs}}/R_{3\text{Myr}}$ and HR diagram age of $3.8 \pm 1.3 \text{ km(s deg)}^{-1}$, $0.74 \pm 0.28 \text{ km/s}$ and $-1.4 \pm 0.58 \text{ km/s}$, respectively. There is a decline in the mean separation of targets with RV when separating the targets into four groups based on their RV. A group of stars with high RVs has been found, which could possibly be a foreground group of stars at $\sim 632_{-29}^{+30} \text{ pc}$, assuming that they are the same age as the rest of the cluster stars. Since the age differences between sub-groups is small, we conclude that any substructure is not the only contributing factor to a spread of radii or ages.

A Appendix 1

The catalog of stars used in this thesis are shown in table A1. The table shows the results for 547 targets in NGC 2264 with resolved RVs, $v \sin i_s > 8 \text{ km/s}$ and signal-to-noise ratio of > 5 . The photometry in the table is from either Lamm et al. (2004) (object name succeeded by ‘l’), Makidon et al. (2004) (object name succeeded by ‘m’) or Sung, Stauffer & Bessell (2009), along with the RA and DEC. The name was produced by the pipeline and corresponds to primary targets (NGC) or secondary targets (NGA or NGB). The RV and $v \sin i_s$, along with their uncertainties are those described in sections 3.4.2 and 3.4.3.

For targets with repeated observations table A1 provides the weighted means of the RV and $v \sin i_s$ according to their errors. The reduction blocks and the dates and contents of these are shown in chapter 3, table 3.1.

Object Name	RA (deg)	DEC (deg)	I (mag)	SNR	RV (km/s)	$v \sin i$ (km/s)
NGB_06405220+0952313	100.3997	9.4525	14.4	71.21	31.58 ± 0.55	8.06 ± 0.50
NGB_06420302+0934131	100.5125	9.5705	13.7	116.4	38.54 ± 0.54	8.07 ± 0.49
NGA_06403720+0931098	100.1550	9.5193	14.0	65.24	20.43 ± 0.56	8.07 ± 0.50
NGC_46151	100.1768	9.5390	14.1	86.61	17.99 ± 0.55	8.09 ± 0.50
NGC_59271	100.2759	9.5524	16.1	27.85	21.73 ± 0.64	8.14 ± 0.52
NGB_06405532+0939585	100.2305	9.6663	15.0	27.27	20.76 ± 0.64	8.15 ± 0.53
NGB_06411031+0921494	100.2929	9.3637	14.1	81.26	18.69 ± 0.55	8.15 ± 0.50
NGB_06410966+0948202	100.2902	9.8056	15.0	32.45	20.10 ± 0.61	8.17 ± 0.52
NGB_06395659+0947141	99.98579	9.7872	15.1	38.06	2.59 ± 0.59	8.17 ± 0.51
NGB_06405367+0958000	99.95029	9.9365	14.4	53.50	88.51 ± 0.57	8.20 ± 0.51
NGA_06410169+0921055	100.2570	9.3515	13.3	77.76	26.70 ± 0.55	8.21 ± 0.50
NGC_41881	100.1525	9.8063	14.0	106.9	20.20 ± 0.54	8.23 ± 0.50
NGC_59141	100.2748	9.5277	16.2	41.92	24.64 ± 0.58	8.23 ± 0.51
NGC_65031	100.3407	9.7585	13.9	106.9	20.65 ± 0.54	8.25 ± 0.50
NGC_77141	100.4053	9.7518	14.0	103.2	18.04 ± 0.54	8.29 ± 0.50
NGC_3321m	100.2471	9.7712	14.1	98.71	26.57 ± 0.54	8.30 ± 0.50
NGC_55521	100.2350	9.5789	18.2	9.86	21.33 ± 1.14	8.33 ± 0.72
NGC_46101	100.1763	9.5736	15.7	55.31	18.44 ± 0.56	8.35 ± 0.51
NGB_06413816+0957464	100.4090	9.9629	13.3	150.6	90.95 ± 0.54	8.35 ± 0.50
NGB_06395559+0935181	99.98162	9.5883	12.8	61.94	30.22 ± 0.56	8.36 ± 0.51
NGB_06404506+0951272	99.97291	9.8891	14.8	52.23	45.83 ± 0.57	8.38 ± 0.51
NGC_60081	100.2851	9.6312	16.7	16.99	16.77 ± 0.79	8.39 ± 0.59
NGC_3651m	100.2945	9.9617	14.8	61.94	23.33 ± 0.56	8.42 ± 0.51
NGC_46381	100.1782	9.5597	15.1	59.63	16.70 ± 0.56	8.47 ± 0.52
NGC_44431	100.1668	9.5841	13.2	122.3	17.74 ± 0.54	8.51 ± 0.51
NGA_06405059+0954573	100.2107	9.9159	13.2	133.5	20.73 ± 0.54	8.53 ± 0.51
NGB_06401979+0920333	100.0824	9.3426	15.1	53.19	-3.4 ± 0.57	8.57 ± 0.52
NGC_60391	100.2878	9.5025	14.4	71.29	20.77 ± 0.55	8.64 ± 0.52

Table A.1 – continued from previous page

Object Name	RA	DEC	I (mag)	SNR	RV (km/s)	$v \sin i$ (km/s)
NGC_5413l	100.2254	9.4975	15.2	51.81	19.45 ± 0.57	8.64 ± 0.53
NGB_06395022+0958171	99.95925	9.9714	14.1	77.40	87.30 ± 0.55	8.68 ± 0.52
NGA_06404936+0952539	100.2056	9.8816	0.00	44.95	24.63 ± 0.58	8.73 ± 0.53
NGB_06413927+0951444	100.4136	9.8624	15.1	36.84	83.19 ± 0.60	8.74 ± 0.54
NGC_6042l	100.2882	9.8658	16.9	27.35	20.42 ± 0.65	8.74 ± 0.56
NGC_5361l	100.2208	9.8898	17.1	17.22	23.22 ± 0.79	8.77 ± 0.61
NGC_8328l	100.4288	9.3910	15.6	43.83	17.74 ± 0.58	8.82 ± 0.54
NGC_4517l	100.1709	9.7993	14.3	99.77	20.64 ± 0.54	8.85 ± 0.53
NGA_06411475+0934134	100.3114	9.5703	0.00	72.75	20.16 ± 0.55	8.86 ± 0.53
NGC_4345l	100.1609	9.8568	18.2	14.44	25.59 ± 0.88	8.87 ± 0.65
NGC_4676l	100.1806	9.8498	13.5	139.5	20.50 ± 0.54	8.90 ± 0.53
NGC_4777l	100.1857	9.8035	13.7	127.2	21.28 ± 0.54	8.92 ± 0.53
NGC_4511l	100.1708	9.4650	14.9	58.58	18.54 ± 0.56	8.93 ± 0.54
NGC_3276m	100.2407	9.5139	14.4	61.86	24.68 ± 0.56	8.96 ± 0.54
NGB_06420843+0933212	100.5351	9.5560	12.7	226.6	38.85 ± 0.54	9.01 ± 0.53
NGC_1748l	100.0265	9.6593	13.6	118.8	16.05 ± 0.54	9.01 ± 0.53
NGC_6407l	100.3326	9.4513	15.3	51.33	18.92 ± 0.57	9.05 ± 0.54
NGB_06414780+0934090	100.4491	9.5693	12.8	169.5	26.35 ± 0.54	9.06 ± 0.53
NGC_4118l	100.1479	9.7078	16.0	45.15	15.40 ± 0.58	9.10 ± 0.55
NGB_06395865+0921343	99.99437	9.3596	15.1	50.43	55.59 ± 0.57	9.13 ± 0.55
NGC_5301l	100.2170	9.8705	14.2	90.82	20.99 ± 0.55	9.13 ± 0.54
NGB_06402347+0959232	100.0977	9.9897	13.3	151.0	38.41 ± 0.54	9.16 ± 0.54
NGC_5791l	100.2640	9.6791	14.1	83.00	19.13 ± 0.55	9.18 ± 0.54
NGA_06395683+0944251	99.98679	9.7403	0.00	336.3	21.87 ± 0.54	9.20 ± 0.54
NGA_06404321+0947072	100.1800	9.7853	0.00	102.3	19.17 ± 0.54	9.21 ± 0.54
NGB_06395328+0949454	99.97200	9.8293	15.1	44.54	19.26 ± 0.58	9.21 ± 0.55
NGB_06403489+0954070	100.4824	9.6661	15.1	53.05	17.35 ± 0.57	9.22 ± 0.55
NGB_06405275+0943000	100.2197	9.7167	15.0	41.97	21.23 ± 0.59	9.23 ± 0.56

Table A.1 – continued from previous page

Object Name	RA	DEC	I (mag)	SNR	RV (km/s)	$v \sin i$ (km/s)
NGC_2525m	100.1388	9.9813	14.8	67.68	20.12 ± 0.56	9.25 ± 0.55
NGC_5134l	100.2072	9.8829	15.7	48.35	20.01 ± 0.58	9.28 ± 0.55
NGB_06395060+0951292	99.96083	9.8581	14.0	104.0	72.84 ± 0.54	9.30 ± 0.54
NGC_6887l	100.3625	9.5036	15.2	56.03	20.16 ± 0.57	9.31 ± 0.55
NGA_06411889+0939440	100.3287	9.6622	13.6	79.97	28.98 ± 0.55	9.33 ± 0.55
NGC_4602l	100.1758	9.6697	14.1	85.86	19.13 ± 0.55	9.33 ± 0.55
NGB_06412621+0947222	100.0152	9.2880	14.5	38.81	74.34 ± 0.60	9.34 ± 0.56
NGC_5628l	100.2475	9.4648	17.4	16.86	21.66 ± 0.81	9.35 ± 0.65
NGC_4204m	100.3939	9.6090	15.1	64.42	20.76 ± 0.56	9.35 ± 0.55
NGC_6476l	100.3382	9.5373	15.4	64.79	19.89 ± 0.56	9.37 ± 0.55
NGC_6585l	100.3462	9.7347	16.2	38.75	20.37 ± 0.60	9.37 ± 0.57
NGC_5902l	100.2739	9.5170	13.5	97.17	21.77 ± 0.55	9.40 ± 0.55
NGC_8778l	100.4476	9.6312	15.2	63.69	18.97 ± 0.56	9.41 ± 0.55
NGC_4468l	100.1684	9.5263	17.2	14.77	17.92 ± 0.88	9.44 ± 0.68
NGC_5974l	100.2805	9.4319	13.7	79.47	19.10 ± 0.55	9.49 ± 0.55
NGC_5880l	100.2712	9.8623	13.8	108.0	21.93 ± 0.54	9.55 ± 0.55
NGA_06404600+0917582	100.1916	9.2995	14.2	54.66	16.20 ± 0.57	9.62 ± 0.56
NGB_06395606+0958505	99.98358	9.9805	15.0	36.21	57.22 ± 0.61	9.72 ± 0.58
NGC_8518l	100.4372	9.7445	14.3	95.08	18.36 ± 0.55	9.72 ± 0.56
NGB_06401376+0952060	100.0573	9.8685	12.7	144.7	27.25 ± 0.54	9.75 ± 0.56
NGC_1317l	100.0111	9.6968	15.3	54.16	19.29 ± 0.57	9.75 ± 0.57
NGC_4503l	100.1704	9.4665	15.2	54.07	18.61 ± 0.57	9.76 ± 0.57
NGC_5263l	100.2144	9.6206	14.9	65.49	17.50 ± 0.56	9.79 ± 0.57
NGB_06393733+0926373	99.90554	9.4437	12.6	143.6	40.92 ± 0.54	9.83 ± 0.56
NGB_06411330+0951545	100.4349	9.5096	14.7	60.14	136.7 ± 0.56	9.91 ± 0.57
NGB_06414131+0956282	100.1407	9.8121	14.3	74.73	16.11 ± 0.55	9.93 ± 0.57
NGB_06400544+0947434	100.0226	9.7955	14.4	103.8	83.39 ± 0.54	9.94 ± 0.57
NGA_06395232+0919094	99.96800	9.3192	13.6	101.0	30.50 ± 0.54	10.01 ± 0.57

Table A.1 – continued from previous page

Object Name	RA	DEC	I (mag)	SNR	RV (km/s)	$v \sin i$ (km/s)
NGC_3434m	100.2636	9.9652	14.1	92.49	19.31 ± 0.55	10.03 ± 0.57
NGB_06420692+0924444	100.5288	9.4122	14.1	72.39	31.49 ± 0.55	10.05 ± 0.58
NGB_06415272+0929252	100.4696	9.4902	14.3	93.55	55.24 ± 0.55	10.08 ± 0.57
NGC_6685l	100.3510	9.5316	14.0	110.3	21.17 ± 0.54	10.10 ± 0.57
NGA_06403636+0922445	100.1515	9.3790	13.5	116.3	27.73 ± 0.54	10.13 ± 0.57
NGC_4896l	100.1925	9.8611	16.4	37.04	26.96 ± 0.61	10.15 ± 0.60
NGC_3972l	100.1398	9.5600	16.0	47.44	20.61 ± 0.58	10.15 ± 0.59
NGB_06394364+0924484	99.93183	9.4133	14.1	75.40	74.40 ± 0.55	10.15 ± 0.58
NGB_06420044+0926323	100.0740	9.3837	14.9	42.37	72.00 ± 0.59	10.20 ± 0.60
NGA_06394819+0959057	99.95079	9.9849	12.5	223.1	28.09 ± 0.54	10.29 ± 0.58
NGA_06403878+0921382	100.1615	9.3606	13.3	60.78	20.25 ± 0.56	10.30 ± 0.59
NGB_06402564+0959595	100.1068	9.9999	15.1	47.85	18.84 ± 0.58	10.30 ± 0.60
NGB_06395699+0949252	99.98745	9.8236	14.1	76.86	2.70 ± 0.55	10.33 ± 0.59
NGC_6260l	100.3183	9.7610	16.3	38.12	22.15 ± 0.60	10.34 ± 0.61
NGC_4271l	100.1570	9.6610	15.0	62.85	17.39 ± 0.56	10.37 ± 0.59
NGC_9482l	100.4714	9.8465	14.0	98.80	21.43 ± 0.55	10.39 ± 0.59
NGA_06401417+0934283	100.0590	9.5745	15.2	59.23	16.73 ± 0.56	10.39 ± 0.59
NGC_7906l	100.4129	9.8711	16.4	35.43	18.46 ± 0.61	10.40 ± 0.61
NGB_06405839+0927252	100.0975	9.9154	14.5	46.09	23.78 ± 0.58	10.41 ± 0.60
NGC_2484m	100.1326	9.6001	14.5	71.93	17.50 ± 0.56	10.44 ± 0.59
NGA_06403668+0922051	100.1528	9.3680	13.5	103.4	32.47 ± 0.54	10.46 ± 0.59
NGC_6126l	100.2992	9.3923	15.4	53.94	18.04 ± 0.57	10.47 ± 0.60
NGC_1177l	100.0050	9.7101	15.8	44.31	15.40 ± 0.59	10.49 ± 0.61
NGC_6175l	100.3053	9.5306	14.6	92.22	24.53 ± 0.55	10.49 ± 0.59
NGC_5303l	100.2170	9.4871	16.2	39.93	18.98 ± 0.60	10.51 ± 0.61
NGA_06405419+0955519	100.2257	9.9310	14.1	67.64	20.64 ± 0.56	10.60 ± 0.60
NGA_06403787+0934540	100.1577	9.5816	13.9	69.66	17.11 ± 0.56	10.61 ± 0.60
NGA_06405272+0928437	100.2196	9.4788	0.00	29.46	22.42 ± 0.65	10.65 ± 0.64

Table A.1 – continued from previous page

Object Name	RA	DEC	I (mag)	SNR	RV (km/s)	$v \sin i$ (km/s)
NGC_3666l	100.1240	9.7058	14.7	55.18	20.32 ± 0.57	10.69 ± 0.61
NGB_06414344+0956525	100.4310	9.9480	13.8	96.51	41.62 ± 0.55	10.69 ± 0.60
NGA_06401535+0942424	100.0639	9.7117	14.4	48.89	27.37 ± 0.58	10.70 ± 0.61
NGB_06413963+0941404	100.4151	9.6946	14.1	88.03	44.97 ± 0.55	10.71 ± 0.60
NGC_5856l	100.2687	9.8701	16.3	26.00	24.61 ± 0.68	10.72 ± 0.66
NGC_6024l	100.2868	9.8836	15.3	50.96	20.43 ± 0.58	10.75 ± 0.61
NGC_5903l	100.2740	9.6088	16.5	37.98	20.31 ± 0.61	10.76 ± 0.63
NGC_3512l	100.1149	9.7628	18.2	11.53	21.76 ± 1.08	10.80 ± 0.88
NGB_06393161+0947353	99.88170	9.7931	12.0	165.8	0.40 ± 0.54	10.84 ± 0.60
NGB_06411288+0946000	100.3036	9.7668	15.0	42.04	17.71 ± 0.59	10.85 ± 0.62
NGA_06395924+0927245	99.99683	9.4568	14.4	53.60	20.77 ± 0.57	10.91 ± 0.62
NGC_3736l	100.1276	9.9101	17.9	14.05	19.95 ± 0.94	10.92 ± 0.81
NGC_4471l	100.1684	9.8506	15.2	52.27	22.51 ± 0.57	10.92 ± 0.62
NGC_7597l	100.4009	9.6556	14.8	69.23	16.98 ± 0.56	10.93 ± 0.61
NGC_3546l	100.1170	9.5926	15.8	50.44	18.97 ± 0.58	11.00 ± 0.62
NGA_06410245+0952249	100.2602	9.8735	0.00	47.52	24.27 ± 0.58	11.00 ± 0.62
NGB_06411650+0926080	100.3187	9.4356	15.0	21.55	19.64 ± 0.74	11.01 ± 0.70
NGC_5391l	100.2234	9.4981	16.3	37.84	21.04 ± 0.61	11.03 ± 0.64
NGB_06413589+0940414	100.3995	9.6783	14.9	41.19	19.68 ± 0.60	11.03 ± 0.63
NGC_5580l	100.2367	9.8657	15.3	53.99	20.41 ± 0.57	11.04 ± 0.62
NGC_6178l	100.3054	9.8651	15.2	62.66	21.08 ± 0.56	11.08 ± 0.62
NGB_06413166+0955151	100.3819	9.9210	12.0	79.46	-26. ± 0.55	11.10 ± 0.61
NGB_06414711+0938040	100.4462	9.6346	13.6	98.89	18.14 ± 0.55	11.10 ± 0.61
NGC_3071l	100.0859	9.6805	15.6	53.94	19.81 ± 0.57	11.12 ± 0.62
NGC_5125l	100.2066	9.8714	16.9	20.36	21.71 ± 0.76	11.13 ± 0.72
NGC_5612l	100.2393	9.4898	15.4	54.75	19.08 ± 0.57	11.14 ± 0.62
NGC_3300m	100.2450	9.6551	14.9	52.37	20.48 ± 0.57	11.14 ± 0.63
NGC_3424l	100.1104	9.5894	15.6	52.46	19.37 ± 0.57	11.15 ± 0.63

Table A.1 – continued from previous page

Object Name	RA	DEC	I (mag)	SNR	RV (km/s)	$v \sin i$ (km/s)
NGC_3615l	100.1205	9.7047	13.9	104.2	20.75 ± 0.55	11.17 ± 0.61
NGC_8668l	100.4435	9.7185	14.3	87.52	17.37 ± 0.55	11.24 ± 0.62
NGC_1704l	100.0250	9.8285	14.8	65.95	22.09 ± 0.56	11.26 ± 0.62
NGB_06403548+0917212	100.1478	9.2893	15.0	47.16	9.64 ± 0.58	11.27 ± 0.63
NGC_5775l	100.2620	9.8933	15.1	53.91	21.05 ± 0.57	11.28 ± 0.63
NGC_6288l	100.3212	9.8779	15.2	57.26	24.58 ± 0.57	11.30 ± 0.63
NGC_3794m	100.3199	9.4583	13.9	142.3	18.58 ± 0.54	11.31 ± 0.61
NGC_5685l	100.2530	9.7585	17.5	16.01	18.26 ± 0.87	11.31 ± 0.79
NGA_06404657+0921410	100.1940	9.3613	12.9	177.4	24.21 ± 0.54	11.35 ± 0.62
NGC_4048l	100.1435	9.5884	15.0	60.40	16.95 ± 0.57	11.40 ± 0.63
NGC_6327l	100.3246	9.5602	13.7	117.3	23.79 ± 0.54	11.41 ± 0.62
NGC_4682l	100.1809	9.4780	14.5	77.27	17.59 ± 0.55	11.45 ± 0.63
NGC_3592l	100.1190	9.5965	14.1	86.50	17.92 ± 0.55	11.47 ± 0.62
NGC_616l	99.98287	9.7110	17.2	20.68	21.35 ± 0.76	11.49 ± 0.74
NGB_06420333+0940181	100.2083	9.7484	14.8	58.03	19.12 ± 0.57	11.50 ± 0.64
NGB_06403787+0926232	100.1577	9.4398	15.0	29.01	70.10 ± 0.66	11.53 ± 0.68
NGB_06415492+0942525	100.4788	9.7146	15.0	50.94	17.75 ± 0.58	11.53 ± 0.64
NGC_6013l	100.2856	9.7143	14.5	76.12	20.70 ± 0.55	11.58 ± 0.63
NGC_5853l	100.2684	9.8572	13.4	146.3	26.92 ± 0.54	11.60 ± 0.62
NGC_5529l	100.2329	9.8981	14.5	80.12	22.07 ± 0.55	11.60 ± 0.63
NGB_06413327+0956393	100.3886	9.9443	14.7	48.18	19.76 ± 0.58	11.62 ± 0.65
NGC_2989l	100.0823	9.5303	16.2	39.74	19.70 ± 0.61	11.75 ± 0.66
NGA_06410171+0942429	100.2571	9.7119	0.00	36.85	17.77 ± 0.62	11.76 ± 0.67
NGC_5306l	100.2175	9.8753	15.1	58.64	20.97 ± 0.57	11.77 ± 0.64
NGC_2027l	100.0370	9.4358	15.8	45.95	17.14 ± 0.59	11.80 ± 0.66
NGC_3874l	100.1348	9.6958	15.8	43.93	18.57 ± 0.59	11.81 ± 0.66
NGC_6342l	100.3262	9.7351	15.3	61.12	21.16 ± 0.57	11.82 ± 0.64
NGB_06413455+0936323	100.0697	9.6985	14.5	68.12	92.52 ± 0.56	11.83 ± 0.64

Table A.1 – continued from previous page

Object Name	RA	DEC	I (mag)	SNR	RV (km/s)	$v \sin i$ (km/s)
NGC_5878l	100.2712	9.8133	14.1	106.6	23.44 ± 0.55	11.85 ± 0.64
NGC_4887l	100.1920	9.7972	15.2	62.09	21.02 ± 0.57	11.90 ± 0.65
NGC_5374m	100.5385	9.7342	14.4	66.79	17.98 ± 0.56	11.91 ± 0.65
NGA_06420256+0936525	100.5106	9.6145	13.4	88.93	17.22 ± 0.55	11.94 ± 0.64
NGC_6642l	100.3484	9.7878	15.6	45.49	17.16 ± 0.59	11.97 ± 0.66
NGB_06401704+0938373	100.0710	9.6436	13.0	98.69	24.01 ± 0.55	12.01 ± 0.64
NGC_5830l	100.2667	9.8190	13.6	128.8	17.49 ± 0.54	12.06 ± 0.64
NGB_06413603+0953070	100.4001	9.8853	15.1	49.33	21.19 ± 0.58	12.14 ± 0.67
NGC_4793l	100.1866	9.8299	15.6	42.07	21.91 ± 0.60	12.17 ± 0.68
NGC_2734l	100.0697	9.5753	17.0	22.62	16.81 ± 0.74	12.19 ± 0.76
NGC_1573l	100.0206	9.5751	15.8	47.82	17.54 ± 0.59	12.27 ± 0.67
NGC_5859l	100.2689	9.4358	16.0	34.74	22.71 ± 0.63	12.28 ± 0.70
NGC_8968l	100.4542	9.6850	14.1	89.23	17.99 ± 0.55	12.32 ± 0.65
NGA_06411013+0931285	100.2922	9.5245	14.4	63.82	20.09 ± 0.56	12.36 ± 0.66
NGC_5332l	100.2194	9.7391	14.5	88.23	19.36 ± 0.55	12.43 ± 0.66
NGA_06413250+0938074	100.3854	9.6353	13.0	116.3	18.90 ± 0.54	12.44 ± 0.65
NGC_6577l	100.3457	9.4918	16.4	31.17	-10. ± 0.65	12.45 ± 0.72
NGC_5876l	100.2710	9.5500	15.6	50.77	23.13 ± 0.58	12.45 ± 0.68
NGA_06403819+0929524	100.1591	9.4978	14.5	48.88	14.91 ± 0.59	12.53 ± 0.68
NGC_5610l	100.2393	9.4380	17.0	26.23	-9.1 ± 0.69	12.55 ± 0.75
NGA_06412100+0933361	100.3375	9.5600	13.1	150.5	18.15 ± 0.54	12.61 ± 0.66
NGB_06411714+0953393	100.3214	9.8943	15.0	43.29	20.54 ± 0.60	12.67 ± 0.69
NGA_06394960+0933221	99.95666	9.5561	13.2	72.30	15.63 ± 0.56	12.68 ± 0.67
NGC_8434l	100.4333	9.7644	17.7	13.34	20.73 ± 1.03	12.71 ± 0.99
NGC_7103l	100.3726	9.6550	15.0	58.41	19.00 ± 0.57	12.74 ± 0.68
NGB_06404459+0932262	100.1857	9.5405	15.0	55.09	18.35 ± 0.58	12.74 ± 0.68
NGC_6179l	100.3055	9.4687	14.5	79.66	18.93 ± 0.55	12.76 ± 0.67
NGC_7961l	100.4150	9.5555	15.4	37.34	18.56 ± 0.62	12.78 ± 0.71

Table A.1 – continued from previous page

Object Name	RA	DEC	I (mag)	SNR	RV (km/s)	$v \sin i$ (km/s)
NGB_06392233+0943212	100.1236	9.3143	14.9	45.25	16.21 ± 0.59	12.80 ± 0.70
NGC_6898l	100.3632	9.8692	15.2	64.39	18.84 ± 0.57	12.89 ± 0.68
NGC_3887m	100.3364	9.5033	14.9	77.12	19.82 ± 0.56	12.92 ± 0.68
NGC_4956l	100.1963	9.7021	15.2	63.72	18.59 ± 0.57	12.93 ± 0.68
NGC_4552l	100.1725	9.8026	13.9	107.7	19.74 ± 0.55	12.99 ± 0.67
NGC_2205l	100.0453	9.6686	15.9	40.18	15.57 ± 0.61	13.03 ± 0.71
NGC_1874m	100.0494	9.3527	14.4	35.00	16.19 ± 0.63	13.04 ± 0.73
NGC_6326l	100.3246	9.4836	15.4	65.09	25.70 ± 0.57	13.11 ± 0.69
NGC_6517l	100.3417	9.8535	14.5	85.03	18.66 ± 0.55	13.24 ± 0.68
NGC_4281l	100.1577	9.8308	14.8	77.22	24.49 ± 0.56	13.27 ± 0.69
NGC_5999l	100.2840	9.9043	16.9	22.65	21.53 ± 0.75	13.28 ± 0.82
NGC_1944l	100.0344	9.6901	17.2	25.31	19.29 ± 0.72	13.33 ± 0.80
NGC_4718l	100.1825	9.8132	17.9	11.55	18.02 ± 1.17	13.36 ± 1.16
NGC_5762l	100.2607	9.5869	13.9	87.29	19.06 ± 0.55	13.37 ± 0.69
NGC_2219l	100.0456	9.6446	15.4	12.76	16.74 ± 1.09	13.44 ± 1.09
NGC_8777l	100.4475	9.7000	15.0	65.89	19.00 ± 0.57	13.53 ± 0.70
NGC_5672l	100.2518	9.6889	16.6	27.94	18.32 ± 0.69	13.55 ± 0.79
NGC_4757l	100.1843	9.8942	15.4	52.93	20.73 ± 0.58	13.57 ± 0.71
NGC_5883l	100.2713	9.8154	14.6	66.06	17.43 ± 0.57	13.67 ± 0.71
NGC_3636l	100.1218	9.7354	15.5	55.09	19.99 ± 0.58	13.87 ± 0.72
NGC_5767l	100.2612	9.3885	14.9	52.11	19.56 ± 0.59	13.93 ± 0.73
NGB_06404492+0949090	100.1871	9.8191	15.0	40.28	-2.1 ± 0.62	13.97 ± 0.75
NGA_06393602+0924261	99.90008	9.4072	12.8	119.2	15.03 ± 0.54	13.99 ± 0.70
NGB_06401727+0925444	100.2354	9.3693	14.7	58.78	65.57 ± 0.58	14.01 ± 0.72
NGC_7049l	100.3699	9.6441	12.8	157.2	18.14 ± 0.54	14.13 ± 0.70
NGB_06410740+0931111	100.1446	9.9963	15.0	53.03	20.34 ± 0.58	14.15 ± 0.73
NGC_2768l	100.0720	9.4289	15.2	46.62	17.16 ± 0.60	14.20 ± 0.75
NGC_5687l	100.2532	9.8561	13.1	126.9	20.23 ± 0.54	14.22 ± 0.71

Table A.1 – continued from previous page

Object Name	RA	DEC	I (mag)	SNR	RV (km/s)	$v \sin i$ (km/s)
NGA_06410403+0923322	100.2667	9.3922	12.6	60.15	23.24 ± 0.57	14.22 ± 0.73
NGC_5817l	100.2655	9.4610	14.4	75.89	19.46 ± 0.56	14.27 ± 0.72
NGC_6438l	100.3355	9.7916	15.0	68.34	18.04 ± 0.57	14.28 ± 0.72
NGC_7939l	100.4140	9.5436	16.1	40.44	17.30 ± 0.62	14.31 ± 0.76
NGC_5408l	100.2247	9.8494	15.9	47.88	22.77 ± 0.60	14.36 ± 0.75
NGC_6210l	100.3103	9.6206	15.1	42.85	18.70 ± 0.61	14.36 ± 0.76
NGB_06400049+0933565	100.0020	9.5656	13.9	91.03	-16. ± 0.55	14.38 ± 0.72
NGC_5849l	100.2680	9.8061	13.4	123.3	19.43 ± 0.54	14.41 ± 0.71
NGB_06404921+0957383	99.88579	9.4790	14.6	37.22	16.59 ± 0.63	14.42 ± 0.78
NGC_2116m	100.0844	9.9350	13.9	112.6	24.21 ± 0.55	14.44 ± 0.71
NGA_06413199+1000244	100.3832	10.006	13.3	105.8	20.20 ± 0.55	14.46 ± 0.72
NGC_9279l	100.4644	9.7360	15.1	66.50	15.19 ± 0.57	14.53 ± 0.73
NGB_06413807+0955000	99.96937	9.9752	14.2	59.67	44.00 ± 0.58	14.69 ± 0.74
NGB_06411705+0932525	100.3210	9.5478	15.1	54.77	21.42 ± 0.58	14.70 ± 0.75
NGA_06400665+0920333	100.0277	9.3425	15.5	27.70	13.05 ± 0.71	14.71 ± 0.85
NGB_06415671+0934070	100.4862	9.5688	14.1	84.13	28.81 ± 0.56	14.71 ± 0.73
NGC_2605l	100.0637	9.7660	16.2	37.75	18.61 ± 0.63	14.74 ± 0.79
NGB_06400758+0956535	100.0316	9.9481	15.0	53.66	20.80 ± 0.59	14.81 ± 0.76
NGB_06395879+0958454	99.99495	9.9793	13.9	99.97	36.72 ± 0.55	14.94 ± 0.73
NGC_5158l	100.2086	9.8743	15.2	59.94	19.26 ± 0.58	15.03 ± 0.76
NGC_3803l	100.1315	9.6043	17.4	21.62	17.64 ± 0.81	15.07 ± 0.95
NGB_06403378+0948434	100.0034	9.5503	14.4	59.01	49.56 ± 0.58	15.08 ± 0.76
NGB_06402313+0956191	100.0963	9.9388	12.4	231.2	-16. ± 0.54	15.14 ± 0.73
NGC_3809l	100.1318	9.8064	14.0	103.9	21.59 ± 0.55	15.23 ± 0.74
NGC_5969l	100.2800	9.7071	16.9	22.53	20.47 ± 0.79	15.25 ± 0.95
NGC_5190l	100.2104	9.7626	16.2	36.06	6.31 ± 0.65	15.38 ± 0.83
NGB_06403786+0935565	100.5381	9.7505	13.9	41.96	-2.3 ± 0.62	15.53 ± 0.81
NGB_06395189+0924474	99.96616	9.4131	15.1	45.89	26.45 ± 0.61	15.60 ± 0.80

Table A.1 – continued from previous page

Object Name	RA	DEC	I (mag)	SNR	RV (km/s)	$v \sin i$ (km/s)
NGC_34211	100.1104	9.4894	17.3	23.14	18.77 ± 0.79	15.70 ± 0.97
NGB_06395232+0925070	99.96800	9.4186	14.4	59.43	9.56 ± 0.58	15.71 ± 0.78
NGC_58471	100.2679	9.5965	15.8	47.02	24.96 ± 0.61	15.75 ± 0.80
NGC_14761	100.0168	9.7179	16.2	42.39	22.56 ± 0.62	15.75 ± 0.82
NGB_06395265+0958313	100.0877	9.7744	14.5	73.75	25.20 ± 0.57	15.79 ± 0.77
NGB_06413328+0941464	100.4399	9.6586	15.1	55.65	17.93 ± 0.59	15.80 ± 0.79
NGB_06405548+0931212	100.2311	9.5227	12.7	196.3	0.83 ± 0.54	15.85 ± 0.75
NGC_33901	100.1090	9.6192	15.7	56.85	20.23 ± 0.59	15.91 ± 0.79
NGC_17431	100.0262	9.5990	14.7	53.90	17.19 ± 0.59	16.05 ± 0.80
NGC_13161	100.0110	9.5900	15.1	54.19	16.99 ± 0.59	16.06 ± 0.80
NGB_06405867+0936131	100.2444	9.6036	13.2	83.01	24.26 ± 0.56	16.15 ± 0.77
NGC_29731	100.0812	9.8384	16.4	35.47	25.68 ± 0.66	16.17 ± 0.87
NGC_58961	100.2727	9.8946	17.4	17.50	21.97 ± 0.95	16.23 ± 1.16
NGC_59681	100.2797	9.4633	13.3	124.4	20.85 ± 0.55	16.25 ± 0.76
NGC_56341	100.2484	9.6159	17.5	11.02	23.74 ± 1.36	16.31 ± 1.61
NGC_20241	100.0370	9.5694	15.5	55.85	18.08 ± 0.59	16.34 ± 0.80
NGC_43671	100.1625	9.5999	14.5	65.04	19.68 ± 0.58	16.37 ± 0.79
NGC_62551	100.3171	9.4454	16.1	34.13	21.22 ± 0.67	16.41 ± 0.89
NGC_59941	100.2833	9.5111	14.2	102.0	22.66 ± 0.55	16.67 ± 0.78
NGB_06410173+0955515	100.3477	9.7662	14.4	64.25	16.65 ± 0.58	16.69 ± 0.80
NGC_46641	100.1801	9.5208	15.0	57.66	18.87 ± 0.59	16.69 ± 0.81
NGB_06415218+0946222	100.4674	9.7727	15.1	48.89	13.69 ± 0.61	16.72 ± 0.83
NGC_52981	100.2167	9.7513	14.0	113.4	24.89 ± 0.55	16.80 ± 0.78
NGC_69871	100.3670	9.5471	16.5	33.75	18.90 ± 0.68	16.81 ± 0.91
NGC_60311	100.2871	9.6874	13.8	112.6	20.18 ± 0.55	16.85 ± 0.78
NGA_06402115+0959024	100.0881	9.9840	14.6	52.26	31.68 ± 0.60	16.85 ± 0.83
NGC_61391	100.3010	9.6700	16.4	32.91	16.93 ± 0.69	16.86 ± 0.92
NGB_06411532+0954505	100.3138	9.9141	15.0	55.52	21.80 ± 0.59	16.88 ± 0.82

Table A.1 – continued from previous page

Object Name	RA	DEC	I (mag)	SNR	RV (km/s)	$v \sin i$ (km/s)
NGC_59871	100.2823	9.6874	14.0	90.75	25.81 ± 0.56	16.93 ± 0.79
NGC_60631	100.2903	9.4151	15.3	59.12	17.12 ± 0.59	16.96 ± 0.82
NGC_55051	100.2317	9.6402	15.9	34.63	22.57 ± 0.67	16.97 ± 0.91
NGC_33321	100.1061	9.8071	14.2	95.89	24.98 ± 0.56	17.13 ± 0.79
NGC_22271	100.0461	9.7572	17.9	14.48	16.90 ± 1.13	17.26 ± 1.44
NGB_06402924+0944070	100.2632	9.4341	14.7	44.19	23.57 ± 0.63	17.26 ± 0.87
NGB_06401168+0945555	100.2654	9.4722	14.2	37.30	23.71 ± 0.66	17.31 ± 0.91
NGB_06413660+0937565	100.1374	9.3863	15.0	41.80	53.84 ± 0.64	17.42 ± 0.89
NGB_06400266+0935242	100.3916	9.9801	14.4	60.84	25.81 ± 0.59	17.52 ± 0.84
NGC_48231	100.1880	9.7983	17.4	18.23	20.46 ± 0.97	17.59 ± 1.27
NGC_2491	99.96954	9.6270	17.4	16.82	17.23 ± 1.02	17.63 ± 1.34
NGC_59781	100.2810	9.5759	16.8	22.30	18.70 ± 0.85	17.65 ± 1.14
NGB_06414070+0924323	100.0251	10.007	14.8	41.78	31.64 ± 0.64	17.68 ± 0.90
NGC_53941	100.2234	9.5568	13.4	119.2	17.26 ± 0.55	17.70 ± 0.80
NGC_61561	100.3034	9.8786	13.9	105.7	21.59 ± 0.55	17.72 ± 0.80
NGC_56771	100.2521	9.4877	13.2	60.87	18.67 ± 0.59	17.78 ± 0.84
NGC_64511	100.3362	9.4792	15.6	44.68	21.13 ± 0.63	17.84 ± 0.89
NGC_72971	100.3816	9.8091	13.3	144.9	20.20 ± 0.54	17.84 ± 0.80
NGC_48071	100.1876	9.7616	14.4	91.53	21.87 ± 0.56	17.98 ± 0.82
NGC_1215m	99.95266	9.6097	14.4	62.10	17.09 ± 0.59	18.04 ± 0.85
NGC_57831	100.2628	9.4845	15.8	51.31	18.43 ± 0.61	18.04 ± 0.88
NGC_49861	100.1979	9.8246	12.7	169.1	27.13 ± 0.54	18.06 ± 0.80
NGC_58741	100.2706	9.8461	13.1	133.2	21.34 ± 0.55	18.13 ± 0.81
NGC_56531	100.2500	9.4805	14.2	102.0	19.38 ± 0.56	18.19 ± 0.82
NGC_43481	100.1611	9.5761	16.6	32.83	17.96 ± 0.71	18.24 ± 0.99
NGC_77501	100.4065	9.8255	16.0	38.50	18.73 ± 0.66	18.29 ± 0.95
NGB_06393635+0956313	100.3379	9.8911	15.0	24.11	-17. ± 0.83	18.38 ± 1.15
NGB_06411514+0930171	100.3130	9.5047	14.4	36.03	17.90 ± 0.68	18.47 ± 0.98

Table A.1 – continued from previous page

Object Name	RA	DEC	I (mag)	SNR	RV (km/s)	$v \sin i$ (km/s)
NGC_5768l	100.2614	9.8100	17.7	15.71	18.42 ± 1.12	18.63 ± 1.53
NGC_1161m	99.94466	9.6816	12.6	140.6	18.46 ± 0.55	18.69 ± 0.82
NGC_5879l	100.2712	9.8417	16.7	29.55	24.46 ± 0.75	18.70 ± 1.06
NGC_5035l	100.2007	9.4502	15.3	59.00	21.93 ± 0.60	18.77 ± 0.88
NGC_4700l	100.1817	9.5865	16.8	26.47	17.23 ± 0.80	18.95 ± 1.14
NGB_06411306+0923040	100.3044	9.3845	14.5	40.50	15.04 ± 0.66	19.05 ± 0.97
NGC_6486l	100.3389	9.8510	16.9	26.29	24.51 ± 0.80	19.06 ± 1.15
NGB_06404246+0955171	100.1769	9.9214	15.1	28.00	21.03 ± 0.78	19.10 ± 1.12
NGC_4568l	100.1735	9.5286	17.5	11.45	18.21 ± 1.48	19.10 ± 2.04
NGC_5770l	100.2616	9.3875	15.6	47.96	18.27 ± 0.63	19.11 ± 0.93
NGB_06414121+0957404	100.4217	9.9613	13.8	102.5	1.98 ± 0.56	19.16 ± 0.84
NGB_06403415+0925121	100.3442	9.8970	13.8	40.13	-36. ± 0.66	19.16 ± 0.98
NGC_3399l	100.1093	9.6337	13.2	130.0	9.05 ± 0.55	19.19 ± 0.83
NGC_4605l	100.1760	9.7688	16.7	28.76	20.91 ± 0.77	19.55 ± 1.14
NGC_5863l	100.2696	9.4187	16.1	32.01	20.99 ± 0.74	19.69 ± 1.09
NGC_6136l	100.3005	9.4978	15.2	52.24	21.09 ± 0.62	19.83 ± 0.94
NGC_4944l	100.1956	9.8133	14.8	69.89	20.72 ± 0.58	19.89 ± 0.89
NGA_06415804+0943062	100.4918	9.7183	13.6	72.32	21.32 ± 0.58	19.91 ± 0.89
NGC_7487l	100.3969	9.4450	17.4	23.07	17.92 ± 0.89	19.95 ± 1.31
NGC_5482l	100.2300	9.6913	17.3	16.38	20.63 ± 1.14	19.95 ± 1.65
NGC_6304l	100.3222	9.7577	16.3	36.89	23.18 ± 0.70	20.01 ± 1.05
NGC_5906l	100.2741	9.5186	17.2	19.91	25.99 ± 0.99	20.04 ± 1.45
NGC_5907l	100.2742	9.8799	14.0	95.89	24.28 ± 0.56	20.17 ± 0.87
NGC_6610l	100.3472	9.6345	17.0	22.33	21.37 ± 0.92	20.18 ± 1.36
NGC_4886l	100.1920	9.7872	17.6	15.79	22.93 ± 1.18	20.19 ± 1.73
NGC_4379l	100.1632	9.8168	16.7	22.41	27.05 ± 0.92	20.26 ± 1.37
NGC_4070l	100.1450	9.7625	15.7	49.24	19.84 ± 0.63	20.31 ± 0.97
NGC_4474l	100.1687	9.5848	15.9	38.90	18.92 ± 0.69	20.54 ± 1.06

Table A.1 – continued from previous page

Object Name	RA	DEC	I (mag)	SNR	RV (km/s)	$v \sin i$ (km/s)
NGC_7303l	100.3820	9.5317	15.2	56.77	23.43 ± 0.61	20.54 ± 0.95
NGB_06404124+0954303	100.2089	9.9510	15.0	46.89	21.58 ± 0.65	20.72 ± 1.00
NGC_9773l	100.4819	9.5885	16.8	17.78	17.82 ± 1.10	20.78 ± 1.66
NGC_8307l	100.4280	9.7157	13.7	125.9	16.77 ± 0.55	20.95 ± 0.88
NGC_4635l	100.1780	9.4518	17.2	12.70	22.17 ± 1.46	20.97 ± 2.21
NGC_3383l	100.1087	9.8358	18.0	12.30	17.83 ± 1.54	21.57 ± 2.39
NGB_06400317+0920434	100.3463	9.6260	15.0	54.47	21.31 ± 0.63	21.77 ± 1.01
NGC_4026l	100.1424	9.7312	16.4	37.08	18.86 ± 0.72	21.82 ± 1.15
NGC_6572l	100.3448	9.5442	17.5	14.81	21.38 ± 1.33	21.84 ± 2.09
NGC_4547l	100.1723	9.9038	12.4	200.9	25.59 ± 0.54	21.89 ± 0.88
NGA_06405362+0947043	100.2234	9.7845	0.00	61.85	19.08 ± 0.61	21.92 ± 0.98
NGC_9083l	100.4584	9.4922	13.9	112.9	20.60 ± 0.56	22.10 ± 0.91
NGC_4207l	100.1532	9.6845	17.3	22.41	19.81 ± 0.98	22.15 ± 1.56
NGB_06411193+0959414	100.2997	9.9947	14.9	49.88	20.54 ± 0.65	22.34 ± 1.06
NGB_06394694+0927343	99.94558	9.4594	13.9	61.75	-35. ± 0.61	22.46 ± 1.00
NGC_4962l	100.1967	9.8858	15.9	36.19	24.87 ± 0.74	22.49 ± 1.21
NGA_06411963+0931443	100.3317	9.5289	12.6	166.1	20.07 ± 0.55	22.63 ± 0.90
NGC_1698l	100.0248	9.5925	15.1	48.32	17.81 ± 0.66	22.75 ± 1.09
NGB_06412320+0930363	100.1453	9.9019	14.7	59.17	21.71 ± 0.62	23.06 ± 1.04
NGC_6439l	100.3355	9.7598	13.6	125.8	17.73 ± 0.56	23.19 ± 0.93
NGC_5184l	100.2097	9.8441	17.2	22.00	13.86 ± 1.04	23.52 ± 1.74
NGC_4975l	100.1972	9.8137	14.0	59.44	19.99 ± 0.63	23.54 ± 1.05
NGB_06411792+0929010	99.98037	9.9864	14.7	48.27	-13. ± 0.67	23.58 ± 1.13
NGB_06412439+0921383	100.3516	9.3608	12.1	191.3	-4.5 ± 0.54	23.62 ± 0.91
NGA_06395638+0943315	99.98491	9.7254	12.7	125.1	34.19 ± 0.56	23.66 ± 0.94
NGC_7451l	100.3951	9.8389	17.5	22.58	22.40 ± 1.02	23.66 ± 1.73
NGC_9037l	100.4566	9.6875	17.9	11.43	15.33 ± 1.81	23.70 ± 3.06
NGB_06392691+0941222	100.4433	9.8861	14.9	57.29	41.70 ± 0.64	23.90 ± 1.08

Table A.1 – continued from previous page

Object Name	RA	DEC	I (mag)	SNR	RV (km/s)	$v \sin i$ (km/s)
NGC_4770m	100.4644	9.8951	12.8	186.8	20.19 ± 0.55	23.93 ± 0.92
NGA_06405884+0930573	100.2451	9.5159	12.2	173.2	20.81 ± 0.55	23.93 ± 0.92
NGC_1025l	99.99933	9.5615	14.9	53.50	17.88 ± 0.65	23.96 ± 1.11
NGC_1533m	99.99850	9.5863	14.2	75.90	8.56 ± 0.60	24.17 ± 1.01
NGC_5924l	100.2758	9.6063	12.5	215.6	20.95 ± 0.54	24.67 ± 0.93
NGC_1490l	100.0175	9.7849	17.7	18.24	17.03 ± 1.26	24.80 ± 2.21
NGB_06413210+0928040	100.3603	9.7349	15.1	40.89	19.67 ± 0.74	24.80 ± 1.28
NGB_06411322+0955080	100.3050	9.9190	13.5	95.81	18.67 ± 0.58	24.95 ± 1.00
NGB_06411652+0952131	100.3187	9.8703	11.8	253.5	58.31 ± 0.54	25.00 ± 0.93
NGC_6344l	100.3266	9.5248	15.7	39.41	67.46 ± 0.76	25.19 ± 1.33
NGC_2608l	100.0639	9.6379	16.8	24.97	22.53 ± 1.00	25.20 ± 1.78
NGB_06410821+0934090	100.0734	9.7994	15.0	65.10	20.03 ± 0.63	25.26 ± 1.09
NGC_2558l	100.0614	9.6869	17.1	25.69	16.45 ± 0.99	25.30 ± 1.75
NGA_06395618+0930461	99.98408	9.5128	12.3	125.7	23.43 ± 0.56	25.37 ± 0.97
NGB_06413682+0927050	100.4034	9.4515	12.9	151.9	16.24 ± 0.55	25.50 ± 0.96
NGC_5015l	100.1996	9.5508	15.8	51.39	17.33 ± 0.68	25.67 ± 1.21
NGC_6014l	100.2857	9.5010	17.2	23.93	21.21 ± 1.05	25.71 ± 1.90
NGC_1822m	100.0429	9.6486	13.3	110.5	19.54 ± 0.57	25.72 ± 1.00
NGC_3379l	100.1085	9.5064	18.5	10.14	20.62 ± 2.22	25.84 ± 4.06
NGC_3907l	100.1366	9.8581	13.9	97.10	23.06 ± 0.58	25.86 ± 1.02
NGC_5852l	100.2683	9.8639	11.4	288.8	25.35 ± 0.54	26.00 ± 0.94
NGC_3973l	100.1398	9.4578	18.1	12.57	20.71 ± 1.85	26.23 ± 3.42
NGC_4098l	100.1465	9.8657	13.9	110.5	25.45 ± 0.57	26.39 ± 1.01
NGC_6253l	100.3170	9.8377	16.8	29.95	21.94 ± 0.92	26.42 ± 1.69
NGA_06404412+0923553	100.1838	9.3986	13.3	85.59	13.75 ± 0.60	26.59 ± 1.06
NGB_06412507+0936000	100.3545	9.6000	15.1	42.02	20.84 ± 0.76	26.67 ± 1.39
NGC_6427l	100.3342	9.8189	16.8	28.86	19.90 ± 0.95	26.74 ± 1.77
NGA_06400268+0918198	100.0111	9.3055	12.2	137.6	24.52 ± 0.56	26.78 ± 0.99

Table A.1 – continued from previous page

Object Name	RA	DEC	I (mag)	SNR	RV (km/s)	$v \sin i$ (km/s)
NGC_5647l	100.2494	9.8258	15.9	41.57	24.97 ± 0.77	26.81 ± 1.41
NGC_9228l	100.4630	9.5035	16.5	33.30	19.36 ± 0.87	26.97 ± 1.62
NGA_06411088+1000409	100.2953	10.011	12.0	208.6	17.25 ± 0.55	26.99 ± 0.97
NGC_7424l	100.3940	9.4824	17.4	16.61	19.63 ± 1.50	27.18 ± 2.85
NGC_5475l	100.2297	9.5551	16.9	30.32	19.38 ± 0.94	27.24 ± 1.76
NGB_06400882+0919090	100.0367	9.3191	13.5	87.70	-5.4 ± 0.60	27.28 ± 1.08
NGB_06393333+0930111	99.88887	9.5032	13.7	52.60	64.90 ± 0.70	27.35 ± 1.28
NGC_7622l	100.4018	9.8595	16.7	32.11	17.36 ± 0.91	27.41 ± 1.71
NGB_06412214+0921313	100.3422	9.3586	14.3	108.7	15.68 ± 0.58	27.47 ± 1.04
NGA_06394264+0931514	99.92766	9.5309	13.7	96.08	27.93 ± 0.59	27.54 ± 1.07
NGB_06394909+0924141	100.4086	9.9168	14.0	73.06	47.40 ± 0.63	27.62 ± 1.15
NGC_5732l	100.2580	9.8343	15.9	45.98	24.41 ± 0.74	27.69 ± 1.39
NGC_1610m	100.0089	9.7539	15.0	57.70	17.31 ± 0.68	27.95 ± 1.26
NGB_06403376+0932575	100.1406	9.5491	11.6	249.7	-27. ± 0.54	28.17 ± 0.98
NGC_4991l	100.1981	9.6758	17.0	21.77	17.45 ± 1.25	28.51 ± 2.47
NGC_503l	99.97862	9.5208	16.7	23.54	2.55 ± 1.18	28.66 ± 2.33
NGB_06405782+0919272	100.4064	9.6779	14.4	71.78	-7.0 ± 0.64	28.76 ± 1.20
NGC_5663l	100.2512	9.5734	16.9	28.62	20.72 ± 1.02	28.78 ± 2.01
NGB_06415283+0954484	100.4701	9.9134	13.5	103.7	-11. ± 0.59	29.09 ± 1.09
NGB_06400043+0956282	100.0017	9.9412	15.1	39.14	-79. ± 0.84	29.27 ± 1.65
NGC_1211l	100.0061	9.6290	17.7	21.38	41.09 ± 1.33	29.72 ± 2.71
NGC_5690l	100.2534	9.5039	16.7	26.56	17.13 ± 1.12	29.83 ± 2.27
NGC_6272l	100.3198	9.8633	18.2	10.11	20.82 ± 2.66	29.86 ± 5.49
NGB_06400859+0949181	100.0357	9.8218	15.0	34.84	29.78 ± 0.94	30.29 ± 1.89
NGC_6119l	100.2976	9.4704	16.9	21.30	22.43 ± 1.41	31.07 ± 2.96
NGB_06402814+0923454	100.1172	9.3960	15.1	52.78	19.31 ± 0.76	31.59 ± 1.54
NGB_06402258+0923020	100.0940	9.3839	13.4	99.14	62.69 ± 0.61	31.89 ± 1.19
NGC_2829l	100.0743	9.7480	17.2	24.15	20.34 ± 1.31	31.98 ± 2.81

Table A.1 – continued from previous page

Object Name	RA	DEC	I (mag)	SNR	RV (km/s)	$v \sin i$ (km/s)
NGC_5336l	100.2196	9.4820	17.1	14.88	16.91 ± 2.02	31.99 ± 4.37
NGC_2883l	100.0766	9.8442	17.5	23.18	25.23 ± 1.36	32.09 ± 2.93
NGB_06414500+0956111	100.4374	9.9364	13.6	78.41	40.87 ± 0.65	32.39 ± 1.31
NGC_5486l	100.2302	9.5569	16.8	20.26	24.00 ± 1.58	32.97 ± 3.49
NGB_06405828+0917090	99.98008	9.6357	14.1	46.44	40.89 ± 0.84	33.06 ± 1.78
NGB_06400082+0933010	100.1136	9.3435	14.7	62.33	-49. ± 0.72	33.08 ± 1.49
NGC_4475l	100.1688	9.5836	15.6	65.86	18.59 ± 0.71	33.13 ± 1.45
NGC_71l	99.96287	9.6091	15.8	38.29	13.92 ± 0.96	33.23 ± 2.07
NGA_06404516+0928444	100.1881	9.4790	12.6	98.90	17.76 ± 0.62	33.34 ± 1.24
NGC_6019l	100.2860	9.6703	16.6	20.07	18.12 ± 1.64	33.69 ± 3.68
NGC_1124m	99.93954	9.3393	14.4	65.42	18.54 ± 0.72	33.96 ± 1.51
NGA_06404713+0918332	100.1963	9.3092	13.2	78.24	35.74 ± 0.67	34.43 ± 1.40
NGC_731l	99.98695	9.5264	17.7	16.80	13.34 ± 2.04	35.07 ± 4.71
NGC_6699l	100.3518	9.5458	14.4	99.22	19.54 ± 0.63	35.11 ± 1.30
NGC_5840l	100.2675	9.4778	17.3	13.91	19.92 ± 2.46	35.27 ± 5.72
NGA_06395562+0947318	99.98175	9.7921	14.1	99.40	-9.3 ± 0.64	35.88 ± 1.33
NGC_5869l	100.2701	9.8737	16.9	25.31	17.82 ± 1.45	35.91 ± 3.38
NGB_06412866+0955303	100.3694	9.9250	13.3	140.5	0.91 ± 0.59	36.16 ± 1.20
NGB_06411709+0952404	100.4029	9.8938	14.6	57.84	56.81 ± 0.81	36.44 ± 1.79
NGB_06410444+0936434	100.2685	9.6120	14.6	53.42	18.18 ± 0.85	36.85 ± 1.93
NGC_5574l	100.2365	9.4998	16.7	33.15	18.26 ± 1.20	36.87 ± 2.80
NGC_6181l	100.3056	9.6371	15.7	49.59	18.38 ± 0.90	36.93 ± 2.04
NGC_5645l	100.2492	9.8635	14.7	71.35	10.75 ± 0.74	37.22 ± 1.63
NGB_06395082+0955080	99.96175	9.9190	14.7	48.25	39.41 ± 0.94	37.91 ± 2.17
NGC_5851l	100.2681	9.4585	15.8	49.31	21.81 ± 0.93	38.07 ± 2.15
NGC_2963l	100.0804	9.8083	14.1	96.05	23.23 ± 0.66	38.27 ± 1.45
NGC_5986l	100.2823	9.4703	14.3	70.72	27.06 ± 0.76	38.37 ± 1.71
NGC_5633l	100.2480	9.5863	13.3	121.3	20.45 ± 0.62	38.45 ± 1.32

Table A.1 – continued from previous page

Object Name	RA	DEC	I (mag)	SNR	RV (km/s)	$v \sin i$ (km/s)
NGA_06412280+0929389	100.3450	9.4941	13.6	91.19	27.43 ± 0.68	38.47 ± 1.49
NGC_5721l	100.2569	9.3843	17.1	17.50	14.23 ± 2.24	38.48 ± 5.50
NGB_06393064+0928565	100.3204	9.9877	14.6	61.36	20.90 ± 0.82	38.52 ± 1.88
NGC_6163l	100.3041	9.4609	14.6	90.00	21.04 ± 0.68	38.72 ± 1.51
NGB_06412303+0927262	100.3459	9.4573	11.7	308.3	31.87 ± 0.55	38.81 ± 1.12
NGC_6308l	100.3226	9.5079	16.8	17.92	20.53 ± 2.24	39.07 ± 5.55
NGB_06415500+0953262	100.4791	9.8905	12.4	227.1	-14. ± 0.56	39.20 ± 1.16
NGC_6340l	100.3262	9.4758	15.7	53.79	20.96 ± 0.91	39.37 ± 2.14
NGB_06410593+0927171	100.2747	9.4548	13.9	121.1	21.42 ± 0.63	39.62 ± 1.36
NGC_6428l	100.3343	9.8137	17.1	22.41	22.99 ± 1.90	40.23 ± 4.77
NGC_5990l	100.2825	9.4401	17.5	16.35	21.67 ± 2.63	41.05 ± 6.74
NGC_4397l	100.1640	9.7602	17.3	21.81	19.47 ± 2.03	41.45 ± 5.21
NGC_4967l	100.1967	9.5190	16.3	13.07	24.48 ± 3.34	41.62 ± 8.64
NGC_4490l	100.1699	9.5741	17.7	11.11	21.32 ± 3.92	41.68 ± 10.17
NGB_06413269+0953242	100.3862	9.8900	13.7	91.55	7.81 ± 0.72	42.44 ± 1.69
NGC_7401l	100.3930	9.4314	15.0	72.79	19.45 ± 0.81	42.48 ± 1.95
NGC_5261l	100.2142	9.8900	16.5	30.38	21.17 ± 1.61	43.39 ± 4.19
NGB_06392300+0920525	99.94941	9.5494	15.1	11.62	22.04 ± 4.02	43.46 ± 10.65
NGC_5897l	100.2730	9.5279	15.1	67.72	27.27 ± 0.87	43.83 ± 2.16
NGC_8595l	100.4406	9.4452	15.6	41.52	23.75 ± 1.25	43.90 ± 3.23
NGC_6582l	100.3460	9.7240	14.9	72.29	23.85 ± 0.85	44.29 ± 2.10
NGC_6383l	100.3302	9.5135	16.5	35.06	24.34 ± 1.47	44.56 ± 3.87
NGC_2756l	100.0710	9.6561	17.7	17.44	23.95 ± 2.83	44.73 ± 7.60
NGC_2969m	100.1952	9.5419	15.0	53.55	21.72 ± 1.05	44.77 ± 2.70
NGC_6220l	100.3118	9.5432	14.2	105.4	21.26 ± 0.71	44.83 ± 1.68
NGC_5478l	100.2298	9.8471	14.2	96.80	21.61 ± 0.74	45.01 ± 1.77
NGB_06421512+0943535	100.3795	9.4518	14.2	64.24	30.88 ± 0.93	45.05 ± 2.36
NGC_6316l	100.3237	9.4905	13.5	149.4	25.03 ± 0.63	45.06 ± 1.43

Table A.1 – continued from previous page

Object Name	RA	DEC	I (mag)	SNR	RV (km/s)	$v \sin i$ (km/s)
NGC_1527m	99.99820	9.9400	14.3	94.87	23.83 ± 0.75	45.33 ± 1.81
NGC_4035l	100.1429	9.4214	16.3	17.38	28.90 ± 2.90	45.33 ± 7.84
NGC_1872m	100.0486	9.7655	15.0	56.29	28.40 ± 1.04	45.70 ± 2.69
NGC_5786l	100.2632	9.5486	16.9	20.93	20.97 ± 2.49	46.07 ± 6.77
NGC_6115l	100.2971	9.5141	17.0	22.64	28.91 ± 2.56	49.17 ± 7.20
NGC_2931l	100.0789	9.6374	16.5	26.38	17.96 ± 2.26	49.77 ± 6.37
NGC_5938l	100.2767	9.9029	14.6	56.49	25.10 ± 1.18	50.38 ± 3.22
NGC_5884l	100.2717	9.8876	13.5	118.9	-30. ± 0.73	50.56 ± 1.85
NGC_5041l	100.2011	9.6107	14.3	90.19	17.86 ± 0.85	50.57 ± 2.22
NGA_06405542+0937237	100.2309	9.6232	13.5	78.24	18.17 ± 0.94	51.19 ± 2.53
NGC_5798l	100.2643	9.5365	16.7	22.07	26.75 ± 2.82	51.30 ± 8.08
NGB_06413625+0951383	100.4010	9.8606	14.9	44.97	44.66 ± 1.46	51.37 ± 4.10
NGA_06403632+0918575	100.1513	9.3159	13.6	96.47	19.18 ± 0.83	51.59 ± 2.19
NGC_7044l	100.3697	9.4529	15.0	55.95	17.07 ± 1.24	52.05 ± 3.46
NGC_6168l	100.3046	9.5185	16.2	35.68	27.80 ± 1.85	52.36 ± 5.30
NGC_6067l	100.2909	9.4533	12.7	149.4	27.96 ± 0.68	52.73 ± 1.72
NGC_5244l	100.2137	9.6108	15.9	31.82	21.32 ± 2.09	52.90 ± 6.04
NGC_6334l	100.3253	9.6403	15.6	46.61	22.29 ± 1.49	53.20 ± 4.26
NGB_06414642+0959525	100.4434	9.9979	13.7	87.59	54.60 ± 0.91	53.25 ± 2.48
NGB_06410253+0934555	100.2605	9.5821	12.7	152.2	22.53 ± 0.68	53.29 ± 1.72
NGA_06410689+0929240	100.2787	9.4900	14.3	62.01	27.51 ± 1.18	53.41 ± 3.32
NGA_06402103+0936319	100.0876	9.6088	12.1	179.8	22.09 ± 0.65	53.81 ± 1.60
NGC_5509l	100.2317	9.8701	16.9	26.49	28.90 ± 2.60	54.34 ± 7.64
NGB_06400525+0945040	100.0218	9.7512	14.7	36.50	26.35 ± 1.93	54.38 ± 5.61
NGB_06403299+0923111	100.3701	9.5816	14.7	61.74	23.96 ± 1.23	54.91 ± 3.52
NGC_3612l	100.1202	9.5515	15.1	53.57	13.68 ± 1.47	57.10 ± 4.32
NGC_5837l	100.2674	9.5825	17.2	22.66	24.46 ± 3.35	57.69 ± 10.12
NGA_06411542+0946396	100.3142	9.7776	12.6	178.0	21.50 ± 0.68	57.77 ± 1.75

Table A.1 – continued from previous page

Object Name	RA	DEC	I (mag)	SNR	RV (km/s)	$v \sin i$ (km/s)
NGC_5803l	100.2645	9.5217	11.9	223.2	22.70 ± 0.63	58.01 ± 1.58
NGC_4721l	100.1827	9.7988	16.3	32.77	17.19 ± 2.39	58.29 ± 7.20
NGC_6022l	100.2867	9.3952	12.9	177.0	20.01 ± 0.69	58.55 ± 1.79
NGC_6201l	100.3088	9.4445	14.5	89.56	22.12 ± 1.02	58.84 ± 2.91
NGC_6592l	100.3465	9.5896	17.0	27.23	21.95 ± 2.92	59.10 ± 8.89
NGB_06420684+0922373	100.3201	9.6057	15.0	56.79	20.12 ± 1.49	59.48 ± 4.45
NGA_06393533+0932323	99.89720	9.5423	13.4	64.33	28.07 ± 1.35	59.83 ± 4.01
NGC_4575l	100.1741	9.8311	14.4	84.30	30.67 ± 1.12	61.04 ± 3.28
NGC_3165l	100.0907	9.8692	16.9	23.98	20.58 ± 3.57	61.69 ± 11.05
NGC_4723l	100.1827	9.8084	14.9	67.35	22.98 ± 1.37	61.88 ± 4.12
NGC_5958l	100.2790	9.6817	15.3	57.12	25.35 ± 1.60	62.30 ± 4.86
NGC_3966l	100.1395	9.5829	15.9	50.61	16.41 ± 1.80	62.69 ± 5.52
NGA_06414382+0940500	100.4325	9.6805	12.5	170.9	28.52 ± 0.74	62.95 ± 2.02
NGC_2867l	100.0759	9.5291	18.0	15.76	18.37 ± 5.64	63.25 ± 17.68
NGB_06413910+0944323	100.4127	9.7425	15.1	33.10	-13. ± 2.74	63.51 ± 8.56
NGC_6678l	100.3508	9.8952	16.4	37.57	18.91 ± 2.43	63.58 ± 7.58
NGC_5857l	100.2687	9.5037	15.4	44.01	18.52 ± 2.11	63.87 ± 6.56
NGC_6162l	100.3039	9.5922	14.6	80.68	24.30 ± 1.28	65.27 ± 3.88
NGC_3494l	100.1143	9.8750	15.9	44.56	26.49 ± 2.19	65.70 ± 6.88
NGC_5495l	100.2306	9.8710	15.9	35.96	20.60 ± 2.86	68.09 ± 9.14
NGA_06410948+0951500	100.2895	9.8638	13.6	132.8	24.93 ± 0.99	71.54 ± 3.00
NGB_06405882+0939181	100.3522	9.6265	14.3	76.22	25.10 ± 1.58	72.48 ± 5.05
NGC_6899l	100.3631	9.5850	13.1	175.0	26.44 ± 0.88	75.67 ± 2.66
NGC_1372m	99.97600	9.9410	15.7	49.55	24.86 ± 2.80	79.98 ± 9.38
NGA_06405154+0943242	100.2147	9.7233	12.7	148.8	38.59 ± 1.06	80.03 ± 3.35
NGB_06412028+0958292	100.3345	9.9748	14.2	89.71	66.99 ± 1.71	82.85 ± 5.68
NGA_06405024+0920023	100.2093	9.3339	13.3	92.07	1.84 ± 1.70	83.89 ± 5.69
NGA_06394771+0926067	99.94879	9.4351	11.6	215.6	30.59 ± 0.91	86.57 ± 2.84

Table A.1 – continued from previous page

Object Name	RA	DEC	I (mag)	SNR	RV (km/s)	$v \sin i$ (km/s)
NGC_6913l	100.3637	9.5351	15.7	47.77	24.93 ± 3.40	87.16 ± 11.66
NGC_8235l	100.4257	9.7070	16.4	36.27	25.69 ± 4.51	87.72 ± 15.53
NGB_06412562+0944030	100.0511	9.9369	14.7	58.08	42.47 ± 2.86	87.98 ± 9.81
NGB_06400600+0949424	100.0413	9.8948	14.7	67.05	21.18 ± 2.78	93.38 ± 9.65
NGC_1473l	100.0167	9.4519	14.5	58.93	19.35 ± 3.40	97.40 ± 11.98
NGC_1932m	100.0585	9.3412	12.6	163.1	15.41 ± 1.34	98.12 ± 4.56
NGC_3617m	100.2889	9.9355	14.4	71.79	23.84 ± 2.89	98.89 ± 10.18
NGB_06395019+0927020	100.0658	9.3592	15.0	74.73	29.62 ± 2.90	101.2 ± 10.28
NGC_5358l	100.2209	9.8831	14.8	67.18	23.41 ± 3.35	103.3 ± 11.93
NGB_06403823+0928191	100.1592	9.4721	14.9	58.90	17.09 ± 4.09	107.3 ± 14.71
NGC_1968l	100.0354	9.7370	14.2	99.67	28.01 ± 2.47	107.7 ± 8.83
NGC_6081l	100.2927	9.5569	15.0	69.26	-0.2 ± 3.82	112.6 ± 13.85
NGB_06414685+0956323	100.4452	9.9422	14.0	82.42	20.25 ± 3.40	115.8 ± 12.37
NGB_06394307+0926010	99.92945	9.4338	12.3	148.2	32.87 ± 2.05	119.5 ± 7.43
NGC_4641m	100.4502	9.7120	12.3	203.5	17.70 ± 1.72	127.6 ± 6.26

A Appendix 2

A list of the recent surveys and catalogs that are available for NGC 2264;

- **X-ray**

- Ramírez et al. (2004) - Chandra X-Ray Observations of 263 sources
- Simon & Dahm (2005) - XMM Newton images of 190 X-ray sources
- Flaccomio, Micela & Sciortino (2006) - Chandra X-ray observations of 420 sources
- Dahm et al. (2007) - XMM Newton images of 300 sources

- **Infrared**

- Sung, Stauffer & Bessell (2009) - Spitzer data of 20,000 objects in NGC 2264
- Cody et al. (2014) - CSI-2264. Simultaneous Spitzer and CoRoT time series photometry
- Rapon et al. (2014) - Spitzer photometry for 10,454 young stellar objects (YSOs)

- **Other Photometric**

- Rebull et al. (2002) - Photometry at optical (UBVRI) and near-infrared (JHK) wavelengths for 5600 stars
- Lamm et al. (2004) - Survey 10 600 stars with I magnitudes 9.8-21mag.
- Drew et al. (2005) - Isaac Newton Telescope (INT) Photometric H α Survey of the Northern Galactic Plane (IPHAS)

- **Variability and rotation**

- Lamm et al. (2004) - 405 periodic pre-MS

- Makidon et al. (2004) - 201 periodic pre-MS stars
- Cody et al. (2014), Affer et al. (2013) - Rotation periods for 209 cluster members (CSI-2264)

- **Spectroscopic**

- Rebull et al. (2002) - Spectral classifications for ~ 400 pre-MS stars.
- Dahm & Simon (2005) - Spectra covering the 6000-8000 Å range for 150 H α and x-ray sources.
- Fűrész et al. (2006) - 1078 high-resolution spectra of 990 stars, confirming 471 stars as members on the basis of their radial velocity and/or H α emission.
- Tobin et al. (2015) - Radial velocities for 695 stars, of which approximately 407 stars are confirmed members

Bibliography

Adams F. C., 2010, *Annu. Rev. Astron. Astrophys.*, 48, 47

Adams M. T., Strom K. M., Strom S. E., 1983, *ApJS*, 53, 893

Affer L., Micela G., Favata F., Flaccomio E., Bouvier J., 2013, *MNRAS*, 430, 1433

Alexander D. R., Ferguson J. W., 1994, *ApJ*, 437, 879

Alves J., Bouy H., 2012, *A&A*, 547, A97

Alves de Oliveira C., Casali M., 2008, *A&A*, 485, 155

Andre P., Ward-Thompson D., Barsony M., 1993, *ApJ*, 406, 122

Andre P., Ward-Thompson D., Barsony M., 2000, *Protostars and Planets IV*, , 59

Auvergne M., Bodin P., Boisnard L., Buey J.-T., Chaintreuil S., Epstein G., Jouret M., Lam-Trong T., Levacher P., Magnan A., Perez R., Plasson P., Plessier J., Peter G., Steller M., Tiphène D., Baglin A., Agogué P., Appourchaux T., Barbet D., Beaufort T., Bellenger R., Berlin R., Bernardi P., Blouin D., Boumier P., Bonneau F., Briet R., Butler B., Cautain R., Chiavassa F., Costes V., Cuvillo J., Cunha-Parro V., de Oliveira Fialho F., Decaudin M., Defise J.-M., Djalal S., Docclo A., Drummond R., Dupuis O., Exil G., Fauré C., Gaboriaud A., Gamet P., Gavalda P., Grolleau E., Gueguen L., Guivarc'h V., Guterman P., Hasiba J., Huntzinger G., Hustaix H., Imbert C., Jeanville G., Johlander B., Jorda L., Journoud P., Karioty F., Kerjean L., Lafond L., Lapeyrere V., Landiech P., Larqué T., Laudet P., Le Merrer J., Leporati L., Leruyet B., Levieuge B., Llebaria A., Martin L., Mazy E., Mesnager J.-M., Michel J.-P., Moalic J.-P., Monjoin W., Naudet D., Neukirchner S., Nguyen-Kim K., Ollivier M., Orcesi J.-L., Ottacher H., Oulali A., Parisot J., Perruchot S., Piacentino A., Pinheiro da Silva L., Platzer J., Pontet B., Pradines A., Quentin C., Rohbeck U., Rolland G., Rollenhagen F., Romagnan R., Russ N.,

- Samadi R., Schmidt R., Schwartz N., Sebbag I., Smit H., Sunter W., Tello M., Toulouse P., Ulmer B., Vandermarcq O., Vergnault E., Wallner R., Waultier G., Zanatta P., 2009, *A&A*, 506, 411
- Bagnulo S., Jehin E., Ledoux C., Cabanac R., Melo C., Gilmozzi R., ESO Paranal Science Operations Team, 2003, *The Messenger*, 114, 10
- Ballesteros-Paredes J., Hartmann L., 2007, *RMxAA*, 43, 123
- Ballesteros-Paredes J., Klessen R. S., Mac Low M.-M., Vazquez-Semadeni E., 2007, *Protostars and Planets V*, , 63
- Ballesteros-Paredes J., Hartmann L., Vázquez-Semadeni E., 1999, *ApJ*, 527, 285
- Banerjee S., Kroupa P., 2014, *ApJ*, 787, 158
- Baraffe I., Chabrier G., Gallardo J., 2009, *ApJL*, 702, L27
- Baraffe I., Chabrier G., Allard F., Hauschildt P. H., 1998, *A&A*, 337, 403
- Baraffe I., Chabrier G., Allard F., Hauschildt P. H., 2002, *A&A*, 382, 563
- Baraffe I., Vorobyov E., Chabrier G., 2012, *ApJ*, 756, 118
- Barentsen G., 2012
- Barentsen G., Vink J. S., Drew J. E., Sale S. E., 2013, *MNRAS*, 429, 1981
- Bastian N., Gieles M., Ercolano B., Gutermuth R., 2009, *MNRAS*, 392, 868
- Baumgardt H., Kroupa P., 2007, *MNRAS*, 380, 1589
- Baxter E. J., Covey K. R., Muench A. A., Fűrész G., Rebull L., Szentgyorgyi A. H., 2009, *AJ*, 138, 963
- Bell C. P. M., Naylor T., Mayne N. J., Jeffries R. D., Littlefair S. P., 2013, *MNRAS*, 434, 806

- Bergin E. A., Tafalla M., 2007, *Annu. Rev. Astron. Astrophys.*, 45, 339
- Bertelli G., Girardi L., Marigo P., Nasi E., 2008, *VizieR Online Data Catalog*, 348, 40815
- Bertin G., 2014, *Dynamics of Galaxies*
- Bertout C., Siess L., Cabrit S., 2007, *A&A*, 473, L21
- Bildsten L., Brown E. F., Matzner C. D., Ushomirsky G., 1997, *ApJ*, 482, 442
- Bouvier J., Cabrit S., Fernandez M., Martin E. L., Matthews J. M., 1993, *A&A*, 272, 176
- Bouvier J., Matt S. P., Mohanty S., Scholz A., Stassun K. G., Zanni C., 2014, *Protostars and Planets VI*, , 433
- Bressert E., Bastian N., Gutermuth R., Megeath S. T., Allen L., Evans, II N. J., Rebull L. M., Hatchell J., Johnstone D., Bourke T. L., Cieza L. A., Harvey P. M., Merin B., Ray T. P., Tothill N. F. H., 2010, *MNRAS*, 409, L54
- Briceño C., Preibisch T., Sherry W. H., Mamajek E. A., Mathieu R. D., Walter F. M., Zinnecker H., 2007, *Protostars and Planets V*, , 345
- Brown A. G. A., Dekker G., de Zeeuw P. T., 1997, *MNRAS*, 285, 479
- Busà I., Aznar Cuadrado R., Terranegra L., Andretta V., Gomez M. T., 2007, *A&A*, 466, 1089
- Camenzind M., 1990, in Klare G., ed., *Reviews in Modern Astronomy*, p. p. 234
- Canuto V. M., Mazzitelli I., 1991, *ApJ*, 370, 295
- Cartwright A., Whitworth A. P., 2004, *MNRAS*, 348, 589
- Chaboyer B., Kim Y.-C., 1995, *ApJ*, 454, 767

- Chabrier G., 2003, *PASP*, 115, 763
- Chabrier G., Baraffe I., Allard F., Hauschildt P., 2000, *ApJ*, 542, 464
- Cieza L., Baliber N., 2007, *ApJ*, 671, 605
- Cieza L. A., Baliber N. R., 2009, American Astronomical Society Meeting Abstracts #213, p. 413.01
- Ciolek G. E., Basu S., 2001, *ApJ*, 547, 272
- Claret A., Diaz-Cordoves J., Gimenez A., 1995, *A&AS*, 114, 247
- Cody A. M., Stauffer J. R., Micela G., Baglin A., CSI 2264 Team, 2013, *Astronomische Nachrichten*, 334, 63
- Cody A. M., Stauffer J., Baglin A., Micela G., Rebull L. M., Flaccomio E., Morales-Calderón M., Aigrain S., Bouvier J., Hillenbrand L. A., Gutermuth R., Song I., Turner N., Alencar S. H. P., Zwintz K., Plavchan P., Carpenter J., Findeisen K., Carey S., Terebey S., Hartmann L., Calvet N., Teixeira P., Vrba F. J., Wolk S., Covey K., Poppenhaeger K., Günther H. M., Forbrich J., Whitney B., Affer L., Herbst W., Hora J., Barrado D., Holtzman J., Marchis F., Wood K., Medeiros Guimarães M., Lillo Box J., Gillen E., McQuillan A., Espaillat C., Allen L., D'Alessio P., Favata F., 2014, *AJ*, 147, 82
- Cottaar M., Meyer M. R., Andersen M., Espinoza P., 2012, *A&A*, 539, A5
- Dahm S. E., Simon T., 2005, *AJ*, 129, 829
- Dahm S. E., The Young Cluster and Star Forming Region NGC 2264, 966, 2008
- Dahm S. E., Simon T., Proszkow E. M., Patten B. M., 2007, *AJ*, 134, 999
- D'Antona F., Mazzitelli I., 1994, *ApJS*, 90, 467
- D'Antona F., Mazzitelli I., 1997, *MmSAI*, 68, 807

- Dolan C. J., Mathieu R. D., 1999, *AJ*, 118, 2409
- Drew J. E., Greimel R., Irwin M. J., Aungwerojwit A., Barlow M. J., Corradi R. L. M., Drake J. J., Gänsicke B. T., Groot P., Hales A., Hopewell E. C., Irwin J., Knigge C., Leisy P., Lennon D. J., Mampaso A., Masheder M. R. W., Matsuura M., Morales-Rueda L., Morris R. A. H., Parker Q. A., Phillipps S., Rodriguez-Gil P., Roelofs G., Skillen I., Sokoloski J. L., Steeghs D., Unruh Y. C., Viironen K., Vink J. S., Walton N. A., Witham A., Wright N., Zijlstra A. A., Zurita A., 2005, *MNRAS*, 362, 753
- Duchêne G., Kraus A., 2013, *Annu. Rev. Astron. Astrophys.*, 51, 269
- Dukes D., Krumholz M. R., 2012, *ApJ*, 754, 56
- Dzib S. A., Loinard L., Rodríguez L. F., Galli P., 2014, *ApJ*, 788, 162
- Elmegreen B. G., 2000, *ApJ*, 530, 277
- Elmegreen B. G., 2007, *ApJ*, 668, 1064
- Elmegreen B. G., Efremov Y., Pudritz R. E., Zinnecker H., 2000, *Protostars and Planets IV*, , 179
- Evans, II N. J., Dunham M. M., Jørgensen J. K., Enoch M. L., Merín B., van Dishoeck E. F., Alcalá J. M., Myers P. C., Stapelfeldt K. R., Huard T. L., Allen L. E., Harvey P. M., van Kempen T., Blake G. A., Koerner D. W., Mundy L. G., Padgett D. L., Sargent A. I., 2009, *ApJS*, 181, 321
- Falgarone E., Phillips T. G., Walker C. K., 1991, *ApJ*, 378, 186
- Fatuzzo M., Adams F. C., 2002, *ApJ*, 570, 210
- Feiden G. A., Chaboyer B., Dotter A., 2011, *ApJL*, 740, L25
- Feigelson E. D., Montmerle T., 1999, *Annu. Rev. Astron. Astrophys.*, 37, 363

- Fernandes B., Gregorio-Hetem J., Hetem A., 2012, *A&A*, 541, A95
- Fernández D., Figueras F., Torra J., 2008, *The Ages of Stars*, p. p. 123
- Fűrész G., Hartmann L. W., Szentgyorgyi A. H., Ridge N. A., Rebull L., Stauffer J., Latham D. W., Conroy M. A., Fabricant D. G., Roll J., 2006, *ApJ*, 648, 1090
- Fűrész G., Hartmann L. W., Megeath S. T., Szentgyorgyi A. H., Hamden E. T., 2008, *ApJ*, 676, 1109
- Fitzpatrick E. L., 1999, *PASP*, 111, 63
- Flaccomio E., Micela G., Sciortino S., Favata F., Corbally C., Tomaney A., 1999, *A&A*, 345, 521
- Flaccomio E., Micela G., Sciortino S., 2006, *A&A*, 455, 903
- Fleck R. C., Hunter J. H., 1976, *MNRAS*, 175, 335
- Geller A. M., Latham D. W., Mathieu R. D., 2015, *ArXiv e-prints*
- Gieles M., Portegies Zwart S. F., 2011, *MNRAS*, 410, L6
- Gieles M., 2010, in de Grijs R., Lépine J. R. D., eds, *IAU Symposium*, p. p. 69
- Gieles M., Sana H., Portegies Zwart S. F., 2010, *MNRAS*, 402, 1750
- Gilmore G., Randich S., Asplund M., Binney J., Bonifacio P., Drew J., Feltzing S., Ferguson A., Jeffries R., Micela G., et al., 2012, *The Messenger*, 147, 25
- Gray D. F., 1992, *The observation and analysis of stellar photospheres*.
- Gustafsson B., Edvardsson B., Eriksson K., Jørgensen U. G., Nordlund Å., Plez B., 2008, *A&A*, 486, 951
- Gutermuth R. A., Megeath S. T., Myers P. C., Allen L. E., Pipher J. L., Fazio G. G., 2009, *ApJS*, 184, 18

- Hartmann L., 1998, *Accretion Processes in Star Formation*
- Hartmann L., 2001, *AJ*, 121, 1030
- Hartmann L., 2003, *ApJ*, 585, 398
- Hartmann L., Ballesteros-Paredes J., Bergin E. A., 2001, *ApJ*, 562, 852
- Hartmann L., Ballesteros-Paredes J., Heitsch F., 2012, *MNRAS*, 420, 1457
- Hayashi C., 1961, *PASJ*, 13, 450
- Herbig G. H., Bell K. R., 1988, *Third Catalog of Emission-Line Stars of the Orion Population : 3 : 1988*
- Herbig G. H., 1954, *ApJ*, 119, 483
- Hillenbrand L. A., White R. J., 2004, *ApJ*, 604, 741
- Hillenbrand L. A., 1997, *AJ*, 113, 1733
- Hillenbrand L. A., 2005, *ArXiv Astrophysics e-prints*
- Hillenbrand L. A., 2009, in *Mamajek E. E., Soderblom D. R., Wyse R. F. G., eds, IAU Symposium, p. p. 81*
- Hillenbrand L. A., Hoffer A. S., Herczeg G. J., 2013, *AJ*, 146, 85
- Horne K., 1986, *PASP*, 98, 609
- Hosokawa T., Offner S. S. R., Krumholz M. R., 2011, *ApJ*, 738, 140
- Iglesias C. A., Rogers F. J., 1996, *ApJ*, 464, 943
- Irwin J., Hodgkin S., Aigrain S., Bouvier J., Hebb L., Irwin M., Moraux E., 2008, *VizieR Online Data Catalog*, 738, 40675
- Jackson R. J., Jeffries R. D., 2010, *MNRAS*, 402, 1380

- Jackson R. J., Jeffries R. D., 2010, MNRAS, 407, 465
- Jackson R. J., Jeffries R. D., 2012, MNRAS, 423, 2966
- Jeans J. H., 1902, Royal Society of London Philosophical Transactions Series A, 199, 1
- Jeffries R. D., 2007, MNRAS, 381, 1169
- Jeffries R. D., Maxted P. F. L., Oliveira J. M., Naylor T., 2006, MNRAS, 371, L6
- Jeffries R. D., Jackson R. J., James D. J., Cargile P. A., 2009, MNRAS, 400, 317
- Jeffries R. D., Littlefair S. P., Naylor T., Mayne N. J., 2011, MNRAS, 418, 1948
- Jeffries R. D., Jackson R. J., Cottaar M., Koposov S. E., Lanzafame A. C., Meyer M. R., Prisinzano L., Randich S., Sacco G. G., Brugaletta E., Caramazza M., Damiani F., Franciosini E., Frasca A., Gilmore G., Feltzing S., Micela G., Alfaro E., Bensby T., Pancino E., Recio-Blanco A., de Laverny P., Lewis J., Magrini L., Morbidelli L., Costado M. T., Jofré P., Klutsch A., Lind K., Maiorca E., 2014, A&A, 563, A94
- Jeffries R. D., James D. J., Thurston M. R., 1998, MNRAS, 300, 550
- Johns-Krull C. M., 2007, ApJ, 664, 975
- Kearns K. E., Eaton N. L., Herbst W., Mazzurco C. J., 1997, AJ, 114, 1098
- Kenyon S. J., Hartmann L., 1995, ApJS, 101, 117
- Kenyon M. J., Jeffries R. D., Naylor T., Oliveira J. M., Maxted P. F. L., 2005, MNRAS, 356, 89
- Köhler R., Petr-Gotzens M. G., McCaughrean M. J., Bouvier J., Duchêne G., Quirrenbach A., Zinnecker H., 2006, A&A, 458, 461
- Konigl A., Pudritz R. E., 2000, Protostars and Planets IV, , 759

- Kroupa P., 2001, in Montmerle T., André P., eds, *From Darkness to Light: Origin and Evolution of Young Stellar Clusters*, p. 387
- Kroupa P., 2007, in Elmegreen B. G., Palous J., eds, *IAU Symposium*, p. p. 230
- Kruijssen J. M. D., Maschberger T., Moeckel N., Clarke C. J., Bastian N., Bonnell I. A., 2012, *MNRAS*, 419, 841
- Kuhn M. A., Feigelson E. D., Getman K. V., Baddeley A. J., Broos P. S., Sills A., Bate M. R., Povich M. S., Luhman K. L., Busk H. A., Naylor T., King R. R., 2014, *ApJ*, 787, 107
- Lada C. J., Lada E. A., 2003, *Annu. Rev. Astron. Astrophys.*, 41, 57
- Lada C. J., 1987, in Peimbert M., Jugaku J., eds, *Star Forming Regions*, p. p. 1
- Lada C. J., 1999, in Lada C. J., Kylafis N. D., eds, p. *NATO Advanced Science Institutes (ASI) Series C*
- Lamm M., Bailer-Jones C. A. L., Mundt R., Herbst W., 2004, in Maeder A., Eenens P., eds, *Stellar Rotation*, p. 125
- Lamm M. H., Mundt R., Bailer-Jones C. A. L., Herbst W., 2005, *A&A*, 430, 1005
- Lanzafame A. C., Frasca A., Damiani F., Franciosini E., Cottaar M., Sousa S. G., Tabernerero H. M., Klutsch A., Spina L., Biazzo K., Prisinzano L., Sacco G. G., Randich S., Brugaletta E., Delgado Mena E., Adibekyan V., Montes D., Bonito R., Gameiro J. F., Alcalá J. M., González Hernández J. I., Jeffries R., Messina S., Meyer M., Gilmore G., Asplund M., Binney J., Bonifacio P., Drew J. E., Feltzing S., Ferguson A. M. N., Micela G., Negueruela I., Prusti T., Rix H.-W., Vallenari A., Alfaro E. J., Allende Prieto C., Babusiaux C., Bensby T., Blomme R., Bragaglia A., Flaccomio E., Francois P., Hambly N., Irwin M., Koposov S. E., Korn A. J., Smiljanic R., Van Eck S., Walton N., Bayo A., Bergemann M., Carraro G., Costado M. T., Edvardsson B., Heiter U., Hill V., Hourihane A., Jackson R. J., Jofré P.,

- Lardo C., Lewis J., Lind K., Magrini L., Marconi G., Martayan C., Masseron T., Monaco L., Morbidelli L., Sbordone L., Worley C. C., Zaggia S., 2015, *A&A*, 576, A80
- Larson R. B., 1973, *Annu. Rev. Astron. Astrophys.*, 11, 219
- Lee Y., Stark A. A., Kim H.-G., Moon D.-S., 2001, *ApJS*, 136, 137
- Lindegren L., Babusiaux C., Bailer-Jones C., Bastian U., Brown A. G. A., Cropper M., Høg E., Jordi C., Katz D., van Leeuwen F., Luri X., Mignard F., de Bruijne J. H. J., Prusti T., 2008, in Jin W. J., Platais I., Perryman M. A. C., eds, *IAU Symposium*, p. p. 217
- Littlefair S. P., Naylor T., Burningham B., Jeffries R. D., 2005, *MNRAS*, 358, 341
- Littlefair S. P., Naylor T., Mayne N. J., Saunders E., Jeffries R. D., 2011, *MNRAS*, 413, L56
- Luhman K. L., 2007, *ApJS*, 173, 104
- Makidon R. B., Rebull L. M., Strom S. E., Adams M. T., Patten B. M., 2004, *AJ*, 127, 2228
- Mariñas N., Lada E. A., Teixeira P. S., Lada C. J., 2013, *ApJ*, 772, 81
- Marsden S. C., Carter B. D., Donati J.-F., 2009, *MNRAS*, 399, 888
- Mayne N. J., Naylor T., 2008, *MNRAS*, 386, 261
- McQuillan A., Mazeh T., Aigrain S., 2014, *ApJS*, 211, 24
- Mendoza V. E. E., Gomez T., 1980, *MNRAS*, 190, 623
- Mestel L., Spitzer, Jr. L., 1956, *MNRAS*, 116, 503
- Mihalas D., Dappen W., Hummer D. G., 1988, *ApJ*, 331, 815

- Moitinho A., Alves J., Huélamo N., Lada C. J., 2001, *ApJL*, 563, L73
- Nakamura F., Li Z.-Y., 2005, *ApJ*, 631, 411
- O'Dell M. A., Hendry M. A., Collier Cameron A., 1994, *MNRAS*, 268, 181
- Padoan P., Haugbølle T., Nordlund Å., 2014, *ApJ*, 797, 32
- Palla F., Stahler S. W., 1999, *ApJ*, 525, 772
- Palla F., Stahler S. W., 2000, *ApJ*, 540, 255
- Palla F., Stahler S. W., Parigi G., 1993, in Weiss W. W., Baglin A., eds, *IAU Colloq. 137: Inside the Stars*, p. 437
- Park B.-G., Sung H., Bessell M. S., Kang Y. H., 2000, *AJ*, 120, 894
- Parks J. R., Plavchan P., White R. J., Gee A. H., 2014, *ApJS*, 211, 3
- Pasquini L., Avila G., Blecha A., Cacciari C., Cayatte V., Colless M., Damiani F., de Propriis R., Dekker H., di Marcantonio P., Farrell T., Gillingham P., Guinouard I., Hammer F., Kaufer A., Hill V., Marteaud M., Modigliani A., Mulas G., North P., Popovic D., Rossetti E., Royer F., Santin P., Schmutzer R., Simond G., Vola P., Waller L., Zoccali M., 2002, *The Messenger*, 110, 1
- Pecaut M. J., Mamajek E. E., 2013, *ApJS*, 208, 9
- Perez M. R., The P. S., Westerlund B. E., 1987, *PASP*, 99, 1050
- Perryman M. A. C., 2005, in Seidelmann P. K., Monet A. K. B., eds, *Astrometry in the Age of the Next Generation of Large Telescopes*, p. 3
- Perryman M. A. C., Lindegren L., Kovalevsky J., Hoeg E., Bastian U., Bernacca P. L., Crézé M., Donati F., Grenon M., Grewing M., van Leeuwen F., van der Marel H., Mignard F., Murray C. A., Le Poole R. S., Schrijver H., Turon C., Arenou F., Froeschlé M., Petersen C. S., 1997, *A&A*, 323, L49

- Pols O. R., Tout C. A., Eggleton P. P., Han Z., 1995, MNRAS, 274, 964
- Pozzo M., Naylor T., Jeffries R. D., Drew J. E., 2003, MNRAS, 341, 805
- Preibisch T., Guenther E., Zinnecker H., Sterzik M., Frink S., Roeser S., 1998, A&A, 333, 619
- Ramírez S. V., Rebull L., Stauffer J., Hearty T., Hillenbrand L., Jones B., Makidon R., Pravdo S., Strom S., Werner M., 2004, AJ, 127, 2659
- Rapson V. A., Pipher J. L., Gutermuth R. A., Megeath S. T., Allen T. S., Myers P. C., Allen L. E., 2014, ApJ, 794, 124
- Rebull L. M., Hillenbrand L. A., Strom S. E., Duncan D. K., Patten B. M., Pavlovsky C. M., Makidon R., Adams M. T., 2000, AJ, 119, 3026
- Rebull L. M., Makidon R. B., Strom S. E., Hillenbrand L. A., Birmingham A., Patten B. M., Jones B. F., Yagi H., Adams M. T., 2002, AJ, 123, 1528
- Reggiani M., Robberto M., Da Rio N., Meyer M. R., Soderblom D. R., Ricci L., 2011, A&A, 534, A83
- Rieke G. H., Lebofsky M. J., 1985, ApJ, 288, 618
- Sacco G. G., Randich S., Franciosini E., Pallavicini R., Palla F., 2007, A&A, 462, L23
- Schmeja S., 2011, Astronomische Nachrichten, 332, 172
- Schultz G. V., Wiemer W., 1975, A&A, 43, 133
- Sergison D. J., Mayne N. J., Naylor T., Jeffries R. D., Bell C. P. M., 2013, MNRAS, 434, 966
- Shu F. H., 1977, ApJ, 214, 488
- Shu F., 1991, *Series of books in astronomy*, The Physics of Astrophysics: Gas dynamics, University Science Books

- Shu F. H., Adams F. C., Lizano S., 1987, *Annu. Rev. Astron. Astrophys.*, 25, 23
- Shu F., Najita J., Ostriker E., Wilkin F., Ruden S., Lizano S., 1994, *ApJ*, 429, 781
- Siess L., Dufour E., Forestini M., 2000, *A&A*, 358, 593
- Siess L., Forestini M., Dougados C., 1997, *A&A*, 324, 556
- Simon T., Dahm S. E., 2005, *ApJ*, 618, 795
- Simon M., Ghez A. M., Leinert C., 1993, *ApJL*, 408, L33
- Soderblom D. R., King J. R., Siess L., Jones B. F., Fischer D., 1999, *AJ*, 118, 1301
- Soderblom D. R., Hillenbrand L. A., Jeffries R. D., Mamajek E. E., Naylor T., 2014, *Protostars and Planets VI*, , 219
- Spitzer L., 1978, *Physical processes in the interstellar medium*
- Stahler S. W., 1983, *ApJ*, 274, 822
- Strom S. E., 1995, in Lizano S., Torrelles J. M., eds, *Revista Mexicana de Astronomia y Astrofisica Conference Series*, p. 317
- Sung H., Bessell M. S., 2010, *AJ*, 140, 2070
- Sung H., Bessell M. S., Lee S.-W., 1997, *AJ*, 114, 2644
- Sung H., Bessell M. S., Chun M.-Y., Karimov R., Ibrahimov M., 2008, *AJ*, 135, 441
- Sung H., Stauffer J. R., Bessell M. S., 2009, *AJ*, 138, 1116
- Swenson F. J., Faulkner J., Rogers F. J., Iglesias C. A., 1994, *ApJ*, 425, 286
- Tan J. C., Krumholz M. R., McKee C. F., 2006, *ApJL*, 641, L121
- Tassis K., Mouschovias T. C., 2004, *ApJ*, 616, 283

- Teixeira P. S., Lada C. J., Young E. T., Marengo M., Muench A., Muzerolle J., Siegler N., Rieke G., Hartmann L., Megeath S. T., Fazio G., 2006, *ApJL*, 636, L45
- Teixeira P. S., Lada C. J., Marengo M., Lada E. A., 2012, *A&A*, 540, A83
- Terebey S., Shu F. H., Cassen P., 1984, *ApJ*, 286, 529
- Tobin J. J., Hartmann L., Furesz G., Mateo M., Megeath S. T., 2009, *ApJ*, 697, 1103
- Tobin J. J., Hartmann L., Fűrész G., Hsu W.-H., Mateo M., 2015, *AJ*, 149, 119
- Tognelli E., Prada Moroni P. G., Degl'Innocenti S., 2011, *A&A*, 533, A109
- Tonry J., Davis M., 1979, *AJ*, 84, 1511
- Tout C. A., Livio M., Bonnell I. A., 1999, *MNRAS*, 310, 360
- Trejo A., Rodríguez L. F., 2008, in Rector T. A., De Young D. S., eds, *Extragalactic Jets: Theory and Observation from Radio to Gamma Ray*, p. 129
- Turner D. G., 2012, *Astronomische Nachrichten*, 333, 174
- Venuti L., Bouvier J., Flaccomio E., Alencar S. H. P., Irwin J., Stauffer J. R., Cody A. M., Teixeira P. S., Sousa A. P., Micela G., Cuillandre J.-C., Peres G., 2014, *A&A*, 570, A82
- Vorobyov E. I., Basu S., 2015, *ApJ*, 805, 115
- Walker M. F., 1956, *ApJS*, 2, 365
- Walker G., Matthews J., Kuschnig R., Johnson R., Rucinski S., Pazder J., Burley G., Walker A., Skaret K., Zee R., Grocott S., Carroll K., Sinclair P., Sturgeon D., Harron J., 2003, *PASP*, 115, 1023
- Weidner C., Kroupa P., 2006, *MNRAS*, 365, 1333

Werner M. W., Roellig T. L., Low F. J., Rieke G. H., Rieke M., Hoffmann W. F., Young E., Houck J. R., Brandl B., Fazio G. G., Hora J. L., Gehrz R. D., Helou G., Soifer B. T., Stauffer J., Keene J., Eisenhardt P., Gallagher D., Gautier T. N., Irace W., Lawrence C. R., Simmons L., Van Cleve J. E., Jura M., Wright E. L., Cruikshank D. P., 2004, *ApJS*, 154, 1

Wilking B. A., Meyer M. R., Robinson J. G., Greene T. P., 2005, *AJ*, 130, 1733

Wilson R. E., 1953, Carnegie Institute Washington D.C. Publication, , 0

Yorke H. W., Bodenheimer P., Laughlin G., 1993, *ApJ*, 411, 274